LOW-TEMPERATURE MAGNETISM

Low-temperature adsorption of gases on metal surfaces (Review)

Yu. G. Ptushinskiĭ*

Institute of Physics of the National Academy of Sciences of Ukraine, pr. Nauki 46, Kiev 03028, Ukraine

A review of the published results on the adsorption of some simple gases on metal surfaces at low substrate temperatures ($T_s \leq 30$ K, down to liquid helium temperatures) is given. The methods of investigating low-temperature adsorption of gases are briefly discussed. Attention is focused primarily on the adsorption of hydrogen on transition metals and noble metals. The results of experimental studies on transition metals include information about the state of the adsorbed particles (atoms or molecules), the spectra of the adsorption states, the kinetics of adsorption–desorption processes, the participation of precursor states in the adsorption mechanism, the role of various quantum properties of the H_2 and D_2 molecules, the influence of two-dimensional phase transitions, the structure of the adsorbed layer (adlayer), and electron-stimulated processes. Experimental studies of the adsorption of hydrogen on noble metals in conjunction with theoretical calculations provide information about the fine details of the quantum sticking mechanism, in particular, the trapping of molecules into quasi-bound states and the influence of diffraction by the lattice of surface atoms. Data on the role of the rotational state of the molecules, ortho–para conversion, and direct photodesorption are examined. A review of the relatively few papers on the adsorption of oxygen, carbon monoxide, and nitrogen is also given. © *2004 American Institute of Physics.* [DOI: 10.1063/1.1645151]

INTRODUCTION

1.1. Gas adsorption and its role

The key role of adsorption in a number of important processes in technology and in the living world is widely known. It suffices to mention heterogeneous catalysis, micro- and nanoelectronics, hydrogen fuel storage, hydrogen embrittlement of metals, corrosion, and the assimilation of atmospheric nitrogen by living organisms. Adlayer are, among other things, low-dimensional systems, and the study of their properties is extremely important for basic physics.

For these reasons there is enormous interest in the study of adsorption processes, and a huge number of both experimental and theoretical papers have been published. The assimilation of ultrahigh-vacuum technique into experimental physics in the early 1960s and the development of many extremely informative surface diagnostic techniques have made for unprecedented progress in this field. As examples we can name the methods of temperature-programmed desorption (TPD) or thermodesorption spectroscopy (TDS), low-energy electron diffraction (LEED), Auger electron spectroscopy (AES), ultraviolet and x-ray photoelectron spectroscopy (UPS and XPS), electron energy-loss spectroscopy (EELS) and its high-resolution version (HREELS), scanning tunneling microscopy (STM), etc.

It would be impossible (and hardly necessary) to cover all of this immense field in a single review article. We have therefore drastically narrowed the scope: First, we consider only adsorption systems in which the adsorbents (substrates) are metals and the adsorbates are molecules of simple gases.

Second, we concentrate mainly on low-temperature adsorption, arbitrarily taking $T_s = 30$ K as the boundary of the adsorbent temperature region considered.

There are several features that make low-temperature adsorption particularly interesting. At sufficiently low temperatures it is possible for weakly bound, physisorbed molecules to be held on the surface and investigated experimentally. Molecular adsorption states are often encountered in the role of precursor states for dissociative chemisorption. Thus the study of the behavior of molecules in such states is important for understanding the mechanism of dissociative adsorption, which is the key stage in the processes mentioned above. The initial stage is the adsorption of monolayers of molecules at low temperatures, which is also of interest for studying the growth of cryocrystals. Studies of the phase state of physisorbed quasi-two-dimensional layers and of possible isotope effects (especially topical in the case of hydrogen) also require experiments at low substrate temperatures and are of independent interest.

As we have said, there have been an enormous number of papers devoted to the study of adsorption, and their results have been summarized in a number of reviews and monographs (see, e.g., Refs. 1–6). However, this is not the case for low-temperature adsorption. We know of only the review by Ilisca[7] in 1992, devoted to ortho–para conversion of physisorbed hydrogen molecules, and the recently published review by Panchenko *et al.*[8] of research on galvanomagnetic size effects on metal surfaces and the use of these effects to study adsorption and processes of ordering of the adsorbate layer. A cursory discussion of the problem of low-

temperature adsorption of gases is given in the review by Naumovets.[9] It should be mentioned that the number of original papers on low-temperature adsorption of gases also falls far short of the number of papers on the adsorption of gases under ordinary temperature conditions. It is our intention to fill this gap in some measure and to discuss research results on the low-temperature adsorption of gases without restriction to a particular technique or surface-sensitive effect.

1.2. General qualitative ideas about the mechanism of gas adsorption on metals

Although molecular physisorption is peculiar to low substrate temperatures, dissociative chemisorption also occurs under these conditions, as will be seen below. It is therefore advisable to touch upon the mechanism of dissociative adsorption of molecular gases. The current ideas as to the mechanism of dissociative adsorption are based on the results of experimental research using molecular beams (most often supersonic with a small spread of molecular energies[2]) and theoretical quantum-dynamics calculations of the multi-dimensional potential energy surface,[1,5,10] though mainly for hydrogen molecules. Of course, the six-dimensional potential energy surface cannot be illustrated, and one often resorts to showing two-dimensional sections through it.[6]

However, for a qualitative interpretation of the experimental results and for greater lucidity, one can even use a one-dimensional Lennard-Jones potential diagram, shown schematically in Fig. 1.[11] As it approaches the surface, a molecule first experiences a van der Waals attraction, which then gives way to Pauli repulsion due to the overlap of the tails of the Bloch wave functions of the metal and the filled
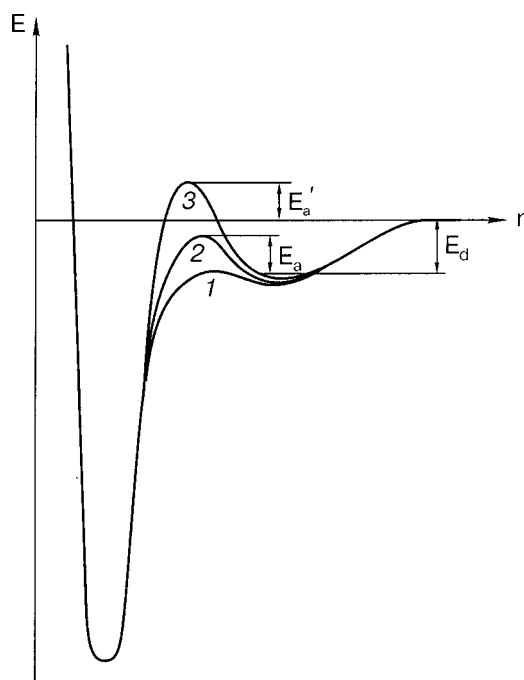

FIG. 1. One-dimensional potential diagram. Chemisorption: *1*—direct; *2*—via a precursor state; *3*—activated. E_a is the activation energy for the transition from the precursor state to a state of chemisorption, E_d is the activation energy for desorption, and E_a' is the activation energy for adsorption.

orbitals of the molecule. These two interactions form a shallow physisorption potential well, which, as the molecule approaches still closer to the surface, gives way to a deep chemisorption well. Between these potential wells is a barrier whose value depends on the mechanism of dissociative adsorption. One can distinguish three types of barrier: 1—The barrier is negligible, and the molecule is not held in a state of physisorption but slides into the chemisorption well. 2—The barrier is appreciable but does not reach the zero level of energy (the potential energy of the molecule at infinite separation). The molecule will spend some time in a state of physisorption and with a certain probability will either pass to a state of chemisorption or be desorbed. This is the mechanism of chemisorption with the participation of a precursor state. Two types of precursor states are distinguished: above an unoccupied adsorption center (intrinsic) and above an occupied center (extrinsic).[12] 3—The barrier is higher than the zero level of energy. For passage to a state of chemisorption a kinetic energy sufficient to overcome this potential barrier must be imparted to the molecule. This is the mechanism of activated chemisorption.

Harris and Andersson[13] considered the transformation of the electronic structure of a (hydrogen) molecule and a metal as they approach. The situation is essentially different for a noble metal (copper) and a transition metal (nickel). In both cases the dissociation of the molecule occurs due to the transfer of electrons from the metal to the antibonding σ_u orbital of the H_2 molecule. Since in the case of copper this process involves $4s$ electrons of the metal, the overlap of their wave functions with the filled σ_g orbital of hydrogen forms an activational barrier, and the aforementioned transfer of electrons to the σ_u orbital can occur only after an activational barrier is overcome. The height of the activational barrier depends on the properties of the interacting partners. For example, according to Ref. 13, for the H_2/Na system the barrier height is equal to 0.2 eV, while for H_2/Al it is 1 eV.

A different situation arises in the case of the transition metal nickel. Because of the presence of unfilled d states near the Fermi level, when a molecule approaches sufficiently close to the surface the $3d$ levels lie below the $4s$ levels on the energy scale, and the latter are vacated. This transition of electrons to the compact $3d$ orbitals prevents the formation of a Pauli activation barrier, and on closer approach to the surface the molecule dissociates.

This qualitative picture of the adsorption interaction of a molecule with a metal surface is not specific for low-temperature adsorption and is suitable for the description of adsorption under any temperature conditions. We will stop at this brief description of the adsorption mechanism and turn to a discussion of the techniques used in the experimental study of low-temperature adsorption of gases.

2. METHODS OF STUDY OF LOW-TEMPERATURE ADSORPTION OF GASES

The general requirements for experimental research on gas adsorption (not only at low temperature) are ultrahigh-vacuum conditions (residual gas pressure $\leqslant 10^{-10}$ torr) and control of the atomic purity and structure of the surface and of the purity of the gas under study. These are usually monitored by the methods of AES, LEED, and mass spectrometry.
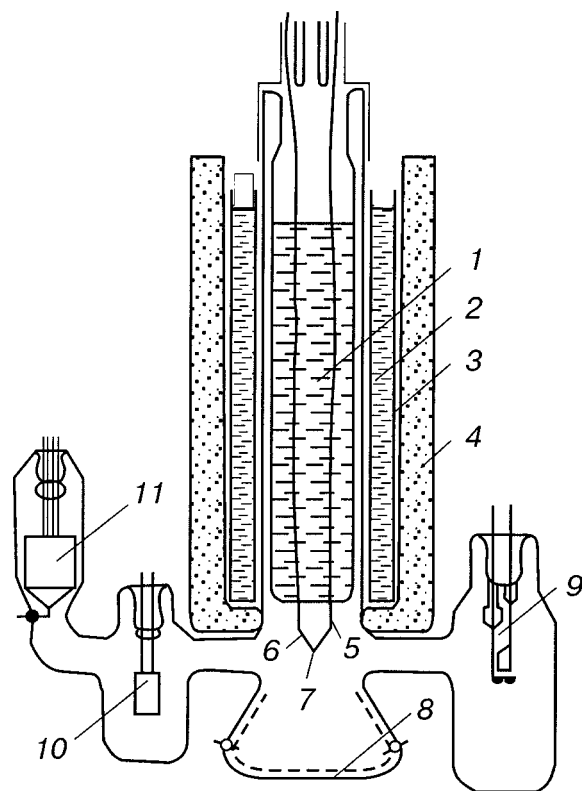
FIG. 2. Field-emission projector with a cooled tip.[17] *1*—Dewar foot containing liquid helium; *2*—copper vessel; *3*—liquid nitrogen; *4*—foam plastic thermal insulation; *5*—molybdenum leads; *6*—tungsten arch; *7*—tungsten tip; *8*—luminescent screen; *9*—titanium pump; *10*—hydrogen source; *11*—manometer.

FIG. 3. Glass electronograph with cooled sample.[20] *1*—Sample; *2*—foot with liquid helium; *3*—hydrogen source; *4*—thermocouple; *5*—electron gun; *6*—luminescent screen; *7*—telescopic photometer.

Let us briefly discuss some of the techniques used to acquire data on the characteristics of the low-temperature adsorption of gases. Since all of the techniques used for adsorption studies are thoroughly described in the literature, we will only briefly touch on the features of their application in the low-temperature region.

2.1. The field-emission microscope (FEM) method[14,15]

The earliest paper known to the author on the use of the FEM method for studying the mobility of hydrogen on the surface of a tungsten tip cooled by liquid helium is that of Gomer *et al.*[16] An adlayer of hydrogen was deposited on a region with a sharp boundary on the surface of the tip, and the advance of this boundary to the uncoated part was tracked. A device of this type has also been used by Medvedev and Snitko in a study of the field emission of hydrogen ions.[17] A diagram of this device is shown in Fig. 2. Later Mazenko, Banavar, and Gomer modified the FEM method for measuring the parameters of surface diffusion by observation of the correlation of the fluctuations of the field emission current from different parts of the tip.[18]

The FEM method was also used by Polizotti and Erlich for a comparative study of the adsorption of hydrogen (and nitrogen) on different faces of tungsten and rhodium, although at tip temperatures not lower than 38 K.[19]

2.2. The low-energy electron diffraction (LEED) method

The LEED method is one of the most informative and widely used methods for studying the structure of the surface
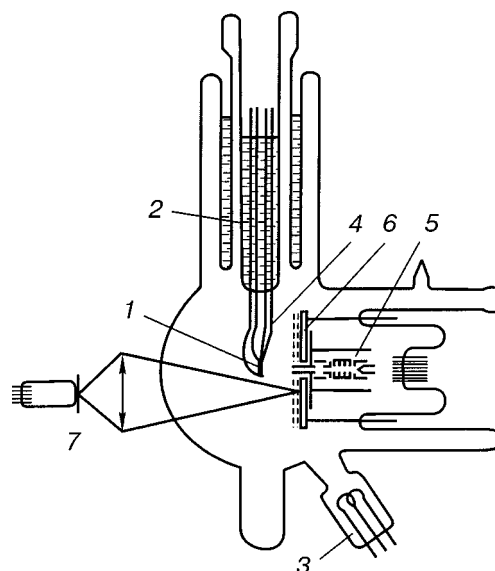
and of the adlayer. Figure 3 shows a diagram[20] of a low-voltage electronograph in a glass envelope, created by Fedorus for investigating the structure of adlayers at $T_s \sim 5$ K. Fedorus also developed an electronograph that can be mounted in a metallic Riber ultrahigh-vacuum unit and is intended for operation at $T_s \sim 5$ K.[21] An electronograph of a similar type was made by Strongin *et al.*[22]

2.3. Method of galvanomagnetic size effect

Panchenko and co-workers have developed a method of studying the low-temperature adsorption of gases based on measurement of the magnetoresistance (static skin effect[23]) and the Sondheimer oscillations[24] in thin single-crystal slabs of a metal (mainly tungsten). Figure 4 shows a diagram[25] of a glass ultrahigh-vacuum device designed for studying the static skin effect and equipped with a low-voltage electronograph.

The method is based on the fact that the scattering and diffraction of conduction electrons on the surface are sensitive to its structure and the structure of the adlayer, and one can therefore assess the structural changes from the variation of the magnetoresistance during the adsorption process. An important feature of the method is its nondestructive character. To become acquainted with the details of this method we recommend the review article cited as Ref. 8.

2.4. Methods of electron spectroscopy[26]

Several versions of electron spectroscopy are used to study the low-temperature adsorption of gases: Auger electron, ultraviolet and x-ray photoelectron, and electron energy loss. To determine the physical state and the character of the excitations of gaseous adsorbates at low T_s a particularly effective method is high-resolution electron energy loss spectroscopy (HREELS).[27,28]
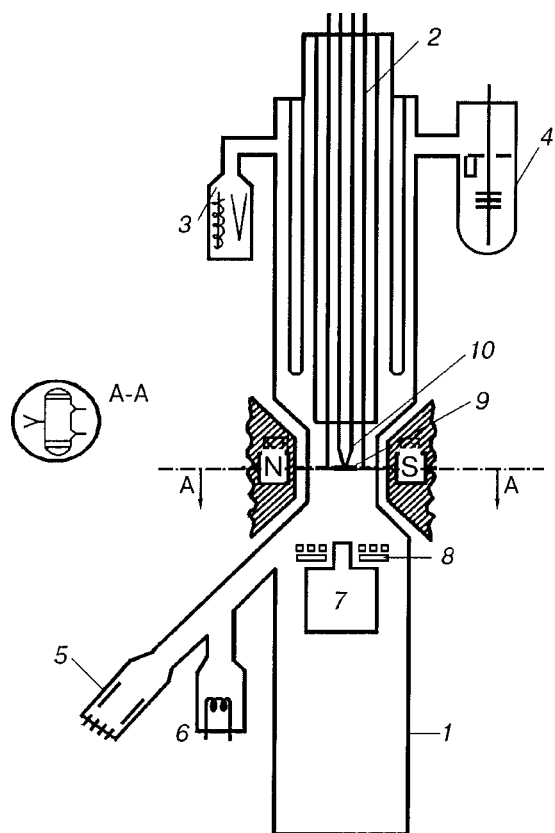
FIG. 4. Device combining the static skin-effect and LEED methods.[8,25] *1*—Glass envelope; *2*—helium cryostat; *3*—manometer; *4*—getter pump; *5,6*—sources of adsorbate; *7*—electron gun; *8*—grids and luminescent screen; *9*—sample; *10*—thermocouple.

FIG. 5. Fragment of the restricted-volume apparatus for accumulation of the desorbed gas.[31] *1*—Sample; *2*—capacitive ring; *3*—glass bell jar; *4*—ion source chamber; *5*—filament of the ion source; *6,7*—parts of the quadrupole mass spectrometer; *8*—baffle.

2.5. Methods of molecular beam and temperature-programmed desorption

To determine such parameters of the low-temperature adsorption as the surface density of molecules n, the sticking coefficient S, the spectra of the adsorption states, and the activation energy for desorption, ultrahigh-vacuum equipment is used to implement the molecular-beam and temperature-programmed desorption methods. The molecular-beam method is used in two modifications: with a source of the effusion or supersonic-nozzle[29] type. The latter has the advantage of a lower energy spread of the molecules in the beam, but it is more complicated to implement because of the necessity of several steps of differential pumping.

An extremely refined apparatus with a monoenergetic molecular beam of the nozzle type has been built at Chalmers University and is described in Ref. 30. The apparatus has been used to study the sticking (and scattering) of normal gases (n-H_2 and n-D_2) and also of the para and ortho modifications (p-H_2 and o-D_2) with the goal of elucidating how the sticking is influenced by the rotational states of the molecules. The beams of the latter molecules were obtained by conversion of the normal gases with the use of a nickel silicate catalyst at a temperature of 25 K. A single-crystal copper sample was cooled by helium gas to $T_s \sim 10$ K. The detector of the scattered molecules was a movable ionization manometer with a narrow entrance channel, making it possible to observe the diffraction of the molecular beam on the surface of the sample. The apparatus had provisions for vary-
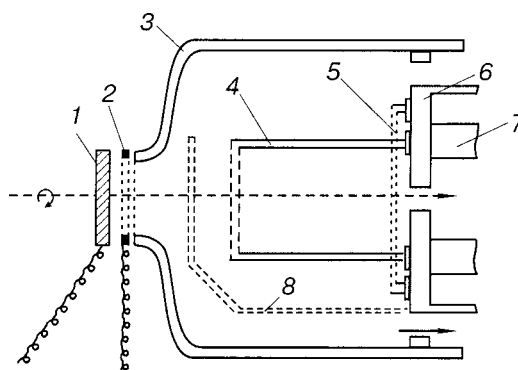
ing the angle of incidence of the molecular beam over rather wide limits. Measurement of the sticking coefficient as a function of coverage was done by recording the partial pressure of the gas under study in the main chamber with the aid of a mass spectrometer during both the gas adsorption and desorption processes.

An extremely original method of measuring the sticking coefficient and coverage was implemented by Schlichting and Menzel.[31] Those parameters were determined from the increase in pressure during the thermodesorption of adsorbed particles in a glass bell jar of small volume in which the ion source of the mass spectrometer was placed. The bell jar was separated from the main chamber by a narrow gap with low transmission. This measure improves the sensitivity of the thermodesorption method considerably in comparison with that obtained when the pressure increase is registered in the main chamber of large volume. After completion of an adsorption cycle the liquid-helium-cooled sample is moved into position in front of the entrance of the bell jar and the thermodesorption is carried out. This part of the experimental apparatus is shown schematically in Fig. 5.[31] The gas under study was delivered to the sample from an effusion source. The cooling of the sample was done through a copper block in contact with the liquid helium.[32]

Finally, let us briefly discuss the technique used in the author's laboratory for studying low-temperature adsorption of gases. We have built an ultrahigh-vacuum device of the "black chamber" type,[33,34] the basic features of which are the possibility of forming an effusion molecular beam and the line-of-sight registration of the desorbed or scattered molecules. The line-of-sight registration regime eliminates the influence of secondary processes on the chamber walls, which distorts the results of the measurements. The line-of-sight registration regime and the formation of the molecular beam were achieved by means of a double-walled jacket built into the vacuum chamber; the jacket was cooled by liquid nitrogen and was coated with a freshly deposited titanium film. This apparatus is shown schematically in Fig. 6.[34] The cooling of the sample was done through a copper rod directly in contact with liquid helium poured into the tubular manipulator. A tungsten tube was tightly fitted on the rod, and the sample was resistance welded to the opposite end of the tube to form a bottom.
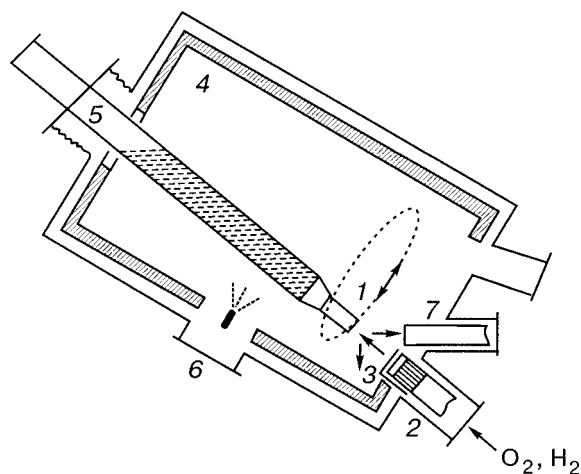
FIG. 6. Diagram of an apparatus with an effusion molecular beam and line-of-site registration.[34] *1*—Sample; *2*—source of molecular beam; *3*—baffle; *4*—nitrogen-cooled jacket; *5*—manipulator; *6*—titanium evaporator; *7*—mass-spectrometric detector.

Let us discuss the definitions of such parameters of the adsorption process as the sticking coefficient (or sticking probability) S of a molecule, the surface density n of the adsorbate (or the degree of coverage θ), and the spectrum of the adsorption states. The sticking coefficient is the fraction of molecules that stick from the flow incident on the surface:

$$S = \frac{dn}{dt}\frac{1}{F}, \qquad (2.1)$$

where F is the flux density of molecules onto the surface.

There are two main methods of measuring the sticking coefficient. One of them is to differentiate the experimental time dependence of the surface density determined by the thermodesorption method. This method was used, e.g., by Friess, Schlichting, and Menzel.[35,36] The second method is based on measurement of the flux density of molecules scattered or desorbed by the surface. We shall mention two variants of this method. The first was proposed by King and Wells[37,38] and is based on measurement of the gas pressure in the chamber under conditions when the molecular beam is incident on the surface of the sample and when the sample has been moved to the side of the molecular beam zone. The second variant was proposed by Bosov and Chuĭkov[39] and is based on continuous measurement of the flux density of scattered or desorbed molecules through the ion source of a mass-spectrometric detector prior to interaction with the walls of the chamber. The importance of the latter condition, especially in measurement of the thermodesorption spectrum, is illustrated by the results of Refs. 40 and 41. The oxygen thermodesorption spectrum measured under conditions when the desorbed particles can strike the ion source not only directly but also after interacting with the walls contains CO, O_2, and CO_2 as well as atomic oxygen.[40] However, if the influence of the walls is eliminated, then only atomic oxygen remains in the spectrum.[41]

In the method of Bosov and Chuĭkov the sticking coefficient is determined from the equation

$$S(t) = 1 - I(t)/I_m, \qquad (2.2)$$

where $I(t)$ and I_m are the ion currents of the detector at time t and after the formation of a saturated adlayer, respectively. The surface density of molecules is determined from the equation

$$n(t) = F \int_0^t S(t)dt. \qquad (2.3)$$

The degree of coverage $\theta(t) = n(t)/n_a$, where n_a is the density of surface atoms of the substrate ($\sim 1.4 \times 10^{15}$ for the (110) face of W and Mo). If this is not specifically stipulated, we shall henceforth use θ to mean to number of molecules per surface atom of the substrate, regardless of whether or not the molecule is dissociated.

Let us turn to a discussion of the research results on the low-temperature adsorption of gases. We shall concentrate in the greatest detail on the results for hydrogen, in less detail on the results for oxygen, and only briefly on those for carbon monoxide and nitrogen, primarily because of the volume of published results for these gases but also to reflect the scientific interests of the author. For brevity we use the following terms used in the literature: *adatom* for adsorbed atom, *admolecule* for adsorbed molecule, *adparticle* for adsorbed particle, and *adlayer* for adsorbed layer.

3. HYDROGEN

Hydrogen is the simplest of the simple gases (H_2, N_2, O_2, CO, CO_2). The hydrogen atom has only one electron (the molecule, two), and that makes it amenable to theoretical treatment of the adsorption interaction with a metal surface. Hydrogen is of considerable interest from the standpoint of practical use, as a participant in important catalytic processes (e.g., the synthesis of ammonia), as a prospective environmentally clean fuel, etc. The key link in catalysis and in the dissolution of hydrogen fuel in a solid-state carrier is the dissociative chemisorption of hydrogen. Hydrogen isotopes have a unique mass ratio (D_2 is twice as heavy as H_2), making it the most favorable for manifestation of various isotope effects.

The study of hydrogen adsorption at low temperatures is of both purely scientific and applied interest. It is only for temperatures close to liquid-helium temperature that hydrogen can be steadily held in molecular adsorption states on a surface and that one can study the properties of such physisorbed layers, including phase transitions, isotope effects, and quantum effects in them. In addition, physisorbed molecules can act as precursor states for dissociative chemisorption, and the study of the behavior of molecules in a state of physisorption is very important for understanding the mechanism of chemisorption.

3.1. Adsorption–desorption processes for hydrogen on the surface of transition metals

3.1.1. Dissociative chemisorption

An important characteristic of an adsorption system is the state of the adsorbed particles: dissociative atomic or molecular. In particular, only those surfaces on which dissociative chemisorption occurs can be catalytically active. The first papers known to the author on the low-temperature ($T_s \sim 4.2$ K) adsorption of hydrogen on tungsten were published in 1955–1957 by Gomer *et al.*[16,42,43] A detailed de-

scription of the experiments and results is given in Ref. 16. The experiments were done in a field-emission projector with a tungsten tip cooled by liquid helium. A hydrogen ad-layer with a sharp boundary was deposited on one side of the tip, and the propagation of the boundary along the (110) surface at the end of the tip was followed on a luminescent screen. At high coverages the motion of the boundary was observed even at $T_s < 20$ K and was attributed to the migration of physisorbed hydrogen molecules along a chemisorbed atomic layer. If the initial coverage was substantially lower, the motion of the boundary began only at $T_s \geq 180$ K, and this was most likely surface diffusion of atomic hydrogen. Thus the authors of Ref. 16 arrived at the conclusion that dissociative chemisorption of hydrogen on the clean W(110) surface occurs at liquid-helium temperature.

Polizotti and Erlich[19] arrived at the opposite conclusion. Studying hydrogen adsorption at $T_s = 80$ K in a field-emission projector, they observed[19] that the change in the (electron) work function φ_{110} of the W(110) face (measured using a probe orifice) begins only after the averaged work function over the whole tip, φ_{mean}, has stopped changing. Since the change in work function is caused by adsorption, those authors[19] concluded that dissociative adsorption of hydrogen on W(110) does not occur under those conditions, and the delayed change in φ_{110} is due to the creeping of hydrogen atoms from the peripheral less densely packed parts of the tip. At $T_s = 38$ K the work functions φ_{110} and φ_{mean} vary synchronously, but when the tip is heated to 77 K, φ_{110} returns to its original value with no sign of conversion of molecular to atomic hydrogen. Thus the authors of Ref. 19 assert that dissociative adsorption of hydrogen does not occur on the W(110) surface at low temperature.

It is hard to assess the reasons for such a difference in the conclusions of Refs. 16 and 19. One can only assume that the character of the change in work function measured from the field-emission current from a very small part of the surface is affected by the high electric field necessary for field emission. Although a high field was also present in the experiments of Ref. 16, the characteristic of the adsorption was not judged from the work function but from the motion of the boundary of the adlayer on the field-emission image. Below we give several more arguments in favor of dissociative adsorption at $T_s \sim 5$ K, based on experiments with macrocrystals in the absence of any electric field.

The thermodesorption spectrum (Fig. 7)[44] of the hydrogen adlayer formed on the W(110) surface at $T_s \sim 5$ K, in addition to having the low-temperature peaks belonging to molecular adsorption states (the details of which are discussed below), also contains two high-temperature peaks (410 and 550 K), which belong to atomic chemisorption and have been observed previously by Tamm and Schmidt.[45] The atomic nature of these states has been established by the isotopic exchange method.[45,46] Granted, it cannot in principle be ruled out that the atomic chemisorbed phase was formed not in the process of adsorption at 5 K but as a result of conversion of the molecular phase at a higher temperature. However, the results of Ref. 46 prove that that is not the case. If the molecular phase of the adsorption participated in the formation of the atomic phase, then the number of molecules in the low-temperature phase of desorption would be
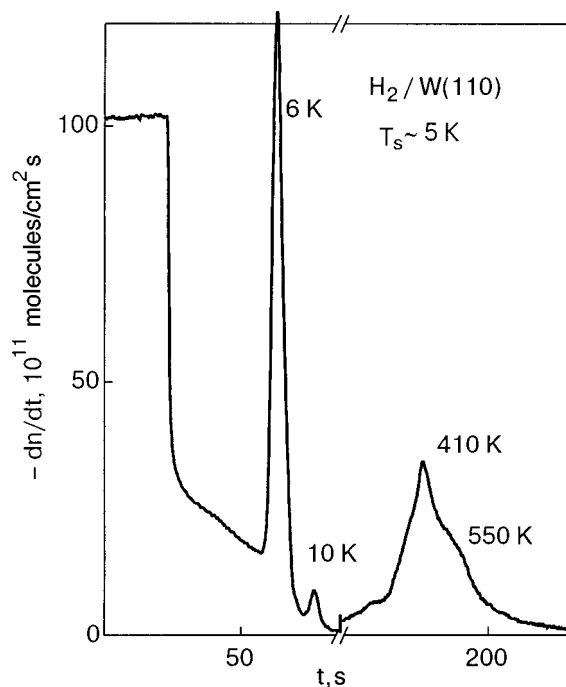

FIG. 7. Thermodesorption spectrum for hydrogen.[44]

substantially smaller in the case when the adsorption occurs on the initially clean surface than in the case of adsorption on a previously formed atomic phase (in the latter case the molecular phase would not be expended on the formation of the atomic phase). In actuality, the thermodesorption spectra in the two cases were found to be identical.

More evidence for dissociative adsorption of hydrogen on W(110) at $T_s \sim 5$ K in the initial stage of the process is given by the character of the dependence of the sticking coefficient on the degree of coverage, $S(\theta)$. The accumulation of weakly bound molecules on the surface from the very start of the adsorption process should be accompanied by an increase in the sticking coefficient, as was observed by Andersson *et al.*[30] for the adsorption of H_2 on copper, when dissociation of the H_2 molecules does not occur. The results of experiments on the H_2/W(110) system attest to a decrease in the sticking coefficient with increasing coverage in the initial stage. This is seen in Fig. 8, taken from Ref. 47 (for more details about $S(\theta)$ see below).

Evidence for a dissociative mechanism of hydrogen adsorption on the W(111) surface at $T_s \sim 5$ K is given by the results of Refs. 46 and 48. This evidence comes from the isotopic exchange for the high-temperature peaks of the desorption and the absence of an influence of the substrate temperature on the kinetics of the initial stage of adsorption in the interval 5–150 K. If a change in the adsorption mechanism occurred in going from $T_s = 150$ K to $T_s = 5$ K, this would be reflected in the kinetics of the process. The statement that the adsorption of hydrogen (and deuterium) on the transition metal ruthenium at $T_s \sim 5$ K is of a dissociative character in the initial stage of the process was made in the paper by Friess, Schlichting, and Menzel.[35] Indirect signs of dissociative adsorption of hydrogen on Mo(110) at $T_s \sim 5$ K can be found in Ref. 49, which will be discussed in more detail below.

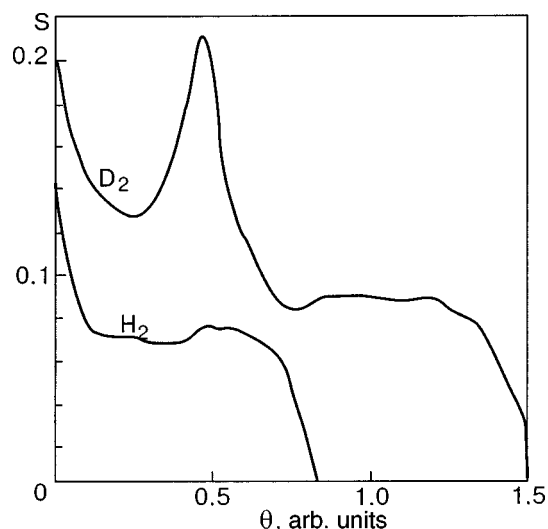Thus there are sufficient grounds, in my view, to assert

FIG. 8. Sticking coefficient for H_2 and D_2 versus the degree of coverage.[47]

FIG. 10. Initial sticking coefficient for H_2 and D_2 on Mo(110) versus the gas temperature.[49]

that dissociative chemisorption of hydrogen (deuterium) occurs at $T_s \sim 5$ K on the surface of transition metals (W, Mo, Ru) in the initial stage of the process up until the formation of a monoatomic layer, after which molecular adsorption phases are formed on the metal surface coated by the chemisorbed monolayer of atoms.

3.1.1.1. Initial sticking coefficient. Information about the initial sticking coefficient S_0 (for $\theta \rightarrow 0$) and the influence on it of such factors as the substrate temperature and the temperature and pressure (flux density) of the gas being adsorbed are of significant interest as a source of information about the character of the gas–metal interaction potential, in particular, about the question of which of the versions of the potential in Fig. 1 is realized. Since in the initial stage the adsorption of H_2 on transition metals at low temperatures is dissociative, it is appropriate to examine the data on the initial sticking coefficient in the Section devoted to dissociative adsorption. Figures 9 and 10 show the dependence of the initial sticking coefficient on the gas temperature, $S_0(T_g)$,
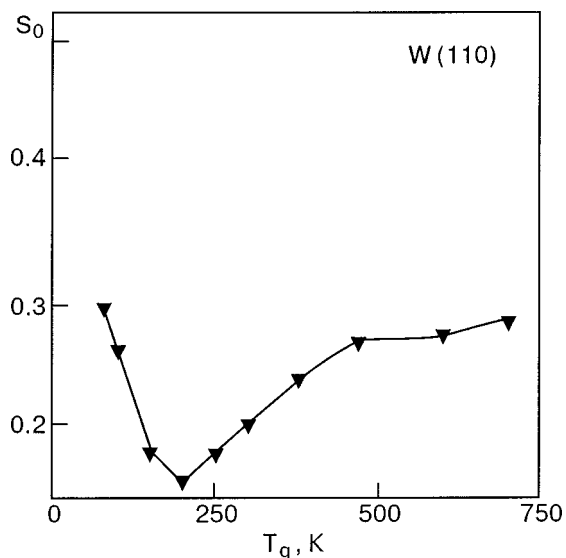

FIG. 9. Initial sticking coefficient for D_2 on W(110) versus the gas temperature.[47]
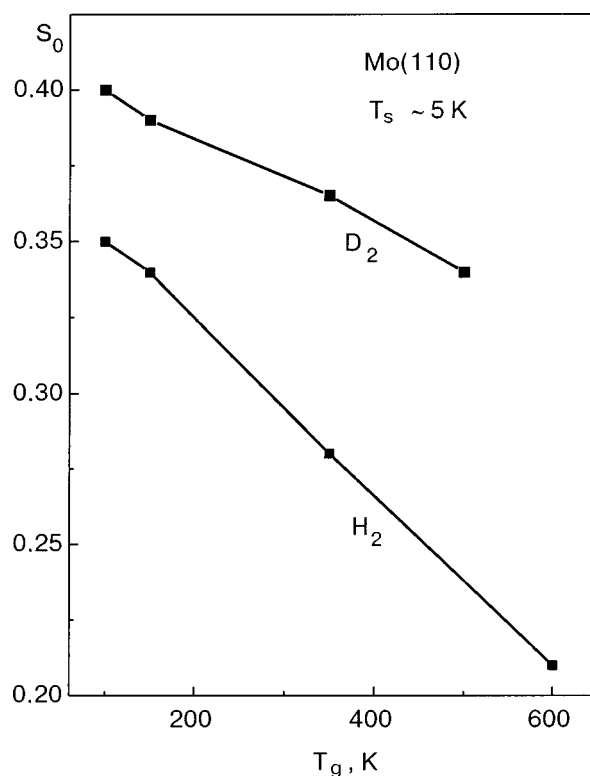
for the systems $D_2/W(110)$ (Ref. 47) and $H_2/Mo(110)$ and $D_2/Mo(110)$ (Ref. 49), respectively. In the case of $D_2/W(110)$ the dependence is nonmonotonic: S_0 decreases with increasing T_g for $T_g < 200$ K and increases for $T_g > 200$ K. This sort of dependence of $S_0(T_g)$ for the adsorption of D_2 on W(110) attests to the presence of two channels of adsorption: 1) via an intrinsic precursor state, in which case the probability of capture to the precursor state naturally decreases with increasing kinetic energy of the incident molecule; 2) through an activation barrier, when the probability of dissociative chemisorption by overcoming of the barrier increases with increasing kinetic energy of the molecules. Thus two versions of the potential, 2 and 3 in Fig. 1, are operative in this case.

In the case of adsorption on Mo(110), both for hydrogen and for deuterium, a monotonic decrease of S_0 with increasing T_g is observed (Fig. 10), i.e., dissociative adsorption occurs predominantly by the second path—via an intrinsic precursor state. It should be noted that this last assertion is not indisputable, and some authors give preference to a steering-effect mechanism, which also explains the decrease of S_0 with increasing T_g (Refs. 50–54). The essence of the steering effect is that a molecule coming in slowly has more time to come to the energetically most favorable configuration in the field of the surface forces. Although this effect is quite possible, and there is experimental evidence of its important role,[52–54] the participation of a precursor state in the mechanism of dissociative adsorption of hydrogen cannot be disregarded in the calculations. In particular, the results of Ref. 55, discussed below, are evidence of this.

Figure 11, taken from Ref. 55, shows the dependence of S_0 on the flux density of H_2 and D_2 molecules on W(110). In
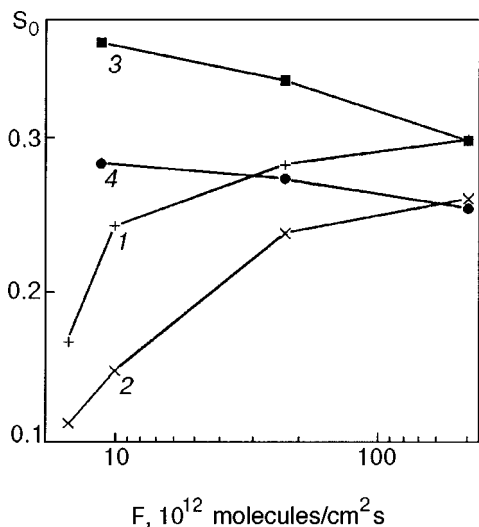
FIG. 11. Initial sticking coefficient for H_2 and D_2 on W(110) versus the flux density of gas molecules.[55] 1,3—For H_2 and D_2, respectively, on the clean surface; 2,4—for H_2 and D_2 on a surface coated beforehand with a chemisorbed monolayer.

FIG. 12. Sticking coefficient versus degree of coverage for H_2 on the W(110) surface filled beforehand with a chemisorbed monolayer.[59] The solid curves are experimental, the points are from a Monte Carlo simulation; flux density F [$cm^{-2}s^{-1}$]: 0.6×10^{13} (1), 0.9×10^{13} (2); 4×10^{13} (3); 20×10^{13} (4).

the case of H_2 an appreciable growth of S_0 is observed as the flux density increases from $\sim 5\times10^{12}$ to 2×10^{14} molecules/cm^{2}s. There appears to be no doubt that the observed variation of S_0 with increasing S_0 can occur in the case when the adsorption mechanism involves the participation of an intrinsic precursor state, and the molecules sojourning in the precursor state interact with each other. It is shown in Ref. 55 that when the data on the mobility of H_2 molecules in the precursor state and the real characteristics of the instrumentation are taken into account, the approach and interaction of molecules in the precursor state are entirely possible, and the increase in the sticking coefficient is due to the formation of clusters of a 2D condensed phase and the hindered thermodesorption of molecules from such clusters. If the elastic reflection of molecules is ignored, the sticking coefficient can be expressed as follows:[11,56]

$$S_0 = \left[1 + \frac{\nu_d}{\nu_a}\exp\left(\frac{E_a - E_d}{kT_s}\right)\right]^{-1}, \tag{3.1}$$

where ν_a and ν_d are frequency factors, E_a and E_d are the activation energies for the transition from the precursor state to a state of chemisorption and desorption, respectively. The activation energy for desorption of a molecule from a cluster should be larger because of the lateral attractive interaction of the molecules in the cluster. It is see from Eq. (3.1) that an increase of E_d leads to an increase of S_0.

As is seen in Fig. 11, for deuterium adsorption such an increase of S_0 with increasing flux density does not occur (moreover, S_0 even exhibits a slight decrease which has not yet been explained). We assume that the absence of an increase in S_0 for deuterium is the impossibility of forming clusters of a 2D phase as in the case of hydrogen. This, in turn, is explained by the deeper position of the level of zero-point vibrations of the D_2 molecule in the physisorption potential well, i.e., the deeper potential relief along the surface than in the case of H_2. The influence of quantum tunneling diffusion in the case of hydrogen also cannot be ruled out. There is no other apparent explanation for the growth of the
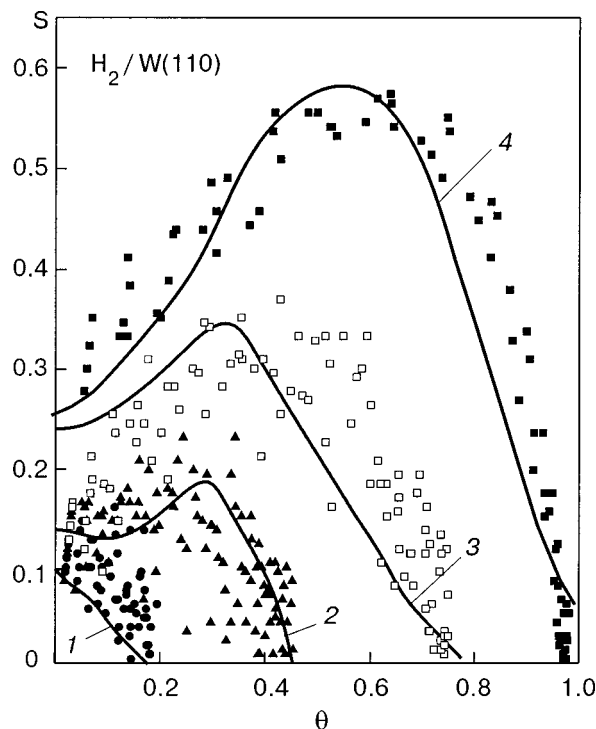
initial sticking coefficient with increasing flux density at T_s ~ 5 K on W(110) except an interaction of the molecules in the intrinsic precursor states and, thus, at least for the H_2/W(110) system, such an interaction is operative.

3.1.2. Adsorption–desorption processes in the molecular phase

3.1.2.1. Adsorption kinetics. To the author's knowledge the kinetics of low-temperature adsorption of hydrogen on transition metals has been investigated in our previous studies for W and Mo (Refs. 46–49, 55, 57, and 58) and by Friess, Schlichting, and Menzel for ruthenium.[35]

Figure 12, taken from Ref. 59, shows the dependence of the sticking coefficient for H_2 on the coverage for a W(110) surface filled beforehand by a chemisorbed monolayer of hydrogen atoms. Such a surface was formed by annealing at ~ 100 K a sample previously saturated with hydrogen at T_s ~ 5 K. The $S(\theta)$ curves were obtained at different intensities of the molecular beam. The solid curves show the experimental dependence[55] and the points show the results of a Monte Carlo computer simulation.[59] Let us first discuss one of the curves, e.g, that for the highest flux density, $F = 2 \times 10^{14}$ molecules/cm^{2}s. The observed growth of the sticking coefficient with coverage is explained by an increase in the efficiency of kinetic energy loss by the incident molecule in its collision with a previously adsorbed, weakly bound molecule. This occurs because the masses of the collision partners become equal, whereas when striking the clean surface or a surface coated with tightly bound hydrogen atoms the mass difference is very large and the accommodation coeffi-

cient is small. A similar growth of the sticking coefficient with increasing coverage in a molecular adsorbed phase was observed in our earlier studies[47,58] for W(110) and also by Friess, Schlichting, and Menzel for ruthenium,[35] and by Andersson et al.[30] and by Wilzen et al.[60] for adsorption on copper (the results for copper will be discussed in detail below). We call this the amortization effect.

The subsequent decrease in the sticking coefficient with increasing θ (Fig. 12) may be due to several causes. One of the main causes is thermodesorption. Evidence for this is the strong dependence of the equilibrium degree of coverage on the gas flux density. In the absence of a deficit of unoccupied adsorption sites, an equilibrium coverage was established such that the flux densities of the desorbed and incident molecules were equal. In addition, the results of the Monte Carlo simulation[59] with amortization, thermodesorption, and a weak lateral interaction between molecules taken into account agree satisfactorily with experiment (Fig. 12), confirming the conclusion that thermodesorption plays a governing role in the appearance of the descending branch of $S(\theta)$.

An extremely original interpretation of the cause of the decrease in the sticking coefficient in the region of completion of the first physisorbed monolayer of H_2 on the (001) surface of ruthenium was proposed by Friess, Schlichting, and Menzel.[35] Those authors[35] see the decrease in the sticking coefficient in the region $\theta \approx 1$ as being caused by an increase in the lattice stiffness of the molecular adlayer of hydrogen owing to the lateral compression of this layer in comparison with a molecular plane of the hydrogen crystal. The driving force of this compression is the rather large difference in the binding energy of the molecules with the substrate in the first and second physisorbed layers (E_d is substantially larger in the first layer). Therefore, it is energetically more favorable for a molecule striking the surface to ''squeeze'' into the first monolayer than to be incorporated in the second layer. This possibility, in turn, is explained by the anomalously high compressibility of the hydrogen layer owing to the large amplitude of the zero-point vibrations of the H_2 molecule. Anomalous compressibility of the hydrogen crystal was reported in Ref. 61. Figure 13, which is reproduced from Ref. 35, shows the sticking
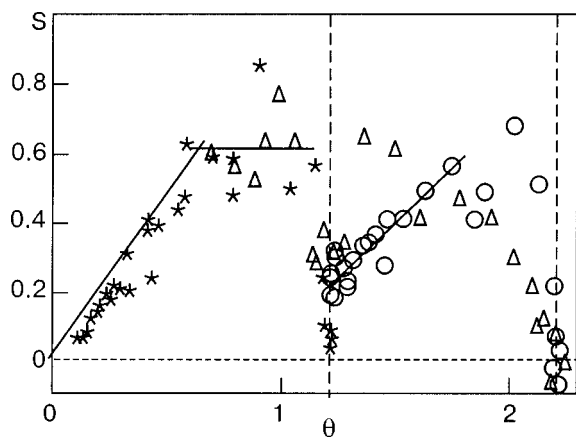
coefficient of H_2 on Ru(001) as a function of the degree of coverage. It is seen that S decreases sharply upon completion of the first monolayer. In Ref. 35 two peaks were observed in the thermodesorption spectrum, corresponding to the first and second layers, at $T_s = 4.8$ K. When the adsorption temperature was increased to 5.5 K, so that the second layer was not held, one peak remained in the thermodesorption spectrum, and the $S(\theta)$ curves in Ref. 35 and in our studies are qualitatively similar. As we have said, a Monte Carlo simulation taking thermodesorption into account but not the compressibility of the adlayer gives a satisfactory description of our experimental results,[59] although it cannot be ruled out that the compressibility effect may have a slight influence on the descending branch of $S(\theta)$. To obtain a more reliable answer to this question we are planning to conduct experiments at lower temperature, where several molecular layers will be held.

In comparing the results of our studies for the $H_2/W(110)$ system[55,58,59] with the results of Ref. 35 for the $H_2/Ru(001)$ system, we must address two questions. The first is, why in our case does the measured $S(\theta)$ curve extend to $\theta \approx 1$, while in Ref. 35 it extends to $\theta \approx 2$. A possible reason for this difference is that the activation energy of H_2 desorption from ruthenium (~ 30 meV[35]) is substantially higher than that for tungsten (~ 15 meV[58,59]). Probably the value of E_d for the second molecular adlayer is also larger in the case of Ru(001) than for W(110). That may be the reason why our experiments do not achieve the density of the first adlayer at which the compression effect and the enhanced lattice stiffness of the adlayer can play a substantial role.

The second question pertains to the hydrogen thermodesorption spectra. Both in our studies and in Ref. 35, two main peaks of desorption of the molecular phase of adsorption are observed. However, in our case both peaks represent the desorption of a single physisorbed layer in which the molecules are found in different states.[44,57] In Ref. 35 each of

FIG. 13. Dependence of the sticking coefficient of H_2 on the degree of coverage on the Ru(001) surface filled beforehand with a chemisorbed monolayer.[35] Δ—$T_s = 4.8$ K; $\star$—$T_s = 5.5$ K; $\bigcirc$—adsorption in a second layer at $T_s = 4.8$ K.
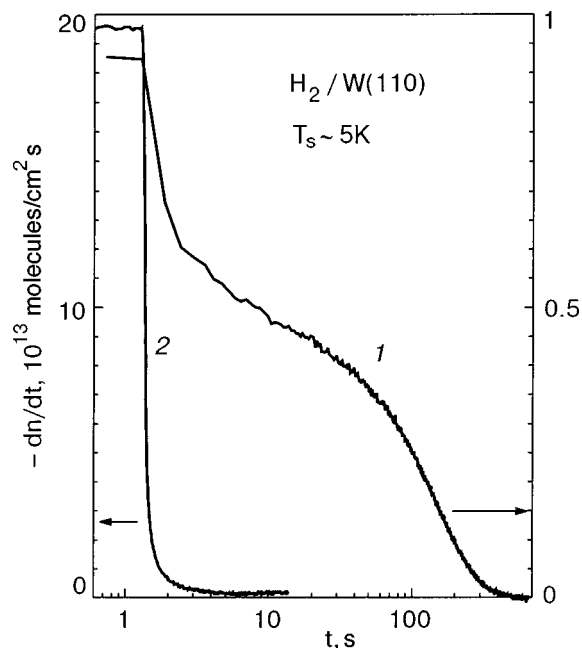
FIG. 14. Rate of isothermal desorption of H_2 versus time.[57] *1*—Low flux density; *2*—high flux density.

the two thermodesorption peaks represents a separate mono-layer.

3.1.2.2. Kinetics of the isothermal desorption of H_2 *from* W(110). Since a change in the flux density of molecules onto the surface has an influence on the kinetics of the low-temperature adsorption of H_2 on W(110), according to the principle of detailed balance, one can expect that the desorption kinetics will also be influenced by the flux density. The results of a study of how the value of the molecular flux density in the formation of a hydrogen adlayer influences the subsequent isothermal desorption at $T_s \sim 5$ K are reported in Refs. 44 and 57.

Figure 14, taken from Ref. 57, shows the time dependence of the rate of isothermal desorption of H_2 from W(110) at $T_s \sim 5$ K from adlayers formed at flux densities of $\sim 1 \times 10^{13}$ and 2×10^{14} molecules/cm^{2}s. It is seen that increasing the flux density sharply suppresses the isothermal desorption: the number of molecules desorbed at the higher flux density is smaller by approximately a factor of 50 than for the case of the lower flux density. In Refs. 44 and 57 the suppression of the isothermal desorption of H_2 is interpreted as being a consequence of a phase transitions from a 2D gas to a 2D condensate in the adlayer. It is known that the critical size of the condensed-phase nuclei decreases with increasing supersaturation. For this reason one expects that the probability of realization of a gas–condensate phase transition during the time of an experiment increases with increasing flux density, and that is most likely what is observed. The activation energy for desorption from a 2D condensed phase should be larger than that for a 2D gas phase because of the lateral attractive interaction of the molecules. This is the reason for suppression of the isothermal desorption with increasing flux density.

At a low flux density one observes a fast stage (several seconds) and a slow stage (hundreds of seconds) of desorption. At a high flux density only the fast stage of desorption is observed. The fast stage involves the desorption of the insignificant number of molecules contained in the second molecular layer. The slow stage can be analyzed using the Polyani–Wigner equation in logarithmic form:

$$\log\left(-\frac{dn}{dt}\right) = \log \nu_d + a \log n - 0.43\frac{E_d}{kT_s}, \qquad (3.2)$$

where n is the surface density, ν_d is a frequency factor, E_d is the activation energy for desorption, and a is the order of the desorption reaction.

Figure 15, taken from Ref. 57, shows the dependence of the rate of desorption on the density. It is seen that a large part of the adlayer is desorbed in the first order of the reaction, which is reasonably ascribed to desorption from a 2D gas phase. However, in a small interval of densities, 10^{12}–10^{13} molecules/cm^2, the order of the reaction is close to zero. In Refs. 44 and 57 this last result is interpreted as being a consequence of the replenishment of the 2D gas phase due to "melting" of islands of the 2D condensate. Apparently, even in the case of a low flux density (during the formation of the adlayer) islands of the 2D condensate form near defects of the surface, but they contain a very insignificant fraction of the total number of molecules in the adlayer.
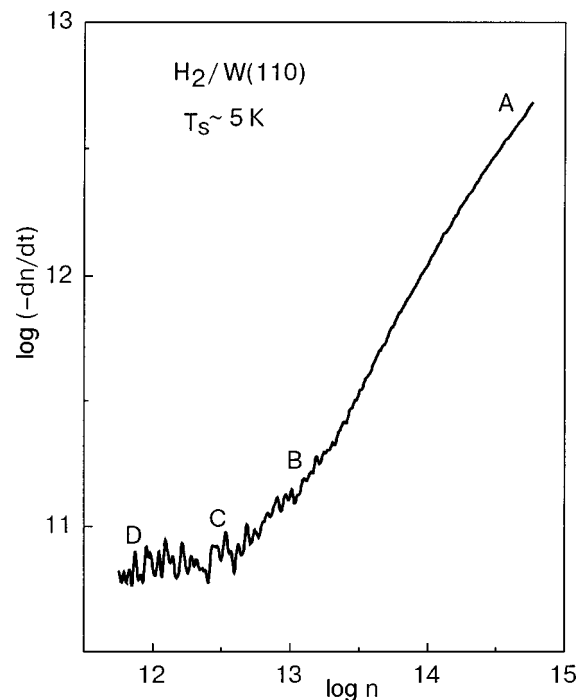

FIG. 15. Rate of isothermal desorption of H_2 versus density on a logarithmic scale.[44,57] On segment AB one has $a \approx 1$; on segment CD, $a \approx 0$.

Evidence in favor of this interpretation comes from the thermodesorption spectra of adlayers formed at low and high flux densities. Such spectra are shown in Fig. 16.[57] It is seen that for a low flux density the desorbed molecules are mainly found in the 6 K (2D gas) peak and only an insignificant number of them are found in the 10 K (2D condensate) peak. In the case of the high flux density the number of molecules in the 10 K peak was tens of times larger.

Based on the results discussed, a hypothetical model of the hydrogen adlayer on W(110) at $T_s \sim 5$ K was proposed in Refs. 44 and 57. In this model, which is illustrated in Fig. 17, the first molecular layer contains a 2D gas with neighboring islands of the 2D condensate, and the second molecular layer, in equilibrium with the intense flux, contains a quite small number of molecules, which very rapidly fly off when the incident flux is shut off.

It is of interest to elucidate the character of the transition from the 2D gas to the 2D condensate with increasing flux density of molecules onto the surface. Figure 18, taken from Ref. 57, shows the total number of isothermally desorbed H_2 molecules (in fractions of a monolayer) as a function of the flux density. Up to a flux density of $\sim 1 \times 10^{14}$ molecules/cm^{2}s the experimental points fall on the Langmuir isotherm.[62] This means that at such flux densities there are no substantial changes in the adlayer. However, at a flux density of 2×10^{14} molecules/cm^{2}s the number of desorbed molecules falls off sharply. Thus there exists a critical value of the flux density (supersaturation) that must be exceeded for the phase transition from the 2D gas to the 2D condensate to occur.

We conclude this paragraph by noting that appreciable isothermal desorption of deuterium at $T_s \sim 5$ K is not observed. We attribute this circumstance to the deeper position
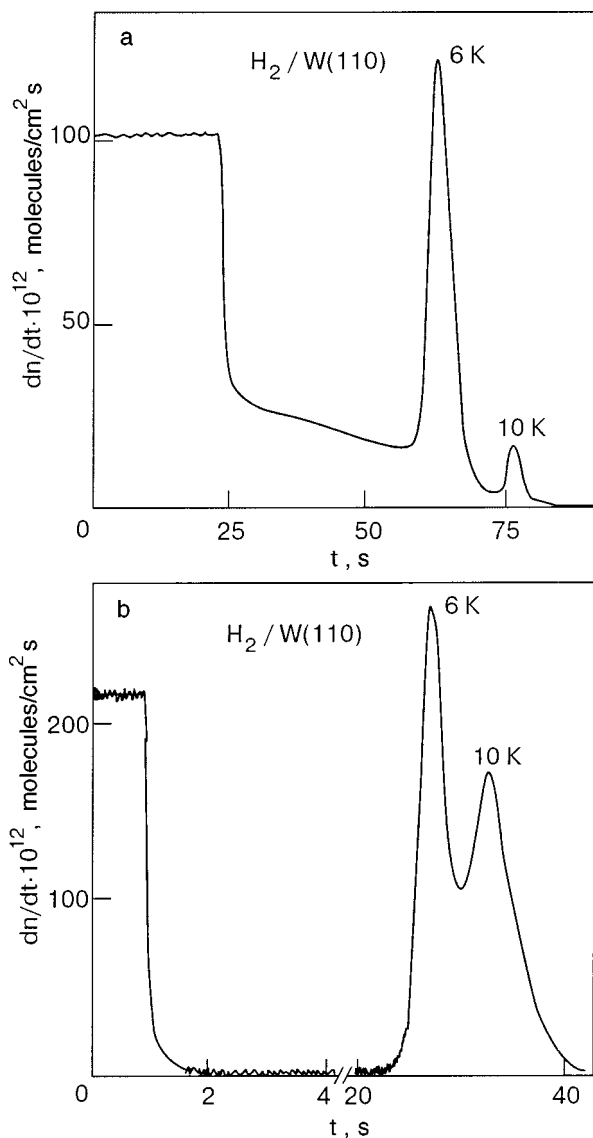
FIG. 16. Thermodesorption spectra for low (a) and high (b) flux densities.[44,57]

FIG. 18. Langmuir isotherm.[57] ■—Experimental points.

process (for D_2 it is practically constant) is evidence of a mechanism of adsorption via an extrinsic precursor state, unlike that which is observed for W(110) (see Sec. 3.1.1, Fig. 8). As we have said, the absence of appreciable growth of the sticking coefficient indicates that hydrogen (deuterium) initially accumulates on the surface in atomic and not molecular form. One notices a sharp and deep minimum near $\theta = 0.5$ for hydrogen, which corresponds to a monolayer of chemisorbed atoms.

of the level of zero-point vibrations of the heavier D_2 molecule in the physisorption potential well.

3.1.2.3. Features of the adsorption kinetics of hydrogen on the Mo(110) *surface at* $T_s \sim 5$ K. The Mo(110) surface has an atomic structure that is practically identical to that of W(110), but the electronic structure of these metals is somewhat different. It is of interest to compare the kinetics of H_2 adsorption on these surfaces. Figure 19, taken from Ref. 57, shows the sticking coefficient of H_2 and D_2 on the Mo(110) surface as a function of coverage. The very weak variation of the sticking coefficient in the initial stage of the adsorption
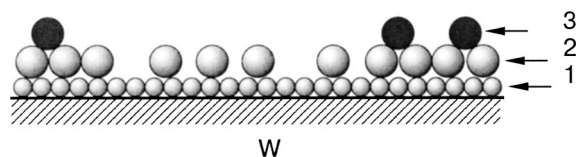

FIG. 17. Model of a hydrogen adlayer at $T_s \approx 5$ K.[57] *1*—Monolayer of chemisorbed atoms; *2*—monolayer of physisorbed molecules in the form of a 2D gas and a 2D condensate; *3*—polylayer condensation.
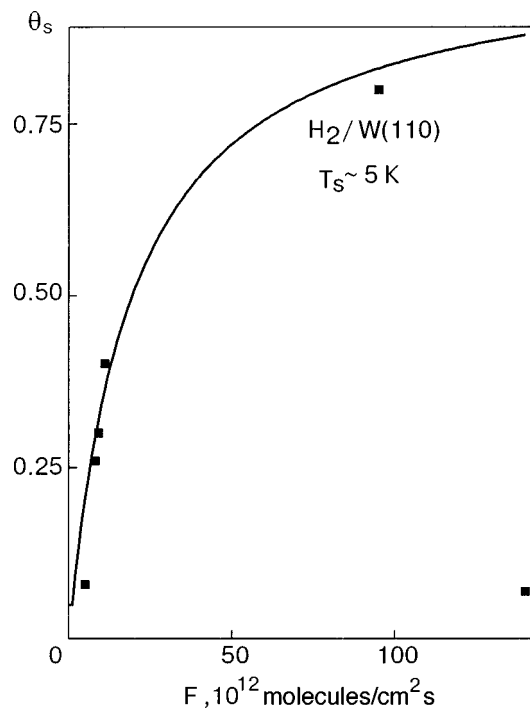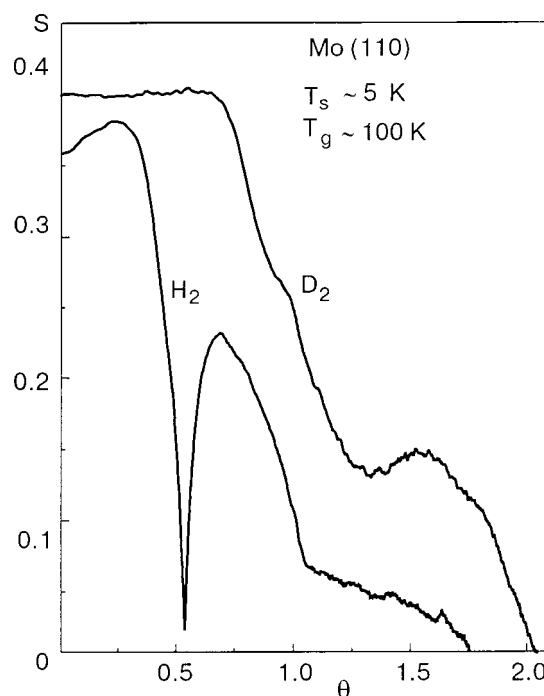

FIG. 19. Sticking coefficient for H_2 and D_2 on Mo(110) versus the degree of coverage.[49,57]

The following explanation for this feature was proposed in Refs. 49 and 57. Up until the layer of chemisorbed atoms is practically complete, the H_2 molecules, owing to their anomalously high mobility on the layer of adatoms, find unoccupied parts of the surface and are dissociatively chemisorbed. Once filled with a chemisorbed monolayer of atoms, the surface becomes inert (the unsaturated valence bonds are exhausted), and the sticking coefficient falls catastrophically. Since the temperature is low enough for a physisorbed molecular layer to be held, weakly bound molecules begin to accumulate on the surface, the accommodation improves, and the sticking coefficient increases.

One might well ask why this feature is not observed in the case of deuterium adsorption. We assume that once again the cause lies in the difference of the quantum properties of the D_2 molecule. The deeper position of the level of zero-point vibrations (in comparison with hydrogen) makes for a better-developed potential relief and lower mobility of the molecules. Therefore, D_2 molecules begin to accumulate on the surface even before completion of the chemisorbed atomic phase, and that compensates the decrease in the sticking coefficient caused by the lowering of the chemical activity of the surface. We do not rule out the possibility that the quantum diffusion of molecules plays some role in the formation of the feature on the $S(\theta)$ curve for $H_2/Mo(100)$. To check this possibility one must lower the sample temperature.

3.1.3. Structure of the hydrogen adlayer at $T_s \approx 5$ K

The structure of hydrogen adfilms on the transition metals W, Mo, and Ni at $T_s \sim 5$ K has been studied by the LEED method by Fedorus and co-workers.[63–68] Some of the results of those studies have been discussed in the review by Naumovets.[9] The main and most reliable data pertain to the structure of an atomic chemisorbed layer, obtained by annealing a hydrogen adlayer formed at $T_s \sim 5$ K, on the close-packed (110) faces of tungsten and molybdenum. Adsorption at $T_s \sim 5$ K leads to the formation of an almost completely disordered layer, although the authors of Refs. 63 and 68 discern in the diffraction patterns a slight manifestation of some sort of order. As was shown in Refs. 34, 44, 46–49, and 57, on the W(110) and Mo(110) surfaces at $T_s \sim 5$ a monolayer of chemisorbed atoms is formed, with a molecular physisorbed layer formed on top of it. An analogous result was obtained in Ref. 35 for the adsorption of hydrogen on the surface of ruthenium. Clearly, for such a composite adlayer it is scarcely possible to interpret the LEED patterns reliably.

Clear and well-interpretable LEED patterns for the system of hydrogen on W(110) are obtained after an adlayer formed at $T_s \sim 5$ K is annealed at 120–160 K. After the annealing the sample was again cooled to 5 K, and the structures $p(2 \times 1)$, (2×2), and (1×1) were observed for coverages of $\theta = 0.5$, $\theta = 0.75$, and $\theta = 1$, respectively. Models of the first two structures are shown in Fig. 20, taken from Ref. 63. Also shown in this figure are the intensities of the reflections of these structures as functions of the substrate temperature. It is seen that an order–disorder phase transition occurs at temperatures significantly below room temperature, and the transition temperature is higher for the (2×2) struc-
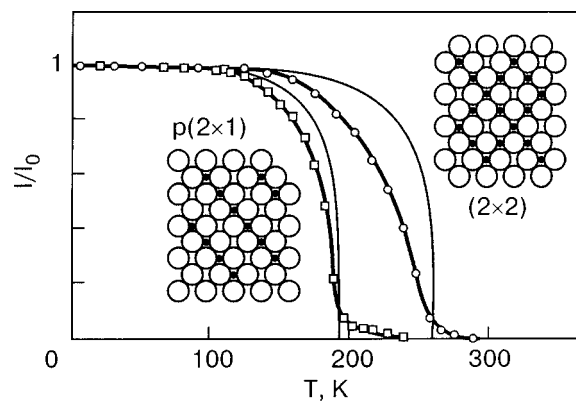

FIG. 20. Temperature dependence of the intensity of the diffraction peaks for the $p(2 \times 1)$ and (2×2) structures of hydrogen on W(110);[63] the fine lines show an Ising model calculation.

ture than for $p(2 \times 1)$, a circumstance which is explained by the stronger interaction of the hydrogen adatoms in the more densely packed structure. Lyuksyutov and Fedorus[20] did a detailed study of the order–disorder transitions in the structures $p(2 \times 1)$ and (2×2); they established that the the temperature dependence of the intensities of the corresponding reflections obeys a power law and determined the critical exponents $\beta = 0.13$ for $p(2 \times 1)$ and $\beta = 0.25$ for (2×2). For hydrogen on the Mo(110) surface the $p(2 \times 1)$ structure was not observed, but only the (2×2) structure at a degree of coverage $\theta = 0.5$, and the authors of Ref. 64 proposed a model for such a structure.

Fedorus and co-workers observed an electron-stimulated disordering (ESD) effect in a chemisorbed hydrogen layer at $T_s \sim 5$ K on the W(110) surface[63] and on the Mo(110) surface,[64] and then an electron-stimulated ordering (ESO) effect[64,66] as well. It was shown in Ref. 66 that in both the ESD and ESO effects the degree of order tends with time to the same level of incomplete ordering, which suggests a universality of the mechanisms of ESD and ESO. The cause of the incomplete ESD is the competing ESO effect. Typically, in the case of adsorption on W(110) the ESD reaches a significantly higher degree than in the case of adsorption on Mo(110).[65] This difference can be explained by the substantially lower mobility of adatoms on W(110) (the greater depth of the potential relief along the surface). One can discern a certain analogy between this difference in the behavior of hydrogen films on W(110) and Mo(110) and the difference in the kinetics of hydrogen adsorption on these substrates.[49] The ESD and ESO effects were subsequently investigated in detail, and a mechanism for them was proposed.[64–69] One of the most likely mechanisms involves the excitation of vibrational states of the hydrogen adatoms, which can migrate along the surface, bringing about a higher mobility of the adatoms. Because of the low mass of the hydrogen atom, high-frequency vibrations are excited, which are long-lived because of the inefficient energy exchange with the substrate.[69]

Let us say a few words about isotope effects in the structure of hydrogen adfilms. Adlayers of H, D, and H+D on W(110) are characterized by the same set of structures: $p(2 \times 1)$, (2×2), and (1×1); an isotope effect in the order–disorder phase transitions is not observed: films of H, D, and

H+D disorder at practically the same temperatures.[65] However, a strong isotope effect is observed in the rate of ESD: in deuterium films the ESD occurs one-fifth as fast as in hydrogen films.[65,66]

A characteristic feature of the ESD of hydrogen and deuterium adlayers is the absence of an energy threshold: the effect occurs even at thermal energies of the electrons.[65–68] This is explained by the fact that when the electron strikes the surface, an energy of ~ 5 eV (the difference between the vacuum level and the Fermi level of the metal) is released, and that energy is expended on excitation of vibrations of an adatom. The authors of Ref. 65 point out several signs of quantum diffusion in the molecular phase. It should be noted, however, that at degrees of coverage $\theta < 1$ (in atoms) practically all the hydrogen is contained in an atomic chemisorbed phase, especially for the Mo(110) surface,[49] and the facts observed in Ref. 65 can scarcely be applied to the molecular phase. In the opinion of the authors of Ref. 65, the conclusion reached in the paper by Di Foggio and Gomer[70] that tunneling diffusion of hydrogen adatoms on W occurs at $T_s < 140$ K is mistaken.

Some information about the structure of a hydrogen adlayer at $T_s \approx 5$ K can be obtained from studies by the static skin-effect method.[71–79] Since Panchenko and coauthors have recently published a review devoted to galvanomagnetic size effects, of which the static skin effect is one,[8] there is no need to present a detailed description of this method here. However, in order to achieve a certain independence of this review article we shall not simply refer the reader to that review[8] but will give a brief account of the essence of the method and the experimental results only insofar as they pertain to the structure of an adsorbed hydrogen layer.

If a single-crystal slab of a pure metal is cooled to a temperature of ~ 5 K and placed in a sufficiently strong magnetic field directed parallel to the surface of the slab, for example, the conductivity of the slab will be determined by a narrow subsurface layer (with a thickness of the order of the Larmor radius), since the deeper layers will be "magnetized." This is a consequence of the fact that electrons colliding with the surface have the opportunity to propagate a distance of the order of the mean free path, and their contribution to the conductivity will be the greater the higher the degree of specularity of their reflection.[8]

According to the ideas set forth in the article by Andreev,[74] the reflection of conduction electrons by the surface of a metal is governed by diffraction effects on the outermost atomic layer. Therefore, the character of the reflection of electrons depends on the structure of this outermost layer. The reflection of electrons should also be influenced by the structure of an adsorbed layer. This has been confirmed in the experiments by Panchenko and co-workers:[23,25,72,74,75] the adsorption of a disordered monolayer (oxygen) led to a twofold increase in the magnetoresistance of a tungsten slab with a (110) surface.

The influence of an ordered monolayer of hydrogen on the magnetoresistance of a tungsten slab with the (110) surface was investigated in Ref. 25 using a device which combined the method of the static skin effect with the LEED method (Fig. 4). The LEED method gave the same sequence of structures with changing coverage as in the papers by
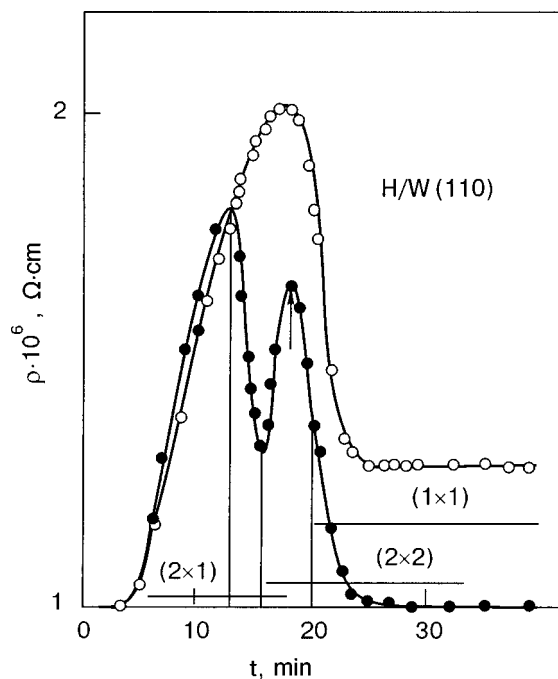

FIG. 21. Dependence of the magnetoresistance of a W(110) slab on the exposure time in hydrogen.[8,25] ○—adsorption at $T_s = 4.2$ K; ●—annealing to 200 K; the vertical lines are the boundaries of the existence regions of the structures.

Fedorus and coauthors: $p(2 \times 1)$, (2×2), and (1×1).[63] In the process of adsorption at 5 K the diffraction patterns are smeared out; the reflections become distinct after a brief annealing to $T \sim 200$ K. Figure 21, taken from Ref. 25, shows the time dependence of the magnetoresistance of a W(110) slab after the adsorption of hydrogen at $T_s \sim 5$ K and after annealing. After adsorption on the cooled substrate the resistance initially increases, as a result of the random distribution of the adatoms, and then decreases, reaching a certain steady level. This decrease is apparently due to the partial ordering of the adlayer, while the steady level indicates that a limiting degree of order has been attained. Thus an ordering process occurs even at $T_s \sim 5$ K. After annealing, the initial part of the curve is nearly the same as before, but then a deep minimum, corresponding to the maximum development of the $p(2 \times 1)$ structure, appears. After that the resistance again rises, falls, passes through a second maximum, and reaches the value characteristic for the pure substrate upon the formation of the (1×1) structure. Thus the leading role is played by the symmetry and not by the chemical nature of the surface layer. The analysis of the possible electronic transitions between different parts of the Fermi surface in Ref. 25 explains the sharp decrease of the resistance upon the formation of the $p(2 \times 1)$ structure and its growth upon the formation of the (2×2) structure as being due to the switching on of electron–hole transfers.

Since the magnetoresistance of a slab is sensitive to the degree of order in an adsorbed layer, Panchenko and co-workers, after studying the dependence of the resistance of a slab with a saturated adlayer of hydrogen (deuterium) adsorbed at 5 K on the annealing time in the temperature interval 160–190 K, estimated the activation energy and the diffusion coefficient of atomic hydrogen and deuterium.[77] The authors were convinced that the surface diffusion of atomic
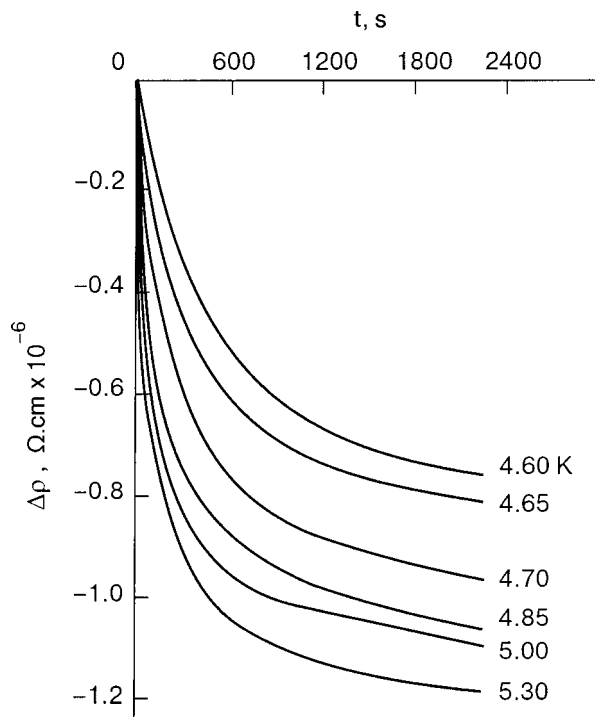
FIG. 22. Magnetoresistance of a W(110) slab with a fixed density of H_2 versus the annealing time at various T_s (Refs. 8 and 78).

hydrogen on the W(110) face is of a thermally activated character, contrary to the conclusions of Di Foggio and Gomer that the diffusion of atomic hydrogen was of a quantum nature.[70] The activation energy was estimated as 0.33 eV for hydrogen and 0.35 eV for deuterium.

Studies by the static skin-effect method made it possible for Panchenko and co-workers[8,78] to observe the kinetics of the transition to the first (atomic) layer by hydrogen (deuterium) molecules adsorbed in the second layer in the form of an extrinsic precursor state for dissociative chemisorption. It was found that the slow decrease of the magnetoresistance on the descending branch of its time dependence continues after the surface is no longer accessible to the gas. This is shown for the system H_2/W(110) in Fig. 22, which is taken from Ref. 8. The authors of Refs. 8 and 78 assumed with complete justification that the cause of the decrease in the resistance is the increase in the area of the islands of the (1×1) atomic phase due to the diffusion of molecules toward the edge of the island and their transition to the first layer, accompanied by dissociation. A similar relaxation of the magnetoresistance has also been observed for the systems H_2/Mo(110), H_2/W(110), and D_2/W(110). Measurement of the temperature dependence of the rate of decrease of the resistance allowed the authors of Refs. 8 and 78 to estimate the activation energy for surface diffusion of molecules over the chemisorbed atomic layer: $E_m = 6.4 \pm 0.7$ meV for D_2/W(110), 2.7 ± 0.5 meV for H_2/W(110), 1.1 ± 0.2 meV for D_2/Mo(110), and 0.8 ± 0.2 meV for H_2/Mo(110). A significant isotope effect in the surface diffusion was explained by the authors of Ref. 8 as being due to the difference in the position of the levels of the zero-point vibrations of the H_2 and D_2 molecules, as in the explanations for the isotope effects in Refs. 44, 49, 55, and 57. It can be thought that the very small value of E_m for H_2/Mo(110) compared

to those for D_2/Mo(110) and H_2/W(110) is manifested in the appearance of a sharp feature on the $S(\theta)$ curve for the first system.[49,57]

Studies by Panchenko and co-workers[79] of the adsorption of deuterium on the W(100) surface by the static skin-effect method revealed certain differences from the D_2/W(110) system. It was found that relaxation of the magnetoresistance is not observed after the D_2 flux is shut off at 4.2 K. This circumstance was explained by the authors as being due to the absence of islands of the ordered atomic phase $c(2 \times 2)$ on that surface at 4.2 K. In my opinion this may also be caused by the hindered surface diffusion of D_2 molecules over the layer of atomic deuterium on W(100) in comparison with W(110). In addition, the value estimated in Ref. 79 for the activation energy of the ordering process in the atomic phase turned out to be substantially larger than for W(110): ~ 0.6 eV as compared to ~ 0.3 eV.[77]

3.2. Adsorption of hydrogen on noble metals

3.2.1. State of adsorbed particles

As was mentioned in Sec. 1.2, in the interaction of an incident hydrogen molecule with the surface of copper or another noble metal, the presence of the Pauli repulsion gives rise to an appreciable activation barrier on the path of the molecule toward dissociation, and this barrier can be overcome only if the incident molecule has sufficient kinetic energy. This fact has been confirmed by many experiments with monoenergetic molecular beams (see, e.g., Refs. 80–83). For H_2 a kinetic energy >200 meV must be imparted to the molecules for the adsorption to become noticeable.[82] Thus for beams with ordinary thermal energies and at the usual substrate temperatures there is no noticeable adsorption of hydrogen on the surface of copper.

The situation is radically altered in the case of deep cooling of the sample. Here a state of physisorption becomes stable, and hydrogen accumulates on the surface. The physisorption of hydrogen (deuterium) on the surface of noble metals silver and copper upon their cooling by liquid helium was first reliably detected by Avouris et al.[27] and by Andersson and Harris.[28] Using the HREELS method, the authors of those papers[27,28] observed a very slight difference in the spectra of the characteristic energy loss to rotational and rotational–vibrational excitations in physisorbed molecules in comparison with those in the gas phase. This was evidence that the state of physisorption is close to the state of the free molecule and that the physisorbed molecule behaves as an almost unhindered rotator. Such behavior of H_2 molecules physisorbed on silver has also been observed in Ref. 84.

In Refs. 27 and 28 some contradictory data were obtained as to conversion of o-H_2 into p-H_2 as a result of adsorption. In Ref. 27 the conversion of o-H_2 into p-H_2 in the physisorbed state was reported. In Ref. 28, on the contrary, no appreciable o–p conversion in the physisorbed layer was observed during the time of the experiment. Granted, in a later study[85] Svensson and Andersson observed o–p conversion in a physisorbed layer on the same Cu(100) surface at a rate of approximately 1 monolayer in 4 min. The authors did not offer a clear explanation for the cause of the difference in the results of Refs. 28 and 85 but suggested that the Cu(100) samples in Refs. 28 and 85 could somehow

differ in structure or by the presence of impurities. An attempt to explain the difference in the rate of $o-p$ conversion on different surfaces by invoking a mechanism of virtual exchange of an electron between the metal and an antibonding orbital of the molecule was made by Iliska.[86]

The authors of Ref. 28 found that the relative occupations of the o and p states of hydrogen in a physisorbed layer differ substantially from those in the gas phase: whereas in the gas phase at 300 K the population ratio o-H_2 : p-H_2 is equal to 3, in a physisorbed layer this ratio turned out to be 1.4. In the opinion of the authors of Ref. 28, this is evidence of a predominant adsorption of p-H_2, with $j=0$, in comparison with o-H_2, with $j=1$.

Andersson and Harris made a more detailed study[87] of the influence of the rotational state of the hydrogen gas (n-H_2, p-H_2, D_2, HD) on the sticking probability for a Cu(100) surface cooled to 10 K. As a measure of the adsorption they used the intensities of the corresponding peaks in the spectrum of EELS and also the change in the work function. The authors of Ref. 87 found that the ratio of the sticking coefficients of p-H_2 and n-H_2 equals 1.4, i.e., molecules with $j=0$ are adsorbed with a higher probability than are molecules with $j=1$. The authors of Ref. 87 also came to the conclusion that a large part of the kinetic energy of the molecule upon impact with the surface is converted into rotational energy.

Information about how the rotational state of the incident hydrogen molecules influences the sticking probability is also found in a number of other papers (see, e.g., Refs. 52–54 and 88), although for higher T_s and other substrates (Pd, Pt, Rh). Incidentally, the authors of those papers assume that the influence of the rotational state on the sticking coefficient is proof of the realization of the dynamic steering mechanism[50,51] and of the unimportant role of adsorption via a precursor state.

Thus, on the surface of noble metals upon deep cooling a physisorbed film of hydrogen (deuterium) forms which is in direct contact with the surface atoms of the metal. For transition metals at helium temperatures, on the other hand, first a monolayer of chemisorbed atoms forms on the surface and then a physisorbed layer of molecules forms on top of that monolayer (Sec. 3.1).

3.2.2. Adsorption kinetics

3.2.2.1. Dependence of the sticking coefficient on the degree of coverage.   Since in the adsorption of hydrogen on copper, dissociation of molecules incident at moderate thermal velocities does not occur, the initial sticking coefficient (at zero coverage) is very small. The reason for this is the enormous mass difference of the colliding partners and, as a consequence, the small accommodation coefficient. However, as physisorbed molecules accumulate on the surface it becomes increasingly probable for an incident molecule to collide with a previously adsorbed molecule, which has an equal mass.[30,60] Figure 23, taken from Ref. 30, shows the sticking coefficient of deuterium on the Cu(100) surface at $T_s\sim10$ K as a function of the degree of coverage. In Ref. 30 the experimental dependence obtained is written in the form
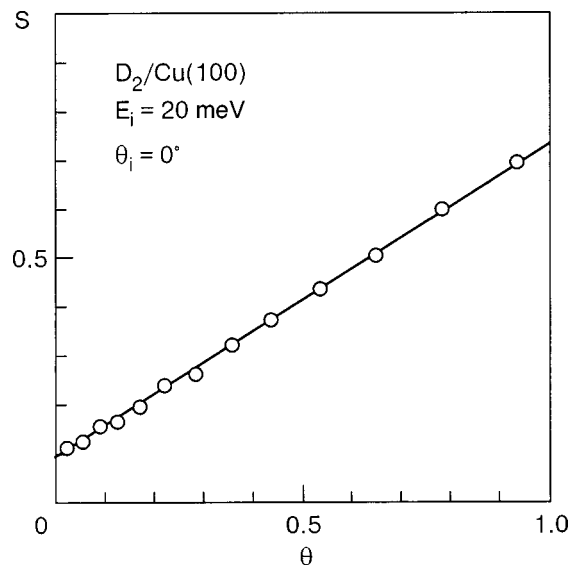
$$S=S_0(1-\theta)+S_1\theta, \qquad (3.3)$$

FIG. 23. Sticking coefficient for D_2 on the Cu(100) surface at $T_s\sim10$ K versus the degree of coverage.[30] E_i is the energy of the incident molecules, and θ_i is the angle of incidence.

where S_0 and S_1 are the sticking probabilities of a molecule in collision with the clean surface and with a previously adsorbed molecule, respectively. For the particular system D_2/Cu(100) the value of S_1 is approximately 8 times larger than S_0. In the case of copper this sort of amortization effect is observed starting at zero coverage, whereas in the case of the transition metals tungsten and molybdenum this effect is manifested in the region of completion of a chemisorbed atomic phase (paragraphs 3.1.2.1 and 3.1.2.3).

3.2.2.2. Dependence of the initial sticking coefficient on the energy and angle of incidence of the molecules.   Important and interesting features of the sticking of hydrogen molecules to the copper surface are revealed by studying the influence of the energy E_i and angle of incidence of a molecular beam on the initial sticking coefficient. The main contribution to the investigation of this question was made by group of investigators from Chalmers University of Technology in Göteborg, Sweden. The combination of precision experiments with monoenergetic molecular beams of H_2 and D_2 and theoretical calculations permitted the authors of Refs. 30 and 89 to create an extremely complete and complex picture of the interaction of hydrogen and deuterium molecules with the surface of a metal single crystal.

The authors of Refs. 30 and 89 showed by comparison of the experimental results with the results of theoretical calculations that the sticking process for a molecule in the physisorption potential well cannot be interpreted on the basis of a purely classical model, which predicts that the sticking coefficient of a light inert particle (in the case of hydrogen, without dissociation) in the limit of zero energy must equal unity and decrease to zero at an energy of the incident particles of several millielectron-volts. However, the experiment shows that the sticking coefficient of hydrogen (deuterium) on the Cu(100) surface varies from ~0.2 to a very small value in the energy range 0–30 meV, which is approximately equal to the width of the phonon bands. Such behavior of the sticking coefficient agrees with quantum calculations in the forced-oscillator model (FOM) or in the distorted-wave Born
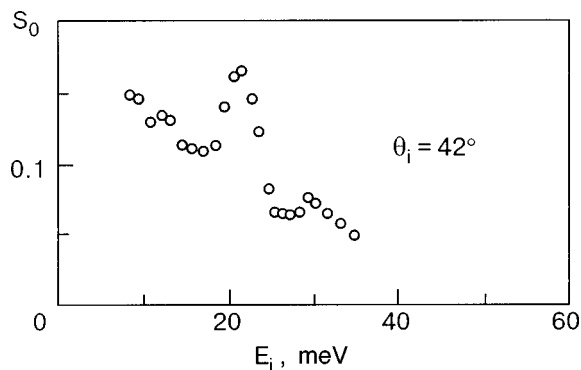
FIG. 24. Initial sticking coefficient for H_2 on Cu(100) at $T_s \sim 10$ K versus the energy of the molecules.[30]

FIG. 25. Initial sticking coefficient for D_2 on Cu(111) (●), Cu(100) (■), and Cu(110) (▲) at $T_s \sim 10$ K versus the energy of the molecules at normal incidence.[89]

approximation (DWBA). At low energies of the molecules a one-phonon process occurs, and at high energies a multiphonon process. Thus these results attest to the important role of the quantum mechanism of sticking for light inert particles.

According to Refs. 30 and 89, the sticking of molecules occurs with the participation of a normal and a resonance process. The normal process includes trapping of the particle after the first impact on account of inelastic scattering on the phonon system; this gives a contribution to the so-called background sticking. The probability of such sticking decreases smoothly with increasing E_i within the width of the phonon bands. Figure 24, taken from Ref. 30, shows the experimental dependence $S_0(E_i)$ for an angle of incidence of 42° relative to the normal. The $S_0(E_i)$ curves exhibit a sharp peak at a molecular energy of ~ 20 meV and a less noticeable peak at $E_i \approx 25$ meV. According to the interpretation of those authors,[30,89] the main cause of the peaks is the trapping of a molecule into a quasibound state on the surface under resonance excitation of the rotational states of the molecule. Probably a transformation of the kinetic energy of the molecule into rotational energy occurs here which is accompanied by a decrease in the translational velocity and makes for a higher sticking probability. Although in itself the excitation of rotational states can have a negative effect on the sticking probability,[28,52–54] the decrease in the translational velocity has a greater positive effect.

A molecule in a quasibound state (with positive total energy) moves rather freely along the surface and can ultimately either stick as a result of excitation of a phonon or be ejected back into the vacuum as a result of diffraction on the lattice of surface atoms of the substrate.[30,89] In general diffraction effects, according to Refs. 30 and 89, play an extremely important role in the mechanism of sticking in the physisorption potential well. As to the subsequent fate of a physisorbed molecule, it can also be ejected into the vacuum as a result of a thermodesorption process if the substrate temperature is high enough to foster an appreciable desorption rate. As was shown in Sec. 3.1, thermodesorption has a substantial influence on the sticking coefficient of hydrogen on the surface of tungsten at $T_s \sim 5$ K.

Besides sticking, the authors of Refs. 30 and 89 also studied the scattering of molecules by the surface and observed a clear correlation of those processes.
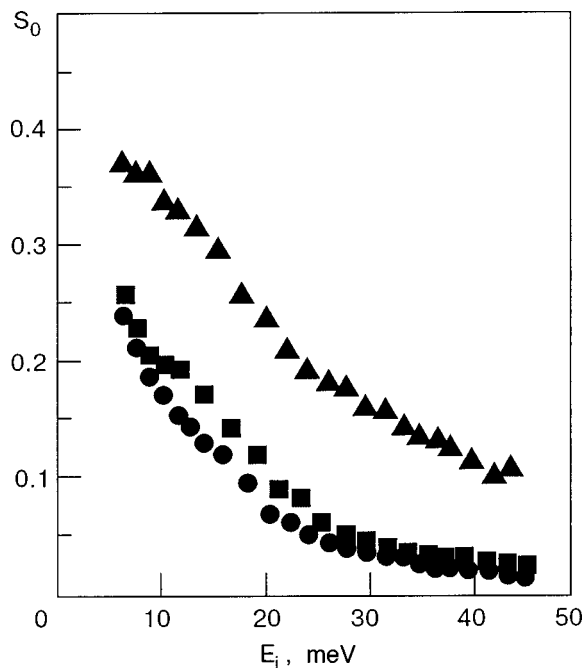
3.2.3. Influence of the structure of the surface on adsorption

The Chalmers research group also devoted considerable attention to the influence of the structure of the surface of the crystal on the parameters of the physisorption of hydrogen. Experiments and theoretical calculations were carried out for the low-index faces of copper[89–92] and aluminum.[92] Figure 25, taken from Ref. 89, shows the dependence of S_0 on E_i for normal incidence of the beam. It is seen that in the energy range 5–45 meV the initial sticking coefficient (in this case for deuterium) is substantially larger on the less densely packed face (110) than on the more densely packed faces (111) and (100). DWBA theory for a one-phonon mechanism of energy transfer from the molecule to the substrate explains the observed tendency. A comparison of the experimental and theoretical results permits the conclusion[89,90] that the observed differences in the sticking probability on the non-close-packed and close-packed faces are caused by structurally specific differences in the molecule–phonon interaction. The transfer of energy is more efficient, and, hence, the sticking is more intense, on a non-close-packed surface, with a larger surface unit cell (and, accordingly, a smaller reciprocal lattice vector).

In Refs. 91 and 92 those same authors studied the influence of the crystallographic orientation (structure) of the surface on the binding energy of physisorbed H_2 and D_2 molecules. It was shown[91] that for adsorption on copper the depth of the physisorption potential well decreases on faces in the sequence $(110) \rightarrow (100) \rightarrow (111)$, a fact which, in the words of the authors, contradicts the usual concepts of the existing theory. The contradiction is eliminated if the profiles of the electron density and their dynamic response, which depend on the face, are taken into account; the latter, in the case of the open (110) face, makes for a larger contribution to the physisorption potential from the van der Waals attrac-

tion than from the Pauli repulsion. In Ref. 92 aluminum, which also has a face-centered lattice, was investigated as a substrate as well as copper. In the case of aluminum the influence of the surface structure is more pronounced in relation to the binding energy. It was found that for the Al(111) and Al(110) faces the depths of the physisorption potential well are close to each other and 40% larger than the well depth for the Al(100) face. For a more rigorous interpretation of the effects observed, the authors of Ref. 92 consider it necessary to construct a theory on a more fundamental level.

3.2.4. Spectra of excitation of rotational states of physisorbed hydrogen

In the papers by the Chalmers group significant attention is paid to the spectra of rotational states of physisorbed hydrogen, which were obtained by the HREELS method.[85] It was found that the intensities of the peaks of the characteristic energy loss to rotational excitation of molecules of o-H_2 ($j=1\rightarrow3$) and p-H_2 ($j=0\rightarrow2$) molecules physisorbed at $T_s\sim10$ K on Cu(100) are in inverse relation to the ratio of the densities of these molecules in the gas phase. This effect is explained by an accelerated ortho–para conversion of H_2 in the adsorbed state as compared to the gas phase.

Very interesting features of the adsorption properties of the H_2 molecule have been revealed the research of the Chalmers group in studies of the rotational states of molecules adsorbed on the terraced Cu(510) face.[93,94] By combining measurements by the HREELS method and calculations of the total energy by the density-functional approach, the authors of Refs. 93 and 94 found unusual adsorption properties of a hydrogen molecule occupying a site above a copper atom at the edge of a step. The energies of rotational–vibrational transitions turned out to be close to those for the ideal two-dimensional quantum rotator, and the internal vibrations of the molecule are dipole-active and are characterized by an extraordinarily small energy. This last circumstance and also the fact that the Cu–H_2 bond length is shortened considerably while the H–H bond length in the molecule is lengthened are the characteristic signs of chemisorption. However, the fact that the energy of adsorption of the H_2 molecule in this state is less than 100 meV is characteristic of physisorption. The reason that the intramolecular bond is perturbed, as in the case of chemisorption, while the binding energy of the molecule with the surface is small, is seen by the authors of Refs. 93 and 94 as being due to the very high energy of zero-point vibrations of the molecule in the narrow and anharmonic potential well over a copper atom located at the edge of a step.

Calculations by the authors of Refs. 93 and 94 have also shown the existence of strong orientational anisotropy, which constrains a molecule above a single copper atom on a step to rotate in the plane perpendicular to the direction of the H_2–Cu bond. This explains why an H_2 molecule in such a state behaves as an almost ideal 2D rotator. Unlike adsorption on the smooth Cu(100) face, when an accelerated o–p-H_2 conversion is observed and the adsorption states of parahydrogen are predominantly occupied,[85] on the terraced Cu(510) face one observes a sharp enrichment of the adsorbed layer in orthohydrogen. A similar enrichment was observed in Refs. 93 and 94 at a somewhat higher (up to
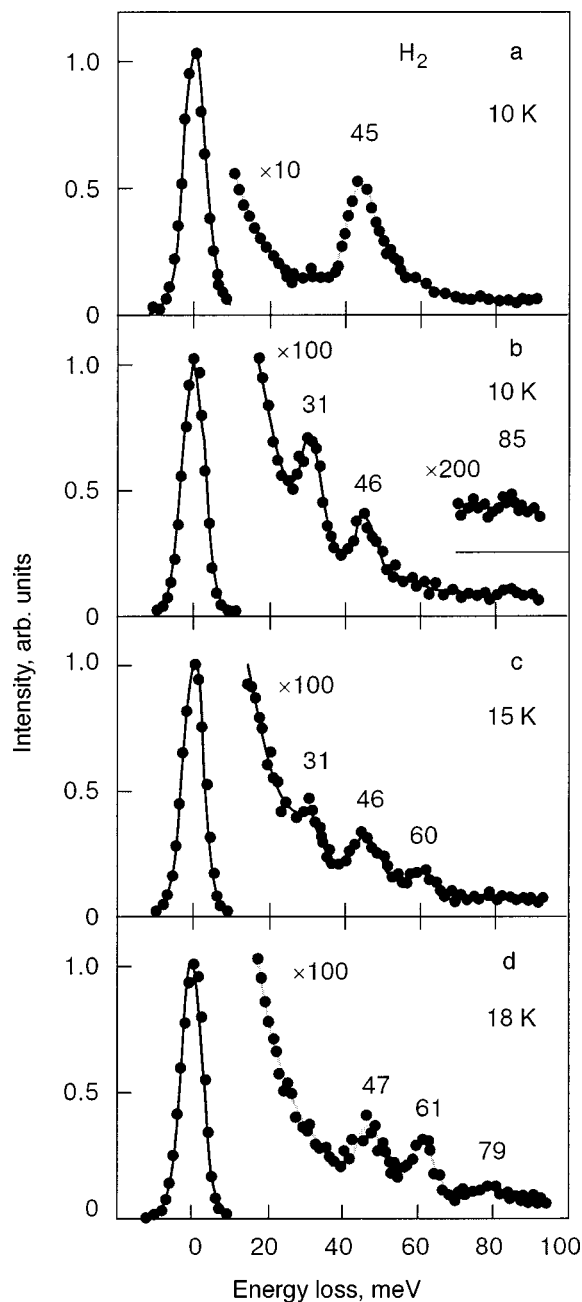
FIG. 26. Characteristic electron energy loss spectra for H_2 on Cu(510).[94] Complete monolayer at 10 K (a); steps coated at different T_s (b–d).

~18 K) temperature. At such a temperature the density of H_2 molecules on the terraces becomes negligible, and all of the hydrogen is concentrated at special adsorption sites above copper atoms on the edge of a step.

As is seen in Fig. 26, taken from Ref. 94, the peaks of the electron energy loss spectrum at 31 and 46 meV, which, according to theoretical calculations, pertain to the $0\rightarrow2$ rotational transitions of the two-dimensional and three-dimensional p-H_2 rotators, respectively, are present in the spectrum at a substrate temperature of 10 K. At 16 K the intensity of the 31 meV peak is significantly lower, and at 18 K this peak has vanished completely, and a pronounced peak at 61 meV, corresponding to the 2D rotational transition $1\rightarrow3$ for o-H_2, has appeared.

3.2.5. Photodesorption of physisorbed hydrogen

The Chalmers group has also done research on photodesorption of physisorbed hydrogen under infrared radiation. The desorption of hydrogen from vacuum cryopanels, initiated by the thermal radiation from the walls of the chamber, was noted quite some time ago.[95] Subsequent studies[96–98] confirmed the existence of such desorption, and the results of those studies indicate a nonthermal character of the process. The authors of Refs. 96 and 98 assumed that the desorption of a molecule is initiated by a phonon arising upon the absorption of an infrared photon in the substrate, after which the energy of the phonon is transferred to an adsorbed molecule.

Another point of view as to the mechanism of photodesorption was stated in Ref. 99: direct photodesorption via excitation of the molecule from the lowest vibrational level in the physisorption potential well to a state of the continuum. Direct proof of the realization of such a mechanism was obtained by the Chalmers group.[100,101] They did an experimental and theoretical study of the photodesorption of H_2, HD, and D_2 from the terraced Cu(510) surface under the influence of blackbody radiation. The desorption is significant, since only a few bound states are contained in the shallow physisorption well, the vibrational motion of a molecule is dipole-active, and the dipole moment of the molecule–surface bond is a highly nonlinear function of the displacement.[102] The calculations showed that the rate of desorption initiated by an indirect process involving the excitation of phonons in the substrate is several orders of magnitude lower than that observed in experiment and calculated for the direct photodesorption mechanism.

Using the HREELS method, the authors of Refs. 100 and 101 had the capability of observing separately the photodesorption of molecules adsorbed on the flat terraces and on the edges of the steps. It was shown that the process of desorption from the steps is considerably more intense than from the terraces, and an isotope effect is also observed: deuterium is desorbed at a lower rate than hydrogen. The existence of such an isotope effect is explained by the theory. Without going into the details of the theory, we can posit that the deeper position of the level of zero-point vibrations of the D_2 molecule in the physisorption potential well in itself has an effect on the photodesorption rate. The differences in the rates of photodesorption from the terraces and edges of the steps is partly explained by the larger dipole activity of H_2 edge molecules, but additional study is required.[101]

4. OXYGEN, CARBON MONOXIDE, AND NITROGEN

4.1. Oxygen

The study of the low-temperature adsorption of oxygen on metals is of significant interest for at least two reasons. First, in interacting with a surface, oxygen, the most active component of the Earth's atmosphere, radically alters the properties of the surface (the electronic properties, catalytic reactions, corrosion, etc.), and the key stage of this interaction is adsorption. As in the case of hydrogen, the mechanism of dissociative adsorption may be a multistep one and might involve a precursor state—a state of physisorption. This state is characterized by a very small binding energy (although larger for oxygen than for hydrogen), and deep cooling of the substrate is necessary in order to study it experimentally. Second, the formation of an adsorbed monolayer is the initial stage in the growth of an oxygen crystal, and the properties of this adlayer undoubtedly influence the properties of the cryocrystal that will grow.

The low-temperature adsorption of oxygen has been the subject of considerably fewer papers than hydrogen adsorption. Therefore, this Section of the paper is substantially shorter in length. We shall mainly discuss the low-temperature adsorption of oxygen on transition metals.

4.1.1. Adsorption on metal films

The earliest study known to the author on the adsorption of oxygen under deep cooling of the substrate was done by Rühl,[103] who studied adsorption on as-deposited films of Mg, Mn, Al, In, Ga, Cd, Pb, and Sn with thicknesses of 50–150 Å, cooled to as low as 1.5 K. It was found that the adsorption (condensation) of oxygen at low temperatures (from 1.5 to 7 K for the different metals) does not have a substantial effect on the electrical resistivity of the film. However, increasing the temperature of the film to some characteristic temperature (e.g., in the range 20–40 K for Pb) leads to an irreversible increase in the resistance, which can be explained as being the start of an oxidation process which leads to an effective thinning of the film. Thus at low temperature oxygen is not chemisorbed on the surface of films of these metals but forms a layer of physisorbed or condensed molecular oxygen.

Similar results we later obtained by Chottiner and Glover[104] for tin films. Those authors point out[104] that in the condensation of a thick layer of oxygen at 5 K the resistance of the film increased somewhat, corresponding to the loss of metallic conduction by a layer with an effective thickness of 0.1 Å (their Sn film had a thickness of ~150 Å). Increasing the temperature of the film above 13 K led to an irreversible increase in the resistance owing to the chemisorption of oxygen. The authors of Ref. 104 estimated that this increase in resistance corresponds to eliminating a layer of tin ~11 Å thick from participation in the electrical conduction, and the activation energy of the chemisorption process is ~35 meV. A slight increase in the resistance of the film at 5 K can be explained as being due a change in the conditions of scattering of conduction electrons on the $Sn-O_2$ interface, since in the case of physisorption there is practically no exchange of electrons between the adsorbent and adsorbate.

4.1.2. Adsorption on single crystals

4.1.2.1. Spectra of adsorption states. The adsorption of oxygen on single-crystal tungsten (the (110) face) at 20 K was first studied by Leung and Gomer,[105] who measured the thermodesorption spectra for the first time. They showed that at a relatively low exposure the thermodesorption spectrum of an adlayer formed at 20 K does not differ from that observed after adsorption at 300 K, and oxygen is desorbed predominantly in the form of atoms. The desorption of atomic oxygen after adsorption at room temperature has also been observed in our studies.[40,41,106] With increasing exposure to oxygen at 20 K the authors of Ref. 105 observed the
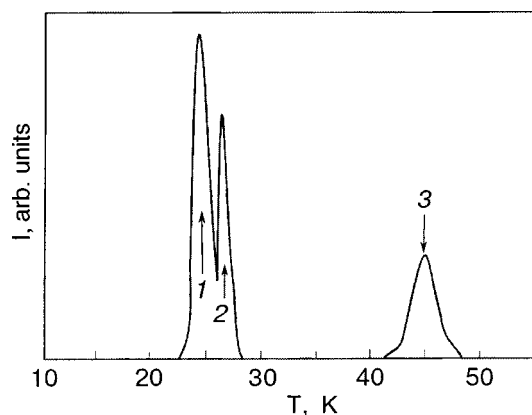
FIG. 27. Thermodesorption spectrum for oxygen from W(110); adsorption at 20 K.[105] *1*—Condensation; *2*—physisorption; *3*—weak molecular chemisorption.

FIG. 28. Model of an oxygen adlayer at $T_s \sim 5$ K.[34] *1*—Atomic chemisorption; *2*—molecular chemisorption; *3*—physisorption; *4*—condensation.

appearance of low-temperature peaks at 45 K, then at 27 K, and, finally, at 25 K. The corresponding adsorption states will be referred to by the temperature of the peaks. A thermodesorption spectrum of this type is shown in Fig. 27. The peaks at 45 and 27 K saturate with increasing exposure, while the peak at 25 K grows without bound. On the basis of measurements of the work function and electron-stimulated desorption, the authors of Ref. 105 concluded that the 27 and 25 K adsorption states are almost identical in their properties and pertain to physisorption and condensation, respectively. The 45 K adsorption state was attributed in Ref. 105 to a state of weak molecular chemisorption, and it was assumed that it is populated via conversion from a state of physisorption as the temperature is raised. A similar point of view is also expressed in the paper by Wang and Gomer,[107] but this interpretation was later acknowledged by Gomer *et al.*[108] to be incorrect.

To elucidate the nature of the adsorbed particles (atoms or molecules) on W(110) at $T_s \sim 20$ K, an experiment was done using the oxygen isotopes $^{16}O_2$ and $^{18}O_2$, and the desorption was observed at 45 K.[108] The idea of the experiment was as follows. If $^{18}O_2$ and then $^{16}O_2$ are adsorbed in sequence, then under the condition that all of the oxygen is adsorbed in a molecular state, the number of $^{18}O_2$ and $^{16}O_2$ molecules desorbed at 45 K will be in the same ratio as the number of these molecules adsorbed. The experiment showed, however, that only desorption of $^{16}O_2$ is observed at 45 K. This means that the first portion of the molecules ($^{18}O_2$) dissociated, and the desorption of chemisorbed oxygen atoms occurs at $T > 2000$ K. However, the authors of Ref. 108 note that in the given experimental setup one cannot rule out that the atomic phase of adsorption was formed not directly during adsorption but as a result of conversion when the sample temperature was raised to bring about thermodesorption. That that was in fact not the case is shown by the experiments of Opila and Gomer using photoelectron spectroscopy,[109] which we shall discuss below.

The above-described state of the adsorbed oxygen is typical for tungsten, but in the case of platinum Artsyukovich and Ukraintsev[110] observed the conversion of O_2 molecules physisorbed at $T_s \sim 20$ K to a chemisorbed state when the temperature T_s was raised to 30–40 K. An atomic chemisorbed state is observed when T_s is increased to 100–160 K.
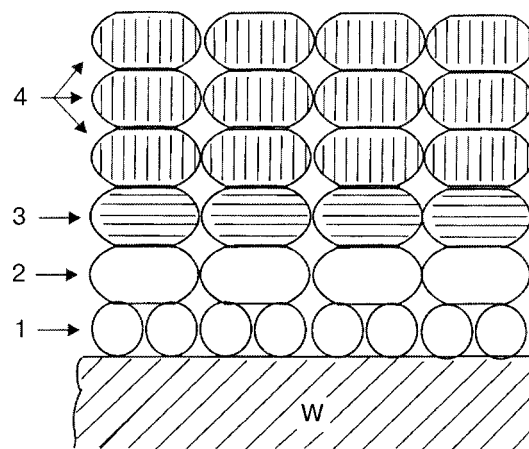
We have measured the thermodesorption spectrum of oxygen adsorbed at $T_s \sim 5$ K on different faces of tungsten.[33,34,111] The thermodesorption spectra of molecular oxygen from the W(110), (100) and (112) surfaces[33,34] are similar to each other and are practically the same as the spectrum obtained for W(110) by Leung and Gomer.[105] What is new here is evidence of the absence of oxygen adsorption states on the tungsten surface with a binding energy less than that for the 25 K state. The spectrum of thermodesorption of oxygen from the W(111) surface is somewhat different from the spectra discussed above for the W(110), (100) and (112) faces. The difference is that the peak corresponding to weak molecular chemisorption is shifted to 60 K.[111] An estimate of the activation energy for desorption for the 25, 27, 45, and 60 K adsorption states gives 65, 70, 117, and 156 meV, respectively. We see the cause of the increase in the binding energy of O_2 in the state of weak molecular chemisorption on the (111) face as being that this face is the least densely packed, and molecules on this face can touch a larger number of neighboring W atoms than in the case of the smoother faces. Based on the results discussed above, a hypothetical model for the layer-by-layer growth of an oxygen cryocrystal was proposed in Ref. 34 and is illustrated in Fig. 28.

Let us conclude by discussing the results of direct observations by the method of scanning tunneling microscopy of the oxygen atoms and molecules on the surface of a metal cooled to 4 K[112] The authors of Ref. 112 observed individual O_2 molecules, clusters of O_2 molecules, and also oxygen atoms adsorbed on the Cu(110) surface at $T_s \sim 4$ K. Figure 29 shows an STM image of a 37×37 Å region of the surface, on which one can see an oxygen molecule (the bright spot) and pairs of oxygen atoms (dark spots). The authors of Ref. 112 see these results as proof that a molecular precursor state actually exists on the surface and participates in the mechanism of dissociative adsorption, although some recent papers have cast doubt on the role of the precursor state.[50–53] The important fact is that molecules are present on a surface on which dissociative adsorption occurs.

4.1.2.2. Adsorption kinetics. Let us consider the curves measured in our laboratory by the molecular-beam method (Sec. 2.5) for the dependence of the oxygen sticking coeffi-
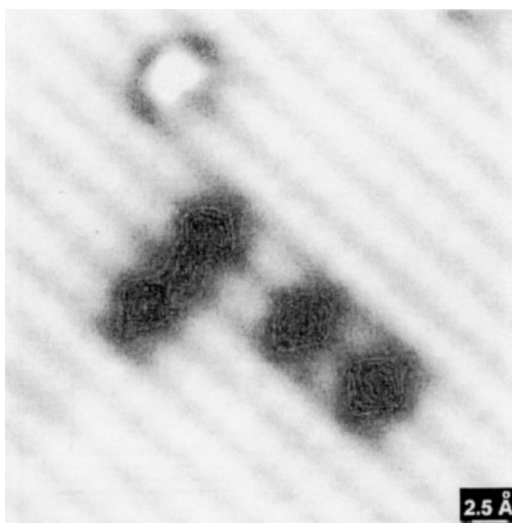
FIG. 29. STM image of oxygen adparticles on Cu(110) at 4 K.[112]

cient on the degree of coverage θ for different faces of W.[33,34,111,113,114]

Figure 30, taken from Ref. 34, shows the dependence of the sticking coefficient on θ for different substrate temperatures T_s for the (100) and (110) faces of tungsten. We note that here and below, θ is the number of oxygen atoms per atom of the substrate surface. In the case of the W(100) surface the $S(\theta)$ curves are characterized by the following features. The initial sticking coefficient is independent of T_s
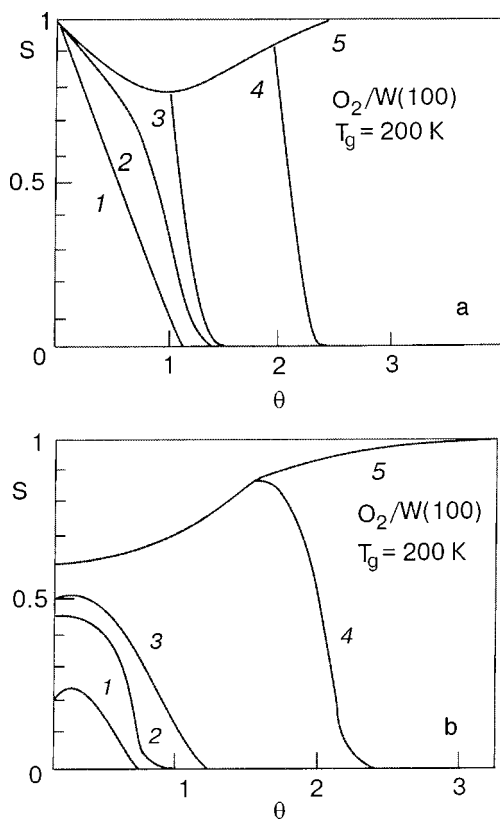

FIG. 30. Sticking coefficient for O_2 versus the degree of coverage.[34] a) W(100), T_s [K]: 340 (*1*), 200 (*2*), 80 (*3*), 35 (*4*), 5 (*5*); b) W(110), T_s [K]: 300 (*1*), 80 (*2*), 60 (*3*), 35 (*4*), 5 (*5*).

and equal to unity. The initial sticking coefficient is also independent of T_g. This attests to direct, nonactivated chemisorption.

In the previous paragraph we presented evidence that oxygen is dissociatively chemisorbed in the form of atoms on tungsten up to a certain coverage at $T_s > 20$ K. It seems to us that the results presented in Fig. 30 attest to the fact that dissociative adsorption of oxygen also occurs at 5 K. It is seen that curves *4* and *5* in Fig. 30 coincide at coverages up to one monolayer. That means that in this coverage range the mechanism of adsorption is unchanged on going from $T_s \approx 35$ K to $T_s \approx 5$ K, i.e., the adsorption is dissociative at $T_s \approx 5$ K also.

Let us now discuss the influence of the substrate temperature in the range 5–350 K on the kinetics of filling of the first monolayer. Such data have been obtained for $T_g = 200$ K. It is seen in Fig. 30 that for $T_s \approx 350$ K the sticking coefficient decreases sharply with coverage, attesting to a Langmuir mechanism of adsorption, wherein a molecule incident on an occupied adsorption center is reflected back. Lowering T_s leads to a decrease in the slope of the $S(\theta)$ curve, which indicates the turning on of a mechanism of adsorption via an extrinsic precursor state, when a molecule incident on an occupied center migrates along the surface and may find an unoccupied center and be adsorbed. Some qualitative ideas as to the cause of the increased role of adsorption via an extrinsic precursor state as T_s is lowered can be found in our review article;[11] these ideas are based on a comparison of the lifetime of a molecule on the surface in respect to the thermodesorption process, τ, and the time required for traversing a certain diffusion path, t_m. Since the activation energy for desorption, E_d, is always larger than the activation energy for surface diffusion, E_m, with decreasing temperature the balance of these times changes in favor of diffusion:

$$\frac{\tau}{t_m} \approx \exp\left(\frac{E_d - E_m}{kT_s}\right). \tag{4.1}$$

The next feature of the curves shown in Fig. 30 is that after completion of the first monolayer the sticking coefficient increases, approaching unity. This effect, as in the adsorption of hydrogen (paragraph 3.1.2.1), is explained by the increase in the efficiency of kinetic energy loss in the collision of a molecule with the surface as the surface fills with the weakly bound molecular adsorption phase on account of the equal mass of the colliding partners.

The kinetic energy of the incident molecules, while not affecting the initial sticking coefficient, nevertheless has a substantial influence on the sticking coefficient in the region $\theta \approx 1$, where the formation of the molecular adsorption phase begins. The sticking coefficient at $\theta \approx 1$ decreases with increasing T_g as a result of the decrease in the probability of trapping to a state of physisorption. A qualitatively similar influence of the energy of the incident particles on the sticking probability has been observed, e.g., for nitrogen on W(100) (Ref. 115) and CO and Ar on Ir(110) (Ref. 116) (granted, at significantly higher T_s).

The adsorption of oxygen on the W(112) surface at $T_s \sim 5$ K is characterized by $S(\theta)$ curves like those shown in Fig. 30,[34] except for substantial differences in the case of

adsorption on the close-packed W(110) surface. As is seen in Fig. 30, the initial sticking coefficient for W(110) is substantially less than unity and it decreases with increasing T_s. The reason why S_0 is substantially less on the W(110) surface may be discerned in the fact that the number of broken bonds per unit area on this surface is 1.4 times less than on the W(100) surface.

The decrease of S_0 with increasing T_s is a sign of participation of an intrinsic precursor state in the dissociative adsorption mechanism (arguments toward a similar conclusion are given in paragraph 3.1.1.1). In contrast to W(100) and W(112), in the case W(110) the signs of adsorption via an extrinsic precursor state are manifested at room temperature. This can be explained by the higher mobility of the O_2 molecules in the precursor state on the close-packed, smooth W(110) surface. The increase in the sticking coefficient on the W(110) surface for $\theta > 1$ is similar to the W(100) case and is explained by the same cause.

We know of no studies in which $S(\theta)$ has been measured for adsorption on a metal at $T_s \sim 5$ K. However, Wang and Gomer[117] have obtained similar curves for W(110) at $T_s \geq 20$ K. In their general features these curves for $T_s \sim 20$ K are similar to that shown in Fig. 30: the values of the initial sticking coefficients are close, and one observes an increase in the sticking coefficient with increasing coverage. However, according to our measurements, the increase of S with increasing θ does not become noticeable at zero coverage, as in Ref. 117, but for $\theta > 0.5$. The authors of Ref. 117 also attribute the increase of S with increasing θ to more efficient kinetic energy loss by the incident molecule in its impact on a previously adsorbed molecule. What is hard to explain is the finding of Ref. 117 that S increases starting at zero coverage, when, according to the our data and the data of Gomer et al.,[107,108] tightly bound chemisorbed oxygen atoms accumulate on the surface. The O–W complex is essentially a unified quasimolecule with a very large mass, and the collision of an O_2 molecule with it is characterized by inefficient accommodation.

4.1.2.3. Electron spectroscopy and the state of adsorbed particles. Let us discuss the results of several studies using photoelectron spectroscopy to elucidate the state of adsorbed particles at low temperatures and also a study using x-ray absorption-edge fine structure (NEXAFS) for the same purpose. We have already mentioned the paper by Opila and Gomer,[109] in which the adsorption of oxygen on W(110) at $T_s = 26$ K was studied by the methods of ultraviolet (UPS) and x-ray (XPS) photoelectron spectroscopy. It was found that from the start of the oxygen admission only atomic chemisorbed oxygen is formed, and only after saturation of the atomic layer does a layer of weakly bound molecular oxygen begin to grow (and, with time, saturate). In the XPS spectrum one observes two main oxygen peaks, one of which (530.5 eV) belongs to atomic oxygen and does not undergo any changes (Fig. 31), unlike the 536 eV peak, which vanishes from the spectrum after the substrate is heated to 90 K (the molecular phase is desorbed). Based on the fact that for the molecular phase a single unsplit peak is observed in the XPS spectrum, the assumption was made in Ref. 109 that both atoms of the O_2 molecule are found in an identical
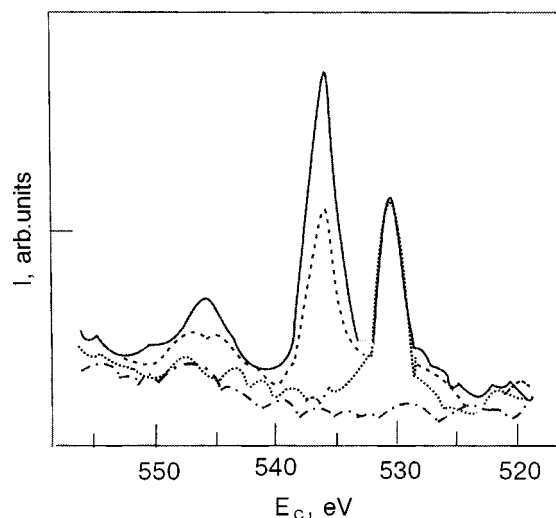

FIG. 31. Photoelectron spectrum of adsorbed oxygen.[109] The solid curve is for a saturated layer at 26 K; the dashed curve—heated to 36 K; the dotted curve—heated to 90 K; the dot-and-dash curve—clean W.

position with respect to the substrate, i.e., the axis of the molecule is oriented parallel to the surface.

We know of several more studies in which the method of photoelectron spectroscopy was used to elucidate the state of oxygen adsorbed on a metal surface at low temperatures. Schmeisser and Jacobi[118] did a UPS study of the adsorption of oxygen on the surface of sputtered gallium films. It was found that at 10 K the oxygen molecules are physisorbed in the first monolayer, and above it several additional O_2 monolayers can be condensed. When T_s is increased to 70 K the O_2 molecules are chemisorbed (without dissociation), and at 300 K the oxygen is bound dissociatively and forms a bulk oxide.

The UPS method was used by Jacobi et al.[119] in a study of the adsorption of oxygen on the Ni(100) surface ($T_s = 20$ K). The authors of Ref. 119 showed that at submonolayer coverages, oxygen is adsorbed mainly dissociatively, although physisorbed molecules are also noticeable. With increasing exposure a layer of physisorbed molecules is formed exclusively atop the chemisorbed monolayer. Thus on the Ni(100) surface the low-temperature adsorption of oxygen occurs in a manner similar to that on the W surface (see above).

A study of oxygen adsorption at $T_s = 25$ K on the Pt(111) surface has been done by Lunz et al.[120] with the use of XPS and TPD. The photoelectron and thermodesorption spectra reveal four different states of the adsorbed particles: polylayer condensation (desorption temperature $T_d = 30$ K), physical adsorption ($T_d = 45$ K), and molecular chemisorption ($T_d = 750$ K). The physisorption serves as a precursor state for molecular chemisorption, and the latter, in turn, is a precursor state for atomic chemisorption. The position of the O1s peak in the spectrum of physisorbed oxygen is close to that for the gas phase.

The same adsorption system O_2/Pt(111) was studied by Ranke[121] by the methods of XPS and UPS. In that paper it was also shown that at 20 K oxygen is physisorbed in molecular form. As a result of a heating of the substrate to 90 K the photoelectron spectrum is transformed, attesting to mo-

lecular chemisorption in the form of O_2^- or O_2^{2-} (the super-oxo and peroxo configurations, respectively). Such states of the oxygen molecules adsorbed on platinum have been identified by calculations from first principles in the local-spin-density approximation.[122] In their general features the results of Ref. 121 agree with those obtained by the TPD method in Ref. 110.

High-resolution electron-energy loss spectroscopy (HREELS) has been used to study the states of adsorbed oxygen at $T_s \leqslant 20$ K on the surfaces Ni(111) (Ref. 123) and Nb(110) (Ref. 124). This variety of electron spectroscopy is extremely efficient for identifying physisorbed molecules from the corresponding characteristics of energy loss to the excitation of intermolecular vibrations. In the study by Beckerle *et al.*[123] an attempt was made to observe O_2 molecules in a precursor state at $T_s = 8$ K in the limit of zero coverage. However, this attempt was not successful, apparently because of the very short lifetime of molecules in the precursor state and their very low density.

Franchy *et al.*[124] established that at $T_s = 20$ K at low exposures the oxygen on the Nb(110) surface is chemisorbed dissociatively, a circumstance that the authors associate with the formation of the oxide NbO. At high exposures a physisorbed molecular layer forms above the chemisorbed atomic monolayer, much like what happens on the surface of tungsten (see above).

The HREELS method has also been used for studying the resonance scattering of electrons by an oxygen layer physisorbed on the surface of silver in the studies of Tang *et al.*[125] and Lacombe *et al.*[126] In particular, in Ref. 126 it is shown that the angular dependence of the scattered electrons changes at the transition from monolayer coverage to multilayer coverage; this is a consequence of the different orientation of the molecules in the monolayer and multilayer regimes.

Still another variety of electron spectroscopy—transmission spectroscopy—was used by Shayegan *et al.*[127] to study the state of the adparticles in the adsorption of oxygen on the Ni(111) surface at $T_s = 5.5$ K. In measuring the current–voltage characteristic in a retarding field in the saturation region one observes current oscillations characterizing the state of the adsorbed layer.[128] The form of the spectrum obtained in Ref. 127 indicates that the O_2 molecules are physisorbed on the surface. Heating of the sample leads to the formation of a chemisorption state; the activation energy of this process is ~13 meV. At first glance the results of the studies of low-temperature adsorption of oxygen on nickel in Refs. 127 and 119 are contradictory: in Ref. 119 the dissociative chemisorption of oxygen was observed. It should be taken into consideration, however, that different faces of single-crystal nickel were investigated in Refs. 127 and 119, and, furthermore, the temperature of the sample in Ref. 119 was substantially higher than in Ref. 127 (20 K rather than 5.5 K). It is quite possible that a temperature of 20 K is sufficient for overcoming the insignificant activation barrier between the states of physisorption and chemisorption.

Important information about the state of adsorbed oxygen can be obtained by the NEXAFS method. Such experiments done in synchrotron radiation for the adsorption system O_2/Pt(111) at $T_s = 17$ K are described by Wurth *et al.*[129]

At a substrate temperature $T_s < 30$ the NEXAFS spectrum and, accordingly, the intramolecular structure of the adsorbed oxygen are almost indistinguishable from the van der Waals-bound solid oxygen, and this is a state of physical adsorption with van der Waals bonding. When the substrate temperature is raised to 80 K conversion to a chemisorbed molecular state is observed, as is attested by the transformation of the NEXAFS spectrum. Because of the involvement of the π^* orbital perpendicular to the surface in the chemisorption bond, the corresponding resonance is weak and broadened, while the π^* orbital parallel to the surface remains unperturbed. The results indicate that in both the physisorption and chemisorption states the axis of the O_2 molecule is oriented parallel to the surface. The transition to the state of chemisorption also leads to a change in the magnetic properties of the O_2 molecule, which is manifested in exchange splitting of the σ^* resonance. Thus in the case of the low-temperature adsorption of oxygen on platinum, dissociation of the O_2 molecule does not occur, as it does in the case of adsorption on tungsten.

4.1.2.4. Adsorption of oxygen and scattering of conduction electrons. Panchenko and co-workers used the static skin-effect method not only to study the low-temperature adsorption of hydrogen (Sec. 3.1.3) but also to study the adsorption of oxygen.[23,25,75,76,130] It was shown[23] that the resistivity of thin (~0.1 mm) single-crystal slabs of tungsten and molybdenum with (110) surfaces in a strong magnetic field parallel to the surface is anomalously sensitive to the adsorption of oxygen. The deposition of a disordered monolayer of oxygen leads to a twofold increase in the magnetoresistance. In Refs. 75 and 76 it was established that the effect depends on the crystallographic orientation of the surface of the slab, and for a slab with the (100) surface the resistivity remains practically unchanged. An interpretation of this difference in the behavior of the resistivity of slabs with the (110) and (100) surfaces was proposed in Refs. 75 and 76, based on taking into account the electron–hole transfers in the scattering of conduction electrons by the surface.

The combined use of the static skin-effect and LEED methods in a single experimental apparatus[25,130] has permitted the establishment of a clear correlation between the resistance of the slab and the structure of the adsorbed oxygen layer, which is ordered by means of annealing. Figure 32, taken from Ref. 25, shows the dependence of the magnetoresistance of a tungsten slab with the (110) surface on the oxygen adsorption time; the vertical lines bound the existence intervals of the corresponding structures of the adlayer. It is seen that the sharp minimum of the magnetoresistance is achieved at the maximum development of the $p(2 \times 1)$ structure, and upon the formation of the (2×2) structure the magnetoresistance again increases. Analysis of the electronic transitions in scattering from the corresponding surface structures explains the specular character of the electron scattering for the $p(2 \times 1)$ surface and the diffuse character of the scattering for (2×2).

A substantially different situation obtains for the adsorption of oxygen on the Mo(110) surface.[131] On that surface the $p(2 \times 1)$ structure does not form, and therefore the dependence of the magnetoresistance on the oxygen adsorption time does not have a sharp minimum like that observed for
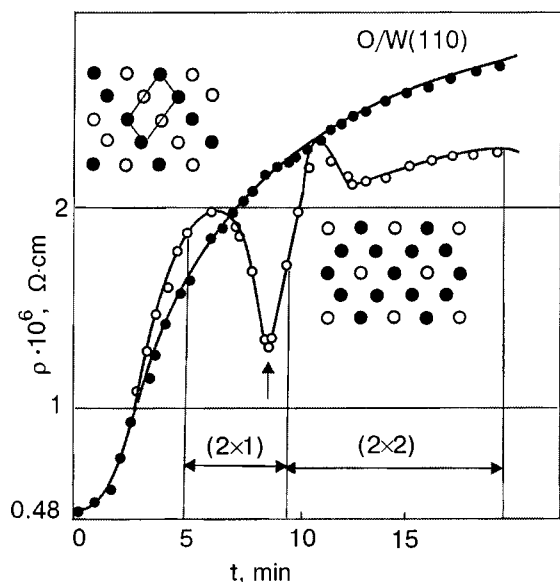
FIG. 32. Magnetoresistance of a W(110) slab versus the exposure time in oxygen.[8,25] ●—Adsorption at $T_s = 4.2$ K; ○—annealing to 200 K; the vertical lines are boundaries of the existence regions of the structures illustrated in the figure.

the W(110) surface. Thus, as in the case of hydrogen adsorption (Sec. 3.1.3), the static skin-effect method can serve as a nondestructive indicator of the structure of an oxygen adlayer.

4.2. Carbon monoxide and nitrogen

Study of the low-temperature adsorption of carbon monoxide and nitrogen is of interest from the standpoint of elucidating the mechanism of their adsorption and participation in important catalytic processes (in particular, in the role of an adsorption precursor state), e.g., the oxidation of CO in automobile exhaust or the synthesis of ammonia, and also as the initial stage of the growth of cryocrystals. We know of only a small number of papers devoted to the study of low-temperature adsorption of these gases, and so this Section will be extremely short.

4.2.1. Carbon monoxide

Let us briefly discuss a few of the papers known to us on the low-temperature adsorption of carbon monoxide. Leung, Vass, and Gomer[132] have studied the influence of CO adsorption on the W(110) surface at $T_s = 20$ K on the work function and electron-stimulated desorption. It was shown that the work function increases by 0.6 eV and that electron-stimulated desorption of CO^+ ions from the adlayer occurs.

Norton et al.[133] have studied the adsorption of CO on the surface of the noble metals copper and gold at $T_s = 20$ K by the method of photoelectron spectroscopy. The spectra of physisorbed CO exhibit only a slight broadening and shift of the 5σ, 1π, and 4σ levels in comparison with the gas phase. Heating of the substrate to 30 K leads to conversion of the physisorbed to a chemisorbed state, which indicates that this process has a very low activation energy.

The resonance scattering of electrons from a silver surface coated with a CO adlayer at 20 K has been investigated by Demuth et al.[134] It was found that the frequency of intermolecular vibrations differs little from that in the gas phase.

It was also shown that the differences in the electron spectra of the adsorbed and condensed phases of CO permit one to delimit the monolayer and multilayer deposition regimes.

The adsorption of CO on the Ni(100) surface at $T_s = 20$ K was studied by Jacobi et al.[119] by the UPS method. Those authors found that on this surface CO is chemisorbed in the first layer. This is evidence of a low activation energy for chemisorption. Information about the dependence of the sticking coefficient of CO on the coverage was also obtained, and it was stated that the sticking coefficient is constant up to a coverage of $\theta = 0.9$.[119] This last result indicates that the mobility of the CO molecule is very high, and it can therefore easily find an unoccupied adsorption center (adsorption via an extrinsic precursor state).

Shayegan et al.[135] have used the method of transmission electron spectroscopy to study the adsorption of CO on the Ni(111) surface at $T_s = 5.5$ K. The suppression of the electron current in the saturation region of the current–voltage characteristic attests to the formation of a physisorbed layer.[128] The authors of Ref. 135 called attention to the fact that the physisorbed CO is present at $T_s = 5.5$ K even at submonolayer coverages. This conclusion contradicts the conclusions of Ref. 119, though it must be taken into consideration that in Ref. 119 the temperature was significantly higher. Furthermore, the Ni(100) surface studied in Ref. 119 is less densely packed than the Ni(111) surface investigated in Ref. 135, making it more favorable for the formation of a chemisorption bond.

Kawai and Yoshinobu have studied the low-temperature ($T_s \sim 20$ K) adsorption of CO on the Pt(111) and Ni(100) surfaces by the method of infrared spectroscopy.[136,137] By comparing the intensity of the different peaks in the spectra, those authors[136,137] determined the relationship between the occupations of the adsorption sites (centers) of different kinds in different stages of the adsorption process and arrived at the conclusion that under conditions of suppressed surface migration of the CO molecules (because of the low T_s) there occurs not only direct adsorption at energetically favorable sites but also stimulated occupation of neighboring adsorption sites in collisions of the incident molecules with previously adsorbed molecules.

In concluding our review of papers on the low-temperature adsorption of CO we point out the study by Sautet et al.,[138] who used the STM method at $T_s = 25$ K to observe individual CO molecules adsorbed at different kinds of sites on the Pd(111) surface. Figure 33 shows an STM image of individual CO molecules. The molecules are seen as protrusions of height ~ 0.25 and ~ 0.15 Å above the surface, which indicates that they are adsorbed at sites of two different types. This interpretation is confirmed by theoretical calculations of the total energy in the density-functional approximation.

4.2.2. Nitrogen

Research on the adsorption of nitrogen on metals surfaces at low temperatures ($T_s \leqslant 20$ K) has been the subject of a small number of papers known to us.[84,119,134,139–142] These are mainly studies using methods of electron spectroscopy. Using the XPS method, Grunze et al.[139] observed a significant difference in the spectra of N($1s$) for nitrogen chemi-
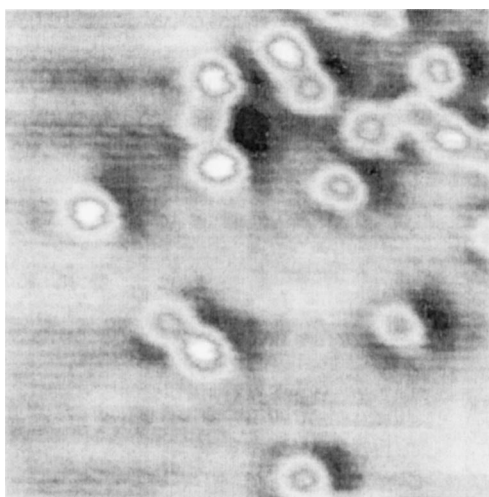
FIG. 33. STM image of CO on Pd(111) at 25 K.[138]

sorbed and physisorbed on the Ni(100), Re(0001), and W(100) surfaces, while the spectra of physisorbed and gas-phase nitrogen are similar. An attempt to detect the nitrogen molecule in an intrinsic precursor state above the clean surface was unsuccessful, most likely because of the very fast conversion of the N_2 molecule from an intrinsic precursor state to a state of chemisorption. If that is the case, then the activation barrier for the transition to a state of chemisorption is very low ($\leqslant 30$ meV).

Jacobi et al.[119] used an angle-resolved UPS method to study the adsorption of nitrogen on the Ni(100) surface at $T_s = 20$ K. At submonolayer coverages they detected mainly chemisorbed N_2 molecules, although there was an "impurity" of physisorbed molecules. With increasing exposure a layer of physisorbed molecules was formed. The positions of the peaks of the valence levels were shifted by an amount equal to the change in work function due to the adsorption of the first monolayer. From the fact that chemisorption is present at 20 K, as in Ref. 139, Jacobi et al.[119] concluded that the activation energy for chemisorption of N_2 on Ni(100) is very small.

Schmeisser et al.[140] used the UPS method to study the adsorption of nitrogen on the surface of nickel films at $T_s = 7$ K. The photoelectron spectrum shows the characteristic signs of physisorbed N_2 molecules. From the relative intensities of the peaks of the 4σ, 1π, and 5σ levels and the weakly expressed splitting of the 1π level, those authors concluded that the molecules are oriented not randomly, as in a gas, but with their axes parallel to the surface.

In several studies the adsorption of nitrogen on the surface of silver has been studied at low T_s by methods of electron spectroscopy. Gruyters and Jacobi[84] observed inhomogeneous inelastic scattering of electrons on the Ag(111) surface owing to excitation of vibrational and rotational modes in physisorbed nitrogen molecules. The overlap of the vibrational and rotational modes in the case of nitrogen leads to the formation of structureless inelastic tails of the stretching vibrations and their overtones. The coadsorption of nitrogen and hydrogen was also studied.

As in Ref. 84, Demuth et al.[134] studied the resonance inelastic scattering of electrons from a layer of nitrogen mol-

ecules physisorbed on the surface of a silver film. This scattering is due to the formation of a short-lived state of the negative ion (lifetime $\leqslant 10^{-14}$ s). An incident electron of resonant energy is trapped, and after the decay of this state the N_2 molecule is left vibrationally excited. The vibrational frequency differs insignificantly from that for the gas phase. Slight differences in the excitation spectrum allow one to distinguish an adsorbed monolayer from a condensed multilayer.

Bartolucci and Franchy[141] used the HREELS, TDS, and LEED methods to study the adsorption of nitrogen on the Ag(110) surface at $T_s = 15$ K. They observed an ordered structure matched with the substrate in the first monolayer and an unmatched hexagonal structure in the condensed multilayer. For the multilayer they observed a resonance inelasticity scattering of electrons involving the excitation of the N–N bond with the participation of a short-lived state of the negative ion.

Jacobi et al.[142] studied the resonance negative-ion scattering of electrons from an N_2 monolayer adsorbed at $T_s = 20$ K on the Al(111) surface. The stretching vibrations were excited by resonance scattering of electrons with the formation of a short-lived state of the negative ion. In addition, the authors of Ref. 142 observed suppression of the mode of stretching vibrations of N_2 upon the coadsorption of 0.16 monolayer of water. This effect was attributed to quenching of the negative-ion resonance of the N_2 molecules by the water.

5. CONCLUSION

The main feature of the low-temperature adsorption of gases is the formation and steady maintenance of a physisorbed layer of molecules (for transition metals this occurs after the formation of a chemisorbed adlayer, while for noble metals it occurs right from the start). This makes it possible to study the properties of the physisorbed layer and the mechanisms of its formation.

The most diverse and interesting effects have been observed for the adsorption of hydrogen. The difference of the quantum properties (the levels of zero-point vibrations) of the H_2 and D_2 molecules give rise to various isotope effects, particularly in the kinetics of adsorption–desorption processes on surfaces of W and Mo. This, in turn, is due to the very high mobility of the H_2 molecules and the possibility of formation of clusters or islands of the 2D condensate. It is possible that the anomalously high mobility of the H_2 molecules is the cause of a "catastrophic" drop in the sticking probability at coverages where the formation of an atomic adsorption phase on Mo(110) is completed. We do not rule out the possibility that quantum tunneling diffusion is involved in this process, and to check this the substrate temperature should be lowered to $\leqslant 3$ K. The strong isotope effect in the electron-stimulated disordering of the adlayer is also worthy of note. Study of the adsorption kinetics has yielded considerable information about the role of the precursor state and the character of the molecule–surface interaction potential.

Much valuable information has been obtained in the study of hydrogen adsorption on the surfaces of noble metals with the use of monoenergetic molecular beams and the

methods of electron spectroscopy. It has been established that the vibrational–rotational properties of physisorbed molecules are similar to the properties of the molecules in the gas phase. It was concluded from the experiments and theoretical calculations that the classical model is inadequate, and it is necessary to employ a quantum model of sticking which takes into account the inelastic interaction of the molecules with the surface with excitation of phonons. Subtle mechanisms of sticking with the participation of trapping of the molecule in a quasibound adsorption state in the resonance excitation of rotational states and diffraction on the lattice of surface atoms have been revealed. Substantial differences in ortho–para conversion on flat and terraced faces of single crystals have been found. The amortization effect, which leads to an increase in the sticking coefficient with coverage, is interesting.

Research results on the low-temperature adsorption of oxygen and, especially, carbon monoxide and nitrogen are much more scarce. For oxygen the set of adsorption states realized at $T_s \geqslant 5$ K has been determined. On transition metals these states are, in order of increasing surface density, atomic chemisorption, weak molecular chemisorption, physisorption, and condensation. The initial stage of growth of an oxygen cryocrystal looks the same. For studying the adsorption of O_2, CO, and N_2 the method of photoelectron spectroscopy is often used, and the state of the adparticles (chemisorption or physisorption) and the orientation of the molecules relative to the surface have been determined. Isolated attempts to observe atoms and molecules adsorbed at low temperature by STM should also be mentioned.

So, has it been worth it to "break the bank" in struggling with the difficulties of adsorption experimentation at low temperatures? This is for the reader to judge, but the author wishes to answer in the affirmative. Without lowering the temperature of the sample one could not observe the many subtle and beautiful effects that enrich our understanding of the mechanism of adsorption phenomena. We think it advisable to do research at still lower temperatures, especially for hydrogen.

*E-mail: ptush@iop.kiev.ua

[1] K. Christmann, Surf. Sci. Rep. **9**, 1 (1988).
[2] C. R. Arumainayagam and R. J. Madix, Prog. Surf. Sci. **38**, 1 (1991).
[3] K. D. Rendulic, Surf. Sci. **272**, 34 (1992).
[4] A. Gross, Surf. Sci. Rer. **32**, 291 (1998).
[5] G. J. Kroes, Prog. Surf. Sci. **60**, 1 (1999).
[6] É. Zenguil, *Surface Physics* [Russian translation], Part 2, Mir, Moscow (1990).
[7] E. Ilisca, Prog. Surf. Sci. **41**, 217 (1992).
[8] O. A. Panchenko, P. P. Lutsishin, and S. V. Sologub, Prog. Surf. Sci. **69**, 193 (2002).
[9] A. G. Naumovets, Fiz. Nizk. Temp. **20**, 1091 (1994) [Low Temp. Phys. **20**, 857 (1994)].
[10] E. Pijper, M. F. Somers, G. J. Kroes, R. A. Olsen, E. J. Baerends, H. F. Busnengo, A. Salin, and D. Lemoine, Chem. Phys. Lett. **347**, 277 (2001).
[11] Yu. G. Ptushinskiĭ and B. A. Chuĭkov, Poverkhnost'. Fiz. Khim. Mekh., No. 9, 5 (1992).
[12] P. Kisliuk, J. Phys. Chem. Solids **3**, 95 (1957).
[13] J. Harris and S. Andersson, Phys. Rev. Lett. **55**, 1583 (1985).

[14] M. I. Elinson and G. F. Vasil'ev, *Field Emission* [in Russian], Gos. Izd-vo Fiz. Mat. Lit., Moscow (1958).
[15] L. N. Dobretsov and M. V. Gomoyunova, *Emission Electronics* [in Russian], Nauka, Moscow (1966).
[16] R. Gomer, R. Wortman, and R. Lundy, J. Chem. Phys. **26**, 1147 (1957).
[17] V. K. Medvedev and A. O. Snitko, Zh. Tekh. Fiz. **57**, 1638 (1987).
[18] G. Mazenko, J. R. Banavar, and R. Gomer, Surf. Sci. **107**, 459 (1981).
[19] R. S. Polizotti and G. Ehrlich, J. Chem. Phys. **71**, 259 (1979).
[20] I. F. Lyuksyutov and A. G. Fedorus, Zh. Éksp. Teor. Fiz. **80**, 2511 (1981) [Sov. Phys. JETP **53**, 1317 (1981)].
[21] V. V. Gonchar, O. V. Kanash, I. A. Kotlyarova, A. G. Fedorus, and A. F. Fedosenko, Zh. Éksp. Teor. Fiz. **95**, 1773 (1989) [Sov. Phys. JETP **68**, 1023 (1989)].
[22] M. Strongin, J. M. Dickey, H. H. Farrell, T. F. Arns, and G. Hrabak, Rev. Sci. Instrum. **42**, 311 (1971).
[23] O. A. Panchenko, P. P. Lutsishin, and Yu. G. Ptushinskiĭ, Zh. Éksp. Teor. Fiz. **66**, 2191 (1974) [Sov. Phys. JETP **39**, 1079 (1974)].
[24] V. F. Koval, P. P. Lutsishin, O. A. Panchenko, and S. V. Sologub, Surf. Sci. **331−333**, 1317 (1995).
[25] P. P. Lutsishin, T. N. Nakhodkin, O. A. Panchenko, and Yu. G. Ptushinskiĭ, Zh. Eksp. Teor. Fiz. **82**, 1306 (1982) [Sov. Phys. JETP **55**, 759 (1982)].
[26] V. T. Cherepin and M. A. Vasil'ev, *Methods and Devices for Analysis of the Surface of Materials* [in Russian], Naukova Dumka, Kiev (1982).
[27] Ph. Avouris, D. Schmeisser, and J. E. Demuth, Phys. Rev. Lett. **48**, 199 (1982).
[28] S. Andersson and J. Harris, Phys. Rev. Lett. **48**, 545 (1982).
[29] É. Zenguil, *Surface Physics* [Russian translation], Mir, Moscow (1990).
[30] S. Andersson, L. Wilzen, M Persson, and J. Harris, Phys. Rev. B **40**, 8146 (1989).
[31] H. Schlichting and D. Menzel, Surf. Sci. **285**, 209 (1993).
[32] H. Schlichting and D. Menzel, Rev. Sci. Instrum. **64**, 2013 (1993).
[33] B. A. Chuikov, V. D. Osovskii, Yu. G. Ptushinskii, and V. G. Sukretnyi, Surf. Sci. **213**, 359 (1989).
[34] Yu. G. Ptushinskii, B. A. Chuikov, V. D. Osovskii, and V. G. Sukretnyi, Fiz. Nizk. Temp. **19**, 570 (1993) [Low Temp. Phys. **19**, 406 (1993)].
[35] W. Friess, H. Schlichting, and D. Menzel, Phys. Rev. Lett. **74**, 1147 (1995).
[36] H. Schlichting and D. Menzel, Surf. Sci. **272**, 27 (1992).
[37] D. A. King and M. G. Wells, Surf. Sci. **29**, 454 (1972).
[38] D. A. King and M. G. Wells, Proc. R. Soc. London, Ser. A **339**, 245 (1974).
[39] V. S. Bosov and B. A. Chuĭkov, Ukr. Fiz. Zh. **18**, 1568 (1973).
[40] Yu. G. Ptushinskii and B. A. Chuikov, Surf. Sci. **6**, 42 (1967).
[41] Yu. G. Ptushinskii and B. A. Chuikov, Surf. Sci. **7**, 90 (1967).
[42] R. Gomer and R. Wortman, J. Chem. Phys. **23**, 1741 (1955).
[43] R. Wortman, R. Gomer, and R. Lundy, J. Chem. Phys. **24**, 161 (1956).
[44] V. D. Osovskiĭ, Yu. G. Ptushinskiĭ, V. G. Sukretnyĭ, and B. A. Chuĭkov, JETP Lett. **67**, 959 (1998).
[45] P. W. Tamm and L. D. Schmidt, J. Chem. Phys. **54**, 4775 (1971).
[46] B. A. Chuikov, V. V. Dvurechenskikh, V. D. Osovskii, Yu. G. Ptushinskii, and V. G. Sukretnyi, Surf. Sci. **285**, 75 (1993).
[47] V. D. Osovskiĭ, Yu. G. Ptushinskiĭ, V. G. Sukretnyĭ, and B. A. Chuĭkov, JETP Lett. **60**, 586 (1994).
[48] V. V. Dvurechenskikh, V. D. Osovskiĭ, Yu. G. Ptushinskiĭ, V. G. Sukretnyĭ, and B. A. Chuĭkov, Ukr. Fiz. Zh. **37**, 716 (1992).
[49] B. A. Chuikov, V. D. Osovskii, Yu. G. Ptushinskii, and V. G. Sukretnyi, Surf. Sci. **448**, L201 (2000).
[50] A. Gross, S. Wilke, and M. Scheffler, Phys. Rev. Lett. **75**, 2718 (1995).
[51] M. Kay, G. R. Darling, S. Holloway, J. A. White, and D. M. Bird, Chem. Phys. Lett. **245**, 311 (1995).
[52] M. Beutl, M. Riedler, and K. D. Rendulic, Chem. Phys. Lett. **247**, 249 (1995).
[53] M. Beutl, M. Riedler, and K. D. Rendulic, Chem. Phys. Lett. **256**, 33 (1996).
[54] M. Beutl, J. Lesnik, and K. D. Rendulic, Surf. Sci. **429**, 71 (1999).
[55] B. A. Chuikov, V. D. Osovskii, Yu. G. Ptushinskii, and V. G. Sukretnyi, Surf. Sci. **473**, 143 (2001).
[56] C. T. Rettner, H. Stein, and E. K. Schweizer, J. Chem. Phys. **89**, 3337 (1988).
[57] V. D. Osovskiĭ, Yu. G. Ptushinskiĭ, V. G. Sukretnyi, and B. A. Chuĭkov, Fiz. Nizk. Temp. **27**, 1138 (2001) [Low Temp. Phys. **27**, 843 (2001)].
[58] V. D. Osovskii, Yu. G. Ptushinskii, V. G. Sukretnyi, and B. A. Chuikov, Fiz. Nizk. Temp. **23**, 779 (1997) [Low Temp. Phys. **23**, 587 (1997)].
[59] N. V. Petrova, I. N. Yakovkin, and Yu. G. Ptushinskii, Surf. Sci. **497**, 349 (2002).

[60]L. Wilzen, S. Andersson, and J. Harris, Surf. Sci. **205**, 387 (1988).
[61]I. L. Silvera, Rev. Mod. Phys. **52**, 393 (1980).
[62]E. A. Moelwyn-Hughes, *Physical Chemistry*, 2nd ed., Pergamon Press, Oxford (1961), Izd-vo Inostr. Lit., Moscow (1982).
[63]V. V. Gonchar, O. V. Kanash, A. G. Naumovets, and A. G. Fedorus, JETP Lett. **28**, 330 (1978).
[64]V. V. Gonchar, O. V. Kanash, and A. G. Fedorus, JETP Lett. **38**, 189 (1983).
[65]V. V. Gonchar, Yu. M. Kagan, O. V. Kanash, A. G. Naumovets, and A. G. Fedorus, Zh. Éksp. Teor. Fiz. **84**, 249 (1983) [Sov. Phys. JETP **57**, 142 (1983)].
[66]V. V. Gonchar, O. V. Kanash, I. A. Kotlyarova, A. G. Fedorus, and A. A. Fedosenko, Zh. Éksp. Teor. Fiz. **95**, 1773 (1989) [Sov. Phys. JETP **68**, 1023 (1989)].
[67]A. G. Fedorus, V. V. Gonchar, O. V. Kanash, E. V. Klimenko, A. G. Naumovets, and I. N. Zasimovich, Surf. Sci. **251/252**, 846 (1991).
[68]A. G. Fedorus, E. V. Klimenko, A. G. Naumovets, E. M. Zasimovich, and I. N. Zasimovich, Nucl. Instrum. Methods Phys. Res. B **10**, 207 (1995).
[69]O. M. Braun and É. A. Pashitskiĭ, Poverkhnost'. Fiz. Khim. Mekh., No. 7, 49 (1984).
[70]R. Di Foggio and R. Gomer, Phys. Rev. B **25**, 3490 (1982).
[71]V. G. Peschanskiĭ and M. Ya. Azbel', Zh. Éksp. Teor. Fiz. **55**, 1980 (1968) [Sov. Phys. JETP **28**, 1045 (1969)].
[72]O. A. Panchenko and P. P. Lutsishin, Zh. Éksp. Teor. Fiz. **57**, 1555 (1969) [Sov. Phys. JETP **30**, 841 (1970)].
[73]O. A. Panchenko, P. P. Lutsishin, Yu. G. Ptushinskii, and V. V. Shishkov, Surf. Sci. **34**, 187 (1973).
[74]A. F. Andreev, Usp. Fiz. Nauk **105**, 113 (1971) [Sov. Phys. Usp. **14**, 609 (1972)].
[75]O. A. Panchenko, A. A. Kharlamov, and Yu. G. Ptushinskiĭ, Zh. Éksp. Teor. Fiz. **67**, 780 (1974) [Sov. Phys. JETP **40**, 386 (1975)].
[76]A. A. Kharlamov, O. A. Panchenko, and Yu. G. Ptushinskii, Solid State Commun. **15**, 1793 (1974).
[77]P. P. Lutsishin, O. A. Panchenko, and S. V. Sologub, Poverkhnost'. Fiz. Khim. Mekh., No. 8, 22 (1987).
[78]P. P. Lutsishin, O. A. Panchenko, and V. E. Shpagin, Surf. Sci. **278**, 218 (1992).
[79]P. P. Lutsishin, O. A. Panchenko, and S. V. Sologub, Poverkhnost'. Fiz. Khim. Mekh., No. 11, 69 (2001).
[80]H. F. Berger, M. Leisch, A. Winkler, and K. D. Rendulic, Chem. Phys. Lett. **175**, 425 (1990).
[81]H. F. Berger and K. D. Rendulic, Surf. Sci. **253**, 325 (1991).
[82]B. E. Hayden and C. L. A. Lamont, Chem. Phys. Lett. **160**, 331 (1989).
[83]C. T. Rettner, M. A. Michelsen, and D. J. Auerbach, J. Chem. Phys. **102**, 4625 (1995).
[84]M. Gruyters and K. Jacobi, Chem. Phys. Lett. **225**, 309 (1994).
[85]K. Svensson and S. Andersson, Surf. Sci. **392**, L40 (1997).
[86]E. Ilisca, Phys. Rev. Lett. **66**, 667 (1991).
[87]S. Andersson and J. Harris, Phys. Rev. B **27**, 9 (1983).
[88]M. Beutl, E. Lunden, C. Konvicka, P. Varga, and K. D. Rendulic, Surf. Sci. **447**, 245 (2000).
[89]M. Persson and S. Andersson, Surf. Rev. Lett. **1**, 187 (1994).
[90]S. Andersson and M. Persson, Phys. Rev. Lett. **70**, 202 (1993).
[91]S. Andersson and M. Persson, Phys. Rev. B **48**, 5685 (1993).
[92]S. Andersson, M. Persson, and J. Harris, Surf. Sci. **360**, L499 (1996).
[93]K. Svensson, L. Bengtsson, J. Bellman, M. Hassel, M. Persson, and S. Andersson, Phys. Rev. Lett. **83**, 124 (1999).
[94]L. Bengtsson, K. Svensson, M. Hassel, J. Bellman, M. Persson, and S. Andersson, Phys. Rev. B **61**, 16921 (2000).
[95]J. N. Chubb, L. Gowland, and I. E. Pollard, J. Phys. D **1**, 361 (1968).
[96]C. Benvenuti, R. S. Calder, and G. Passardi, J. Vac. Sci. Technol. **13**, 1172 (1976).
[97]J. Cui, S. C. Fain, Jr, and W. Liu, J. Vac. Sci. Technol. A **7**, 1850 (1989).
[98]P. M. Ferm, S. M. Kurtz, and K. A. Pearlstine, Phys. Rev. Lett. **58**, 2602 (1987).
[99]K. A. Pearlstine and G. M. McClelland, Surf. Sci. **134**, 389 (1983).
[100]M. Hassel, K. Svensson, M. Persson, and S. Andersson, Phys. Rev. Lett. **80**, 2481 (1998).

[101]M. Hassel, K. Svensson, J. Bellman, S. Andersson, and M. Persson, Phys. Rev. B **65**, 205402 (2002).
[102]K. Svensson and S. Andersson, Phys. Rev. Lett. **78**, 2016 (1997).
[103]W. Rühl, Z. Phys. **176**, 409 (1963).
[104]G. Chottiner and R. E. Glover, J. Vac. Sci. Technol. A **15**, 429 (1978).
[105]C. Leung and R. Gomer, Surf. Sci. **59**, 638 (1976).
[106]Yu. G. Ptushinskiĭ and B. A. Chuĭkov, Fiz. Tverd. Tela (Leningrad) **10**, 722 (1968) [Sov. Phys. Solid State **10**, 565 (1968)].
[107]C. Wang and R. Gomer, Surf. Sci. **74**, 389 (1978).
[108]H. Michel, R. Opila, and R. Gomer, Surf. Sci. **105**, 48 (1981).
[109]R. Opila and R. Gomer, Surf. Sci. **105**, 41 (1981).
[110]A. N. Artsyukovich and V. A. Ukraintsev, Surf. Sci. **347**, 303 (1996).
[111]V. D. Osovskii, Yu. G. Ptushinskii, V. G. Sukretnyi, B. A. Chuikov, V. K. Medvedev, and Yu. Suchorski, Surf. Sci. **377−379**, 664 (1997).
[112]B. G. Briner, M. Doering, H.-P. Rust, and A. M. Bradshaw, Phys. Rev. Lett. **78**, 1516 (1997).
[113]V. V. Zhukov, V. D. Osovskiĭ, Yu. G. Ptushinskiĭ, V. G. Sukretnyĭ, and B. A. Chuĭkov, Ukr. Fiz. Zh. **31**, 1374 (1986).
[114]V. V. Zhukov, V. D. Osovskiĭ, Yu. G. Ptushinskiĭ, V. G. Sukretnyĭ, and B. A. Chuĭkov, Izv. AN SSSR Ser. Fiz. **52**, 1462 (1988).
[115]C. T. Rettner, E. K. Schweizer, and H. Stein, J. Chem. Phys. **93**, 1442 (1990).
[116]H. P. Steinruck and R. J. Madix, Surf. Sci. **185**, 36 (1987).
[117]C. Wang and R. Gomer, Surf. Sci. **84**, 329 (1979).
[118]D. Schmeisser and K. Jacobi, Surf. Sci. **108**, 421 (1981).
[119]Ya-po Hsu, K. Jacobi, and H. H. Rottermund, Surf. Sci. **117**, 581 (1981).
[120]A. C. Lunz, J. Grimblot, and D. E. Fowler, Phys. Rev. B **39**, 12903 (1989).
[121]W. Ranke, Surf. Sci. **209**, 57 (1989).
[122]A. Eichler and J. Hafner, Phys. Rev. Lett. **79**, 4481 (1997).
[123]J. Beckerle, O. Yang, A. Jonson, and S. Ceyer, Surf. Sci. **195**, 77 (988).
[124]R. Franchy, T. U. Bartke, and P. Gassmann, Surf. Sci. **366**, 60 (1996).
[125]K. B. K. Tang, J. Villette, D. Teillet-Billy, J. P. Gauyacq, and R. E. Palmer, Surf. Sci. **368**, 43 (1996).
[126]S. Lacombe, F. Cemič, P. He, H. Dietrich, P. Geng, and K. Jacobi, Surf. Sci. **368**, 38 (1996).
[127]M. Shayegan, J. M. Cavallo, R. E. Glover, III, and R. L. Park, Phys. Rev. Lett. **53**, 1578 (1984).
[128]G. Bader, G. Petruzzo, L. G. Caron, and L. Sanche, Phys. Rev. B **30**, 78 (1984).
[129]W. Wurth, J. Stöhr, P. Feulner, K. R. Bauchspiess, Y. Baba, E. Hudel, G. Rocker, and D. Menzel, Phys. Rev. Lett. **65**, 2426 (1990).
[130]P. P. Lutsishin, T. N. Nakhodkin, O. A. Panchenko, and Yu. G. Ptushinskiĭ, JETP Lett. **31**, 563 (1980).
[131]V. I. Vatamanyuk, D. A. Gorodetskiĭ, A. G. Kundzich, P. P. Lutsishin, Yu. P. Mel'nik, O. A. Panchenko, V. A. Usenko, and A. A. Yas'ko, Poverkhnost'. Fiz. Khim. Mekh., No. 1, 18 (1990).
[132]C. Leung, M. Vass, and R. Gomer, J. Vac. Sci. Technol. **13**, 286 (1976).
[133]P. R. Norton, R. L. Tapping, and J. W. Goodale, Surf. Sci. **72**, 33 (1978).
[134]J. E. Demuth, D. Schmeisser, and Ph. Avouris, Phys. Rev. Lett. **47**, 1166 (1981).
[135]M. Shayegan, E. D. Williams, R. E. Glover, III, and R. L. Park, Surf. Sci. **154**, L239 (1985).
[136]J. Yoshinobu and M. Kawai, Surf. Sci. **363**, 105 (1996).
[137]M. Kawai and J. Yoshinobu, Surf. Sci. **368**, 239 (1996).
[138]P. Sautet, M. K. Rose, J. C. Dumphy, S. Behler, and M. Salmeron, Surf. Sci. **453**, 25 (2000).
[139]M. J. Grunze, J. Fuhler, M. Neumann, C. R. Brundle, D. J. Auerbach, and J. Behm, Surf. Sci. **139**, 109 (1984).
[140]D. Schmeisser, K. Jacobi, and D. M. Kolb, Vacuum **31**, 439 (1981).
[141]F. Bartolucci and R. Franchy, Surf. Sci. **368**, 27 (1996).
[142]K. Jacobi, M. Bertolo, P. Geng, W. Hansen, and C. Astaldi, Chem. Phys. Lett. **173**, 97 (1990).

Translated by Steve Torstveit

Phenomenological description of the multidomain state of the easy-plane antiferromagnet NiCl$_2$

V. M. Kalita, A. F. Lozenko,* P. A. Trotsenko, and T. M. Yatkevich

Institute of Physics, National Academy of Sciences of Ukraine, pr. Nauki 46, Kiev 03650, Ukraine

An analysis is made of the experimental data on the magnetic-field dependence of the magnetostriction and magnetization of the NiCl$_2$ crystal at its transition from the multidomain antiferromagnetic state to a uniform state. It is shown that their field dependence is determined by the mean orientation of the domains, which is characterized by a domain coalignment parameter. That parameter is used to give a phenomenological description of the multidomain state of the antiferromagnet NiCl$_2$. © *2004 American Institute of Physics.*
[DOI: 10.1063/1.1645152]

INTRODUCTION

The antiferromagnetic phase of the layered easy-plane crystal NiCl$_2$ (Refs. 1–3) is realized in the form a multidomain state in the entire temperature range of its existence.[4] In the multidomain state the antiferromagnetic vector **L** is uniform in each of the domains, and on passage from one domain to another, **L** changes direction while remaining in the easy plane (EP). By means of an external magnetic field the crystal can be brought from the multidomain state to a uniform state with **L**⊥**H**, this transition occurring in fields much less than the sublattice collapse field:[5–7] for $T = 4.2$ K the ratio of the corresponding field strengths is greater than 10. The uniform state has been well studied, and its behavior in a magnetic field satisfies the Néel theory[8] for antiferromagnets (AFs).

In spite of the fact that the NiCl$_2$ crystal is a classic object in the enormous family of AFs, the nature of its multidomain state has not been studied before. The same is also true for other EP crystals belonging to the family of iron-group dihalides. Generally speaking, unlike ferromagnets, for which the multidomain state arises because it is energetically unfavorable for the sample as a whole to have a magnetic moment, the cause of the formation of a multidomain antiferromagnetic state is not so obvious, since magnetization is always absent at $H = 0$ both in the uniform and multidomain states.

In a study of the data on the field dependence of the induced magnetostriction of the NiCl$_2$ crystal[7] it was shown that the multidomain state is "almost" reversible in cycles of imposing and removing a magnetic field. In Ref. 7, with consideration of the data on the experimental observations of the induced magnetostriction, it was conjectured that the formation of the multidomain state in NiCl$_2$ is of a magnetoelastic character. In the multidomain state one observes a complete compensation (for the whole crystal) of the anisotropic magnetostriction of the domains, wherein each of the domains has a spontaneous strain but the crystal as a whole does not. When an external magnetic field is imposed the spontaneous magnetostriction is restored upon the transition to the uniform state.

The reversible formation of a multidomain state may be due to the effect of lattice defects, which, moreover, can promote a multidomain state. The formation of a multidomain state can be brought about by screw dislocations.[9,10] The essence of such a mechanism of domain formation reduces to the circumstance that the spontaneous strain domains surrounding a dislocation screen its elasticity, thereby making the multidomain state energetically favorable.

A different mechanism of magnetoelastic formation of a multidomain state was proposed in Ref. 12 on the basis of taking into account the matching of the strains of the surface of the crystal and the spontaneous bulk strain arising when antiferromagnetic order is established in the crystal.

One can determine which of the proposed mechanisms is preferable by studying the properties of the multidomain state. For example, in a study of the temperature features in the behavior of the induced magnetostriction of CoCl$_2$ upon rearramgement of the domain structure of the multidomain state by a field,[13] it was shown that a magnetoelastic mechanism involving the influence of lattice defects is the dominant mechanism for that crystal.

In a study[14] of the multidomain state of NiCl$_2$, the authors analyzed data not only on the induced magnetostriction but also on the dependence of the magnetization on the applied field strength. In light of the magnetoelastic nature of the formation of the multidomain state, it is of fundamental imortance to establish the interrelationship between these observables. It was shown that the field curves of the magnetostriction and magnetization are in good agreement with each other, equally reflecting the restructuring of the multidomain state.

In the present study we have carried out an analysis of the field curves of the induced magnetostriction and the magnetization of the NiCl$_2$ crystal in the field region corresponding to the restructuring of the multidomain state. It will be shown from these curves that the process of transition from the multidomain to the uniform state comes about in accordance with a magnetoelastic mechanism involving the influence of defects. The multidomain state will be described using a "domain coalignment parameter" (DCP).
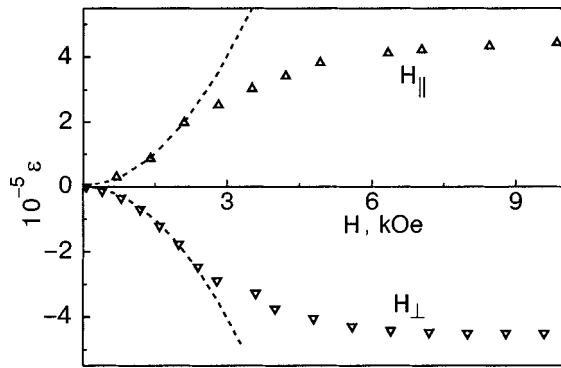
FIG. 1. Curves of the reversible component of the relative lengthening of the NiCl$_2$ crystal as a function of the magnetic field strength at $T=4.2$ K for the magnetic field directions along ($H_\parallel$) and perpendicular to ($H_\perp$) the direction of measurement.

FIG. 2. Dependence of the reversible component of the magnetization of the NiCl$_2$ crystal on the magnetic field strength at $T=4.2$ K.

EXPERIMENTAL OBSERVATIONS AND DATA ANALYSIS

Figure 1 shows the reversible (in a cycle of imposing and removing a magnetic field) component of the field dependence of the elongation of the NiCl$_2$ crystal in the basal plane at $T=4.2$ K in crossed magnetic fields:[7] the field $H_\parallel$ is directed along the measurement direction (the upper curve in Fig. 1), and the field $H_\perp$ is perpendicular to the measurement direction (the lower curve in Fig. 1). Both fields lie in the easy plane. The induced magnetostriction of the crystal in the multidomain state is anisotropic, and it changes sign when the field direction is changed to the transverse. The crystal lengthens in a field $H=H_\parallel$ and contracts by the same amount in a field $H=H_\perp$. At high fields (≥ 10 kOe) a transition to a uniform (single-domain) state occurs independently of the direction of **H** in the easy plane. The behavior of the magnetostriction of NiCl$_2$ in the uniform state was studied in Ref. 15.

The irreversible component of the magnetostriction leads to the hysteresis ''loop'' observed in cycles of field imposition and removal.[14] The irreversibility arises because of the formation of an excess number of domains whose antiferromagnetic vectors remain perpendicular to the direction of the imposed field after the field is removed. Naturally this will give rise to a residual magnetostriction, which has been observed in experiments. In this paper we shall discuss only the reversible component of the magnetostriction, which is of the main interest.

According to the data shown in Fig. 1, the uniform magnetostriction is restored at fields ~ 10 kOe. At higher fields, up to the spin-flip field $H_f=129$ kOe,[16] further straining of the crystal will occur only on account of the canting of the sublattice spins toward the magnetic field.[15] At fields lower than 10 kOe the main contribution to the magnetostriction is found to be due to growth in the number (and volume) of domains with a favorable orientation of spins in them when **L**$\perp$**H**.

At the very beginning of the process of restructuring of the multidomain state ($H\to 0$) the value of the relative elongation of the crystal has a quadratic dependence on the applied field strength:

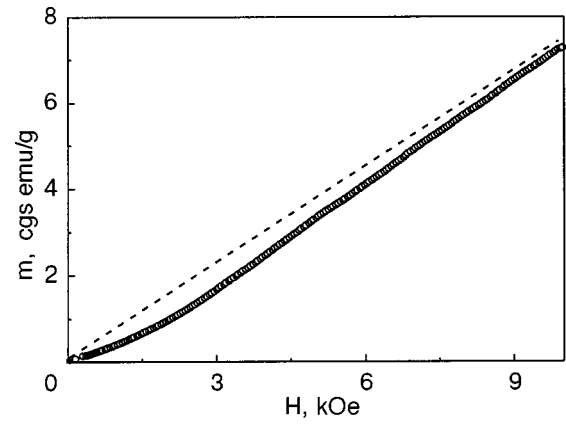$$\varepsilon_{\parallel,\perp}=(\varepsilon_{\parallel,\perp})_s\frac{H^2}{H_d^2}, \tag{1}$$

where $\varepsilon_{\parallel,\perp}$ is the relative elongation of the crystal in the direction along the field when $H=H_\parallel$ or perpendicular to the field when $H=H_\perp$; $(\varepsilon_{\parallel,\perp})_s$ is the spontaneous magnetostriction of the crystal determined from the extrapolation of the asymptote of the field dependence of the uniform state to $H\to 0$, and here $(\varepsilon_\parallel)_s\approx-(\varepsilon_\perp)_s$ by virtue of the anisotropy of the magnetostriction of the uniform state with respect to the direction of **L**; H_d is an empirical parameter which for NiCl$_2$ has a value $H_d=(3.6\pm 0.4)$ kOe.[15] Relation (1) is plotted for fields $H_\parallel$ and $H_\perp$ by the dashed curves in Fig. 1. We see that the real trend of the magnetostriction at fields above ~ 2 kOe is much slower than the quadratic dependence (1). At such fields the value of the magnetostriction is still far from its value in the uniform state.

Figure 2 shows the field dependence of the reversible part of the magnetization $m(H)$ of the NiCl$_2$ crystal at $T=4.2$ K.[14] As was shown in Ref. 14, the magnetic susceptibility for the reversible component of the magnetization of the multidomain state, obtained in field imposition–removal cycles, at $H\to 0$ is half as large as the values for the uniform state. The irreversible component leads to an increase in the value of the magnetic susceptibility for $H\to 0$. According to the Néel theory, the magnetization of an easy-plane antiferromagnet in a field perpendicular to the hard axis should have a linear trend. Indeed, according to the data of Ref. 6, the magnetization of NiCl$_2$ in the uniform state is directly proportional to the magnetic field strength. In Fig. 2 the dashed line is the straight line along which the magnetization of the crystal would proceed for $H\to 0$ in the case of a uniform state with **L**$\perp$**H**. It is seen that the magnetization has a nonlinear dependence on magnetic field in the restructuring process.[5,6]

Figure 3 shows the field dependence of the ratio $m(H)/H$ according to the data on the magnetization of the NiCl$_2$ crystal. The ratio $m(H)/H$ is an ascending function in the entire range of fields. At the start of the restructuring of the multidomain state this ratio is equal to the magnetic susceptibility of the multidomain state: $\chi_d=m(H\to 0)/H$. In fields ~ 10 kOe, when the restructuring of the multidomain state is almost completed and the further magnetization is due solely to the canting of the spins toward the field, the ratio of the magnetization to the field will be equal to the magnetic susceptibility of the uniform state, χ_e. It should be
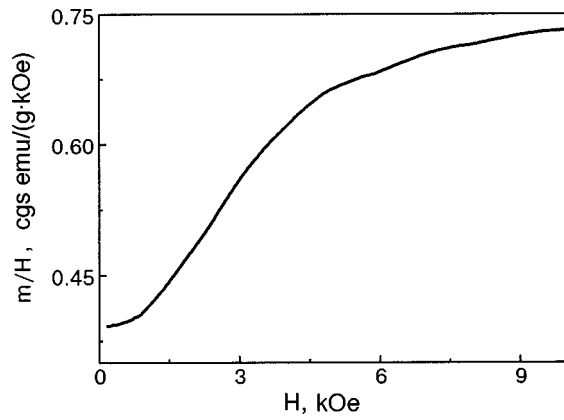
FIG. 3. Ratio of the magnetization to the magnetic field strength, $m(H)/H$, as a function of the magnetic field strength.

noted here that the field dependence of $m(H)/H$ is on the whole very similar to that of $\varepsilon(H)$.

The magnetic susceptibility is a differential characteristic and is defined as the derivative $\chi = dm(H)/dH$. Figure 4 shows the dependence of the magnetic susceptibility on the applied magnetic field strength according to the data of Fig. 2. We see that the magnetic susceptibility increases rapidly in fields up to 3 kOe. This faster growth of $\chi(H)$ with field appears to disagree with the curves for the magnetization and for the ratio $m(H)/H$, according to which the process of transition to the uniform state has not gone to completion even at a field of 10 kOe. Furthermore, the $\chi(H)$ curve has a maximum.

To explain the differences in the field dependence of the magnetostriction, magnetization, and magnetic susceptibility we must analyze the experimental data with allowance for the process of restructuring of the multidomain state, answering the question of how these observables change upon changes in the number and orientation of the domains under the influence of the field. In Refs. 11, 13, and 15 it was assumed that the domains are oriented in the easy plane and have a continuous distribution over orientations, and the orientation of the domains in the plane was specified in terms of the angle φ between the magnetization vector of the domain, $\mathbf{M} = \mathbf{s}_1 + \mathbf{s}_2$, and the magnetic field vector $\mathbf{H}$, where $\mathbf{s}_1$ and $\mathbf{s}_2$ are the magnetic moments of the sublattices, and the mo-
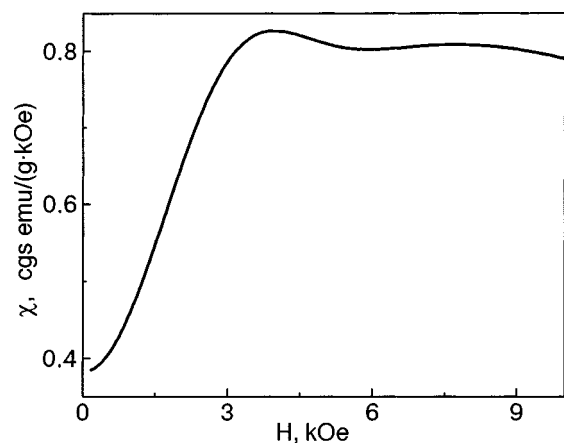

FIG. 4. Dependence of the magnetic susceptibility on the magnetic field strength in the multidomain state of the NiCl$_2$ crystal.
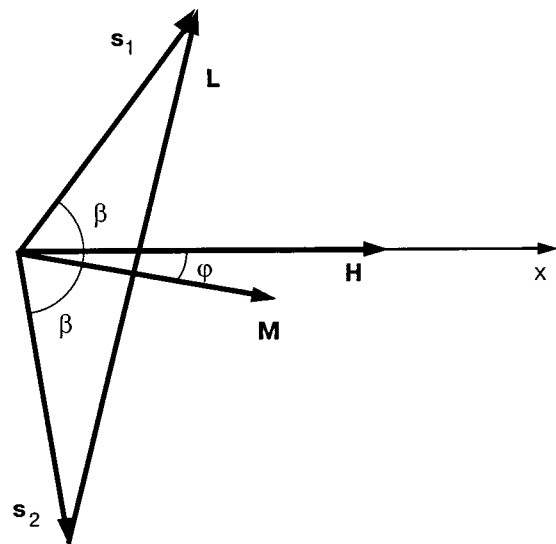

FIG. 5. Orientations of the sublattice spin vectors $\mathbf{s}_1$ and $\mathbf{s}_2$ and of the magnetization $\mathbf{M}$ of the domain and the antiferromagnetic vector $\mathbf{L}$ with respect to the magnetic field vector $\mathbf{H}$.

ments $\mathbf{s}_1$ and $\mathbf{s}_2$ and the vector $\mathbf{M}$ all lie in the easy plane (see Fig. 5). The vector $\mathbf{H}$ lies in the plane and is directed along the X axis. The antiferromagnetic vector, which also lies in the plane, is defined in the standard way in the form of the difference $\mathbf{L} = \mathbf{s}_1 - \mathbf{s}_2$. The distribution function $p(\varphi)$ of the domains is given as the ratio of the volume of domains with orientation φ to the volume of the crystal, the normalization condition being written in the form

$$\frac{1}{\pi} \int_{-\pi/2}^{\pi/2} p(\varphi) d\varphi = 1.$$

As an averaged characteristic for the orientation of the domains we use a parameter which we call the "domain coalignment parameter" (DCP). Here it must be kept in mind that the transition from the multidomain state to the uniform state in a magnetic field ends with the restoration of a uniform state with $\mathbf{L} \perp \mathbf{H}$. During such a transition it is impossible to define uniquely the direction of the vectors $\mathbf{L}$, since in a high-symmetry antiferromagnet (such as NiCl$_2$) the direction along the antiferromagnetic vector is physically indistinguishable from the opposite direction. This means that in defining the mean orientation of the domains in the multidomain state, one should approach the direction specified by the vector $\mathbf{L}$ as a director determining the orientation of the axes along which the vectors $\mathbf{L}$ lie. In the case of an easy-plane antiferromagnet, where the $\mathbf{L}$ vectors lie in the easy plane, the orientations of such axes will be determined by the value of $n_L = 2(\cos^2 \varphi - 1/2)$. Accordingly, the averaged characteristic for the orientation of the domains or the DCP will be calculated as

$$\bar{n}_L = \frac{1}{\pi} \int_{-\pi/2}^{\pi/2} 2 \left(\cos^2 \varphi - \frac{1}{2} \right) p(\varphi) d\varphi. \qquad (2)$$

Expression (2) for $\bar{n}_L$ characterizes the degree of coalignment of the domains in the multidomain antiferromagnetic state: at $H = 0$ one has $\bar{n}_L = 0$ in the multidomain state and $\bar{n}_L = 1$ in the uniform state.

We shall show that the mean magnetostriction of the crystal in the multidomain state is directly proportional to $\bar{n}_L$. In fact, in view of the anisotropy of the spontaneous magnetostriction of the uniform state of NiCl$_2$ (perpendicular to **L** it is equal to ε_s and along **L** it has the opposite sign and is equal to $-\varepsilon_s$),[15] we find that the value of the magnetostriction of the multidomain state of the crystal in the field direction will be equal to

$$\varepsilon = \frac{1}{\pi} \int_{-\pi/2}^{\pi/2} \varepsilon_s (\cos^2 \varphi - \sin^2 \varphi) p(\varphi) d\varphi$$

$$= \frac{\varepsilon_s}{\pi} \int_{-\pi/2}^{\pi/2} 2\left(\cos^2 \varphi - \frac{1}{2}\right) p(\varphi) d\varphi, \tag{3}$$

or

$$\varepsilon = \varepsilon_s \bar{n}_L. \tag{4}$$

Let us establish the connection between the magnetization and the DCP. We shall assume that the moduli of the vectors $\mathbf{s}_1$ and $\mathbf{s}_2$ are equal: $|\mathbf{s}_1| = |\mathbf{s}_2| = s$. A domain with orientation $\mathbf{L} \perp \mathbf{H}$ ($\varphi = 0$) will have magnetization $\mathbf{M} = \chi_e \mathbf{H}$. When the domain has an arbitrary orientation ($\varphi \neq 0$), $\mathbf{M}$ is not parallel to $\mathbf{H}$, and its value is given by $M = \chi_e H \cos \varphi$. The magnetization of the crystal arising along the field in the X direction will be equal to

$$m = \frac{1}{\pi} \int_{-\pi/2}^{\pi/2} \chi_e H \cos^2 \varphi\, p(\varphi) d\varphi. \tag{5}$$

We see that the value of the mean magnetization is also proportional to the DCP:

$$m = \frac{1}{2} \chi_e H(1 + \bar{n}_L). \tag{6}$$

According to Eq. (6), the magnetic susceptibility of the multidomain state will have a more complicated relation to the DCP; it can be written in the form

$$\chi = \frac{1}{2} \chi_e \left(1 + \bar{n}_L + H \frac{d\bar{n}_L}{dH}\right). \tag{7}$$

The magnetic susceptibility depends not only on the value of the DCP but also on on its derivative, $d\bar{n}_L/dH$, which in the given case determines the rate of change of the mean orientation of the domains upon a change in magnetic field. To determine the influence of this differential component on the magnetic susceptibility, let us analyze the field dependence of the derivative itself, $d\bar{n}_L/dH$. It follows from (6) that the ratio of the magnetization to the field is proportional to the value of the DCP. The derivative of this ratio will therefore be proportional to the derivative of the DCP:

$$\frac{d(m/H)}{dH} \sim \frac{d\bar{n}_L}{dH}. \tag{8}$$

Figure 6 shows the field dependence of the field derivative of the ratio of the magnetization to the field strength. We see that this derivative has a maximum in the field region ~ 3 kOe. Its position corresponds to the inflection point on the $\varepsilon(H)$ curve (Fig. 1).

Thus the faster growth of the magnetic susceptibility upon the restructuring of the multidomain state should be
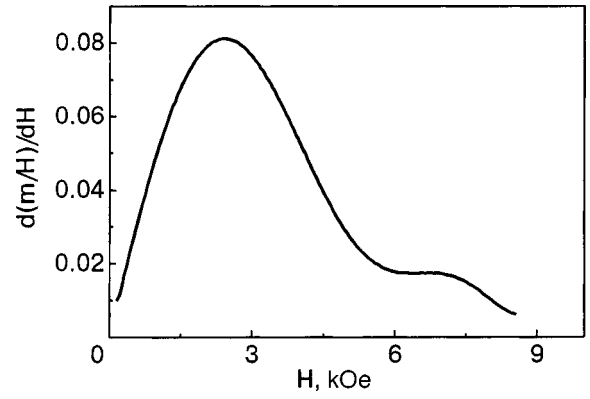

FIG. 6. Field dependence of the derivative with respect to magnetic field strength of the ratio of the magnetization to the magnetic field strength, $d(m/H)/dH$.

attributed to its proportionality to the field derivative of the DCP, the value of which derivative characterizes the rate of restructuring of the multidomain state by the field. The presence of a maximum in this derivative as a function of field leads to the formation of a maximum (although not very pronounced) in the $\chi(H)$ curve (Fig. 4).

PHENOMENOLOGICAL DESCRIPTION OF THE MULTIDOMAIN STATE

The description of the restructuring of the multidomain state under the influence of an external magnetic field is done in accordance with the principle of minimum free energy of the crystal.[17] The free energy of the multidomain state is written as a sum of two contributions: the reaction of the spin system to the imposition of a field, taking into account that the spins in the domains are canted toward the magnetic field, and a contribution reflecting the process of restructuring of the multidomain state.

The canting of the spins of the domain toward the field is described by the exchange energy and the Zeeman term, the value of which per unit cell is given by the expression

$$E = zI_{12}\mathbf{s}_1 \cdot \mathbf{s}_2 - \mathbf{H} \cdot (\mathbf{s}_1 + \mathbf{s}_2), \tag{9}$$

where $\mathbf{s}_1$ and $\mathbf{s}_2$ are the spin vectors of the sublattices, z is the number of nearest neighbors, and I_{12} is the intersublattice exchange constant. In Eq. (9) and below the magnetic field is given in energy units.

For a domain with orientation φ (see Fig. 5) expression (9) becomes

$$E = zI_{12}s^2(2\cos^2 \beta - 1) - 2Hs \cos \beta \cos \varphi. \tag{10}$$

Here we assume that the moduli of the vectors $\mathbf{s}_1$ and $\mathbf{s}_2$ do not change in the restructuring of the domains, $|\mathbf{s}_1| = |\mathbf{s}_2| = s$, and therefore the angles between $\mathbf{s}_1$ and $\mathbf{M}$ and between $\mathbf{s}_2$ and $\mathbf{M}$ will be the same and equal to β, and the vector $\mathbf{M} \perp \mathbf{L}$.

Minimizing (10) with respect to β, we obtain the dependence of the energy E on the orientation of the domain:

$$E(\varphi) = -\frac{H^2 \cos^2 \varphi}{2zI_{12}}. \tag{11}$$

The crystal-averaged mean energy of reaction of the spin subsystem of a domain to the imposition of a field as a result of the canting of the spins is given by

$$\bar{E} = -\frac{1}{\pi}\int_{-\pi/2}^{\pi/2} p(\varphi)\frac{H^2\cos^2\varphi}{2zI_{12}}\,d\varphi. \tag{12}$$

Relation (12) allows us to write $\bar{E}$ in terms of the DCP as

$$\bar{E} = -\frac{\chi_e}{4}H^2(\bar{n}_L + 1), \tag{13}$$

where we have taken into account that, according to the Néel theory,[8] the magnetic susceptibility of of the uniform state is $\chi_e = 1/zI_{12}$.

The contribution to the free energy from the term reflecting the process of restructuring of the multidomain state is written phenomenologically in the form of a power series in the DCP $\bar{n}_L$. We note that such a representation is equivalent to the thermodynamic description of the ordered state of liquid crystals.[18] Indeed, from symmetry considerations such a phenomenological approach to the description of the free-energy contribution responsible from the formation of the multidomain state of an antiferromagnet is possible, since the direction of the antiferromagnetic vector in a high-symmetry antiferromagnet is defined only up to a sign, and therefore one can distinguish only an axis that is related to the orientation **L** in the domain: directions of **L** along and perpendicular to this axis are equivalent. Accordingly, the orientation of the **L** vector and, hence, the orientation of the domains in the most general form must be described by an orientation tensor n_{ik} constructed in terms of the direction cosines of the axis along which **L** lies. With the use of the angle φ introduced to characterize the orientation of the domains in the plane, the components of the orientation tensor will be $n_{xx} = \cos^2\varphi$, $n_{yy} = \sin^2\varphi$, $n_{xy} = \sin\varphi\cos\varphi$.

In the absence of intraplane anisotropy, for the choice of one of the coordinate axes along the field (as in Fig. 5) the mean values of the off-diagonal components of the orientation tensor will equal zero. Also, for $H = 0$ the mean values of the diagonal components of the orientation tensor will be equal to each other; when a magnetic field is imposed, their values will differ. Therefore, in the case of an easy-plane antiferromagnet the phenomenological description of the multidomain state can be done with the use of the DCP $\bar{n}_L$. Such a free energy should also include the energy (13) as a term. Accordingly, we write the phenomenological expression for the free energy of a multidomain antiferromagnetic state in the form

$$F = a\bar{n}_L^2 + c\bar{n}_L^3 + b\bar{n}_L^4 - \frac{\chi_e}{4}H^2(\bar{n}_L + 1), \tag{14}$$

where a, b, and c are phenomenological parameters that do not depend on H.

The equilibrium multidomain state corresponds to a minimum of F. Therefore, the equation of state of a multidomain antiferromagnet in a field is obtained by setting the derivative of the free energy with respect to the DCP equal to zero: $dF/d\bar{n}_L = 0$. For free energy (14) this equation of state has the form

$$2a\bar{n}_L + 3c\bar{n}_L^2 + 4b\bar{n}_L^3 - \frac{\chi_e}{4}H^2 = 0. \tag{15}$$

The state with $\bar{n}_L = 0$, in which the domains are distributed equiprobably in the plane, will be the equilibrium state for $H = 0$ when the model parameters satisfy the conditions $a > 0$, $b > 0$, $9c^2 < 32ab$.

Let us consider the simplest case of the phenomenological description, when the parameters $b = 0$, $c = 0$. This "quadratic" model is quite relevant, since it is assumed that the parameter a is always positive. This treatment is valid for $H \to 0$, or, more precisely, for $H < H_d$, and was used in Ref. 15. In this model it is found that the value of DCP is directly proportional to the square of the magnetic field strength:

$$\bar{n}_L = \frac{\chi_e}{8a}H^2. \tag{16}$$

Substituting (16) into (4) and (6), we find that the magnetostriction during the restructuring of the multidomain state is proportional to the square of the magnetic field strength and that the magnetization is nonlinear and contains the third power of the field strength. Comparison of (16) with (1) allows us to relate the model parameter a with the field H_d: $a = \chi_e H_d^2/8$. Thus the quadratic model is (quite naturally) in good agreement with the experimental data for $H \to 0$.

In Refs. 12 and 19 an essentially quadratic model (from the standpoint of the proposed phenomenological theory) was used in the entire field interval in which the multidomain antiferromagnetic state exists. It was stated in those papers that the multidomain state is stabilized by a free-energy contribution proportional to the square of the mean magnetostriction. It follows from Eq. (4) that the square of the mean magnetostriction in the multidomain state is proportional to the square of the DCP. Let us analyze the results of the quadratic model on the assumption that it extends over the whole existence region of the multidomain state in respect to magnetic field.

Substituting $\bar{n}_L = 1$ into (18), we find that the multidomain state is realized only in the interval $H \in [0, H_d]$. In this interval the magnetic susceptibility is described by the expression

$$\chi = \frac{1}{2}\chi_e\left(1 + 3\frac{H^2}{H_d^2}\right). \tag{17}$$

At the point $H = H_d$ a "transition" from the multidomain state to the uniform state occurs. This transition is accompanied by a jump in the magnetic susceptibility, which has the behavior shown in Fig. 7. The susceptibility in the multidomain state is shown by the solid curve in Fig. 7, while the susceptibility of the uniform region is denoted by a solid straight line parallel to the abscissa. The dashed straight line is the susceptibility of the single-domain state for $H \to 0$. It is seen that in the multidomain state as $H \to H_d$ the magnetic susceptibility becomes twice as high as the magnetic susceptibility of the uniform state, and at the "homogenization field" $H = H_d$ a jump occurs. In this case the DCP is an increasing function in the multidomain state, its value being proportional to the field strength: $d\bar{n}_L/dH = 2H/H_d^2$, in disagreement with the data of Fig. 6.
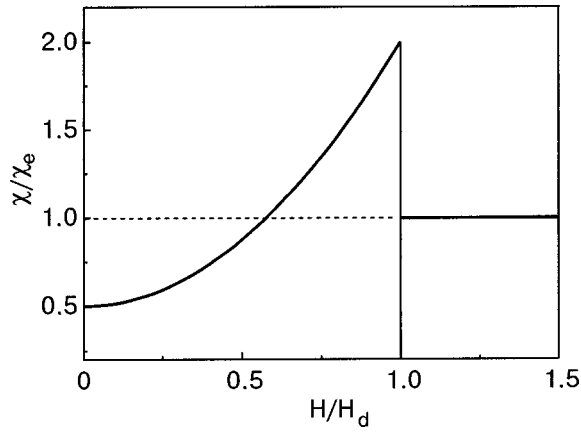
FIG. 7. Graph of the dependence of the magnetic susceptibility on the magnetic field strength, $\chi(H)$, during the restructuring of the multidomain state for the "quadratic" phenomenological model.
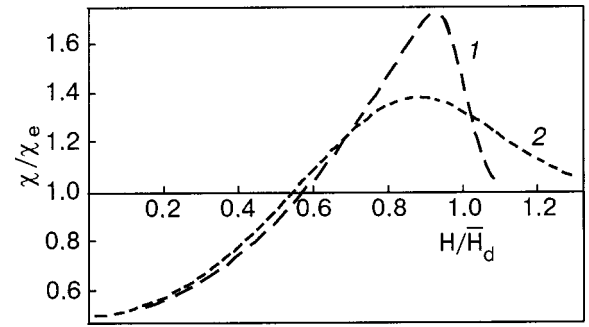

FIG. 8. Field dependence of the magnetic susceptibility, $\chi(H)$, in the multidomain state with allowance for scatter of the values of the homogenization fields H_d: $\sqrt{\sigma}/\bar{H}_d = 0.05$ (*1*) and 0.2 (*2*).

Thus at high fields, and especially in the final stage, the quadratic model disagrees with the experimental curves presented for the magnetostriction, magnetization, and magnetic susceptibility and also for the rate of change of the number of domains in the NiCl$_2$ crystal (Figs. 1, 2, 4, and 5). We see that in the form presented, such a quadratic model cannot be extended to the whole field region in which the multidomain state of the crystal exists. In addition, we know of no other antiferromagnets for which the transition to the uniform state would be accompanied by a jump in susceptibility, and we note that the jump under discussion is similar to the jump in susceptibility at a spin flip.[1]

However, the quadratic model can be extended to the whole field region in which the restructuring of the multidomain state takes place in the case when the multidomain state arises on account of a magnetoelastic mechanism based on the matching of the elasticity of defects and domains[11] if the inevitable (and even obligatory) scatter of the values of the parameter H_d in that case is taken into account.

Let us analyze the behavior of the magnetic susceptibility of the multidomain state in the approximation that the scatter of values of the homogenization field H_d is described by a normal distribution, which we write in the form

$$p(H_d) = \frac{1}{\sqrt{2\pi\sigma}} \exp\left(-\frac{(H_d - \bar{H}_d)^2}{2\sigma}\right), \qquad (18)$$

where $\bar{H}_d$ is the mean value of the homogenization field of the whole crystal, and σ is the variance of H_d.

We now note that the magnetic susceptibility of the domains without allowance for the scatter of H_d depends on the value of the applied field: if $H < H_d$, then it is described by expression (17), while if $H > H_d$ it is a constant and equal to χ_e. Accordingly, the magnetic susceptibility of the multidomain state of the whole crystal with allowance for the scatter in H_d will be

$$\chi = \frac{1}{2}\chi_e\left[1 + \frac{3H^2}{\sqrt{2\pi\sigma}}\int_H^\infty \frac{1}{H_d^2}\exp\left(-\frac{(H_d - \bar{H}_d)^2}{2\sigma}\right)dH_d\right.$$

$$\left. + \frac{1}{\sqrt{2\pi\sigma}}\int_0^H \exp\left(-\frac{(H_d - \bar{H}_d)^2}{2\sigma}\right)dH_d\right]. \qquad (19)$$

Figure 8 shows plots of $\chi(H)$ for two values of the standard deviation, $\sqrt{\sigma} = 0.05\bar{H}_d$ and $\sqrt{\sigma} = 0.2\bar{H}_d$. In both cases the $\chi(H)$ curve is continuous, and at $H < 0.5\bar{H}_d$ it will have a quadratic dependence on H, but now H_d in (17) should be replaced by $\bar{H}_d$. In addition, an increase in the variance leads to a decrease in the height and a broadening of the maximum. We note that the experimental data on $\chi(H)$ for the NiCl$_2$ crystal (see Fig. 4) with a small but strongly broadened maximum corresponds to the case of a large scatter in H_d, with $\sqrt{\sigma}/\bar{H}_d \sim 1$.

It should be noted, however, that the phenomenological model (14) in its most general form, without any assumptions about the mechanisms, can also be used to describe the multidomain state. Indeed, by inverting the equation of state (15) we obtain an expression for the field dependence of the DCP:

$$\bar{n}_L = \frac{H^2}{H_d^2} - \frac{3}{2}\frac{c}{a}\left(\frac{H^2}{H_d^2}\right)^2 + \frac{1}{2}\left(9\frac{c^2}{a^2} - 4\frac{b}{a}\right)\left(\frac{H^2}{H_d^2}\right)^3, \qquad (20)$$

which depends on the ratios of the model parameters c/a and b/a. Using the least-squares method, we determine the form of the expansion for $\bar{n}_L(H)$ from the magnetostriction data. For the field interval from 0 to 4 kOe we obtained the following expression for this expansion:

$$\bar{n}_L = 0.092H^2 - 0.0054H^4 + 1.166\times 10^{-4}H^6, \qquad (21)$$

in which the values of H are given in kOe. Comparing (20) with (21), we find that the ratios of the phenomenological parameters have the values $c/a = 0.45$ and $b/a = 1.5$ and satisfy the stability requirements of the model (14).

Relation (20) for the DCP gives a rather good description of the process of restructuring of the multidomain state. The negative sign of the H^4 term agrees with the slow growth of the magnetostriction in fields above 2 kOe and with the presence of an inflection point on the $\varepsilon(H)$ curve. In addition, relation (20) can be used to describe the maximum on the $\bar{n}_L(H)$ curve, which means that the trend of the susceptibility in this model will correspond to the data of the experimental observations.

In spite of these rather good results from the phenomenological model containing the fourth power of $\bar{n}_L$, it must be said that relation (20), obtained by inverting the equation of state (15), is not applicable in the entire interval of fields where the restructuring of the multidomain state of the crys-

tal takes place, viz., up to fields ~ 10 kOe for $NiCl_2$. In addition, and this is important, it is impossible to find a satisfactory polynomial approximation to the experimental data for the magnetostriction or for the magnetization in the whole field interval where the restructuring of the multidomain state takes place. Accordingly, it must be stressed that a quadratic model incorporating the nonuniformity of the homogenization fields due to the influence of defects is more convincing.

CONCLUSION

From experimental data presented for the field dependence of the magnetostriction and magnetization of the $NiCl_2$ crystal, we see that a description of the process of restructuring of the multidomain state under the influence of magnetic field can be obtained by introducing an averaged characteristic for the direction of the domains—a domain coalignment parameter (DCP). Indeed, as was shown above, the values of the magnetostriction and magnetization are proportional to the value of this parameter, and the magnetic susceptibility depends in addition on the rate of change of this parameter with variation of the applied field. The use of such an averaged parameter makes it possible to describe the interrelationship between the field dependence of the physical observables in the multidomain state.

In addition, with the aid of the DCP one can obtain a phenomenological description of the multidomain state of an antiferromagnet in an external field. Here a phenomenological expression for the free energy of the multidomain state can be written in the form of a power series in the DCP. By minimizing this energy, one can determine the equilibrium state of the DCP for a given magnetic field strength and, hence, determine the characteristics of the multidomain state.

In the phenomenological approach it has turned out to be very constructive (from the standpoint of the results obtained) to employ a model which is quadratic in the DCP and which takes into account the nonuniformity of the homogenization fields for different domains. This approach agrees well with the magnetoelastic mechanism of formation of the multidomain state, which, as discussed above, requires matching of the elasticity of the domains and defects. Here the introduction of a scatter in the values of the homogenization fields results in continuity of the transition from the multidomain to the uniform state. It is perfectly obvious that

such a scatter of the homogenization fields is related to the quality of the crystal, to the degree of perfection of the crystal lattice. In our view, it would be extremely interesting to study the restructuring of the multidomain state of crystals of different quality: for perfect crystals the susceptibility peak should be higher, meaning that the transition to the uniform state would be more pronounced.

*E-mail: lozenko@iop.kiev.ua

———————————

[1] A. S. Borovik-Romanov, "Antiferromagnetism," in *Progress in Science* [in Russian], Izd-vo AN SSSR (1962).

[2] M. K. Wilkinson, J. W. Cable, E. O. Wollan, and W. C. Koehler, Phys. Rev. **113**, 497 (1959).

[3] M. O. Kostryukova and L. M. Kashirskaya, JETP Lett. **9**, 238 (1969).

[4] M. M. Farztdinov, Usp. Fiz. Nauk **84**, 611 (1964) [*sic*].

[5] W. J. De Haas, B. H. Schultz, and J. Koolhaas, Physica **7**, 57 (1940).

[6] D. Billerey, C. Terrier, A. J. Pointon, and J. P. Redoules, J. Magn. Magn. Mater. **21**, 187 (1980).

[7] V. M. Kalita, A. F. Lozenko, S. M. Ryabchenko, and P. A. Trotsenko, Ukr. Fiz. Zh. **43**, 1469 (1998).

[8] L. Neel' (L. Néel), Izv. Akad. Nauk SSSR, Ser. Fiz. **21**, 890 (1957).

[9] A. S. Kovalev and A. M. Kosevich, Fiz. Nizk. Temp. **3**, 259 (1977) [Sov. J. Low Temp. Phys. **3**, 125 (1977)].

[10] I. E. Dzyaloshinskiĭ, JETP Lett. **25**, 98 (1977).

[11] V. M. Kalita and A. F. Lozenko, Fiz. Nizk. Temp. **27**, 489 (2001) [Low Temp. Phys. **27**, 358 (2001)].

[12] H. Gomonay and V. M. Loktev, J. Phys.: Condens. Matter **14**, 3959 (2002).

[13] V. M. Kalita and A. F. Lozenko, Fiz. Nizk. Temp. **27**, 827 (2001) [Low Temp. Phys. **27**, 649 (2001)].

[14] V. M. Kalita, A. F. Lozenko, S. M. Ryabchenko, P. A. Trotsenko, and T. N. Yatkevich, Fiz. Tverd. Tela (St. Petersburg), **46**, 317 (2004) [Phys. Solid State **46** (2004)].

[15] V. M. Kalita, A. F. Lozenko, and A. P. Trotsenko, Fiz. Nizk. Temp. **28**, 378 (2002) [Low Temp. Phys. **28**, 263 (2002)].

[16] J. Gunzbourg, S. Papassimacopoulos, A. Mieden-Gros, and A. Allain, J. Phys. **32**, 125 (1971).

[17] V. G. Bar'yakhtar, A. N. Bogdanov, and D. A. Yablonskiĭ, Usp. Fiz. Nauk **156**, 47 (1988) [Sov. Phys. Usp. **31**, 810 (1988)].

[18] P. G. de Gennes and J. Proust, *The Physics of Liquid Crystals*, Oxford, Clarendon Press (1993).

[19] E. V. Gomonaj and V. M. Loktev, Fiz. Nizk. Temp. **25**, 699 (1999) [Low Temp. Phys. **25**, 520 (1999)].

Translated by Steve Torstveit

Size effect in the desorption of excited atoms and molecules from clusters of inert elements under electron bombardment

É. T. Verkhovtseva,* E. A. Bondarenko, and Yu. S. Doronin

B. Verkin Institute for Low Temperature Physics and Engineering, National Academy of Sciences of Ukraine, pr. Lenina 47, Kharkov 61103, Ukraine

New channels of desorption of excited atoms and molecules from clusters of argon, krypton, and xenon under electron bombardment are found by the method of vacuum ultraviolet emission spectroscopy. The maximum yield of particles is registered in the interval of average sizes of 50–100 atoms/cluster. The regularities and features of the desorption of excited particles are revealed, making it possible to establish a new desorption mechanism called nonradiative excimeric dissociation. It is shown that the main stages of this mechanism are: the formation of molecular centers of the nature of highly excited diatomic excimer molecules in clusters in the process of self-trapping of high-energy p excitons ($n=1$); the nonradiative dissociation of these molecules to excited atoms and atoms in the ground state with large kinetic energies. It is established that the appearance of new channels of desorption of excited atoms and molecules from clusters under bombardment by electrons is due to features of the physical properties of clusters in the interval of average sizes 50–100 atoms/cluster, in particular, to features of the energy spectrum, vibrational frequency spectrum of the atoms, and exciton energy relaxation. © *2004 American Institute of Physics.* [DOI: 10.1063/1.1645153]

INTRODUCTION

The processes of desorption of neutral excited and charged particles from solidified rare gases have been studied by many authors.[1–7] However, at the present time the experimental data on the desorption of excited particles from clusters of inert elements are of an incomplete and fragmentary nature and have been interpreted in terms of the well-known solid-state desorption mechanisms.[8,9] Nevertheless, the size dependences of the intensity of the emissions of the cathodoluminescence spectra of argon and krypton clusters in the vacuum ultraviolet (VUV), first measured by the present authors in Ref. 10, attest to the existence of previously unknown channels of efficient desorption of excited atoms and molecules from clusters. It should be noted that in Ref. 10 we used calculated values of the mean cluster sizes which were checked against experimental values only in a limited region of sizes obtained by the electron diffraction method. However, later studies[11,12] of the fcc structure of inert elements have revealed stacking faults of a deformation type and have demonstrated their governing role in the mechanism of formation and growth of the crystalline phase. The observation of stacking faults has made it necessary to reexamine the experimental values of the mean size of the clusters in a wide range of sizes, since stacking faults influence the width of the diffraction peaks, and the measured width is used in the Selyakov–Scherrer expression for determining the characteristic mean size of the clusters.[13] A reexamination of the mean sizes and, hence, of the types of electronic excitations arising in the clusters under electron bombardment, has provided the prerequisites for revealing the desorption mechanism and has stimulated new and detailed studies of the desorption of excited particles from clusters of inert elements.

The goal of the present paper is to establish the regularities and features of the desorption of excited atoms and molecules from clusters of inert elements under electron bombardment and to ascertain the mechanism of desorption of excited particles. The measurements were made by the method of VUV emission spectroscopy. We studied the features of the VUV spectra of the cathodoluminescence of Ar_N, Kr_N, and Xe_N clusters in the region of atomic resonance transitions and the regularities in the size dependences of the intensity of the emissions of the VUV radiation spectrum of desorbed excited particles.

EXPERIMENTAL EQUIPMENT AND MEASUREMENT TECHNIQUES

Free clusters of argon, krypton, and xenon were formed during homogeneous condensation of the gas in supersonic jets of the rare gases flowing from a conical nozzle into a vacuum chamber. The mean size of the clusters at the place where the jet was excited by electrons was varied by means of the pressure P_0 and temperature T_0 of the gas at the entrance to the nozzle. For studying the VUV spectra of cathodoluminescence of the clusters and also of excited particles desorbed from clusters, it was necessary to solve two methodological problems. One of them involves choosing an experimental geometry that provides locality of the measurements, i.e., the selection of radiation from a region of the jet within which the mean cluster size varies insignificantly. For this a careful diagnostics of the parameters of the jet along its axis and in the transverse direction was carried out. The parameters of the jet were determined theoretically by means of two-dimensional calculations of the jet flow of argon with homogeneous condensation using the code described in Ref. 14.

The parameters of the gas–condensate system were calculated in the range of pressures $P_0 = 0.02-0.5$ MPa and temperatures $T_0 = 150-550$ K. It follows from an analysis of the data that at distances from the exit section of the nozzle $l \geq 30$ mm, where the emitting region of the jet to be studied is a cylinder only 6 mm long and 3 mm in diameter, the parameters of the gas–condensate system vary insignificantly, by not more than $\pm 15\%$, and the mean cluster size, by $\pm 5\%$. The main studies of Ar_N, Kr_N, and Xe_N in clusters supersonic jets were therefore done at a distance $l = 30$ mm, which ensured locality of the measurements.

The other methodological problem was to obtain calibration curves relating the mean cluster size $\bar{N}$ (atoms/cluster) at the site of excitation of the jet by electrons with the values of the pressure P_0 and gas temperature T_0 at the entrance to the nozzle at which the measurements were made. The calibration curves $\bar{N}(P_0, T_0)$ were obtained by an electron diffraction method on an electronographic device.

Thus the experimental equipment complex on which the measurements of the VUV spectra were made consisted of the following:

1) A spectroscopic device for studying the VUV spectra of the cathodoluminescence of clusters of inert elements in a supersonic jet over a wide range of mean cluster sizes ($10 - 4 \times 10^4$ atoms/cluster) and wavelengths (50–250 nm).

2) An electronographic device for determining the structure, temperature, and mean size of the clusters in a supersonic jet.

A diagram of the experimental setups is shown in Fig. 1. The spectroscopic device (Fig. 1a) consists of a small-scale gas-jet VUV source[15] and an SP-68 vacuum monochromator. The working principle of the apparatus is as follows. The gas to be studied passes from a high-pressure bottle through a regulating valve and into a heat exchanger *5*. After reaching the specified temperature of the heat exchanger, the gas is formed into a jet *6* by a conical nozzle *4* and flows into a vacuum chamber *1*. A cryogenic pump *7*, cooled with liquid hydrogen, is used to pump out the jet gas. The gas pressure in the chamber in the presence of the jet does not exceed 10^{-3} Pa. An electron beam with an energy of 1 keV[1)] and beam current of 20 mA crosses the jet at a distance of 30 mm from the exit section of the nozzle in the direction perpendicular to its axis. The VUV radiation arising falls on the entrance slit of an SP-68 vacuum monochromator and is dispersed into a spectrum by a diffraction grating *2* having 600 lines/mm. After the exit slit of the SP-68 monochromator the radiation is registered by an FEU-79 photomultiplier *3* with sodium salicylate deposited on the end of it and, in a number of experiments, a VÉU-6 secondary electron multiplier. The output signal of the detectors was recorded by a pulse-counting circuit with storage.

In the experiments we used a conical supersonic nozzle with a throat diameter of 0.34 mm, a cone angle of 8.6°, and an area of the exit section relative to the throat of 36.7. As we have said, the size distribution of the clusters in the jet was varied by means of the pressure P_0 and temperature T_0 of the gas at the entrance to the nozzle. The VUV radiation spectra of supersonic jets of argon, krypton, and xenon were measured in the interval of pressures $P_0 = 0.02-0.3$ MPa and temperatures $T_0 = 116-700$ K. The correlation between the
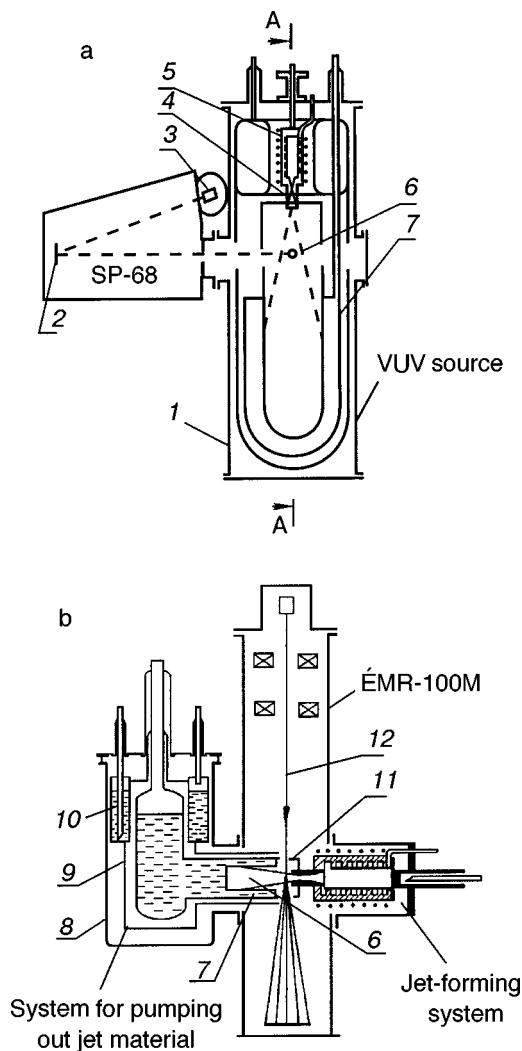

FIG. 1. Diagram of the experimental equipment complexes: spectroscopic (a), electronographic (b). *1*—Vacuum chamber, *2*—diffraction grating, *3*—radiation detector, *4*—nozzle, *5*—heat exchanger, *6*—supersonic jet, *7*—cryogenic pump, *8*—chamber, *9*—copper shield, *10*—Dewar, *11*—shield, *12*—electron beam.

VUV spectra recorded at different P_0 and T_0 and the mean cluster size $\bar{N}$ at the site of excitation of the jet by the electron beam was established by means of calibration curves $\bar{N}(P_0, T_0)$ obtained by the method of electron diffraction on an electronographic device.

The experimental device (see Fig. 1b) on which the electronographic measurements were made consists of an ÉMR-100M electronograph and systems for forming a supersonic gas jet and pumping out the jet material. The two systems were mounted on opposite windows of the electronograph chamber. It should be noted that the jet-forming system and the nozzle parameters of the electronographic device were identical to those used in the spectroscopic device. The gas pressure in the electronograph chamber was 5×10^{-4} Pa prior to admission of the jet and 10^{-3} with the jet (at a gas flow rate of 50 cm³/s at standard conditions). The jet gas was pumped out by a cryogenic pump *7* cooled by liquid hydrogen (see Fig. 1b). The pump was mounted in the chamber *8* and shielded from the thermal radiation of the chamber walls by a copper shield *9*, which was soldered to a Dewar *10* containing the liquid nitrogen. For pumping out the particles

scattered by angles $\theta > \theta_{\text{theor}}$ in the emergence of the gas from the exit of the nozzle, a copper shield *11* soldered to the hydrogen pump was used. There are two openings in the shield: an electron beam *12* with energy 60 keV passes through the upper opening into the jet zone at a distance of 30 mm from the nozzle exit, and the diffracted electrons pass through the lower opening to the detector. The diffraction patterns were recorded by electrometric and photographic means. In the first case a retarding field was used to eliminate a large fraction of the incoherently scattered electrons, substantially improving the accuracy of determining the shapes of the diffraction peaks. The photographic registration was used for precise determination of the position of the diffraction peaks.

The diffraction patterns from Ar_N, Kr_N, and Xe_N clusters formed in the corresponding supersonic jets were recorded in the pressure range $P_0 = 0.2-0.6$ MPa and temperature range $T_0 = 150-200$ K in the case of Ar_N and Kr_N clusters and in the range $P_0 = 0.08-0.16$ MPa at $T_0 = 200$ K for Xe_N clusters. As an example, Fig. 2 shows a typical diffractogram for the argon clusters studied. Analogous diffractograms were obtained from the clusters formed in krypton and xenon jets in the indicated ranges of pressures P_0 and gas temperatures T_0. The analysis in Refs. 11 and 12 of similar diffractograms recorded from Ar_N, Kr_N, and Xe_N clusters in jets shows that the clusters have a crystalline fcc structure with stacking faults of a deformation type.

The lattice parameter of crystalline clusters was usually found using photographic registration of the diffraction patterns. The lattice parameter a was calculated from the brightest diffraction rings by the following formula for substances with a cubic lattice:[13]

FIG. 2. Diffractogram of the clusters of an argon jet ($P_0 = 0.6$ MPa, $T_0 = 150$ K); $s = 4\pi \sin \vartheta / \lambda$, where ϑ is the Bragg angle.

$$a = d_{hkl} \sqrt{h^2 + k^2 + l^2}, \tag{1}$$

where d_{hkl}, the interplane distance for the hkl peak, was determined from the widely used formula in electronography

$$d_{hkl} = 2L\lambda / D_{hkl}, \tag{2}$$

where $L\lambda$ is a device constant (L is the distance from the sample to the device registering the diffraction pattern, and λ is the electron wavelength) which was determined from the electronogram of the reference standard TlCl, the correctness of the use of which is discussed in Ref. 16; D_{hkl} is the diameter of the diffraction ring on the electronogram, and hkl are the indices of the reflecting planes. The relative error in the determination of the lattice parameter was 0.2%, and the absolute error did not exceed ± 0.010 Å.

The temperature of the crystalline clusters was determined from the values of the lattice parameter of the clusters and the data on the temperature dependence of the lattice parameter of the substance under study. For this we used the data on the temperature dependence of the lattice parameter of island films of solidified rare gases with a size of 4 to 6 nm,[17] which is a typical size for the clusters studied here.

In accordance with the theory of x-ray scattering,[13] the characteristic linear mean size of the crystalline clusters, $t \sim \bar{N}^{1/3}$, was determined from the formula[2]

$$1/t = 1/t^* - 1/t_s, \tag{3}$$

where $1/t_s$ is the broadening due to stacking faults, and t^* is the effective characteristic linear size determined from the total broadening of the diffraction peak with the use of the Selyakov–Scherrer relation, according to which

$$t^* = \frac{kL\lambda}{(B_{hkl}^2 - b_0^2)^{1/2}} \frac{1}{\cos \vartheta}, \tag{4}$$

where k is a constant that depends on the shape of the crystallites and has a value close to unity (in the case of a sphere $k = 1.07$);[18] B_{hkl} is the half-width of the diffraction peak of the object under study, b_0 is the instrumental width of the electron beam, determined from the half-width of the diffraction peaks of the reference standard TlCl; ϑ is the Bragg diffraction angle. Since $\vartheta = 2-3°$ in electronographic studies, one can set $\cos \vartheta = 1$. The correctness of the use of the Selyakov–Scherrer relation for crystalline clusters with the fcc structure and mean size $\bar{N} > 10^3$ atoms/cluster is based on calculations done in Ref. 19. According to the theory of Ref. 13

$$1/t_s = \{(1.5\alpha + \beta)/d_{111}\} j \cos \varphi, \tag{5}$$

where α and β are the density of stacking faults of the "deformation" and "twin" types; d_{111} is the distance between close-packed planes, and $j \cos \varphi$ is the crystallographic constant for the given family of planes, which in the case of the (111) reflection is equal to 1/4. According to Refs. 11 and 12, the density of stacking faults of the "twin" type in crystalline clusters of inert elements in the region of mean sizes investigated here is small, and we therefore neglect β in Eq. (5). The value of α was calculated from the displacement of the centroids of the (111) and (220) diffraction peaks (see Fig. 2) relative to their positions in the defect-free microcrystal. The latter was found by using the (311) diffraction
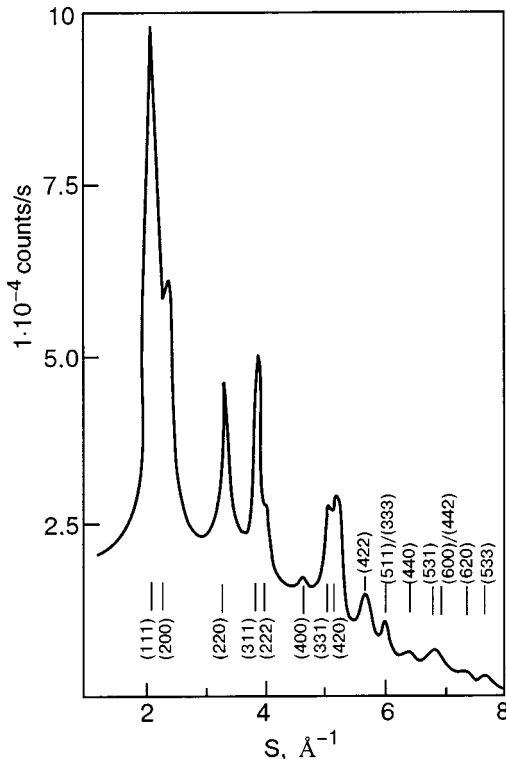
ring of the object under study, the position of the maximum intensity of which is independent of the presence of stacking faults. The values of α were calculated according to the Patterson formula,[20] which in the case of diffraction of fast electrons, because of the smallness of the Bragg angles, takes the form[21]

$$\Delta D_{SF}/D = G j \alpha^* /2, \qquad (6)$$

where $\Delta D_{SF}/D$ is the relative change in diameter of the diffraction ring under the influence of the stacking faults, G is a constant for a given family of planes (hkl), averaged over all groups of planes $[hkl]$ having the same displacement; j is the fraction of the family of planes $[hkl]$ affected by the stacking faults, and α^* is a parameter related to the density of stacking faults by the relation

$$\alpha^* = \frac{4\pi}{3\sqrt{3}} \left[\frac{1}{2} - \frac{3}{2\pi} \arctan \sqrt{3}(1-2\alpha) \right]. \qquad (7)$$

Three series of experiments were done in this study. In the first series we investigated the dependences of the mean cluster size in the jet on the pressure P_0 and gas temperature T_0 at the entrance to the nozzle. For this we measured the diffraction patterns from Ar_N, Kr_N, and Xe_N clusters for pressures P_0 and temperatures T_0 of the gas in the intervals given above. Measurements were made at least five times for each flow regime of the jet. By interpretation of the diffraction patterns we determined the structure, mean size, and temperature of the cluster and established the dependences of the mean cluster size on the pressure P_0 and temperature T_0 of the gas at the entrance to the nozzle. The relative error in the determination of the characteristic mean size t of the clusters did not exceed 10%.

In the second series of experiments we investigated the features of the VUV cathodoluminescence spectra of Ar_N, Kr_N, and Xe_N clusters in the wavelength interval 100–200 nm. For this we measured the fine structure of the spectra of the clusters in the region of the atomic resonance transitions $^1P_1 \rightarrow {}^1S_0$ and $^3P_1 \rightarrow {}^1S_0$ in the first and second orders of diffraction. In addition, we did a recalibration of the values of the mean cluster sizes in other VUV radiation spectra which we had obtained previously.[10,22]

In the third series of experiments we studied the regularities in the size dependences of the intensities of certain emissions in the VUV spectra of Ar_N, Kr_N, and Xe_N clusters. For this we measured the intensity I of the individual emissions in the VUV spectra of a supersonic jet of xenon and also that of the emissions in the regions of atomic resonance transitions in the spectra of jets of argon and krypton as a function of the gas temperature at the nozzle entrance, T_0, at a constant pressure P_0 in the interval $P_0 = 0.02-0.3$ MPa. In addition, we did a recalibration of the values of the mean cluster sizes in the size dependences of the intensities of other emissions in the VUV spectra of Ar_N and Kr_N clusters which we had measured previously in Ref. 10. The accuracy of the measurements of the position of the features in $I/\rho_0(T_0)$ (ρ_0 is the density of atoms at the entrance to the nozzle) on the scale of temperatures T_0 varied from 2 to 4 K for different emissions in the VUV spectra of the Ar_N, Kr_N, and Xe_N clusters.

The VUV radiation of excited atoms and molecules desorbed from clusters was separated from the VUV radiation from particles of the gas phase of the jet with the aid of the law of "corresponding jets,"[23] i.e., the dependences of $I/\rho_0(T_0)$ (at $P_0 = $ const) for the emissions from desorbed excited atoms and molecules for different pressures P_0 reached their maxima on the curve $P_0 T_0^{-2.5} = $ const, which corresponds to an identical size distribution of the clusters.

RESULTS AND DISCUSSION

Dependences of the mean cluster size on the pressure P_0 and temperature T_0 of the gas at the nozzle entrance

It follows from the electron diffraction studies that in the gas flow regimes set by values of the pressure P_0 and gas temperature T_0 in the intervals given above, crystalline clusters Ar_N, Kr_N, and Xe_N having the fcc structure with stacking faults are formed. The mean cluster size in the jet varied over the limits $\Delta\bar{N}$ [atoms/cluster]: $\Delta\bar{N}_{Ar} = 2.4 \times 10^3 - 5.8 \times 10^4$, $\Delta\bar{N}_{Kr} = 7 \times 10^3 - 1.8 \times 10^5$, and $\Delta\bar{N}_{Xe} = 4.2 \times 10^3 - 1.5 \times 10^4$.

As a result of the mathematical processing of the data we established the mean values of the lattice parameter: $\bar{a} = 5.326 \pm 0.010$ Å for Ar_N, $\bar{a} = 5.683 \pm 0.010$ Å for Kr_N, and $\bar{a} = 6.155 \pm 0.010$ Å for Xe_N. The temperature of the clusters determined from the value of the lattice parameter and its temperature dependence for island films of solidified rare gases[17] was found to be 35 ± 4 K, 55 ± 3 K, and 57 ± 3 K for Ar_N, Kr_N, and Xe_N clusters, respectively. It should be noted that the values obtained for the temperature of the clusters of inert elements do not vary outside the error limits of the measurements in the above-mentioned intervals of mean sizes investigated.

The data obtained on the mean characteristic linear sizes t were used to construct calibration curves $t(P_0)$ for $T_0 = $ const and $t(T_0)$ at $P_0 = $ const. As an example, Figure 3a,b shows the experimental curves of the mean characteristic linear size of argon clusters as a function of the pressure P_0 at a constant gas temperature $T_0 = 200$ K and as a function of the temperature T_0 at a constant gas pressure $P_0 = 0.3$ MPa. Analogous curves were obtained for Ar_N and Kr_N clusters at other values of the temperature T_0 and pressure P_0 of the gas in the ranges of values investigated. In addition, an analogous $t(P_0)$ dependence was obtained for Xe_N clusters at $T_0 = 200$ K. In constructing the $t(P_0)$ and $t(T_0)$ curves we used the values of the mean characteristic linear size determined from the Selyakov–Scherrer relation (4), i.e., without allowance for stacking faults and with the stacking faults taken into account by formula (3). It follows from an analysis of the data in Fig. 3 that the curves shown are well approximated by the expressions $t \propto P_0^{0.6}$ and $t \propto T_0^{-1.5}$. If it is taken into account that the number of atoms in a cluster $\bar{N} \propto t^3$, then the value of $\bar{N}$ varies with pressure P_0 and gas temperature T_0 as $\bar{N} \propto P_0^{1.8}$ and $\bar{N} \propto T_0^{-4.5}$. We have also established in this study that clusters of the same mean size form in the jet at values of P_0 and T_0 connected by the relation $P_0 T_0^{-2.5} = $ const (see Fig. 3c). This power-law relation is in rather good agreement with the data of electron-diffraction and mass-spectrometric measurements of other
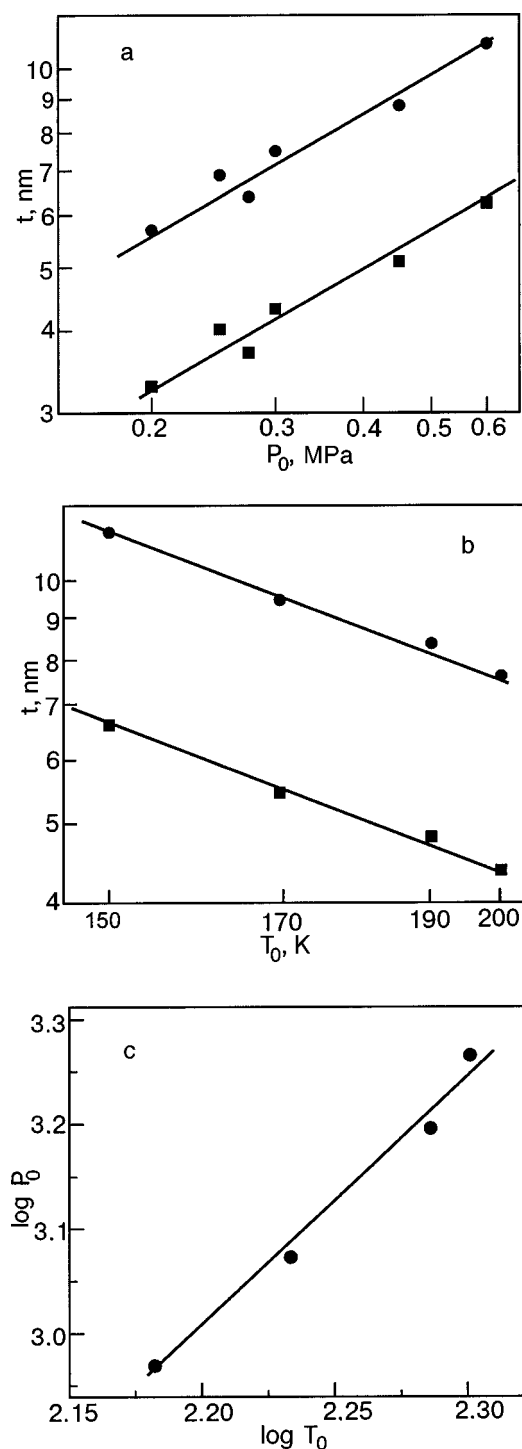
FIG. 3. Characteristic linear mean size t of argon clusters as a function of the pressure P_0 at a gas temperature $T_0 = 200$ K (a) and as a function of the temperature T_0 at a pressure $P_0 = 0.3$ MPa (b); dependence of the pressure P_0 on the gas temperature T_0 for argon clusters of identical mean size $\bar{N} = 3800$ atoms/cluster (c); without allowance for stacking faults ($\blacksquare$); with allowance for stacking faults ($\bullet$).

authors[24,25] and confirms the correctness of the theory of "corresponding jets." [23]

From an analysis of the data of Fig. 3a,b it also follows that the characteristic linear mean size is noticeably affected by taking stacking faults into account. Therefore in the present spectroscopic studies we have used the calibration curves for $\bar{N}(P_0, T_0)$ obtained by the electron diffraction

method with allowance for stacking faults. In constructing these curves the experimental dependences $t(P_0)$ obtained at different T_0 for crystalline clusters of large sizes were extrapolated to the region of smaller values of t and P_0. Such an extrapolation is based on the fact that the relations $t \propto P_0^{0.6}$ and $t \propto T_0^{-1.5}$ obtained in the present experiments for crystalline clusters of large sizes actually hold over a wide range of cluster sizes, including small ones.[23–25] Armed with the calibration curves for $\bar{N}(P_0, T_0)$ over a wide range of mean sizes ($\bar{N} = 10 – 1.8 \times 10^5$ atoms/cluster), we recalibrated the values of the mean cluster sizes in the VUV radiation spectra and in the size dependences of the intensities of emissions which we had obtained previously for Ar_N and Kr_N clusters.[10,22]

Regularities and features of the VUV radiation spectra of excited atoms and molecules desorbed from clusters of inert elements

Before turning to an analysis of the VUV spectra of the cathodoluminescence of Ar_N, Kr_N, and Xe_N clusters, let us first consider the types of electronic excitations in these clusters. According to Ref. 26, there exist three types of electronic excitations in clusters of inert elements. First are the molecular Rydberg states, for which the radius of the excitation is larger than the radius of the cluster, i.e., the electron is found outside the cluster. Rydberg states exist in a rather wide range of cluster sizes and are manifested in the excitation spectra of VUV fluorescence in the form a broad continuum near the ionization limit. The second type of excitations includes surface and bulk excitons, for which the radius of the excitation is smaller than the radius of the cluster. The energy position of the exciton bands varies weakly with the cluster size and differs only slightly from the position of the corresponding absorption bands of the crystal. The third type of excitations include the so-called "cluster excitons," which exist in a range of sizes for clusters with an icosahedral structure (50 atoms/cluster $< \bar{N} < 500$ atoms/cluster). The radius of these excitons is comparable with the radius of the cluster, and the hole is located in a certain icosahedral shell. It should be noted that the VUV fluorescence yield of surface and bulk excitons of the clusters amounts to several tens of percent, whereas that of "cluster excitons" is less than 1%.[27] Therefore the main contribution to the radiative decay channel of the excitations in Ar_N, Kr_N, and Xe_N clusters comes from the surface and bulk excitons.

Figures 4a–6a show the overall form of the VUV radiation spectra of argon, krypton, and xenon jets in the wavelength region 100–210 nm, recorded for an atomic composition of the jets and in the presence of clusters in them in a range of mean sizes from 30 to 4×10^4 atoms/cluster. Indicated in the upper left-hand corner of the figures are the wavelengths of the maxima of the bands of surface (s) and bulk (t, l) excitons with principal quantum number $n = 1, 1'$ from the excitation spectra of VUV fluorescence for clusters of argon ($\bar{N} = 10^6$ atoms/cluster),[27] krypton ($\bar{N} = 10^4$ atoms/cluster),[26] and xenon ($\bar{N} = 370$ atoms/cluster).[28] Figures 4b–6b, 4c, and 5c show the details of the spectra in the region of the resonance lines of the R atoms (R is an atom of

FIG. 4. Overall form of the VUV radiation spectra of a supersonic jet of argon in the case of an atomic composition of the jet and in the presence of clusters of various mean sizes $\bar{N}$ [atoms/cluster] in the jet (a); spectrum in the region of the resonance lines L_1 and L_2 in the first order of diffraction (b); spectrum in the region of the resonance lines L_1 and L_2 in the second order of diffraction (c).

an inert element) in the first and second orders of diffraction in the presence of clusters in the jet.

It follows from Figs. 4a–6a that the VUV spectra of the argon, krypton, and xenon jets of atomic composition consist of two resonance lines L_1 and L_2, emitted by the excited atoms $R^*(^1P_1)$ and $R^*(^3P_1)$. When clusters appear in the

jets and grow in size, the character of the spectra changes: together with the atomic resonance lines L_1 and L_2 there are band spectra and strong continua. Here the intensity of the lines L_1 and L_2 increases significantly in comparison with their intensity for an atomic composition of the jet. As will be shown below, the observed growth in intensity of lines L_1
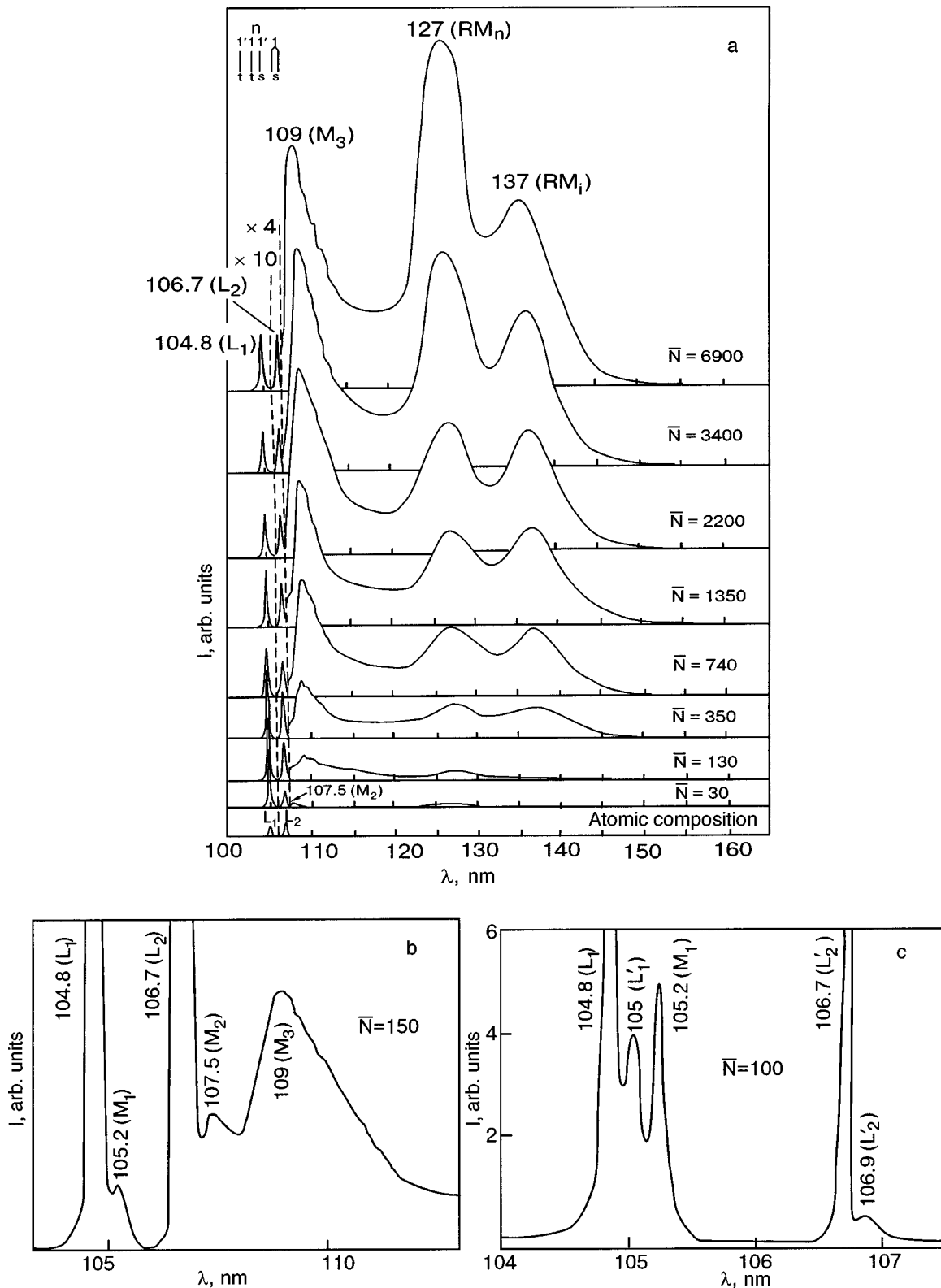
FIG. 5. Overall form of the VUV radiation spectra of a supersonic jet of krypton in the case of an atomic composition of the jet and in the presence of clusters of various mean sizes $\bar{N}$ [atoms/cluster] in the jet (a); spectrum in the region of the resonance lines L_1 and L_2 in the first order of diffraction (b); spectrum in the region of the resonance lines L_1 and L_2 in the second order of diffraction (c).

and L_2 is due to the efficient desorption of excited atoms $R^*(^1P_1)$ and $R^*(^3P_1)$ from the clusters under electron bombardment.

A characteristic feature of the VUV spectra given in Fig. 4a–6a is the strong dependence of the intensity distribution on the mean cluster size. Another feature is the absence of

resonance emission bands of free surface and bulk excitons, the energy position of the maxima of which, as we have said, varies weakly with the cluster size. Instead of the emission bands of free excitons one observes emissions which, according to their characteristic features, can be divided into two groups. The first group of emissions (see Figs. 4–7 and
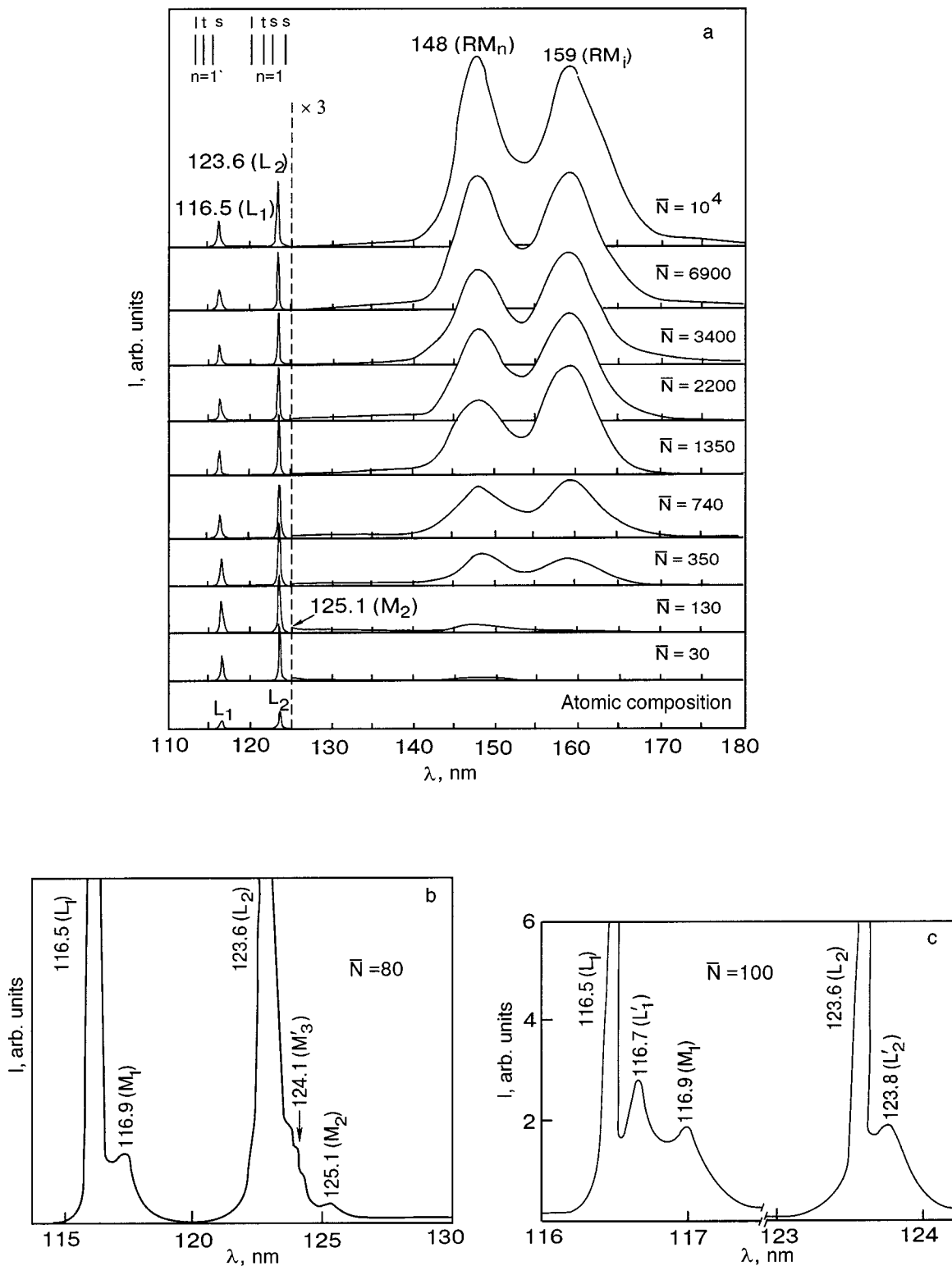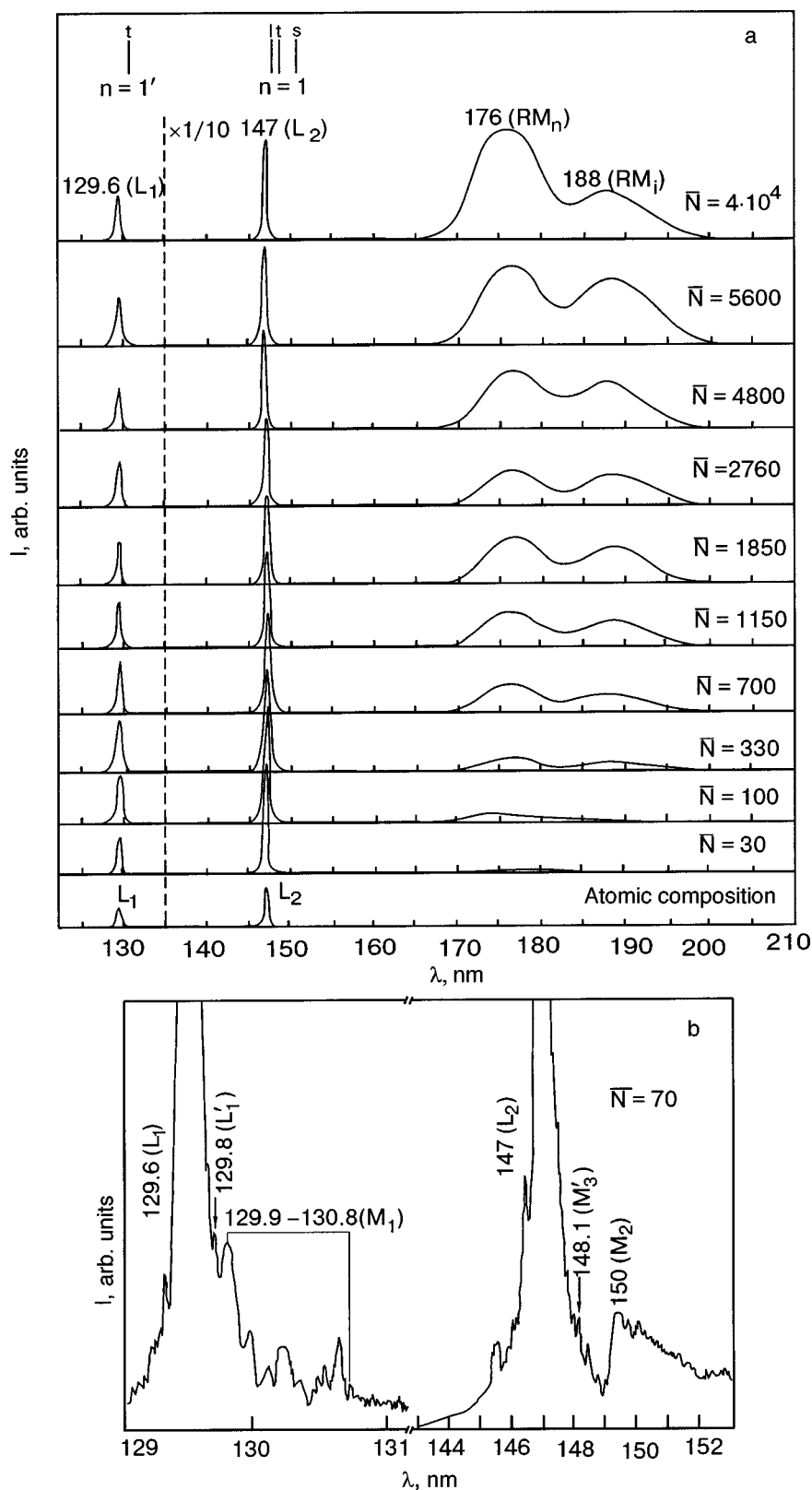
FIG. 6. Overall form of the VUV radiation spectra of a supersonic jet of xenon in the case of an atomic composition of the jet and in the presence of clusters of various mean sizes $\bar{N}$ [atoms/cluster] in the jet (a); spectrum in the region of the resonance lines L_1 and L_2 in the second order of diffraction (b).

Table I) include the strong continua RM_n and RM_i of localized excitons of the excited excimer molecule type R_2^*, which are excimer molecules formed in the neutral and ionic clusters, respectively, in the vibrationally relaxed states $^{1,3}\Sigma_u^+$ (Refs. 8–10, 22, 35, and 36). In addition, in argon clusters localized excitons are also formed in the partially vibrationally relaxed state $B^1\Sigma_u^{+v'}$, radiating the continuum M_3 with a maximum at 109 nm.[37] As is seen in Fig. 8, the

size dependences of the intensity $I/\rho_0(\bar{N})$ of the continua RM_n, RM_i, and M_3 are characterized by sharp growth of the intensity of the radiation with increasing mean cluster size. The second group of emissions (see Figs. 4–7 and Table I) includes the resonance lines L_1 and L_2 of excited atoms $R^*(^{1,3}P_1)$ and the narrow bands L_1' and L_2' adjacent to them, the molecular bands M_1 of the excimer molecules in the vibrationally relaxed state $C^1\Sigma_u^+$, and also the emissions M_2

FIG. 7. Schematic diagram of the potential curves of the ground state and lowest excited states of the R_2 molecule and the electronic transitions forming the VUV spectrum.
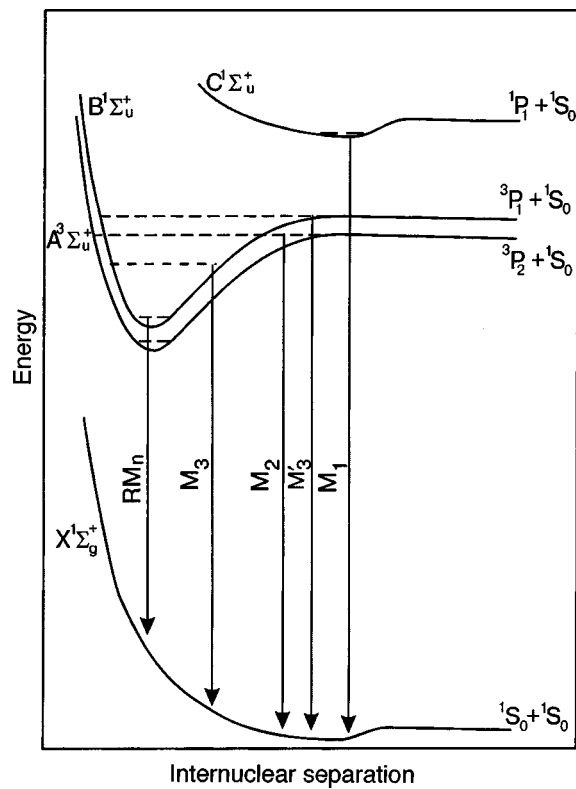
and M_3' of the excimer molecules in the vibrationally excited states $^{1,3}\Sigma_u^{+v}$ and the emission M_3 of excimer molecules in the partially vibrationally relaxed state $B_1\Sigma_u^{+v'}$.

It follows from an analysis of the data in Figs. 8 and 9 that all of the size dependences of the intensity $I/\rho_0(\bar{N})$ of the group-II emissions, unlike the group-I emissions, is char-

acterized by growth of the radiation intensity with decreasing mean cluster size to a pronounced maximum T_2 at mean sizes in the range of 50–100 atoms/cluster. Here the position of the maxima T_2 on the $I/\rho_0(T_0)$ curves of the group-II emissions for different pressures P_0 are described by a relation $P_0 T_0^{-2.5}=$ const (see Fig. 10 for the illustrative case of the emissions from argon clusters), which corresponds to an identical distribution of clusters over sizes and is confirmed by the theory of "corresponding jets." [23] The fact that the maxima T_2 conform to the scaling law $P_0 T_0^{-2.5}=$ const indicates that excited atoms and molecules radiating the group-II emissions are "genetically" related to clusters, i.e., they are "born" in them. On the other hand, it follows from the spectra shown in Figs. 4–6 that the group-II emissions are observed at the wavelengths of transitions of free excited atoms and molecules. From these results we conclude that the excited atoms and molecules emitting the group-II radiating are "born" in clusters and are desorbed from them.

Thus on the basis of the foregoing analysis of the experimental results we can conclude that the group-II emissions are radiated by excited atoms and molecules desorbed from Ar_N, Kr_N, and Xe_N clusters under electron bombardment. In this regard the narrow bands L_1' and L_2', which are shifted to longer wavelengths from the resonance lines (see Figs. 4c, 5c, and 6b), are of definite interest. It should be noted that the bands L_1' and L_2' have the same character of the dependence of the intensity on the cluster size as do the emissions of the excited particles desorbed from clusters (see Fig. 9 for the illustrative case of the L_1' band of argon). Furthermore, the position of the maximum T_2 on the $I/\rho_0(T_0)$ curves of the L_1' and L_2' bands for different pressures P_0 is described by the relation $P_0 T_0^{-2.5}=$ const, which corresponds to an identical distribution of clusters over sizes (see Fig. 10 for the illustrative case of the L_1' band of argon). On the basis of an analysis of the experimental results, the observed bands

TABLE I. Designations of the emissions in the VUV cathodoluminescence spectra of clusters of inert elements.

No.	Designation	Description	Excited state	Binding energy, eV [Refs.]		
				Ar_2^*	Kr_2^*	Xe_2^*
1	L_1	Resonance line of excited atom R* desorbed from a cluster	$^1P_1$			
2	L_2	Resonance line of excited atom R* desorbed from a cluster	$^3P_1$			
3	L_1'	Narrow band radiated by an atom in the $^1P_1$ state, weakly bound to the surface of the cluster				
4	L_2'	Narrow band radiated by an atom in the $^3P_1$ state, weakly bound to the surface of the cluster				
5	M_1	Band of the vibrationally relaxed excimer molecule R_2^* desorbed from a cluster	$C^1\Sigma_u^+$	0.056 [29]	0.058 [30]	0.19 [31]
6	M_2	Band of the vibrationally excited excimer molecule R_2^* desorbed from a cluster	$A^3\Sigma_u^{+v}$			
7	M_3'	Band of the vibrationally excited excimer molecule R_2^* desorbed from a cluster	$B^1\Sigma_u^{+v}$			
8	M_3	Continuum of the partially vibrationally relaxed excimer molecule Ar_2^* localized in a neutral cluster of argon	$B^1\Sigma_u^{+v'}$	$\simeq 0.15$		
9	RM_n	Continuum of the vibrationally relaxed excimer molecule R_2^* localized in a neutral cluster	$A^3\Sigma_u^+(v=0)$ $B^1\Sigma_u^+(v=0)$	0.78 [32] 0.74 [33]	0.69 [34] 0.69 [34]	0.52 [31] 0.55 [31]
10	RM_i	Continuum of the vibrationally relaxed excimer molecule R_2^* localized in an ionic cluster	$A^3\Sigma_u^+(v=0)$ $B^1\Sigma_u^+(v=0)$			

FIG. 8. Dependences of the intensity $I/\rho_0(T_0)$ at $P_0=0.1$ MPa (lower scale) or $I/\rho_0(\bar{N})$ (upper scale) for emissions in the VUV spectrum for clusters of argon (a), krypton (b), and xenon (c); $(-\,-\,-)$ shows an extrapolation of the dependence of the intensity curve $I/\rho_0(T_0)$ of the 109 nm continuum (M_3); the shaded region is the contribution to the intensity of the M_3 continuum due to radiation from desorbed excimer molecules. The feature T_4 reflects the finishing stage of the condensation of gas in the jet.[37]

L_1' and L_2' can be attributed to radiation from excited atoms that upon desorption from the clusters have time to interact with surface atoms of the clusters and be localized near the cluster surface. This point of view as to the origin of the L_1'; and L_2'; bands is also confirmed by calculations of the binding energy of an excited atom Kr* localized near the surface

of solid argon. According to the results of those calculations, the luminescence band of the Kr* atom has a slight shift to longer wavelengths with respect to the resonance line of the free krypton atom.[38]

Finally, we should discuss one more interesting result pertaining to the M_3 continuum of argon, with a maximum
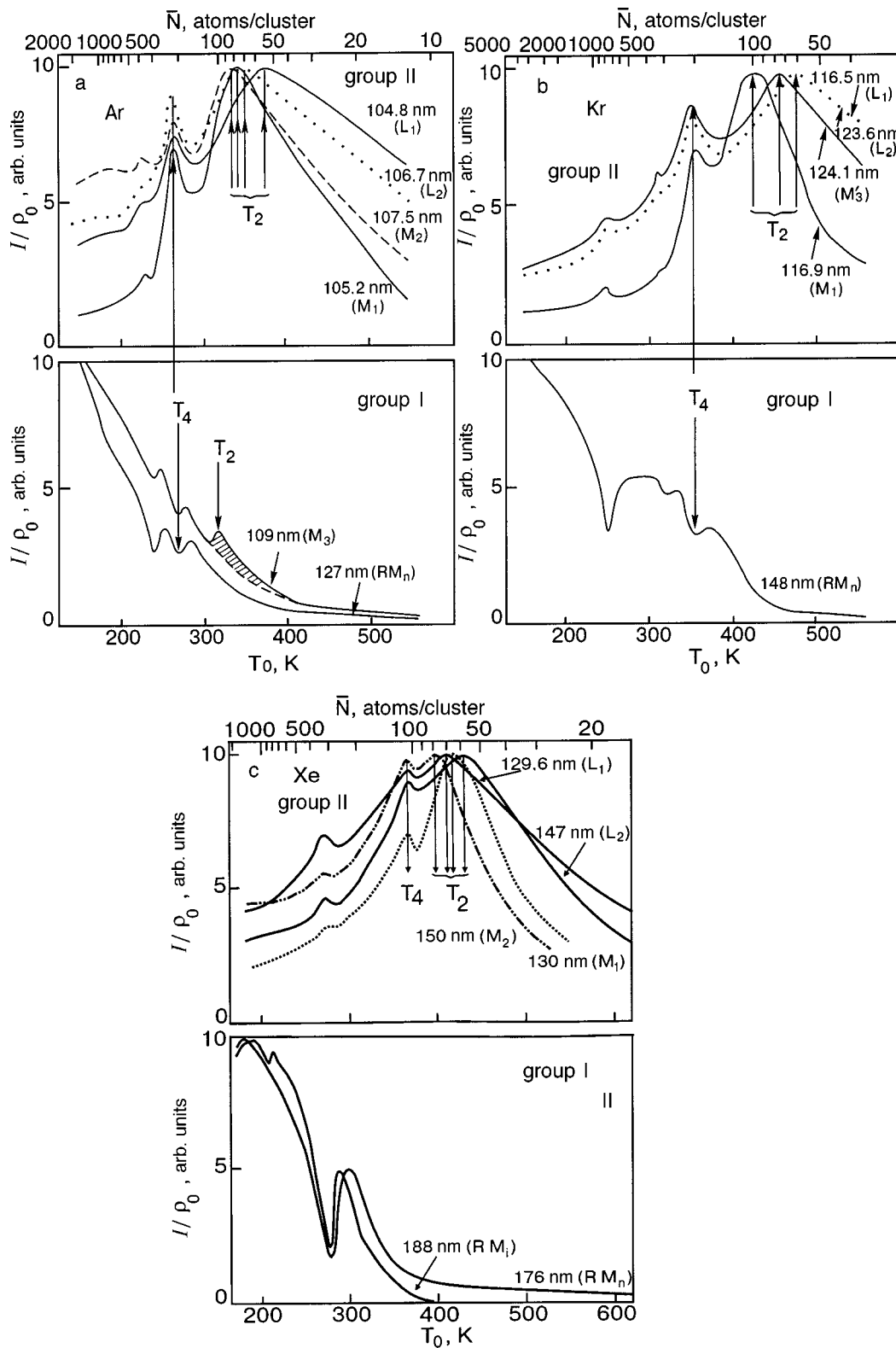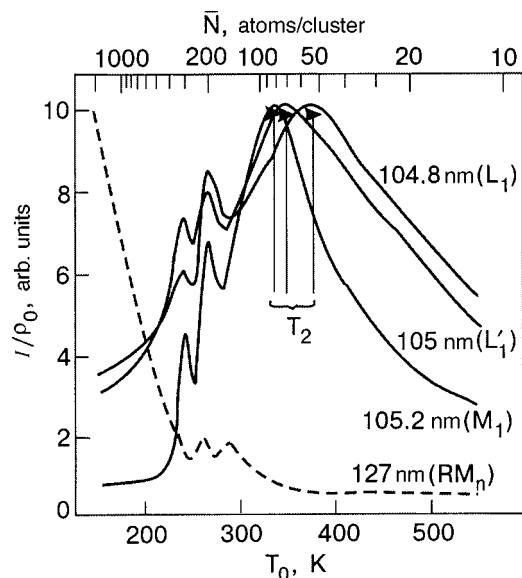
FIG. 9. Dependences of the intensity $I/\rho_0(T_0)$ at $P_0=0.1$ MPa (lower scale) and $I/\rho_0(\bar{N})$ (upper scale) for some emissions in the VUV spectrum of argon clusters.

intensity at 109 nm. As is seen in Fig. 8a, the character of the size dependence of the intensity of the M_3 continuum and its features are similar in their general traits to the size dependence of the intensity of RM_n continuum for argon clusters over a wide range of sizes. However, unlike the RM_n continuum, the $I/\rho_0(\bar{N})$ curve of the M_3 continuum has a maximum T_2 in the region of mean sizes $\bar{N}\cong100$ atoms/cluster, which is characteristic for excited particles desorbed from clusters (see Fig. 8a and 10). On this basis we can conclude that a certain contribution to the intensity of the M_3 continuum in the size region $\bar{N}\cong100$ atoms/cluster comes from the radiative decay of excimer molecules in the partially vibrationally relaxed state $B^1\Sigma_u^{+v'}$ desorbed from the argon clusters.

The identical features in the size dependences of the intensities of all the emissions from excited particles desorbed
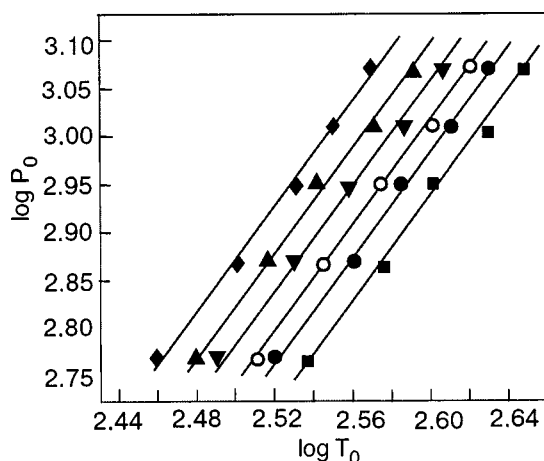

FIG. 10. Position of the maximum T_2 for the group-II emissions and of the continuum with maximum at 109 nm (M_3) for argon clusters on the T_0, P_0 plane: 104.8 nm (L_1) (■); 106.7 nm (L_2) (●); 105 nm (L_1') (○); 105.2 nm (M_1) (▼); 107.5 nm (M_2) (▲); 109 nm (M_3) (◆). The straight lines are described by the law $P_0T_0^{-2.5}=$ const.

from clusters is evidence that their radiators have the same mechanism of formation. In this regard we should note the following. In the electron bombardment of Ar_N, Kr_N, and Xe_N clusters the VUV radiation spectra of excited particles desorbed from the clusters have important distinguishing regularities and features in comparison with the corresponding VUV spectra of excited particles desorbed from solidified inert elements and also from Ar_N, Kr_N, and Xe_N clusters under excitation by photons. These regularities include:

1) sharp growth of the intensities of all emissions in the spectrum with decreasing mean cluster size, starting in the size region $\Delta\bar{N}\cong150-200$ atoms/cluster;

2) each emission in the spectrum reaches an intensity maximum T_2 in collisions of electrons with clusters of the same definite size in the range of 50–100 atoms/cluster.

A feature of the VUV spectra of particles desorbed from Ar_N, Kr_N, and Xe_N clusters is the presence of the following nontrivial emissions in them:

1) resonance lines L_1 and L_2 of excited atoms $R^*(^{1,3}P_1)$;

2) narrow bands L_1' and L_2' of excited atoms $R^*(^{1,3}P_1)$ localized near the cluster surface;

3) a molecular band M_1 of excimer molecules with a small binding energy in the state $C^1\Sigma_u^+(^1P_1+^1S_0)$.

All of the emissions listed in 1–3 are absent in the VUV photoluminescence spectra of argon and krypton clusters, which have been studied in a wide range of sizes 2 atoms/cluster $<\bar{N}<10^4$ atoms/cluster predominantly at energies of excitation of surface and bulk excitons ($n=1,1'$) and also at the excitation energy 28.17 eV (above the ionization limit) of Ar_{30} clusters.[8,9,36] Only in the VUV photoluminescence spectra of Xe_{10} clusters is a single resonance line of desorbed $Xe^*(^3P_1)$ atoms observed.[26]

For crystals of argon, krypton, and xenon excited by photons, electrons, and ions,[1,3,8,39] an analogous situation is seen. All of the above-listed emissions are absent in their VUV spectra except for the lines of the desorbed excited atoms $Ar^*(^1P_1, ^3P_1)$. It is well known that the desorption of atoms occurs from the surface of solid argon and is interpreted in terms of a mechanism of dissociative recombination of an electron with a self-trapped hole Ar_2^+ localized near the surface[3,7] and in terms of a mechanism of "ejection from a cavity,"[1] the essence of which is as follows. If solid argon is excited to an excitonic state, in the process of self-trapping of the excitons a deformation of the lattice occurs, with the formation of a cavity around the excitation. The formation of the cavity is a consequence of the negative electron affinity of solid argon.[40,41] If the cavity is formed near the surface, then the repulsive forces of interaction of the localized excited atom with the atoms surrounding it leads to ejection of the excited atom from the surface of the crystal. In this model the desorption of excited particles from the surface of solid krypton and xenon is not observed because of the positive electron affinity of those crystals.[40,41]

Unlike the case of solid argon, the desorption of $Ar^*(^1P_1, ^3P_1)$ from Ar_N clusters excited in the bulk and surface exciton bands ($n=1,1'$) is strongly suppressed because of the higher temperature of the clusters ($T\sim35$ K) in comparison with the temperature of solid argon.[8] On the

other hand, the desorption of excited atoms $Ar^*(^1P_1, ^3P_1)$ from ionized argon clusters in the process of dissociative recombination of a self-trapped hole Ar_2^+ with a secondary electron is strongly hindered in clusters because of the high probability of escape of secondary electrons to outside the cluster.

New mechanism of desorption of excited atoms and molecules from clusters of inert elements under electron bombardment

The experimental results discussed above permit one to conclude that a new mechanism exists for the desorption of excited particles from clusters of argon, krypton, and xenon excited by electrons; this mechanism is realized for clusters in a certain interval of mean sizes but not in solids of inert elements. As will be shown below, this mechanism of desorption involves electronic states whose excitation by photons is forbidden by selection rules but which can be excited by electrons. Among such states are highly excited excitonic states correlated with the atomic states $np^5(n+1)p$ ($n=3$, 4, and 5 for Ar, Kr, and Xe, respectively). It should be noted in this regard that the radius of excitation of the $4p$ electron of argon, which changes from 3.81 to 3.44 Å on going from the argon atom to solid argon,[42] is significantly smaller than the cluster radius 7.7–9.7 Å for clusters in the size range $\bar{N} \cong 50$–100 atoms/cluster, which corresponds to the maximum intensity of the radiation from the desorbed particles under consideration. The same conditions hold for clusters of krypton and xenon.

The essence of the new mechanism of desorption of excited atoms and molecules from Ar_N, Kr_N, and Xe_N clusters in a certain range of sizes is as follows. Upon the excitation of clusters by electrons with energy 1 keV, in the region of sizes where the second and third icosahedral shells are building (13 atoms/cluster $< \bar{N} <$ 147 atoms/cluster), in addition to the molecular Rydberg states, "cluster excitons," and surface ($n=1,1'$ and $2,2'$) and bulk ($n=1,1'$) s excitons[3] (Refs. 26, 27, and 43), the higher-energy p excitons can also arise in the clusters.[4] These excitons are found in an energy region close to the atomic states $Ar(3p^54p)$, $Kr(4p^55p)$, and $Xe(5p^56p)$, which is confirmed by the observations of a broad band in the energy regions 13–13.8 eV for Ar_N and 11.1–12.3 eV for Kr_N in the electron energy loss spectra of argon and krypton clusters with $\bar{N} \cong 100$ atoms/cluster.[45] On the other hand, for Ar_N, Kr_N, and Xe_N clusters in the interval of cluster sizes considered here the characteristic channel in which the energy of free excitons relaxes to the lowest exciton bands in the case of solids and large clusters is strongly suppressed. This is due to the fact that the energy interval between adjacent free-exciton levels in the band, Δ, obtained in the size quantization of the energy inside the exciton band, exceeds the phonon Debye energy $\hbar\omega_D$ in the investigated size interval.[46] As a result of this the one-phonon relaxation process typical for large clusters and solids is replaced by a slower multiphonon process, and the usual relaxation path for free excitons is blocked. For that reason a new possibility arises—the self-trapping of excitons from the higher-energy p band ($n=1$), with the formation of

centers of the highly excited excimer molecule type: R_2^{**}. Thus as a result of the self-trapping of excitons in Ar_N, Kr_N, and Xe_N clusters in the investigated size interval ($\Delta\bar{N} < 150$–200 atoms/cluster), besides molecular centers of the excimer molecule type in the lowest electronic states, R_2^*, molecular centers of the type R_2^{**}, excimer molecules in highly excited states, can form, with a dissociation limit $R^{**}(np^5(n+1)p) + R(^1S_0)$ ($n=3$, 4, and 5, respectively, for Ar, Kr, and Xe). The subsequent transitions of R_2^{**} to the repulsive terms of the lower states, R_2^*, with the dissociation limits $^1P_1 + ^1S_0$, $^3P_0 + ^1S_0$, $^3P_1 + ^1S_0$, and $^3P_2 + ^1S_0$, lead to the appearance of atoms in the excited states $^1P_1$ and $^3P_{0,1,2}$ and ground state $^1S_0$ with high kinetic energies, sufficient for their desorption from the clusters. Besides the excited atoms $R^*(^1P_1, ^3P_{0,1,2})$, excimer molecules in various states can also be ejected from the clusters: in the excited weakly bound vibrationally relaxed state $C^1\Sigma_u^+(^1P_1 + ^1S_0)$, in the vibrationally excited states $A^3\Sigma_u^{+v}(^3P_2 + ^1S_0)$ and $B^1\Sigma_u^{+v}(^3P_1 + ^1S_0)$, and in the partial vibrationally relaxed state $B^1\Sigma_u^{+v'}(^3P_1 + ^1S_0)$.

The excimer molecules in these states radiate the respective molecular emissions M_1, M_2, M_3', and in part M_3 (see Fig. 4–6). These molecules arise as a result of collisions of excited atoms formed in the dissociation of R_2^{**} and found in one of the states $^1P_1$, $^3P_1$, or $^3P_2$ with cluster atoms in the ground state. The important role of highly excited molecular states with the dissociation limit $R^{**}(np^5(n+1)p) + R(^1S_0)$ in the mechanism of desorption of metastable atoms from Ar_{100} clusters excited by electrons was reported in Ref. 47.

The proposed mechanism of desorption of excited particles from clusters of inert elements, which will be called "nonradiative excimeric dissociation" below, is confirmed by the following:

1) the results of an analysis of the scheme of the potential energy curves of the excited states for the example of the Ar_2 molecule (see Fig. 11);

2) the detection of the metastable atoms $Ar^*(^3P_{0,2})$ by the time-of-flight technique in the bombardment of Ar_{100} clusters by a monoenergetic electron beam with low electron energies.[47]

Figure 11 shows the scheme of potential energy curves from Ref. 48 for several excited states of the Ar_2 molecule, with dissociation limits $Ar^*(3p^5 4s) + Ar(3p^6 {}^1S_0)$ and $Ar^{**}(3p^5 4p) + Ar(3p^6 {}^1S_0)$. As we have said, in clusters of argon (and analogously for krypton and xenon, too) in the process of self-trapping of a high-energy p exciton a localized molecule Ar_2^{**}, with a high binding energy of approximately 1–1.26 eV,[49] is formed in one of the highly excited states with the dissociation limit $Ar^{**}(3p^5 4p) + Ar(3p^6 {}^1S_0)$, which are found in the energy region 12.91–13.48 eV.

The most probable relaxation process for highly excited molecular states of argon is nonradiative dissociation. Indeed, in examining Fig. 11 one notices the large number of intersections between the potential curves of the stable molecular Rydberg states ($A\pi_u 4p$, $A\pi_g 4p$, $A\sigma_g 4p$, $A\sigma_u 4p$), with the dissociation limit $Ar^{**}(3p^5 4p) + Ar(3p^6 {}^1S_0)$, and the repulsive potential curves of the lower molecular states ($A\sigma_u 4s$, $B\sigma_g 4s$, $B\sigma_u 4s$), with the dissociation limit
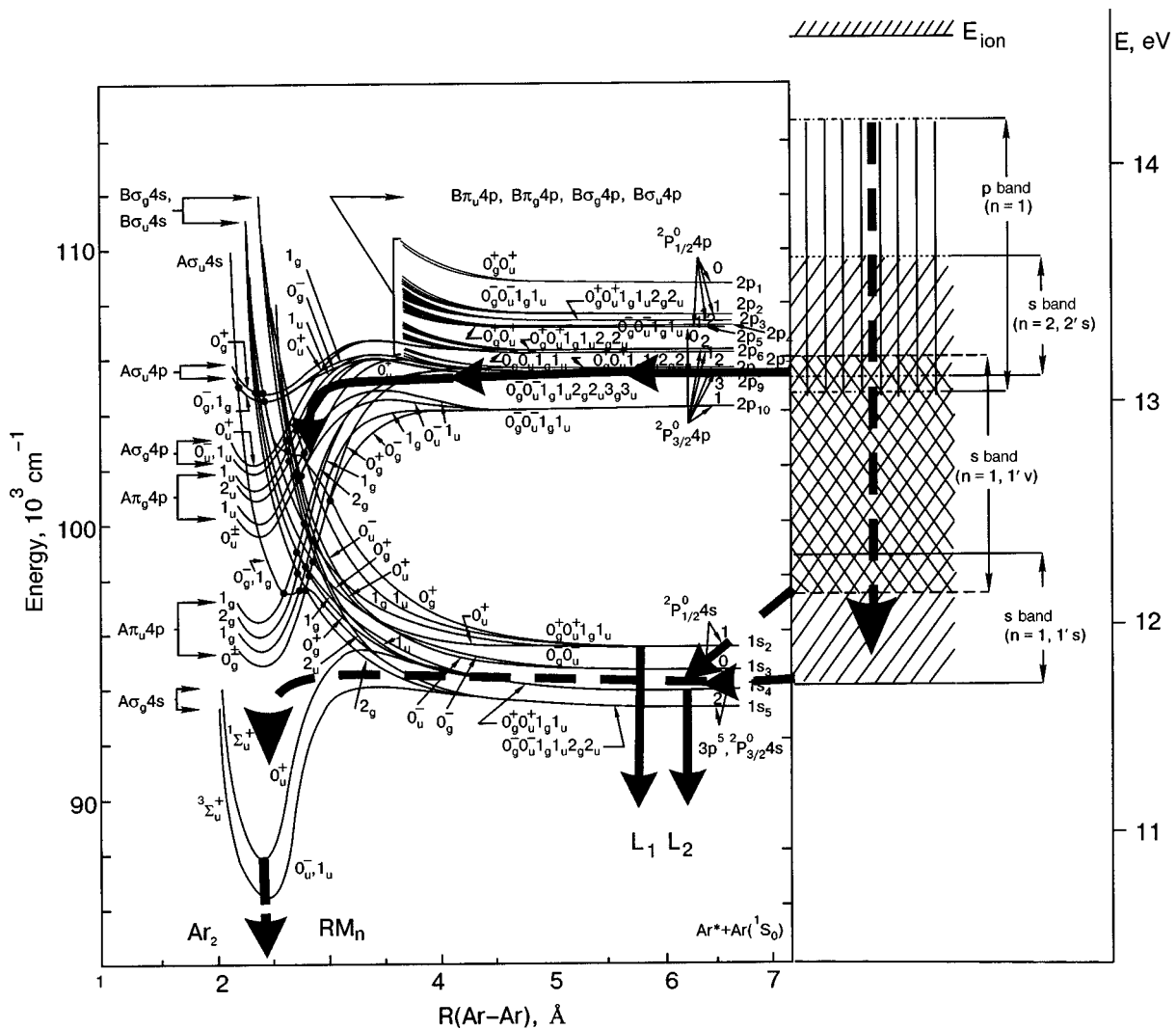
FIG. 11. Energy diagram for desorption by the "nonradiative excimeric dissociation" mechanism. Left: Potential curves of some excited states of the argon molecule with the dissociation limits $Ar^*(3p^5\,4s)+Ar(3p^6\,{}^1S_0)$, and $Ar^{**}(3p^5\,4p)+Ar(3p^6\,{}^1S_0)$.[48] Right: Schematic illustration of the energy regions of the bands of surface (s) and bulk (v) s and p excitons of Ar_{100} clusters.[27,42] The relaxation paths of the excitons: in a small cluster $(\rightarrow)$, in a large cluster (or crystal) $(-\,-\,\rightarrow)$. The bands of bulk excitons with $n=2,3,4$ for large clusters and crystals are not shown in the diagram.

$Ar^*(3p^5\,4s)+Ar(3p^6\,{}^1S_0)$. Each intersection for states with the same symmetry is indicated by a dot. When those points are reached in the process of relaxation of an excimer molecule Ar_2^{**} over vibrational levels there can occur transitions from the potential curve of the highly excited bound state to the potential curve of the less-excited repulsive states. At such a transition the highly excited excimer molecule Ar_2^{**} dissociates into atoms $Ar^*(3p^5\,4s)$ and $Ar(3p^6\,{}^1S_0)$, which fly apart with a high kinetic energy. If the energies of the transitions at the points of intersection of the potential curves in Fig. 11 are taken into consideration along with the fact that the repulsive terms Ar_2^*, with the dissociation limits ${}^1P_1+{}^1S_0$, ${}^3P_0+{}^1S_0$, ${}^3P_1+{}^1S_0$, and ${}^3P_2+{}^1S_0$, tend toward asymptotic limits at energies of 11.83, 11.71, 11.62, and 11.55 eV, respectively, then the estimated kinetic energies shared between the two atoms in the dissociation of Ar_2^{**} varies approximately from 0.2 to 0.74 eV. Since the maximum binding energy of an atom in Ar_N clusters is ~0.05 eV,[50] i.e., considerably less than the estimated values of the kinetic energy of the particles formed in the dissociation of Ar_2^{**}, then real conditions for the de-

sorption of the excited atoms $Ar^*({}^1P_1,\,{}^3P_{0,1,2})$ and ground-state atoms $Ar({}^1S_0)$ from the clusters are created.

The desorption channel under discussion was partially traced for argon clusters by a time-of-flight technique in Ref. 47. The authors of that paper obtained the excitation functions of the metastable atoms $Ar^*({}^3P_{0,2})$ ejected from Ar_{100} clusters and their kinetic energy distribution functions. The clusters were bombarded by an electron beam with an electron energy from 5 to 100 eV and monoenergeticity around 1 eV. It should be noted that the experiments were done in argon cluster beams with a mean size $\bar{N}=100$ atoms/cluster, which precisely fits the range of sizes where the radiation from desorbed excited particles in our spectroscopic experiment had its maximum intensity. At bombarding electron energies of 13.6 ± 0.5 eV, corresponding to the excitation energy of the high-energy p excitons, a high yield of metastable argon atoms with kinetic energies from 0.2 to 1 eV, comparable to the estimated values given for them above, was observed. These results are a direct confirmation of the existence of desorption of excited meta-

stable atoms Ar*($^3P_{0,2}$) by the "nonradiative excimeric dissociation" mechanism in the electron bombardment of Ar_{100} clusters.

The following conclusions can be drawn from what we have said. The desorption of excited atoms and molecules from Ar_N, Kr_N, and Xe_N clusters with a maximum yield of particles in the size interval $\Delta \bar{N} = 50$–100 atoms/cluster is brought about by the "nonradiative excimeric dissociation" mechanism. The main forms of desorption of excited particles by this mechanism according to our observations here by the method of VUV emission spectroscopy are:

1) desorption of excited atoms R*($^1P_1$, $^3P_1$). Here part of the atoms escape into the gaseous "matrix" of the jet and radiate the resonance lines L_1 and L_2 (see Figs. 4–6). Another part of the atoms is desorbed from clusters and is localized near their surface, radiating the bands L_1' and L_2' with a "red" shift of 0.2 nm relative to the resonance lines (see Figs. 4c, 5c, and 6b);

2) desorption of excimer molecules in the weakly bound state $C^1\Sigma_u^+(^1P_1 + {}^1S_0)$ and in the vibrationally excited states $A^3\Sigma_u^{+v}(^3P_2 + {}^1S_0)$ and $B^1\Sigma_u^{+v}(^3P_1 + {}^1S_0)$, and in the partially vibrationally relaxed state $B^1\Sigma_u^{+v'}(^3P_1 + {}^1S_0)$. As we have said, excimer molecules in these states are formed in collisions of excited "hot" atoms R*($^1P_1$, $^3P_{1,2}$) with ground-state atoms of the clusters. The excimer molecules desorbed from clusters in the states indicated above radiate the experimentally observed emissions M_1, M_2, M_3', and in part M_3 (see Figs. 4–8).

An analysis of the size dependences of the intensities of the emissions in the VUV spectrum of the desorbed particles, presented in Figs. 8 and 9, shows that the maximum yield of excited atoms and molecules from the clusters exists in a certain size region $\bar{N} = 50$–100 atoms/cluster. Here an important regularity in the desorption of excited particles is manifested, namely, that the maximum yield of each form of excited atoms and molecules occurs for clusters of the same definite (for the given form of particles) mean size within the size interval $\bar{N} = 50$–100 atoms/cluster.

The observed regularity of the desorption of excited particles is governed by two size effects. The first effect is connected with the features of the size quantization of the energy inside the exciton bands in the region $\bar{N} < 150$–200 atoms/cluster, which lead to a multiphonon process of exciton energy relaxation in the clusters.[46] Because of this the self-trapping of excitons in the clusters can occur from the high-energy p band ($n=1$) with the formation in them of centers of the highly excited excimer molecule type, R_2^{**}.

In addition, the subsequent relaxation of R_2^{**} over vibrational levels to the points of intersection of the potential curves of the stable states with the repulsive terms of the lower molecular states also depends on the size of the clusters, in particular, on the number of atoms interacting with the excimer, the interaction energy, and the spectrum of vibrational frequencies of the atoms in the cluster.[51] Theoretical studies show[52] that the relaxation of the excimers Ar_2^* over vibrational levels of the potential curves of the lowest electronic states of $^{1,3}\Sigma_u^+$ with binding energy ~ 0.75 eV (see Fig. 11) in clusters with $\bar{N} = 55$ atoms/cluster ends in a redis-

tribution of the vibrational energy within the clusters without their fragmentation. Considering that the binding energy of the highly excited excimers Ar_2^{**} is 1.3–1.6 times larger than that of Ar_2^* in the states $^{1,3}\Sigma_u^+$ (Ref. 49), the relaxation of Ar_2^{**} over vibrational levels should go to completion in clusters of somewhat larger sizes within the size range considered.

Thus the first size effect due to the size quantization of the exciton energy governs the initial stage of the desorption process—the formation of highly excited excimers R_2^{**} with a dissociation limit $R^{**}(np^5(n+1)p) + R(^1S_0)$ embedded in the Ar_N, Kr_N, and Xe_N clusters. The second size effect, which is due to the size dependence of the rate of relaxation of the vibrational energy of R_2^{**}, leads, in the final stage of the desorption process, to the nonradiative dissociation of the excimers R_2^{**} into atoms R*($^1P_1$, $^3P_{0,1,2}$) and $R(^1S_0)$ with high kinetic energies sufficient for their desorption from the clusters.

Consequently, the formation of localized highly excited excimer molecules R_2^{**} in the process of self-trapping of p excitons and their subsequent dissociation are the main stages of the new mechanism of desorption of excited atoms R*($^1P_1$, $^3P_{0,1,2}$), excimer molecules $R_2^*(C^1\Sigma_u^+)$, and vibrationally excited molecules $R_2^*(^{1,3}\Sigma_u^{+v})$ from electron-excited Ar_N, Kr_N, and Xe_N clusters in the size range $\Delta \bar{N} \cong 50$–100 atoms/cluster. The "nonradiative excimeric dissociation" mechanism explains not only the fact that desorption occurs but also its basic regularities.

However, an examination of the size dependences of the intensity of the emissions in the VUV spectra of desorbed particles (Figs. 8 and 9) reveals not only regularities common to all the emissions but also individual features of each emission. These features are indicative of possible additional channels for desorption of excited particles. Among them may be desorption channels involving Rydberg states of the clusters, for which the radius of the excitation is larger than the radius of the cluster. In the excitation of Rydberg states the holes R^+ found in the clusters are self-trapped, as a result of which stable diatomic molecules in highly excited Rydberg states appear in the clusters. In that case it is expected that radiative transitions between highly excited molecular Rydberg states are strongly suppressed by the efficient nonradiative relaxation processes. Therefore the possible desorption channels can at once be linked to the nonradiative decay of stable highly excited molecular Rydberg states as a result of the intersection of their potential curves with the repulsive terms of the lower molecular states. Among such channels one can include the desorption of atoms in highly excited states with their subsequent radiative transitions: first to the lowest excited atomic states (including $^1P_1$ and $^3P_1$) and then to the ground state $^1S_0$, with the radiation of the resonance lines L_1 and L_2. This point of view is supported by the fact that the curves of the size dependences of $I/\rho_0(\bar{N})$ of the resonance lines L_1 and L_2 of the desorbed excited atoms R*($^1P_1$, $^3P_1$), shown in Fig. 8, go above the corresponding curves for the molecular emissions in the regions of smaller and larger cluster sizes from the maximum T_2. Although the desorption channels considered can exist over a rather wide range of sizes, they are not the governing channels for clusters in the size range $\Delta \bar{N} \cong 50$–100 atoms/cluster, since they

cannot explain the observed size effect in the desorption and its basic regularities.

The other channels of desorption of excited particles can be linked to the "ejection from a cavity" mechanism typical for solids of inert elements.[1,38,40] As we know, the desorption of vibrationally excited molecules Ar_2^* in the $A^3\Sigma_u^{+v}$ state by the "ejection from a cavity" mechanism has been observed in the photoexcitation of argon clusters over a wide range of sizes in the surface and bulk exciton bands.[8] For krypton and xenon clusters, however, unlike Ar_N, the desorption of vibrationally excited Kr_2^* and Xe_2^* molecules in the $A^3\Sigma_u^{+v}$ state is observed in very narrow size intervals: $\Delta\bar{N}$ <50 atoms/cluster for krypton[9] and $\Delta\bar{N}\leqslant10$ atoms/cluster for xenon.[26] This is due to the fact that, according to the calculations done in Ref. 53, Kr_N and Xe_N clusters have a negative work function only in a very restricted size region: $\Delta\bar{N}<100$ atoms/cluster and $\Delta\bar{N}<12$ atoms/cluster, respectively. It follows from what we have said that the vibrationally excited molecules R_2^* desorbed from clusters by the "ejection from a cavity" mechanism can give a contribution to the VUV cathodoluminescence spectrum of Ar_N clusters in a wide range of sizes, while for Kr_N and Xe_N clusters this is possible only in the restricted size intervals $\Delta\bar{N}<50$ and $\Delta\bar{N}<10$ atoms/cluster, respectively.

As we have shown, Ar_2^* molecules in the state $A^3\Sigma_u^{+v}$ radiating a continuum with a maximum at 107.5 nm (M_2; see Fig. 4b) are desorbed from Ar_N clusters in the size interval $\Delta\bar{N}\cong50-100$ atoms/clsuter mainly by the "nonradiative excimeric dissociation" mechanism. It is this mechanism that determines the main features in the size dependence $I/\rho_0(\bar{N})$ of the continuum M_2 in the indicated range of sizes. However, based on the foregoing analysis of the other desorption mechanisms, there is a possibility that the desorption of Ar_2^* molecules in the $A^3\Sigma_u^{+v}$ state by the "ejection from a cavity" mechanism makes a significant contribution in the region of large sizes of the Ar_N clusters. This is because in clusters in the size region $\Delta\bar{N}>150-200$ atoms/cluster the single-phonon process of exciton energy relaxation, which leads to the "discharge" of energy to the lowest exciton bands (see Fig. 11), begins to prevail. As a result of this, with increasing cluster size the probability of self-trapping of excitons from the p band with the formation of localized highly excited molecules R_2^{**} decreases, and, hence, so does the desorption of excited particles from clusters by the "nonradiative excimeric dissociation" mechanism. On the other hand, with increasing cluster size the probability of self-trapping of s excitons, accompanied by the desorption of $Ar_2^*(A^3\Sigma_u^{+v})$ molecules by the "ejection from a cavity" mechanism, increases on account of the "discharge" of energy from the high-energy to the lowest exciton bands. The possible existence of desorption of Ar_2^* molecules in the vibrationally excited state $A^3\Sigma_u^{+v}$ from cluster of large sizes is evidenced by the somewhat different trend of the size dependences $I/\rho_0(\bar{N})$ of the continuum with maximum at 107.5 nm (M_2) and the nonallowed system of bands of the transition $C^1\Sigma_u^+\to X^1\Sigma_g^+$ with a maximum at 105.2 nm (M_1) in the region of large sizes $\bar{N}$. Indeed, as was shown in Fig. 8a, the intensity of the emission M_1 for the argon clusters de-

creases sharply with increasing $\bar{N}$. In contrast, the intensity of the continuum with a maximum at 107.5 nm (M_2) falls off insignificantly with increasing $\bar{N}$, remaining larger in magnitude than the intensity of the emission M_1. Here it should be stressed that the emission M_1, which is due to desorption of excited molecules R_2^* in the state $C^1\Sigma_u^+(^1P_1+^1S_0)$, is a characteristic feature of the "nonradiative excimeric dissociation" mechanism, which takes place in a certain size region $\Delta\bar{N}\cong50-100$ atoms/cluster in the bombardment of clusters of inert elements by electrons. It is for this reason that the M_1 band is absent in the VUV photoluminescence spectra of Ar_N, Kr_N, and Xe_N clusters[8,9,26] and in the VUV luminescence spectra of solids of inert elements under excitation by photons, electrons, or ions.[1–7,38–40]

Let us conclude with a discussion of the origin of the continuum with maximum at 109 nm (M_3; see Fig. 4a,b). As we have said, the continuum with maximum at 109 nm is radiated by Ar_2^* molecular centers formed in Ar_N clusters in a partially vibrationally relaxed state $B^1\Sigma_u^{+v'}$ in the process of self-trapping of s excitons.[37] The formation of such centers is due to the presence of a high repulsive barrier on the potential curve of the $B^1\Sigma_u^+(^3P_1+^1S_0)$ molecular state of argon,[29] which hinders the relaxation of the excimer $Ar_2^*(B^1\Sigma_u^+)$ over vibrational levels to an equilibrium state in condensed argon.[54,55] However, in addition to the features typical for molecular luminescence centers, the size dependence of the intensity $I/\rho_0(\bar{N})$ of this continuum (see Fig. 8a) has a maximum T_2 in the size region $\bar{N}\cong100$ atoms/cluster, as is characteristic for excited particles desorbed from clusters by the "nonradiative excimeric dissociation" mechanism. We therefore attribute the presence of the maximum T_2 in the size dependence $I/\rho_0(\bar{N})$ of the 109 nm continuum (M_3) to radiation from desorbed excimer molecules in the same state but formed in collisions of "hot" $Ar^*(^3P_1)$ atoms with cluster atoms in the ground state. Furthermore, it is not ruled out that the radiation of the M_3 continuum at wavelength $\lambda=109$ nm contains a certain contribution due to the radiation from desorbed excimer molecules in the state $A^3\Sigma_u^{+v}(^3P_2+^1S_0)$. This is due to the fact that the M_3 continuum, with maximum at 109 nm (the transition $B^1\Sigma_u^{+v'}\to X^1\Sigma_g^+$), overlaps with the M_2 continuum, with maximum at 107.5 nm (the transition $A^3\Sigma_u^{+v}\to X^1\Sigma_g^+$), in the region of the continuous spectrum 107.4–113 nm (see Fig. 4b).

CONCLUSION

Studies of the features of the structure of the VUV cathodoluminescence spectra of Ar_N, Kr_N, and Xe_N clusters in the region of the resonance transitions $^1P_1\to^1S_0$ and $^3P_1\to^1S_0$ and also of the regularities in the size dependences of the intensity of the emissions in the VUV spectra have permitted the experimental detection of new channels for the desorption of excited particles from clusters with maximum yield in a certain size region $\Delta\bar{N}\cong50-100$ atoms/cluster and to establish their desorption mechanism. The new desorption channels were detected thanks to a unique methodological opportunity, the VUV emission of excited atoms and molecules desorbed from clusters under electron bombardment

can be distinguished from the VUV emission of excited particles of the gas phase in the jet with the aid of the law of "corresponding jets." It was established that this law holds only for the emissions from the desorbed particles under study, i.e., the maximum of the curves of the intensity of the emissions of desorbed particles as a function of the gas temperature T_0 at the nozzle entrance for different pressures P_0 is reached on the curve $P_0 T_0^{-2.5} = \mathrm{const}$, which corresponds to an identical distribution of clusters over sizes.

Studies done by the method of VUV emission spectroscopy have revealed channels of desorption of the following particles: excited atoms $R^*(^1P_1, ^3P_1)$ and excimer molecules R_2^* in the weakly bound state $C^1\Sigma_u^+ (^1P_1 + ^1S_0)$ and also in the vibrationally excited states $A^3\Sigma_u^{+v} (^3P_2 + ^1S_0)$ and $B^1\Sigma_u^{+v} (^3P_1 + ^1S_0)$ and the partially vibrationally relaxed state $B^1\Sigma_u^{+v'} (^3P_1 + ^1S_0)$. We have shown that part of the excited atoms $R^*(^1P_1, ^3P_1)$ escape into the gaseous "matrix" of the jet and radiate resonance lines in the free state. Another part of the $R^*(^1P_1, ^3P_1)$ atoms is desorbed from the clusters and localized near their surface, radiating bands with a "red" shift of 0.2 nm relative to the resonance lines. We have established that the maximum yield of excited atoms and molecules from Ar_N, Kr_N, and Xe_N clusters fits into a region of mean sizes $\Delta\bar{N} \cong 50 - 100$ atoms/cluster, and the maximum yield of each form of excited atoms and molecules takes place for clusters of the same definite (for the given type of particles) mean size in the range 50–100 atoms/cluster.

The observed regularities of the process of desorption of excited atoms and molecules from Ar_N, Kr_N, and Xe_N in their bombardment by electrons have revealed a new desorption mechanism: "nonradiative excimeric dissociation." According to this mechanism, the excited atoms $R^*(^1P_1, ^3P_1)$ are desorbed from clusters as a result of the nonradiative dissociation of localized highly excited excimer molecules R_2^{**} with the dissociation limit $R^{**}(np^5(n+1)p) + R(^1S_0)$. These molecules are formed in clusters in the process of self-trapping of excitons from the high-energy p band. The excimer molecules R_2^* desorbed from the clusters arise in the collision of "hot" excited atoms $R^*(^1P_1, ^3P_{1,2})$ with cluster atoms in the ground state.

It follows from the studies reported here that the formation of highly excited molecules R_2^{**} in the process of self-trapping of excitons from the high-energy p band is a consequence of the size quantization of the energy inside the exciton bands, which leads to blocking of the one-phonon process of energy relaxation for excitons in Ar_N, Kr_N, and Xe_N clusters in the region of mean sizes $\Delta\bar{N} < 150 - 200$ atoms/cluster.

On the other hand, the nonradiative dissociation of highly excited excimer molecules R_2^{**} into atoms $R^*(^1P_1, ^3P_{1,2})$ and $R(^1S_0)$ with high kinetic energies is governed by another size effect, namely: the size dependence of the relaxation rate of the R_2^{**} molecules over vibrational levels to points of intersection of the potential curves of the highly excited stable states with the less-excited repulsive states of the same symmetry.

Thus the appearance of new channels of desorption of excited atoms and molecules from Ar_N, Kr_N, and Xe_N clusters under electron bombardment, with a maximum

yield of particles in the size interval $\Delta\bar{N} \cong 50 - 100$ atoms/cluster, is due to features of the physical properties of clusters in this size range, in particular, to features of the energy spectrum, of the spectrum of vibrational frequencies of atoms in the cluster, and of the exciton energy relaxation.

[1)]At an electron energy of 1 keV the impact mechanism of desorption of atoms from clusters of inert elements is not realized.

[2)]In the case of spherical clusters the characteristic linear mean size t of the cluster is related to the mean number of atoms in the cluster $\bar{N}$ by the relation $t = \bar{a}\sqrt[3]{3\bar{N}/2\pi}$.

[3)]Excitons correlated with the atomic Rydberg states $np^5(n+1)s$ and $np^5(n+1)p$ (where $n = 3$, 4, and 5 for Ar, Kr, and Xe, respectively) are denoted as s excitons and p excitons, respectively.

[4)]The existence of p excitons in crystals of inert elements was reported in Ref. 44.

[1] F. Colletti, J. M. Debever, and G. Zimmerer, J. Phys. (France) Lett. **45**, L-467 (1984).

[2] T. Arakawa, T. Adachi, T. Hirayama, and M. Sakurai, Fiz. Nizk. Temp. **29**, 342 (2003) [Low Temp. Phys. **29**, 259 (2003)].

[3] C. T. Reimann, W. L. Brown, D. E. Grosjean, M. J. Nowakowski, and W. T. Buller, Phys. Rev. B **45**, 43 (1992).

[4] R. E. Johnson and J. Schou, Mat. Fys. Medd. K. Dan. Vidensk. Selsk. **43**, 403 (1993).

[5] G. Zimmerer, Nucl. Instrum. Methods Phys. Res. B **91**, 601 (1994).

[6] E. V. Savchenko, J. Electron Spectrosc. Relat. Phenom. **79**, 47 (1996).

[7] O. N. Grigorashchenko, A. N. Ogurtsov, E. V. Savchenko, J. Becker, M. Runne, and G. Zimmerer, Surf. Sci. **390**, 277 (1997).

[8] M. Joppien, F. Groteluschen, T. Kloiber, M. Lengen, T. Möller, J. Wörmer, G. Zimmerer, J. Keto, M. Kykta, and M. C. Castex, J. Lumin. **48-49**, 601 (1991).

[9] R. Karnbach, M. C. Castex, J. Keto, M. Joppien, J. Wörmer, G. Zimmerer, and T. Möller, Chem. Phys. Lett. **203**, 248 (1993).

[10] E. T. Verkhovtseva, E. A. Bondarenko, and Yu. S. Doronin, Chem. Phys. Lett. **140**, 181 (1987).

[11] S. I. Kovalenko, D. D. Solnyshkin, E. T. Verkhovtseva, and V. V. Eremenko, Chem. Phys. Lett. **250**, 3009 (1996).

[12] S. I. Kovalenko, D. D. Solnyshkin, E. A. Bondarenko, and É. T. Verkhovtseva, Fiz. Nizk. Temp. **23**, 190 (1997) [Low Temp. Phys. **23**, 140 (1997)].

[13] V. I. Iveronova and G. P. Revkevich, Teoriya rasseyaniya rentgenovskikh lucheĭ, MGU, Moscow (1972).

[14] P. A. Skovorodko, Rarefied Gas Dynamics, Plenum Press, New York and London (1985), v. **2**, p. 1053.

[15] É. T. Verkhovtseva, V. I. Yaremenko, P. S. Pogrebnyak, and A. E. Ovechkin, Prib. Tekh. Éksp., No. 4, 210 (1976).

[16] S. I. Kovalenko and P. E. Toryanik, Kristallografiya **35**, 1303 (1990) [Sov. Phys. Crystallogr. **35**, 769 (1990)].

[17] S. I. Kovalenko and N. N. Bagrov, Trudy Fiziko-Tekhnicheskogo Instituta Nizkikh Temperatur Akad. Nauk SSSR, Fizika Kondensirovannogo Sostoyaniya, issue 11, 33 (1971).

[18] D. J. Hudson, *Lectures on Elementary Statistics and Probability*, CERN Report CERN 63-29 (Aug. 1963), 101 pp.; *Statistics Lectures II: Maximum Likelihood and Least Squares Theory*, CERN Report CERN 64-18 (April 1964), 211 pp. [Russian translation: *Statistika dlya Fizikov*, Mir, Moscow (1971)].

[19] J. W. Lee and G. D. Stein, J. Phys. Chem. **91**, 2450 (1987).

[20] M. S. Patterson, J. Appl. Phys. **23**, 805 (1952).

[21] Yu. F. Komnik, Fiz. Tverd. Tela (Leningrad) **6**, 873 (1964) [Sov. Phys. Solid State **6**, 672 (1964)].

[22] É. T. Verkhovtseva, E. A. Bondarenko, and Yu. S. Doronin, Khim. Fiz. **10**, 956 (1991).

[23] O. F. Hagena and W. Obert, J. Chem. Phys. **56**, 1793 (1972).

[24] J. Farges, M. F. de Feraudy, B. Raoult, and G. Torchet, J. Chem. Phys. **84**, 3491 (1986).

[25] R. Karnbach, M. Joppien, J. Stapelfeldt, J. Wörmer, and T. Möller, Rev. Sci. Instrum. **64**, 2838 (1993).

[26] T. Möller, Z. Phys. D: At., Mol. Clusters **20**, 1 (1991).

[27] J. Wörmer and T. Möller, Z. Phys. D: At., Mol. Clusters **20**, 39 (1991).

[28] J. Wörmer, V. Guzielski, J. Stapelfeldt, and T. Möller, Chem. Phys. Lett. **159**, 321 (1989).

[29] Y. Tanaka and K. Yoshino, J. Chem. Phys. **53**, 2012 (1970).

[30] P. E. LaRocque, R. H. Lipson, P. R. Herman, and B. P. Stoicheff, J. Chem. Phys. **84**, 6627 (1986).

[31] P. H. Lipson, P. E. LaRocque, and B. P. Stoicheff, J. Chem. Phys. **82**, 4470 (1985).

[32] K. T. Gillen, R. P. Saxon, D. C. Lorents, G. E. Ice, and R. E. Olson, J. Chem. Phys. **64**, 1925 (1976).

[33] R. C. Michaelson and A. L. Smith, J. Chem. Phys. **61**, 2566 (1974).

[34] O. Vallee, Minh N. Tran, and J. Chapelle, J. Chem. Phys. **73**, 2784 (1980).

[35] E. A. Bondarenko, E. T. Verkhovtseva, Yu. S. Doronin, and A. M. Ratner, Chem. Phys. Lett. **182**, 637 (1991).

[36] R. Müller, M. Joppien, and T. Möller, Z. Phys. D: At., Mol. Clusters **26**, 370 (1993).

[37] É. T. Verkhovtseva, *Achievements of Spectroscopy* [in Russian], Nauchn. Sov. Spektroskop. Akad Nauk SSSR, Moscow (1987), Vol. 1, p. 87.

[38] G. Zimmerer, J. Low Temp. Phys. **111**, 630 (1998).

[39] B. I. Verkin and A. F. Prikhot'ko (eds.), Cryocrystals [in Russian], Naukova Dumka, Kiev (1992).

[40] M. Runne and G. Zimmerer, Nucl. Instrum. Methods Phys. Res. B **101**, 156 (1995).

[41] K. S. Song and R. T. Williams, *Self-Trapped Excitons*, Springer-Verlag, Berlin–Heidelberg (1993).

[42] A. M. Ratner, Phys. Rep. **296**, 197 (1996).

[43] M. Joppien, R. Müller, J. Wörmer, and T. Möller, Phys. Rev. B **47**, 12984 (1993).

[44] A. G. Belov, V. N. Svishchev, I. Ya. Fugol', and E. M. Yurtaeva, Fiz. Nizk. Temp. **9**, 1206 (1983) [*sic*].

[45] A. Burose, C. Becker, and A. Ding, Z. Phys. D: At., Mol. Clusters **20**, 35 (1991).

[46] E. T. Verkhovtseva, E. A. Bondarenko, and A. M. Ratner, in *Book of Abstracts of the Fourth International Conference on Cryocrystals and Quantum Crystals*, Freising, Germany (2002), p. B-26.

[47] P. J. M. Van der Burgt and J. W. McConkey, J. Chem. Phys. **102**, 8414 (1995).

[48] R. S. F. Shang and D. W. Setler, J. Chem. Phys. **69**, 3885 (1978).

[49] D. C. Shannon and J. D. Eden, J. Chem. Phys. **89**, 6644 (1988).

[50] I. Last and T. F. George, J. Chem. Phys. **98**, 6406 (1993).

[51] M. R. Hoare and P. Pal, J. Cryst. Growth **176**, 77 (1972).

[52] J. Jortner, Z. Phys. D: At., Mol. Clusters **24**, 247 (1993).

[53] P. Stampfli and K. H. Bennemann, Phys. Rev. A **38**, 4431 (1988).

[54] É. T. Verkhovtseva, V. I. Yaremenko, and Ya. M. Fogel', Opt. Spektrosk. **44**, 389 (1978) [*sic*].

[55] I. Ya. Fugol', E. V. Savchenko, A. G. Belov, and Yu. B. Poltoratskiĭ, JETP Lett. **19**, 378 (1974).

Translated by Steve Torstveit

Toward a theory of the magnetoimpurity states of electrons in conductors

A. M. Ermolaev* and G. I. Rashba

V. N. Karazin Kharkov National University, pl. Svobody 4, Kharkov 61077, Ukraine

Conductors containing impurity atoms capable of localizing electrons in a magnetic field are considered with the use of functional methods for investigating electronic magnetoimpurity states. These states are taken into account in the Keldysh formalism. The theory is illustrated for the example of a two-dimensional electron gas characterizing impurity atoms in a quantizing magnetic field. The characteristics of the magnetoimpurity states are calculated in the case of a Gaussian separable impurity potential. © *2004 American Institute of Physics.*
[DOI: 10.1063/1.1645154]

Functional methods developed in quantum field theory are increasingly finding their way into condensed matter physics.[1] Such methods are used for calculating the kinetic,[2,3] thermodynamic,[4,5] and superconducting[6] characteristics of disordered three-dimensional and two-dimensional metals at low temperatures. It has been shown[2] that the method of continuous integration over Grassman fields can be used for calculating the magnetic Green function in the Keldysh technique[7,8] and the characteristics of disordered conductors in the absence of magnetic field. In Ref. 3 a functional approach based on the Keldysh formalism was used to calculate the low-temperature conductivity and other characteristics of an electron liquid in metals containing impurity atoms. The method of integration over Grassman variables in the study of the equilibrium properties of two-dimensional electron gas in a magnetic field was used in Refs. 4 and 5. The analysis in Ref. 4 was restricted to the case of a high magnetic field, while in Ref. 5 the magnetic field was assumed weak.

In Refs. 2–6 the influence of impurities atoms on the properties of a system was approximated by a Gaussian delta-correlated random potential. Its intensity was characterized by the electron collision frequency calculated in the Born approximation in the electron–impurity interaction. This is permissible only in the case of weak scatterers incapable of localizing electrons. To include consideration of the electronic impurity states at isolated scatterers one must go beyond the Born approximation. Such states were not taken into account in Refs. 2–6.

In the present study we show how arbitrary magnetic fields and the presence of electronic impurity and magnetoimpurity[9,10] states at isolated impurity atoms can be taken into account in the formalism developed in Ref. 2. The theory is applicable both to bulk disordered conductors and to the two-dimensional electron gas in heterostructures. As an illustration we calculate the characteristics of the electronic impurity and magnetoimpurity states in two-dimensional conductors with a Gaussian separable impurity potential, which makes it possible to solve the problem exactly.

The problem of the influence of a short-range perturbation on the energy spectrum of an electron undergoing two-dimensional motion in a magnetic field was first solved in Ref. 11. The authors of that study restricted consideration to the case when the potential of the perturbation is nonzero within a square region lying in the plane of motion of the electron. The general theory of electronic magnetoimpurity states in two-dimensional systems containing point impurity atoms was developed in Refs. 12 and 13 by the zero-radius potential method. The case of a Gaussian separable impurity potential was not considered in Refs. 11–13.

Taking arbitrary magnetic fields into account in the formalism developed in Ref. 2 reduces to switching from a plane-wave basis to a basis of eigenstates of the electron in a magnetic field.[14] We shall therefore only give the final formula, introduced by Keldysh in Refs. 7 and 8, for the matrix Green's function G of the electrons:

$$iG_{12} = \left(\frac{\delta^L}{i\,\delta J_1^*} \frac{\delta^R}{i\,\delta J_2} W[J,J^*] \right)_{\substack{J=0 \\ J^*=0}}. \tag{1}$$

Here $W = \ln Z$ is an arbitrary functional for coupled Green's functions, the indices L and R denote the left and right functional derivatives with respect to the Fermi sources J^* and J, and $1 = (\kappa_1, \alpha_1, t_1)$ (κ is the set of Landau orbital quantum numbers, $\alpha = \pm 1$ is the spin quantum number, and t is the time). The function Z has the form

$$Z[J,J^*] = \exp\left(-i\sum_{12} U_{12} \frac{\delta^R}{i\,\delta J_1} \sigma_3 \frac{\delta^L}{i\,\delta J_2^*} \right)$$

$$\times \exp\left(-i\sum_{34} J_3^* \overset{0}{G}_{34} J_4 \right), \tag{2}$$

where $U_{12} = \langle \kappa_1 | u | \kappa_2 \rangle \delta_{\alpha_1 \alpha_2} \delta(t_1 - t_2)$, u is the energy of interaction of an electron with the impurity atoms, σ_3 is the third Pauli matrix, $\overset{0}{G}$ is the matrix Green function of the electrons in a magnetic field, and

$$\sum_1 = \sum_{\kappa_1 \alpha_1} \int_{-\infty}^{\infty} dt_1.$$

(We are ignoring Coulomb interaction of the electrons, and we have set $\hbar = 1$.) In this way the procedure of calculating

the Green function has been reduced to one of calculating the functional derivatives in formulas (1) and (2).

Formula (2) makes it possible to write the generating functional in the form of a series in powers of the perturbation. The Green function (1) is also written in the form of a series, coinciding with the series obtained on the basis of a diagram technique employing Wick's theorem.[8] In particular, the first-order corrections to the components of the matrix Green function (1) are:

$$\overset{1}{G}_{12}^{++} = \sum_{34} U_{34}\left(\overset{0}{G}_{13}^{+-} \overset{0}{G}_{42}^{-+} - \overset{0}{G}_{13}^{++} \overset{0}{G}_{42}^{++} \right),$$

$$\overset{1}{G}_{12}^{+-} = \sum_{34} U_{34}\left(\overset{0}{G}_{13}^{+-} \overset{0}{G}_{42}^{--} - \overset{0}{G}_{13}^{++} \overset{0}{G}_{42}^{+-} \right),$$

$$\overset{1}{G}_{12}^{-+} = \sum_{34} U_{34}\left(\overset{0}{G}_{13}^{--} \overset{0}{G}_{42}^{-+} - \overset{0}{G}_{13}^{-+} \overset{0}{G}_{42}^{++} \right),$$

$$\overset{1}{G}_{12}^{--} = \sum_{34} U_{34}\left(\overset{0}{G}_{13}^{--} \overset{0}{G}_{42}^{--} - \overset{0}{G}_{13}^{-+} \overset{0}{G}_{42}^{+-} \right).$$

Here $\pm$ are the indices in the two-dimensional Keldysh space. The diagrams for these corrections are given in Ref. 8. They differ from the usual diagrams of the cross technique[15] by the additional indices $\pm$ on the ends of the lines.

Here we limit consideration to a selective summation of the diagrams with one cross for the retarded Green function $G = G^{++} - G^{+-}$ of the electrons in a two-dimensional conductor, averaged over impurity configurations. In this approximation the scattering amplitude for electrons by isolated impurity atoms can be taken into account exactly at low impurity concentrations. The scattering potential is chosen in the form

$$\hat{V} = \sum_j |\eta_j\rangle u_0 \langle \eta_j|, \tag{3}$$

where $|\eta_j\rangle\langle\eta_j|$ are the projection operator onto the vector $|\eta_j\rangle$, u_0 is a constant, and the index j enumerates the impurity atoms. The function $\eta(\mathbf{r}) = \langle \mathbf{r}|\eta\rangle$ will be assumed equal to

$$\eta(\mathbf{r}) = (\sqrt{\pi}a)^{-1}\exp\left(-\frac{r^2}{2a^2}\right),$$

where a is a constant. Such a potential was used in Ref. 16 in a study of magnetoimpurity states in bulk conductors. In formula (3) the transition to a sum of delta functions $v_0\delta(\mathbf{r} - \mathbf{r}_j)$ is achieved with the substitution

$$4\pi \lim_{\substack{a\to 0 \\ u_0\to\infty}} (a^2 u_0) = v_0.$$

The advantage of the potential chosen here is that it contains two independent parameters u_0 and a, while at the same time the point potential is characterized by only one parameter, v_0.

In the case of potential (3) the sum of diagrams with one cross for the average Green function in the $(\kappa, \alpha, \varepsilon)$ representation (ε is the energy variable) is equal to $G = G_0 + G_0 T G_0$, where the quantity

$$T_\alpha(\varepsilon) = u_0 n_i \left(1 - u_0 \sum_\kappa \frac{|\langle \kappa|\eta\rangle|^2}{\varepsilon - \varepsilon_{\kappa\alpha}} \right)^{-1} \tag{4}$$

is proportional to the electron scattering amplitude, $\varepsilon_{\kappa\alpha}$ are the Landau levels, and n_i is the density of impurity atoms. With the impurity potential used in this study the divergence of the sum in formula (4) inherent for a delta-like potential can be avoided more simply than is achieved by the zero-radius potential method. The function $\langle \kappa|\eta\rangle$ appearing in Eq. (4) has the formula

$$\langle nm|\eta\rangle = \sqrt{2}\,\delta_{m0}\frac{l}{a}\left(\frac{l^2}{a^2} + \frac{1}{2}\right)^{-1}\left[\left(\frac{l^2}{a^2} - \frac{1}{2}\right)\left(\frac{l^2}{a^2} + \frac{1}{2}\right)^{-1}\right]^n. \tag{5}$$

Here l is the magnetic length, n is the oscillator quantum number, and m is the quantum number of the orbital angular momentum of the electron in a magnetic field $\mathbf{H}$. The vector $\mathbf{H}$ is perpendicular to the plane $z = 0$ occupied by the electrons. The presence of δ_{m0} in formula (5) means that the potential under consideration, like the point potential,[12] scatters only the state with $m = 0$. It follows from formulas (4) and (5) that the magnetoimpurity energy levels are roots of the Lifshits equation[17] $u_0^{-1} = F_\alpha(\varepsilon)$. In the case under consideration here this equation has the form

$$\frac{\omega_c}{u_0} = -2\left(\frac{l}{a}\right)^2\left[\left(\frac{l}{a}\right)^2 + \frac{1}{2}\right]^{-2}$$
$$\times \Phi\left(\left[\frac{\left(\frac{l}{a}\right)^2 - \frac{1}{2}}{\left(\frac{l}{a}\right)^2 + \frac{1}{2}}\right]^2, 1, \frac{1}{2} - \frac{\varepsilon}{\omega_c} + \alpha\frac{\mu H}{\omega_c}\right), \tag{6}$$

where ω_c is the electron cyclotron frequency, μ is the electron spin magnetic moment, and

$$\Phi(x, 1, v) = \sum_{n=0}^\infty \frac{x^n}{v+n}$$

is a special function.[18] The roots of this equation are determined by the two independent parameters, ω_c/u_0 and l/a. The exact equation (6) for a Gaussian separable impurity potential is obtained for the first time.

It follows from Eq. (6) that the electron energy spectrum contains a system of local levels split off from the Landau levels by the impurity atoms to higher or lower values, depending on the sign of u_0. For $u_0 > 0$ the local energy level of an electron whose spin magnetic moment is oriented along the magnetic field lies in the region $\varepsilon < 0$ if $\mu H > \omega_c/2$ and $u_0 < F_{-1}^{-1}(0)$. Since the spin splitting of the Landau levels was not taken into account in Refs. 11–13, this possibility did not exist there. When a and l differ strongly, the distance Δ between a Landau level and the magnetoimpurity level split off from it is small compared to ω_c:

$$\Delta = \begin{cases} \omega_c\left[\ln\left(2\frac{a^2}{l^2}\right) + (2m_* a^2 |u_0|)^{-1}\right]^{-1}, & a \ll l, \\[2ex] \omega_c\left[\ln\left(8\frac{l^2}{a^2}\right) + \frac{1}{8}\left(\frac{a}{l}\right)^2\frac{\omega_c}{|u_0|}\right]^{-1}, & a \gg l, \end{cases}$$

where m_* is the effective mass of the electron. For $a \ll l$ the limiting value of the magnitude of the splitting agrees with

expressions (25) and (28) in Ref. 11 to within numerical factors stemming from the different model for the impurity potential. In the case $a \ll 1$ the positions of the local levels found here are poles of the scattering amplitude (3.6) in Ref. 12. The Lifshits equation in that paper contains only one parameter—the scattering length of the electrons in the absence of magnetic field. The case $a \gg l$ was not considered in Refs. 11–13. In the quantum limit we obtain from Eq. (6) the expression

$$\Delta = 2u_0 \left(\frac{l}{a}\right)^2 \left[\frac{1}{2} + \left(\frac{l}{a}\right)^2\right]^{-2},$$

which is valid for any value of a/l. If $|u_0| \rightarrow \infty$ the energy of an electron in the bound state is equal to $-|u_0|$. The widths of the magnetoimpurity levels in this approximation are equal to zero.

The scattering amplitude (4) has the usual form[17]

$$T_\alpha(\varepsilon) = u_0 n_i \{1 - u_0[F_\alpha(\varepsilon) - i\pi g_\alpha(\varepsilon)]\}^{-1},$$

where

$$g_\alpha = \frac{8}{\omega_c} \left(\frac{l}{a}\right)^2 \left[2\left(\frac{l}{a}\right)^2 + 1\right]^{-2}$$

$$\times \left[\left(2\frac{l^2}{a^2} + 1\right)\left(2\frac{l^2}{a^2} - 1\right)^{-1}\right]^{2\beta_\alpha} \sum_{n=0}^{\infty} \delta(n + \beta_\alpha),$$

$$\beta_\alpha = \frac{1}{2} + \alpha\frac{\mu H}{\omega_c} - \frac{\varepsilon}{\omega_c}.$$

In the limit $a \rightarrow 0$, $u_0 \rightarrow \infty$ the function $u_0 g_\alpha(\varepsilon)$ goes over to $v_0 \nu_\alpha(\varepsilon)$, where $\nu_\alpha(\varepsilon)$ is the electron density of states in a magnetic field. The residue at the pole of the electron scattering amplitude on an individual impurity center is equal to

$$R = \begin{cases} \dfrac{1}{2}\omega_c^2\left(\dfrac{l}{a}\right)^2 \zeta^{-1}\left(2, -\dfrac{\Delta}{\omega_c}\right), & a \ll l, \\[2ex] \dfrac{1}{8}\omega_c^2\left(\dfrac{a}{l}\right)^2 \zeta^{-1}\left(2, -\dfrac{\Delta}{\omega_c}\right), & a \gg l, \end{cases}$$

where ζ is the generalized zeta function.[18] The wave function of an electron in the bound state with energy ε_l has the form

$$\psi_{m\alpha}(r, \varphi) \sim \exp\left(-\frac{r^2}{4l^2} + im\varphi\right)$$

$$\times \Psi\left(\frac{1}{2} - \frac{\varepsilon_l}{\omega_c} + \alpha\frac{\mu H}{\omega_c}, 1; \frac{r^2}{2l^2}\right),$$

where r, φ are polar coordinates and Ψ is the confluent hypergeometric function.[18]

In the absence of magnetic field the Lifshits equation for impurity states of an electron in the field (3) has the form

$$1 - u_0[F(\varepsilon) - i\pi g(\varepsilon)] = 0, \tag{7}$$

where

$$F(\varepsilon) = \varepsilon_0^{-1} \exp\left(-\frac{\varepsilon}{\varepsilon_0}\right) \begin{cases} E_i\left(\dfrac{\varepsilon}{\varepsilon_0}\right), & \varepsilon > 0, \\[2ex] -E_1\left(-\dfrac{\varepsilon}{\varepsilon_0}\right), & \varepsilon < 0, \end{cases}$$

$$g(\varepsilon) = \Theta(\varepsilon)\varepsilon_0^{-1} \exp\left(-\frac{\varepsilon}{\varepsilon_0}\right).$$

Here $\varepsilon_0 = (2m_* a^2)^{-1}$, E_i and E_1 are exponential integral functions,[18] and Θ is the Heaviside step function.

It follows from (7) that in an attractive field ($u_0 < 0$) a local level ε_l lying below the boundary of the continuous spectrum exists for any value of $|u_0|$. In addition, in the region $\varepsilon > 0$ there exists an antiresonance level ε_a. The presence of such a level means that in an attractive field, states are transferred from the vicinity of the level ε_a to the local level. If $|u_0| \ll \varepsilon_0$ the positions of these levels are given by the formula[14]

$$\varepsilon_{l,a} = \pm\varepsilon_0 \exp\left(-\frac{\varepsilon_0}{|u_0|}\right).$$

The wave function of an electron in the bound state is

$$\psi(r) \sim K_0(\sqrt{2m_*|\varepsilon_l|}\,r),$$

where K_0 is a Macdonald function.[18]

In a repulsive field ($u_0 > 0$) there exists a critical value $u_{0k} \sim \varepsilon_0$ such that impurity states are absent absent for $u_0 < u_{0k}$. If $u_0 > u_{0k}$, however, there exist a resonance level ε_r and an antiresonance level ε_a, with $\varepsilon_r > \varepsilon_a$. If $u_0 < u_{0k}$ the electrons undergo only potential scattering by the impurity centers. The phase shift of the wave function in the scattering process is given by

$$\delta = -\arctan\frac{\pi g}{u_0^{-1} - F}.$$

It changes abruptly by π on passage through the resonance level ε_r. The two-dimensional scattering cross section

$$\sigma = \frac{4}{k}\frac{(\pi u_0 g)^2}{(1 - u_0 F)^2 + (\pi u_0 g)^2}$$

($k = \sqrt{2m_*\varepsilon}$) has a Breit–Wigner maximum at the point ε_r. The width of the maximum is equal to $\pi g(\varepsilon_r)/|F'|$. The prime denotes the derivative at the point ε_r.

*E-mail: alexander.m.ermolaev@univer.kharkov.ua

[1] A. M. Tsvelik, *Quantum Field Theory in Condensed Matter Physics* [in Russian], Fiz.-Mat. Lit., Moscow (2002).
[2] V. S. Babichenko and A. N. Kozlov, Solid State Commun. **59**, 39 (1986).
[3] A. Kamenev and A. Andreev, Phys. Rev. B **60**, 2218 (1999).
[4] E. Brezin, in *Applications of Field Theory to Statistical Mechanics*, Springer-Verlag, Berlin (1985).
[5] I. S. Burmistrov, Zh. Éksp. Teor. Fiz. **122**, 150 (2002) [JETP **95**, 132 (2002)].
[6] M. V. Feigelman, A. I. Larkin, and M. A. Skvortsov, Phys. Rev. B **61**, 12361 (2000).
[7] L. V. Keldysh, Zh. Éksp. Teor. Fiz. **47**, 1515 (1964) [Sov. Phys. JETP **20**, 1018 (1965)].
[8] E. M. Lifshitz and L. P. Pitaevskii, *Physical Kinetics*, Pergamon Press, Oxford–New York (1981), Nauka, Moscow (1979).
[9] A. M. Ermolaev and M. I. Kaganov, JETP Lett. **6**, 395 (1967).
[10] É. A. Kaner and A. M. Ermolaev, Zh. Éksp. Teor. Fiz. **92**, 2245 (1987) [Sov. Phys. JETP **65**, 1266 (1987)].
[11] A. M. Kosevich, L. V. Tanatarov, Fiz. Tverd. Tela (Leningrad) **6**, 3423 (1964) [Sov. Phys. Solid State **6**, 2738 (1964)].

[12] Y. Avishai, M. Ya. Azbel, and S. A. Gredeskul, Phys. Rev. B **48**, 17280 (1993).

[13] S. A. Gredeskul, M. Zusman, Y. Avishai, and M. Ya. Azbel, Phys. Rep. **288**, 223 (1997).

[14] L. D. Landau and E. M. Lifshitz, *Quantum Mechanics: Non-Relativistic Theory*, Pergamon Press, Oxford (1977), Nauka, Moscow (1989).

[15] A. A. Abrikosov, L. P. Gor'kov, and I. E. Dzyaloshinskiǐ, *Methods of Quantum Field Theory in Statistical Physics*, Prentice-Hall, Englewood Cliffs, NJ (1963), Fizmatgiz, Moscow (1962).

[16] M. I. Kaganov and S. Klama, Fiz. Tverd. Tela (Leningrad) **20**, 2360 (1978) [Sov. Phys. Solid State **20**, 1361 (1978)].

[17] I. M. Lifshits, S. A. Gredeskul, and L. A. Pastur, *Introduction to the Theory of Disordered Systems*, Wiley, New York (1988), Nauka, Moscow (1982).

[18] *Higher Transcendental Functions (Bateman Manuscript Project)*, Vols. 1 and 2, edited by A. Érdelyi, McGraw-Hill, New York (1954), Nauka, Moscow, Vol. 1 (1965), Vol. 2 (1966).

Translated by Steve Torstveit

On the magnetization of a low-dimensional electron gas at high magnetic fields

V. M. Gokhfeld*

A. A. Galkin Donetsk Physicotechnical Institute, ul. R. Lyuksemburg 72, Donetsk 83114, Ukraine

The magnetic moment of an electron gas is calculated for two-dimensional and one-dimensional models of the energy spectrum of the particles in the quantum cases, when only the lower magnetic subbands are filled. © *2004 American Institute of Physics.* [DOI: 10.1063/1.1647133]

1. The properties of electron systems at high magnetic fields **H** are attracting the steady interest of investigators, especially if one is talking about highly anisotropic systems with an effectively lowered dimensionality of the charge carrier motion: ''synthetic'' conductors with a layered or chain-like crystal structure, inversion layers, electrons on the surface of liquid helium, etc.[1-3] For example, the well-known de Haas–van Alphen and Shubnikov–de Haas oscillation effects, usually observed at

$$T < \beta H \ll \varepsilon_F, \qquad (1)$$

have been widely used for studying the quasi-two-dimensional electron spectrum of modern organic conductors[4] (here T is the temperature,[1]) $\beta \equiv e\hbar/2mc$ is the Bohr magneton, and ε_F is the Fermi energy). The low-dimensional situation is specific: in the one-dimensional case quantum oscillations are altogether absent because of the impossibility of orbital motion of the carriers. The same situation exists for a two-dimensional electron gas in a magnetic field parallel to the plane of motion of the particle; for a general direction of **H** the effect depends on the corresponding angle.[3,5] In the first two cases the magnetic field acts only on the spin, and the conduction electrons are a simple two-level system for which one can find explicit analytical expressions for the thermodynamic functions, valid for practically any values of temperature and field strength. In the third case the system becomes two-level only in the quantum limit, i.e., at high fields $H \simeq \varepsilon_F / \beta$; here one is interested in the position and shape of the last quantum oscillation, with allowance for the orientation of **H** and finite temperatures.

Calculation of the magnetic moment of the electron subsystem in these particular cases is the goal of the present study. For clarity we restrict the treatment to the effective mass approximation[2)] and avoid the straightforward but cumbersome generalization of the problem to the case of several (nonequivalent) valleys in the electron spectrum; the ionic subsystem is assumed nonmagnetic.

2. Using the well-known results of Shoenberg,[2] we first consider a two-dimensional electron gas in an *inclined* magnetic field[3)] which is assumed to be so high that one can assume that at low temperatures only the two lowest subbands, $\varepsilon_{0,-}$ and $\varepsilon_{0,+}$ or $\varepsilon_{1,-}$, in the spectrum

$$\varepsilon_{n,\pm} = \left(n + \frac{1}{2}\right) \frac{e\hbar H_1}{m'c} + \beta H \qquad (2)$$

are filled (m' is the effective mass in the plane of motion of the carriers). As we know,[3,5] the orbital motion here is deter-

mined by the projection $H_1 \equiv H \cos\theta$ of the magnetic field onto an axis corresponding to the cyclic momentum p_1; the latter takes on values within the unit cell of the reciprocal lattice:[4)] $|p_1| \lesssim \pi\hbar/a_1$. The energy interval between the lowest subbands is

$$\Delta = e\hbar H / [c \max(m, m'/\cos\theta)], \qquad (3)$$

and the thermodynamic potential Ω for such a system is equal to

$$\Omega \cong -T \frac{eH\cos\theta}{2\pi a_1 c\hbar}\left\{\ln\left(1 + \exp\frac{\mu'}{T}\right) + \ln\left(1 + \exp\frac{\mu' - \Delta}{T}\right)\right\}, \qquad (4)$$

where

$$\mu' \equiv \mu + (\beta - \beta')H \equiv \mu + \beta H\left(1 - \frac{m}{m'}\cos\theta\right) \qquad (5)$$

is the chemical potential measured from $\varepsilon_{0,-}$. It must be expressed in terms of the volume density of particles $N \equiv -\partial\Omega/\partial\mu$, since in a homogeneous sample the latter must obviously be assumed fixed.[5)] By definition, the magnetic moment $\mathbf{M} \equiv -\partial\Omega/\partial\mathbf{H}$. As we see from Eq. (4), its limiting value at high fields is

$$M_{\text{sat}}(\theta) = N(\beta - \beta') = N\beta\left(1 - \frac{m}{m'}\cos\theta\right), \qquad (6)$$

which agrees completely with the known result

$$M_{\text{sat}} = N\beta(1 - m/m')$$

for an isotropic metal.[7] We note that the change in the quantum oscillations of the conductivity (the Shubnikov–de Haas effect) with angle θ has been used to estimate the relationship between the ''bare'' and effective masses (the so-called g factor) in a two-dimensional electron gas.[3,5] Expression (6) represents an alternative possibility but at higher—ultraquantum—magnetic fields.

The approach of the moment to its limiting value (6) is preceded by the last quantum oscillation of $M(H)$. Using the formulas given above, one can reduce the calculation of its shape to the joint solution of the equations

$$\frac{\delta M(h)}{N} = 2\frac{\max(\beta, \beta')}{b}\left\{\ln(1 + e^x) + \ln(1 + e^{x-bh})\right.$$

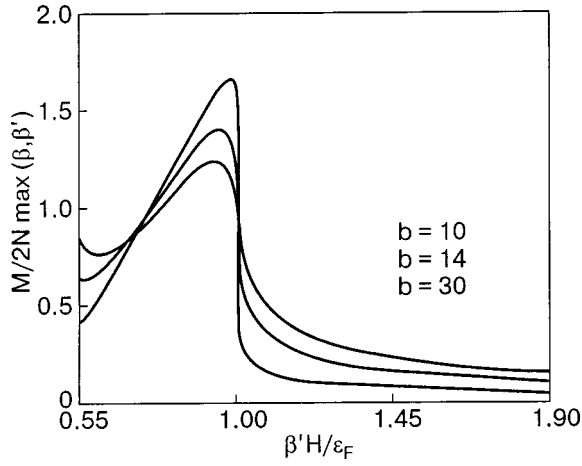$$\left. - \frac{bh}{1 + e^{bh-x}}\right\} \qquad (7)$$

FIG. 1. Magnetic moment of a quasi-two-dimensional electron gas versus the reduced field strength $\beta'H/\varepsilon_F$ [see Eq. (13)] for different values of the parameter $b \equiv 2\varepsilon_F /[T \max(1, m \cos \theta/m')]$. The moment [after subtraction of the constant part $N(\beta - \beta')$] is expressed in units of $2N \max(\beta,\beta')$.
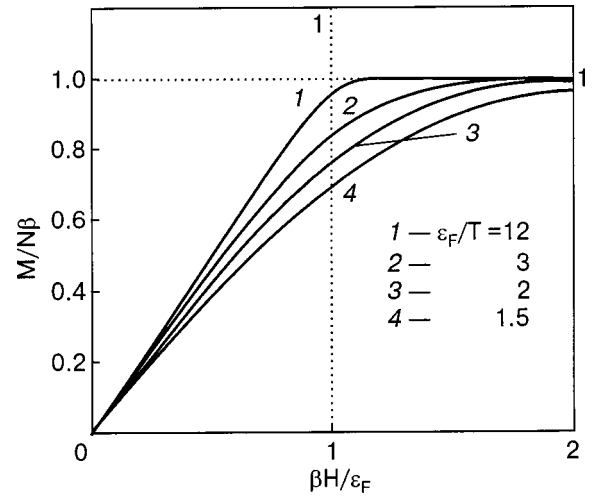

FIG. 2. Magnetic moment of a quasi-two-dimensional electron gas as a function of the magnetic field applied parallel to the plane of motion of the particles [Eq. (19)] for different values of the parameter ε_F /T. The moment is expressed in units of $N\beta$, and the field strength in units of $\beta H/\varepsilon_F$.

and

$$\frac{1}{h} = \frac{1}{1+e^{-x}} + \frac{1}{1+e^{bh-x}}, \tag{8}$$

where we have introduced the variable

$$h \equiv \frac{\beta'H}{\varepsilon_F} \equiv \frac{eH \cos \theta}{2\pi\hbar N a_1 c} \tag{9}$$

and a parameter characterizing the degree of degeneracy of the system

$$b \equiv \frac{2\varepsilon_F}{T \max(1, m \cos \theta/m')} \quad (\varepsilon_F = N\pi a_1 \hbar^2/m'). \tag{10}$$

Although an analytical solution would be too awkward, a graphical solution can be found without difficulty by using the MathCAD software, for example; it is presented in Fig. 1. Even for not very large values of the parameter b the fall of the curve is very sharp; it takes place at $h \cong 1$, i.e., for $H \cong 2\pi\hbar c N a_1 /e \cos \theta$.

We note that this value of the field strength is independent of both the "bare" and effective masses of the electron.

3. Let us turn to the case of parallel magnetic field ($\theta = \pi/2$). At finite temperature there can obviously be small deviations from parallelism:

$$\frac{m}{m'} \cos \theta \ll \frac{T}{2\beta H}. \tag{11}$$

Under this condition the motion of the carriers in the (x_2,x_3) plane can be considered nonquantized, so that the spectrum has the form

$$\varepsilon_\pm(\mathbf{p}_=) = \frac{p_2^2 + p_3^2}{2m'} \pm \beta H. \tag{12}$$

Proceeding in the standard way (see Refs. 2, 8, and 9), we write the thermodynamic potential as

$$\Omega = -\frac{T}{a_1(2\pi\hbar)^2} \sum_{\pm} \int \int dp_2 dp_3$$

$$\times \ln\left[1 + \exp\frac{1}{T}\left(\mu_\pm - \frac{p_2^2 + p_3^2}{2m'}\right)\right], \tag{13}$$

where $\mu_\pm \equiv \mu \pm \beta H$. Using this to calculate the magnetic moment, we find

$$M \equiv -\left(\frac{\partial\Omega}{\partial H}\right)_{\mu,T} = \frac{D}{2}T\beta \ln\left(\frac{1 + \exp(\mu_+ /T)}{1 + \exp(\mu_- /T)}\right), \tag{14}$$

where $D = m'/\pi a_1 \hbar^2$ is the energy density of states at $H = 0$, and the chemical potential μ is to be determined from the equation

$$N = \frac{D}{2}T\sum_{\pm} \ln(1 + \exp(\mu_\pm /T)). \tag{15}$$

The solution giving the dependence of μ on H and T is easily written in explicit form as

$$\mu(H,T) = T \ln(\sqrt{\cosh^2(\beta H/T) + e^{2N/DT} - 1} - \cosh(\beta/T)). \tag{16}$$

In particular,

$$\mu(H \to 0,T) = T \ln(e^{N/DT} - 1) \equiv T \ln(e^{\varepsilon_F /T} - 1);$$

$$\mu(H \to \infty,T) = T \ln(e^{2\varepsilon_F /T} - 1) - \beta H. \tag{17}$$

Substituting (16) into (14) and introducing the notation

$$y \equiv \beta H/T; \quad w \equiv \exp(2\varepsilon_F /T) - 1, \tag{18}$$

we find

$$M(H,T) = \frac{N\beta}{\ln(1+w)} \ln\left(\frac{1 + e^y(\sqrt{\cosh^2 y + w} - \cosh y)}{1 + e^{-y}(\sqrt{\cosh^2 y + w} - \cosh y)}\right). \tag{19}$$

As could be expected, in a magnetic field parallel to the quasi-two-dimensional electron layers they are always paramagnetic, and their magnetic moment increases monotoni-

cally with H: linearly in weak fields ($\beta H \ll \varepsilon_F$) and then approaching saturation with a value $M_{\text{sat}} = N\beta$ (see Fig. 2).

4. Let us consider the case of one-dimensional motion[6] of the carriers (along the **C** axis). Without any dependence on the mutual orientation of **H** and **C** no orbital motion is possible, and the magnetic field acts only on the spin, so that the spectrum has the form

$$\varepsilon_\pm(p_C) = p_C^2/2m_C \pm \beta H. \tag{20}$$

Clearly this case is qualitatively similar to the previous one, and here we limit consideration to the simple limit of low temperatures. Then, at low fields, when both subbands are filled,

$$\Omega = -\frac{T}{2\pi\hbar a_\perp^2} \sum_\pm \int dp_C \ln\left(1 + \exp\frac{1}{T}(\mu_\pm - p_C^2/2m_C) \right)$$

$$\cong -\frac{2\sqrt{2m_C}}{3\pi\hbar a_\perp^2}(\mu_+^{3/2} + \mu_-^{3/2}), \tag{21}$$

where $a_\perp^2$ is the area of the unit cell of the crystal in the plane perpendicular to the **C** axis. The magnetic (clearly, paramagnetic) moment is equal to

$$M \cong \frac{\beta}{\pi\hbar a_\perp^2}\sqrt{2m_C}(\sqrt{\mu_+} - \sqrt{\mu_-}), \tag{22}$$

and the equation for the chemical potential can be written in the form

$$\sqrt{\mu_+} + \sqrt{\mu_-} = 2\sqrt{\varepsilon_F}; \quad \varepsilon_F = N^2\pi^2\hbar^2 a^4/8m_C. \tag{23}$$

For $\beta H < 2\varepsilon_F$ its solution is

$$\mu_\pm = \varepsilon_F(1 \pm \beta H/2\varepsilon_F)^2, \tag{24}$$

and at higher fields the particles completely leave the upper subband and, as follows from (21) for $T \to 0$, we should drop the terms with the index "$-$" in expressions (21)–(23); this gives $\mu_+ = 4\varepsilon_F$. As a result

$$M(H,0) \cong N\beta \begin{cases} \beta H/2\varepsilon_F, & \beta H < 2\varepsilon_F, \\ 1, & \beta H > 2\varepsilon_F. \end{cases} \tag{25}$$

It is clear from the foregoing that at nonzero temperature we would obtain a smoothing of the kink at $\beta H = 2\varepsilon_F$ and a smoother approach to the limiting value $M_{\text{sat}} = N\beta$ [cf. Eq. (19) and Fig. 2].

5. Although the results of paragraphs 3 and 4 pertain to an extremely wide region of magnetic fields, their quantum limit and also the result of paragraph 2 presupposes a field strength exceeding a value

$$H_Q \simeq \frac{\varepsilon_F}{\beta} \simeq \frac{\hbar c}{ea^2} \begin{cases} (Na^3)^{2/3} & (D=3), \\ Na^3 & (D=2), \\ (Na^3)^2 & (D=1), \end{cases} \tag{26}$$

where Na^3 is the number of electrons per unit cell of the crystal, a is an averaged linear dimension of the cell, and $\hbar c/ea^2 \cong 10^8$ Oe is a value of the field at which the radius of localization of the lowest magnetic subband is comparable to a. Since the present-day experimental capabilities for static fields do not exceed $H \sim 10^6$ Oe, the electron density must be much smaller than in an ordinary metal. Note that the lower the dimensionality D of the system, the faster the decrease of H_Q with N.

Thus the conditions for observing the behavior of $M(\mathbf{H},T)$ obtained in this study can be realized in conducting crystals with a comparatively low but fixed (or weakly dependent on magnetic field and temperature) density of free carriers: for example, in layered organic metals based on BEDT–TTF and in quasi-one-dimensional metals based on TCNQ and also in semiconductor inversion layers and heterostructures, where N can be adjusted over a wide range by varying the blocking potential. Generalization of the single-valley spectral models used can alter the picture substantially only in the case of semimetals, where at high fields a transition to an insulator state can occur (see Refs. 11 and 12).

We note in closing that the "true" limiting value of the magnetic moment for $H \to \infty$, i.e., for $H \gg \hbar c/ea^2$, cannot be calculated on the basis of band-spectrum models, since the latter have meaning only for sufficiently extended spatial regions including many cells of the crystal. This (as yet academic) question would require a more detailed quantum-mechanical treatment.

The author thanks V. G. Peschansky and Yu. G. Pashkevich for a discussion of this study.

[1)]More precisely, the effective temperature $T + \hbar/\tau$, which takes into account the collisional broadening of the Landau levels (see Ref. 1).

[2)]In other words, the electron gas is assumed ideal, with Fermi statistics, and *all* interactions are taken into account by renormalization of the masses in the single-particle spectrum. More subtle aspects of the electron–electron interaction, e.g., the appearance of composite fermions,[6] are, of course, outside the scope of this approximation.

[3)]Although extremely thorough, Ref. 2 did not consider the case of an inclined field, and explicit formulas for the quantum limit were not given.

[4)]For definiteness we shall understand the object of study to be a bulk but highly anisotropic crystal with a quasi-two-dimensional (or, later on, quasi-one-dimensional) dispersion relation for the charge carriers. If one is talking about a real two-dimensional situation (surface states, electrons on the surface of liquid He, layered heterostructure), then a_1 should be understood as the size of the localization region of the electron monolayer.

[5)]For an inversion layer found in the "reservoir" of the other electrons of the sample the opposite case, where μ should be considered fixed rather than N, can be realized (see Fig. 2).

[6)]As above, in a homogeneous but highly anisotropic crystal with a filamentary structure (e.g., NbSe$_3$; Ref. 10).

[1]A. A. Abrikosov, Phys. Rev. B **60**, 4231 (1999).

[2]D. Shoenberg, J. Low Temp. Phys. **56**, 417 (1984).

[3]T. Ando, A. Fowler, and F. Stern, "Electronic properties of two-dimensional systems," Rev. Mod. Phys. **54**, No. 2 (1982).

[4]J. Vosnitza, *Fermi Surfaces of Low-Dimensional Organic Metals and Superconductors*, Vol. 134 of Springer Tracts in Modern Physics (1996).

[5]F. F. Fang and P. G. Stiles, Phys. Rev. **174**, 823 (1968).

[6]R. B. Laughlin, Phys. Rev. Lett. **50**, 1395 (1983).

[7]M. Ya. Azbel' and E. G. Skrotskaya, Zh. Éksp. Teor. Fiz. **47**, 1958 (1964) [Sov. Phys. JETP **20**, 1315 (1965)].

[8]S. V. Vonsovskiĭ, *Magnetism* [in Russian], Nauka, Moscow (1971).

[9]I. M. Lifshits, M. Ya. Azbel', and M. I. Kaganov, *Electron Theory of Metals*, Consultants Bureau, New York (1973).

[10]A. A. Mamaluĭ, T. N. Shelest, and Kh. B. Chashka, Fiz. Nizk. Temp. **26**, 176 (2000) [Low Temp. Phys. **26**, 130 (2000)].

[11]L. D. Landau and E. M. Lifshits, *Quantum Mechanics: Non-Relativistic Theory*, 2nd ed., Pergamon Press, Oxford (1965), Nauka, Moscow (1963).

[12]M. Ya. Azbel' and N. B. Brandt, Zh. Éksp. Teor. Fiz. **48**, 1206 (1965) [Sov. Phys. JETP **21**, 804 (1965)].

Stationary nonlinear waves at the surface of a thin liquid layer under inverted gravitation conditions

G. V. Kolmakov,* E. V. Lebedeva, A. A. Levchenko, L. P. Mezhov-Deglin, A. B. Trusov, and V. B. Shikin

Institute of Solid State Physics of the Russain Academy of Sciences, Chernogolovka, Moscow region, 142432, Russia

Instability of the flat surface of a thin liquid layer wetting a solid substrate under inverted gravitation conditions is discovered. The development of this instability leads to the formation of a new stationary nonuniform liquid surface state. It looks like a solitary hill with characteristics sensitive to the liquid film parameters, particularly to the layer thickness at which the instability begins to develop. By application of a variational approach the mechanical stability of such a hill (droplet) in the one-dimensional approximation is proved. A variational picture of the shape evolution for a cylindrical charged droplet in an external electric field is constructed, too. The results obtained are compared with an experiment on liquid hydrogen droplets [A. A. Levchenko, G. V. Kolmakov, L. P. Mezhov-Deglin, M. G. Mikhailov, and A. B. Trusov, Low Temp. Phys. **25**, 242 (1999)]. The theory developed is in good agreement with the results of experiments. © *2004 American Institute of Physics.*
[DOI: 10.1063/1.1645156]

1. INTRODUCTION

A charged or neutral liquid layer is an example of a two-dimensional (2D) system that can exhibit a mechanical instability under inverted gravitation conditions, i.e., under conditions when the layer is suspended on the horizontal surface of a solid substrate. It is known that a liquid layer suspended on a solid substrate under inverted gravitation conditions is absolutely unstable if the van der Waals forces are neglected.[1] In the presence of the attractive van der Waals forces between liquid and substrate, there is a finite interval of layer thicknesses for which a mechanical equilibrium is possible, and a sufficiently thin layer covers the substrate uniformly. At thicknesses larger than some critical value, the van der Waals forces cannot keep a liquid layer in a flat state and the instability develops.[2]

The mechanical instability of the flat free surface of a neutral liquid layer of a thickness larger than the critical value develops at small wave vectors,[2] which is similar to the instability of the charged surface of a thin liquid layer in an external pressing electric field.[3–5] This situation is quite different from the known instability phenomena of charged surfaces of a thick liquid helium layer,[6–11] because in this case the instability develops at a finite wave number of the order of the inverse capillary wavelength. The scenario of development of the long-wave instability of thin layer surfaces was not clear till now.

The main goal of this paper is to study the nonuniform phenomena that occur on neutral and charged surfaces of a thin liquid layer. We show that the instability leads to the formation of a stationary, nonlinear, solitary wave of surface deformations. The wave amplitude increases with increasing liquid layer thickness or with increasing stretching electric field above some critical values. This behavior is quite different from that of a bulk liquid surface, where the final jump of the deformation wave amplitude takes place at a critical point.

The computed evolution of the shape of the reconstructed surface is compared with the data obtained in earlier experiments[12] on neutral and charged liquid hydrogen layers.

The solution to the problem of stationary surface shapes of thick liquid layers and droplets placed at the surface of a solid substrate was proposed many years ago in Frenkel's papers.[13] In that consideration the van der Waals forces between liquid and substrate were neglected, and their interaction was taken into account by fixing the contact angle between the liquid and the solid (the wetting angle). Such a formulation of the problem excludes, by definition, the possibility of considering a transition from the flat to the nonuniform liquid surface shape: in Frenkel's treatment the layer is always in a nonuniform state. As we shall see, the shape of the nonuniform liquid film surface tends to be that of a droplet, as found in Ref. 13, only for a sufficiently large volume of the liquid layer.

To simplify the presentation below we propose to introduce a new term—"reconstruction." Reconstruction implies the transition from the flat to the new mechanically stable nonuniform liquid surface state.

The structure of this paper is as follows. Sec. 2 contains the general mechanical equilibrium equation (11) for a liquid film under inverted gravitation conditions, with comments related to the origin of the instability and the corresponding effective energy definition (24).

The one-dimensional version (22) of Eq. (11) is suitable for analytical description of the reconstruction details. We obtain the explicit solution (27), (28) of the one-dimensional reconstruction problem. In contrast to the bulk situation[6,7,9] this solution is not unique. It contains the arbitrary parameter C which must be physically reasonable. One possibility for

defining this parameter could correspond to a soliton-like representation of the solution (27). It corresponds to the requirement $T \to \infty$, where the period T is given by Eq. (28). But this condition is in contradiction with the normalization condition (14). The second possible picture—the periodic reconstruction—is also invalid. This follows from the properties of the second variation for the functional $\mathcal{E}$ defined by Eq. (24). Finally, the main conclusion of Sec. 2 is the proof of mechanically stable reconstruction of the inverted liquid film in the form of an individual droplet which is sensitive to the boundary conditions.

The one-dimensional speculations from Sec. 2 give us reason to believe that the main characteristics of the reconstruction phenomena remain the same in the 2D case (certainly, this assumption cannot be proved). The variational picture for an individual radial droplet in the neutral and charged states is constructed (see Sec. 3). The results obtained are shown to be in agreement with the currently available experimental data. The corresponding fitting is presented in Sec. 3, too.

2. RECONSTRUCTION OF A THIN LAYER OF NEUTRAL LIQUID

2.1. Instability of the flat surface of a liquid layer

We consider first the stability problem for a neutral liquid layer covering a flat horizontal surface of a solid substrate under inverted gravitation conditions (i.e., when the gravitational force is opposite to the attractive van der Waals force between the liquid and substrate). A schematic picture of the system under study is shown in Fig. 1. We introduce the following frame of reference. The (x,y) plane coincides with the substrate surface. The z axis is directed downward, parallel to the force of gravity. The free liquid surface is described by the equation $z = \zeta(\mathbf{r})$, where $\mathbf{r}$ is the two-dimensional vector within the (x,y) plane.

The equilibrium shape of the free surface of the liquid layer is governed by three forces: the gravitational force, the Laplace capillary force, and the van der Waals force, which holds the liquid on the substrate. Under inverted gravitation conditions the pressure at the free surface is given by the following expression:

$$P = -\frac{\alpha \Delta \zeta}{[1 + (\nabla \zeta)^2]^{3/2}} - \rho g \zeta - P_w(\zeta). \qquad (1)$$

Here α is the surface tension, ρ is the density of the liquid, g is the free fall acceleration, and
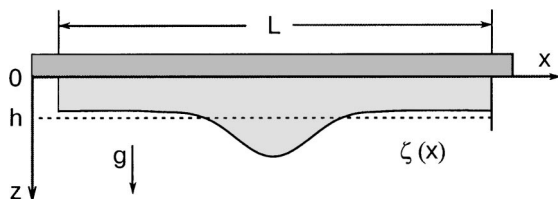

FIG. 1. Schematic view of a reconstructed liquid layer suspended on a substrate. The liquid layer covers a region of the substrate surface between vertical walls. L is the distance between the walls, and h is the mean thickness of layer. The gravitational force is directed downward, along the z axis. The equation describing the free surface is $z = \zeta(x)$.

$$P_w(\zeta) = \frac{f}{\zeta^3}\left(1 + \frac{\zeta}{d_w}\right)^{-1} \qquad (2)$$

is the pressure of the van der Waals forces (f is the van der Waals constant and d_w is some characteristic width).

Expression (1) contains two terms conventional for the capillary problem (the Laplace and the gravitational pressures, see, e.g., Ref. 14). Besides we take into account the van der Waals (vdW) forces between the liquid layer and the solid substrate [the last term $P_w(\zeta)$ of Eq. (1)]. The interpolated form (2) for the van der Waals pressure was proposed in Ref. 15. This expression describes two dependences as limiting cases:

$$P_w(\zeta) = f/\zeta^3 \quad (\text{at } \zeta \ll d_w) \qquad (3)$$

and

$$P_w(\zeta) = f d_w/\zeta^4 \quad (\text{at } \zeta \gg d_w). \qquad (4)$$

The asymptotic expression (3) is applicable in the situations of "thin" films, where the retarding effects in the definition of the vdW forces can be neglected, and expression (4) is valid for "thick" films, for which the retarding effects play a significant role. The measurement of the constants f and d_w is a special problem. It is possible to use some original techniques,[15] or, in the case of superfluid helium, to determine these constants from measurements of the third-sound propagation.[16] For hydrogen films the values of f and d_w are not yet known.

Generally speaking, the definition of the local vdW pressure [like in Eq. (1)] is correct for a flat uniform surface only. It can be used, for example, for estimations of an equilibrium liquid film thickness (see Ref. 17). In the nonuniform case the vdW force has an integral form.[18,19] The local approximation used in Eq. (1) is acceptable if

$$d \ll \lambda, \qquad (5)$$

where λ is the typical nonuniform scale along the liquid surface. For the reconstruction problem under consideration the condition (5) is fulfilled.

If the free surface is flat, and the layer thickness is a constant, $\zeta = h$, then the Laplace term in Eq. (1) goes to zero, and the pressure at the surface is

$$P = -\rho g h - P_w(h).$$

One can introduce the effective gravitational acceleration at the liquid surface $g_{\text{eff}} = \rho^{-1}(\partial P/\partial h)$, which controls the net force acting on the surface. The pressure P has an extremum at the thickness h_*,

$$\partial P/\partial h|_{h=h_*} = 0, \text{ or } \left(-\rho g - \frac{\partial P_w(h)}{\partial h}\right)\Big|_{h=h_*} = 0, \qquad (6)$$

where the derivative $\partial P/\partial h$ changes sign. Thus with increasing layer thickness from $h < h_*$ to $h > h_*$, the effective gravitational acceleration g_{eff} changes sign from positive to negative. This change of the direction of the effective gravitational acceleration implies that the flat state of the free surface should be unstable for thicknesses $h > h_*$, and that small disturbances of the flat surface should grow with time.

In the limiting cases of large or of small thicknesses of the film, the critical thickness h_* is defined as follows:

$$h_* = (4fd_w/\rho g)^{1/5}(h_* \gg d_w), \tag{7}$$

$$h_* = (3f/\rho g)^{1/4} \quad (h_* \ll d_w). \tag{8}$$

Note that a solution of Eq. (6) always exists because the inequality

$$\frac{\partial P_w(h)}{\partial h} < 0 \tag{9}$$

holds for any values of the constants f and d_w.

In the opposite geometry, when the liquid layer covers the upper horizontal surface of the substrate (the gravitational and van der Waals forces have the same direction), the sign of the effective gravitational force is positive for all thicknesses h. This is in agreement with the fact that the flat free layer surface is always stable under "normal" gravitation conditions.

As is shown in the next Section, the instability of flat surface at large h leads to reconstruction, which consists in the creation of a stationary, nonlinear wave of deformations of the free surface.

2.2. Equilibrium shape of the reconstructed liquid surface

In order to describe peculiarities of the reconstruction at the surface of a liquid layer wetting a horizontal flat substrate, we determine the equilibrium shape of the free surface of the layer taking into account the gravitational, capillary, and van der Waals forces. Generally speaking, such a problem reduces to solution of the equilibrium equation

$$P(\zeta) = \text{const}, \tag{10}$$

where $P(\zeta)$ is defined by Eqs. (1) and (2). Equation (10) reflects the fact that in a steady state the pressure at the free surface should be constant over the entire surface. This gives

$$\frac{\alpha \Delta \zeta}{[1 + (\nabla \zeta)^2]^{3/2}} + \rho g \zeta + P_w(\zeta) + p = 0. \tag{11}$$

We denote the constant on the right-hand side of Eq. (10) as p. The value of the constant p should depend on the shape of the liquid surface and should be determined from the "normalization condition"

$$\int d^2\mathbf{r}\,\zeta(\mathbf{r}) = V, \tag{12}$$

where V is the total volume of the liquid in the layer, and the integration is over the area of the substrate covered by liquid.

As is shown below, taking the boundary conditions (wetting the substrate by the liquid) into account is of fundamental importance for consideration of instability and reconstruction phenomena. We discuss here a model case in which the layer is restricted in the horizontal direction by vertical walls (see Fig. 1). The effective wetting angle (the angle of slope of the liquid surface at the point of contact between the liquid and the solid surfaces) we denote as θ. The solution to the set of equations (11), (12) with the following boundary conditions at the vertical walls,

$$|\nabla \zeta| = \tan \theta, \tag{13}$$

will uniquely determine the stationary shape of the liquid surface.

In order to describe the main qualitative features of the reconstruction phenomena we restrict our consideration in this Section to the model case where a one-dimensional (1D) wave of deformation appears at the surface. In this case the function ζ depends on only one horizontal coordinate, x.

The normalization condition (12) in the one-dimensional case reads

$$\int dx\,\zeta(x) = S, \tag{14}$$

where S is the "two-dimensional volume" (area) of the liquid layer.

We suppose, also, that the angle of slope of the free surface with respect to the horizontal plane is small, $|\zeta'| \ll 1$. As is shown below, this condition holds to a high accuracy when $h < 10^3 h_*$, which is true for typical conditions of experiment. In this case one can expand Eq. (11) in the gradient ζ'; as a first approximation this equation will read

$$\alpha \zeta'' + \rho g \zeta + P_w(\zeta) + p = 0. \tag{15}$$

Note that the deformation of the surface is not assumed to be small in the general case, so we keep the term $P_w(\zeta)$ in this equation.

One can show that the development of the instability of the flat surface at the initial stage of the reconstruction, i.e., when

$$(h - h_*)/h_* \ll 1 \quad (h > h_*), \tag{16}$$

does not depend on the model behavior [Eq. (4) or Eq. (3)] assumed for the vdW forces. It is shown below that if the inequality (16) holds, then the stationary nonuniform deviation of the reconstructed surface from the initial flat state is small in comparison to h_*. In this case the surface shape can be calculated using a perturbation approach. For this purpose it is convenient to present the deformation of the surface as

$$\zeta(x) = h_* + \xi(x), \tag{17}$$

where

$$\frac{|\xi(x)|}{h_*} \ll 1. \tag{18}$$

By using the representation (17) the equation (15) can be expanded in a series in the small parameter (18). In this way the deviation $\xi(x)$ should be represented as a series

$$\xi(x) = \xi^{(1)}(x) + \xi^{(2)}(x) + \dots. \tag{19}$$

The term $\xi^{(1)}(x)$ is a small function of the first order, the term $\xi^{(2)}(x)$ is a small function of the second order, etc. Equation (15) reads as a linear approximation

$$\alpha(\xi^{(1)})'' + p^{(1)} = 0. \tag{20}$$

Here $p^{(1)}$ is a first-order correction to the constant p. The second (quadratic) approximation reads

$$\alpha(\xi^{(2)})'' + \frac{1}{2}\left(\frac{\partial^2 P_w}{\partial h^2}\right)_{h_*}(\xi^{(1)})^2 + p^{(2)} = 0. \tag{21}$$

The higher-order equations can be written down in a straightforward way. The values of $p^{(1)}$ and $p^{(2)}$ should be found from the normalization condition (14).

It can be seen that the expression P_w given by Eq. (2) is dropped from the linearized Eq. (20) due to condition (6), and the derivative of P_w (taken at $h=h_*$) is a factor in the quadratic term of the second-order equation (21), only. This means that the choice of the explicit functional dependence of the vdW pressure P_w on the layer thichness $P_w=P_w(h)$ from model (3) or from model (4) is not of importance for analyses of the reconstruction transition at h close to h_*. The derivative $\partial^2 P_w/\partial h^2|_{h=h_*}$ (which can be evaluated easily in both models) controls only the "nonlinearity level" in the system at given h.

As we show in this paper, in the opposite case $h\gg h_*$ the main part of liquid in the layer should be accumulated in a droplet of macroscopic dimension formed at the substrate surface. The thickness of the vdW liquid layer ζ_{min} wetting the substrate outside the droplet should remain small. Moreover, this thickness $\zeta_{min}<h_*$ and it decreases further with increasing total volume V of the liquid. For very large (macroscopic) V the thickness ζ_{min} of the vdW wetting layer should become comparable to or even less than d_w, and in this case the model (3) is more appropriate (see the corresponding estimations in Section 2.3).

Keeping in mind that the goal of this paper is not only to analyze the peculiarities of the reconstruction picture itself but also to compare the results of calculations with the experimental data obtained in[12] for a macroscopic droplet, we will not restrict ourselves to the expansion provided by Eqs. (20), (21) but will consider the more general equation (15). Unfortunately, the integration of Eq. (15) in analytical form with the general expression for $P_w(\zeta)$ from (2) is a complicated problem. But this integraton can be done easily if $P_w(\zeta)$ is taken in a power-like form (3) or (4). In this paper we restrict our consideration to the limiting case (3) for $P_w(\zeta)$. It should be taken into account that the results obtained are valid quantitatively in the macroscopic case $h\gg h_*$ (large V), only. But the qualitative picture of the reconstruction does not depend on the model assumed for the vdW pressure.

Under the above-stated assumptions Eq. (15) reads

$$\alpha\zeta'' + \rho g\zeta + \frac{f}{\zeta^3} + p = 0. \tag{22}$$

In the rest of this Section the solutions of Eq. (22) determined under the additional constraint (14) are analyzed.

It is useful for the next consideration to note here that Eq. (11) with $P_w(\zeta)$ from (3) can be derived from the fol-

lowing variational principle: the total energy of the liquid at equilibrium must reach a minimum, which is found under the additional restriction of Eq. (12), i.e.,

$$\delta\left[\mathcal{E} - p\int d^2\mathbf{r}\zeta(\mathbf{r})\right] = 0. \tag{23}$$

The total energy of the liquid, which includes contributions from the surface tension, the gravitational force, and the van der Waals force, is

$$\mathcal{E} = \int d^2\mathbf{r}\left[\alpha\sqrt{1+(\nabla\zeta)^2} - \frac{1}{2}\rho g\zeta + \frac{f}{2\zeta^2}\right]. \tag{24}$$

The normalization condition (12) is taken into account in Eq. (23) using the Lagrange undetermined multiplier method, the pressure p at surface of liquid playing the role of that undetermined multiplier.

The first integral of the one-dimensional equation (22) is

$$\frac{1}{2}\zeta'^2 + U(\zeta) = C, \tag{25}$$

where $U(\zeta) = (\rho g\zeta^4 + 2p\zeta^3 - f)/2\alpha\zeta^2$.

For analyzing the above set of equations, the following mechanical analogy is useful. Equation (25) can be considered as the energy conservation law for an effective point-like particle with mass $m=1$ moving in an external potential $U(\zeta)$. The variable x plays the role of time, and ζ is the coordinate of the particle. The first term in Eq. (25) is the kinetic energy of the particle, and C is the total energy.

Figure 2 shows the evolution of the effective potential $U(\zeta)$ with increasing layer thickness. Figure 2a illustrates the case of small layer thicknesses $h<h_*$, where h_* is defined by Eq. (6). The point of the maximum $\zeta=h$ on the $U(\zeta)$ curve corresponds to a stable flat surface of the thin liquid layer. The "velocity" of the particle at this point is $\zeta'=0$, and $C=U(h)$.

With increasing h up to the critical value h_* the curve $U(\zeta)$ transforms into a curve with an inflection point at $h=h_*$ (see Fig. 2b). If $h>h_*$, the dip on the curve develops again (Fig. 2c). The point of the minimum of the function $U(\zeta)$ at some $\zeta>h_*$ corresponds to an unstable flat state of the liquid surface. Formation of the possible stationary surface deformation wave is described by periodic motion of the particle in the potential well around the minimum in the region where $U(\zeta)-C<0$.

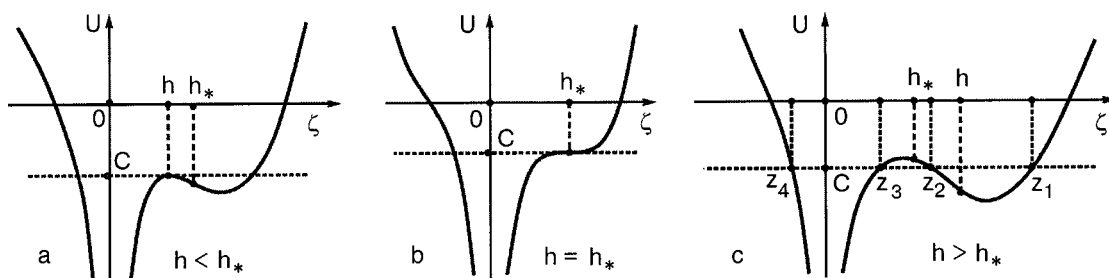The coordinates of the turning points that restrict the motion of the particle can be found from the equation

FIG. 2. Evolution of the effective potential $U(\zeta)$ with increasing mean layer thickness h. a—small thickness, $h<h_*$; b—the thickness of layer is equal to the critical value h_*; c—the thickness $h>h_*$. The points z_i, $i=1,\ldots,4$ correspond to solutions of the equation $U(z)=C$.

$U(\zeta) - C = 0$. In the general case this equation has four different solutions, $\zeta = z_i$, $i = 1,\ldots,4$, which are the roots of the polynomial

$$\rho g \zeta^4 + 2p\zeta^3 - 2\alpha C \zeta^2 - f.$$

We will number these roots in the following order: $z_4 < z_3 < z_2 < z_1$.

Now it is reasonable to remind ourselves that we are trying to find possible nonuniform solutions of the problem (22). In the case of an infinite film area $-\infty < x + \infty$ the non-uniform shape of the surface $\zeta(x)$ can be periodic, or, under some special conditions, a soliton-like one. Therefore we should start by obtaining the periodic solutions of Eq. (22) and investigating their properties.

The general periodic solution to Eq. (25) in the region $z_2 < \zeta < z_1$ can be written in integral form as follows:

$$\int_{z_2}^{\zeta} \frac{d\zeta}{\sqrt{2[C - U(\zeta)]}} = x - x_0. \tag{26}$$

The arbitrary parameter x_0 in the right-hand side of Eq. (26) appears due to the invariance of the initial equation (11) with respect to translations in the horizontal plane.

The integral on the left-hand side of Eq. (26) can be expressed via the elliptic integrals of the first and third kinds, $F(\mu, r)$ and $\Pi(\mu, n, r)$, as follows:

$$\frac{2}{\sqrt{(z_1 - z_3)(z_2 - z_4)}} \left[(z_2 - z_3)\Pi\left(\lambda, \frac{z_1 - z_2}{z_1 - z_3}, r\right) + z_3 F(\mu, r) \right]$$
$$= \frac{x - x_0}{a}, \tag{27}$$

where

$$\lambda = \arcsin \sqrt{\frac{(z_1 - z_3)(\zeta - z_2)}{(z_1 - z_3)(\zeta - z_3)}},$$

$$r = \sqrt{\frac{(z_1 - z_2)(z_3 - z_4)}{(z_1 - z_3)(z_2 - z_4)}},$$

and $a = (\alpha/\rho g)^{1/2}$ is the capillary length.

Equation (27) defines in implicit form the reconstructed shape of the free surface of the liquid layer covering the solid substrate under inverted gravitation conditions. The period T of the surface deformation wave defined by Eq. (27) is equal to

$$T = \frac{4a}{\sqrt{(z_1 - z_3)(z_2 - z_4)}} \left[(z_2 - z_3)\Pi\left(\frac{\pi}{2}, \frac{z_1 - z_2}{z_1 - z_3}, r\right) \right.$$
$$\left. + z_3 F\left(\frac{\pi}{2}, r\right) \right]. \tag{28}$$

We should mention that the roots z_i depend on two free parameters, i.e., on the pressure p at the surface and on the constant of integration C (in addition to the dependence on the constants characterizing the properties of the liquid and its interaction with the substrate). The solution defined by Eq. (27) should obey the normalization condition (14), too. This condition provides an additional relation between the parameters p and C. Thus one can conclude that the function ζ depends on one free parameter, in addition to the dependence on the x coordinate. This parameter can be chosen arbitrarily. In the subsequent analysis we suppose that the constant C plays the role of this parameter. The period T of the stationary wave depends on this parameter, as well.

One possibility of avoiding the problem nonuniqueness of the parameter C could be the realization of a soliton-like solution for $\zeta(x)$. Following the conventional recommendation (see, e.g., the problem of steady-state wave propagation at the free liquid surface in Ref. 20) we have to use for this purpose the additional requirement

$$T \to \infty. \tag{29}$$

However, this requirement turns out to be incompatible with the normalization condition (14), because in this case the integral

$$\int dx (\zeta(x) - h) \tag{30}$$

diverges. Therefore the conventional soliton-like solution is not valid.

Now, turning back to the general periodic picture of reconstruction, we have only one possibility for resolving the problem of nonuniqueness of the parameter C. Here it is necessary to use stability arguments. Using the results obtained below (see paragraph 2.3) as a check, we can show that the deformation $\zeta(x)$ with the maximal period T is the most favorable energetically. For the case of unbounded geometry $-\infty < x < +\infty$ this means that the period of the structure on the reconstructed surface should tend to infinity. Therefore energetically stable periodic reconstruction of the unbounded thin helium film is impossible, too.

Nevertheless, we can bring the factor of stability into the formulation of the problem artificially, by considering a film of limited area. Such a scenario corresponds to the experimental situation. We therefore assume that

$$-L/2 \leq x \leq L/2 \tag{31}$$

and, in addition, that the following boundary conditions are fulfilled:

$$\zeta'|_{\pm L/2} = 0. \tag{32}$$

The simplest boundary conditions (32) with the contact angle at the walls $\theta = 0$ are necessary to save the basic instability indicator h_* in the form (6).

After reformulation (31), (32) the dependence of the function $\zeta(x)$ defined by Eqs. (27), (28) on the parameter C changes its character. Under the new boundary conditions C can take only a definite discrete set of values. Now our objective is to demonstrate that the most energetically preferable solution can be found among the solutions corresponding to these values.

2.3. Reconstruction of the free surface of a thin layer in restricted geometry

Following the speculations above, we have to investigate the solutions (27) under the boundary conditions (32).

The values of the parameter C at which the boundary conditions (32) are satisfied can be found from the requirement that the ratio L/T be equal to some natural number N. The number N coincides with the number of maxima of the
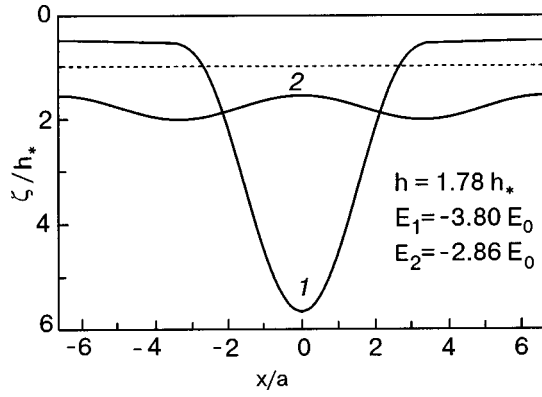
FIG. 3. Results of calculations of the stationary shape of the reconstructed layer with a single droplet (curve *1*) and with two droplets (curve *2*) formed at the surface. The *x* coordinate is normalized to the capillary length *a*, and the layer thickness is normalized to the critical thickness h_*. The distance between the vertical walls is equal to $L=13.3a$. The mean thickness of the layer is $h=1.78h_*$. The dashed line corresponds to the flat surface of a layer with $h=h_*$. The estimated energy of the single- and two-droplet solutions are $E_1=-3.80E_0$, and $E_2=-2.86E_0$, where $E_0=\sqrt{\alpha\rho g}h^2/4$.

function $\zeta(x)$ in the region $-L/2<x<L/2$. Thus such a solution describes the formation of *N* humps, or "droplets," at the liquid surface. These droplets are connected between each other by the liquid layer covering the substrate.

Detailed numerical analysis of the stability problem for the solution with *N* droplets at the surface shows that only the solution with $N=1$ can be realized in experiment; see below.

First, the energy of the liquid layer with *N* droplets at the surface ("*N* droplet configuration") is estimated numerically. The results of estimations show that the configuration with $N=1$ corresponds to a minimum of the energy, while the energy of configurations with $N>1$ is higher. Figure 3 shows an example of two possible stationary profiles of the reconstructed surface with $N=1$ (curve *1*) and $N=2$ (curve *2*) calculated for the case $h=1.78h_*$. The horizontal coordinate *x* is expressed in units of the capillary length *a*, and the vertical coordinate is expressed in units of the critical thickness h_*. The distance between the vertical walls is $L=13.3a$. The line with zero vertical coordinate is the substrate surface. The horizontal dashed line corresponds to the flat layer of thickness $h=h_*$. The estimated energy of the configurations is expressed in units of the energy $E_0=(\alpha\rho g)^{1/2}h^2/4$. The energy of the configuration with $N=1$ (the profile has one maximum) is equal to $E_1=-3.80E_0$, while the energy of the configuration with two maxima is equal to $E_2=-2.86E_0$. Thus the configuration with $N=1$ is energetically preferable and should be realized in experiment.

Now we study the stability of the solution with a single maximum against small perturbations of the surface. For this purpose the sign of the second variation of the energy $\delta^{(2)}E$ at small perturbations of the shape of the liquid surface is determined. For a stable solution the second variation is positive definite (a solution should correspond to a minimum of the total energy). The variation $\delta^{(2)}E$ is represented by the following functional, which is quadratic in the small perturbation $\delta\zeta(x)$ of the steady-state surface profile $\zeta(x)$:

$$\delta^{(2)}E=\int_{-L/2}^{L/2}dx\,\delta\zeta(x)\hat{\Lambda}\delta\zeta(x),$$

where

$$\hat{\Lambda}=-\frac{\alpha}{2}\frac{\partial^2}{\partial x^2}-\frac{\rho g}{2}+\frac{3f}{\zeta^4(x)}$$

is a linear differential operator. The positive definiteness of the second variation of energy is equivalent to the fact that the operator $\hat{\Lambda}$ has only positive eigenvalues $\lambda_n>0$. The problem of finding the spectrum λ_n of the operator $\hat{\Lambda}$ can be mapped onto the well-known problem of the energy spectrum of a quantum particle with mass $m=1/\alpha$ moving in the potential well $U=-\rho g/2+3f/\zeta^4(x)$. We study the stability problem for the case when the perturbation does not affect the wetting conditions at the walls, so the boundary conditions for the "wave function" are $\delta\zeta'(x)=0$ at $x=\pm L/2$. It is clear from this consideration that the perturbation that corresponds to the lowest eigenvalue of the "Hamiltonian" $\hat{\Lambda}$ (i.e., to the "ground state level") is the most dangerous for destroying the stability of the steady-state surface shape.

The low-energy part of the spectrum of the operator $\hat{\Lambda}$ is found numerically, by direct diagonalization of the matrix corresponding to the operator $\hat{\Lambda}$. The matrix elements Λ_{mn} are calculated in an orthogonal normalized basis consisting of a set of symmetric (*g*) and antisymmetric (*u*) functions

$$\sqrt{2/L}\cos(q_n^{(g)}x),\quad\sqrt{2/L}\sin(q_n^{(u)}x),$$

where $q_n^{(g)}=2\pi(n+1)/L$,

and $q_n^{(u)}=\pi(2n+1)/L$, $n=0,1,2,...$.

The function $\zeta(x)$ is symmetric with respect to inversion of the *x* coordinate, $\zeta(-x)=\zeta(x)$. This means that the matrix is diagonal with respect to the index of the perturbation parity, i.e., only the matrix elements with two *u* or two *g* indices are nonzero. This enables examination of the stability problem against symmetric and antisymmetric perturbations separately. The matrix element calculated for two basis functions of the same parity corresponding to excitation levels *n* and *m* is

$$\Lambda_{nm}=\left[\frac{\alpha}{2}-\frac{\rho g}{2}\right]\delta_{mn}+3f\left(\frac{1}{\zeta^4(x)}\right)_{nm},$$

where δ_{nm} is the Kroneker delta, and the index *u* or *g* is omitted. The elements $(1/\zeta^4)_{nm}$ are calculated numerically for the lowest 10 harmonics, $n,m\leqslant10$. Numerical estimations show that taking higher harmonics ($n,m>10$) into account does not change noticeably the character of the lower part of the spectrum of the operator $\hat{\Lambda}$. We study the case where $L<15a$ and $h<10h_*$. Analysis show that all eigenvalues are positive, $\lambda_n>0$. This means that small perturbations of the reconstructed surface with $N=1$ increase the total energy, and, hence, the shape of the steady state of the surface is stable.

Such a direct stability analysis cannot be done successfully by numerical reasoning if the mean thickness of the liquid layer $h>10h_*$ or the dimension $L>15a$, due to losses of accuracy in the numerical calculations of the values of the roots z_i.

Meanwhile, at high h one can use the following qualitative considerations to demonstrate the fact that the solution with one droplet on the reconstructed surface is energetically preferable, and only this configuration can be formed.[21] In the general situation, the profile of the steady state of the reconstructed surface corresponds to the formation of N droplets at the surface, which are connected by the liquid layer covering the substrate. In the limiting case where the volume of liquid is macroscopically large, the thickness of such a layer is small in comparison to the height of the droplet. The main part of the liquid is accumulated in droplets, and the volume of liquid contained in the layer covering the substrate between the droplets is negligibly small. As a first approximation the shape of each droplet can be described by the 1D Frenkel solution (see Ref. 13)

$$\zeta(x) = \frac{A_0}{2}(1 + \cos x/a),\qquad(33)$$

where the height of the droplet is

$$A_0 = S/\pi a,\qquad(34)$$

and S is the "two-dimensional volume" (area) of the droplet. The energy of a single droplet whose shape is described by Eq. (33) can be calculated directly. This gives

$$E_1(S) = -\frac{\alpha}{2\pi a^3}S^2.\qquad(35)$$

The total energy of the liquid can be estimated as a sum of energies of each "isolated" droplet. If the total volume of liquid, S, is distributed among N identical droplets, then the energy of such a configuration can be estimated as follows:

$$E = NE_1(S/N) = -\frac{\alpha}{2\pi a^3}\frac{S^2}{N}.\qquad(36)$$

Thus the energy of the liquid is increased if the liquid is redistributed from one droplet into a number of droplets. In the macroscopic case $h \gg h_*$ the solution with one droplet formed inside a cell is also preferable from energy considerations.

From the results obtained it follows that the consideration of the reconstruction process can be restricted to the case where a single droplet is formed at the surface. Below we present results of numerical computations of the evolution of the shape of the reconstructed layer with one droplet formed at the surface with increasing mean layer thickness h.

Figure 4 shows the shape of the reconstructed surface obtained by numerical integration of Eq. (22) in cases where the mean liquid layer thickness is equal to $h = 1.5h_*$ (curve *1*), $2.2h_*$ (curve *2*), and $7h_*$ (curve *3*). The x coordinate at the graph is expressed in units of the capillary length a, and the z coordinate is expressed in units of the critical thickness h_*. The distance L between the vertical walls is equal to $9a$. The z coordinate of the substrate surface is equal to zero.

It can be seen from Fig. 4 that the amplitude of the wave of surface deformation increases gradually with increasing h above h_*. The maximum of the deformation is situated at the center of the cell. The wave acquires a droplet-like shape at sufficiently large h. The characteristic horizontal size of the droplet is of the order of a few capillary lengths, and it
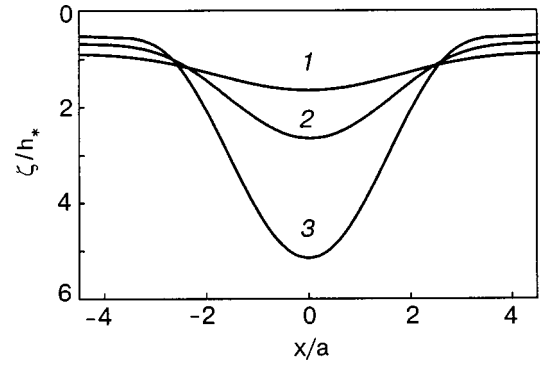

FIG. 4. Evolution of the shape of the reconstructed liquid layer with a single droplet at the center with increasing mean thickness h. Curve *1*: $h = 1.5h_*$, curve *2*: $h = 2.2h_*$, curve *3*: $h = 7h_*$. The thickness of the layer is expressed in units of the critical thickness. The distance between the vertical walls is $L = 9a$.

depends weakly on the mean thickness h. The thickness $\zeta_{min} = \zeta(\pm L/2)$ of the liquid layer covering the substrate outside the droplet is less than the critical thickness h_*, and it decreases with increasing mean thickness h. In the case $h \gg h_*$ the main part of the liquid is concentrated in the droplet, and the volume of liquid in the thin layer wetting the substrate outside the droplet is much smaller than the total liquid volume.

As was shown in Ref. 21

$$\left(\frac{\zeta_{min}}{h_*}\right)^3 \simeq \frac{h_*}{3\zeta_{max}},\quad \zeta_{max} \simeq A_0 + \zeta_{min}.\qquad(37)$$

Here A_0 is given from Eq. (34). The combination of Eq. (37) with the requirement $\zeta_{min} < d_w$ leads to estimates of the critical value S_{min} necessary for simplification (3). Thus it should be

$$S > S_{min},\quad \text{where}\quad S_{min} = \pi a h_*^4/3d_w^3.\qquad(38)$$

Estimate (38) confirms the propositions made in the preceding qualitative analysis.

Figure 5 shows the dependence of the droplet height $A = \zeta(0) - \zeta(L/2)$ on the parameter $\delta = (h - h_*)/h_*$ (the overcriticality parameter). For comparison of our results with the results of macroscopic considerations,[13] the droplet height A
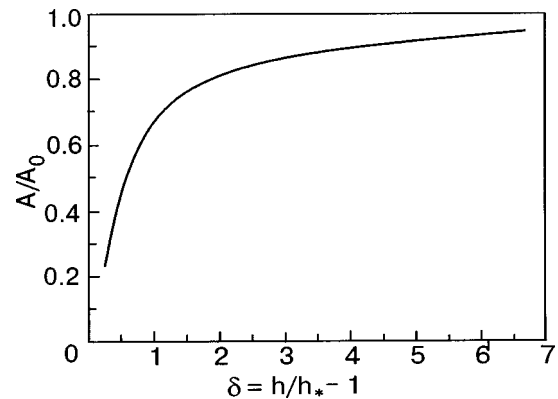

FIG. 5. Dependence of the amplitude of the wave of surface deformation on the overcriticality parameter $\delta = h/h_* - 1$. Amplitudes are measured in units of A_0, where $A_0 = S/4\pi a$ is the amplitude of Frenkel's droplet, and S is the total area of the one-dimensional layer.

is normalized to the height A_0 given by Eq. (34) for Frenkel's droplet, i.e., on the height of the droplet formed under inverted gravitation conditions from a liquid of the same volume $S=Lh$ and calculated in the case where the angle of wetting of the substrate (not the walls) by the liquid is $\theta =0$. In these calculations the horizontal dimension of the cell is $L=9a$, which is the same as in Fig. 4.

It follows from Fig. 5 that at large thicknesses $h \gg h_*$ (i.e., at high overcriticality level, $\delta \gg 1$) the height of the droplet formed at the center of the cell is close to the height of Frenkel's droplet of the same volume. The difference between the heights of the ''van der Waals droplet'' and Frenkel's droplet is about 10% at $\delta \approx 6$ and decreases with increasing δ. Thus, at a layer thickness one order of magnitude higher than the critical thickness h_* the shape of the droplet formed under inverted gravitation conditions can be described to rather good accuracy by the ''macroscopic'' solution (33). The effective angle of wetting of the substrate by liquid at the edges of the macroscopic droplet is

$$\theta_{\text{eff}}=0. \tag{39}$$

The characteristic horizontal dimension of the droplet is of the order of the capillary length at $\delta > 1$. Thus, if the overcriticality level is not very small and the dimensions of the cell are much larger than a, then the boundary conditions should have a weak effect on the equilibrium shape of the droplet.

At $h \sim h_*$ the dependence of the droplet height $A =A(h)$ differs significantly from that obtained in the macroscopic approximations, and at $h=h_*$ (at overcriticality $\delta =0$) the height of the droplet tends to zero. At thicknesses smaller than the critical thickness the flat liquid surface is stable, and the layer is in the nonreconstructed state (no deformation wave appears at the surface). Details of the behavior of the surface shape at h close to h_* depend on the value of the wetting angle θ. The corresponding analysis will be published elsewhere.

Let us consider in addition to (38) the limitations for applicability of the results obtained. The main assumption in the treatments presented is the small-angle approximation, $|\zeta'(x)| \ll 1$. The characteristic length scales in the horizontal and vertical directions differ drastically. The horizontal size of the deformation wave is of the order of the capillary length. For liquid hydrogen it is equal to $a \approx 0.2$ cm. The characteristic thickness scale is represented by the critical thickness h_*, and in the case of a hydrogen film covering a dielectric substrate it is $h_* \approx 10^{-4}$ cm. The condition at which our treatment fails can be written as $A/a \sim 1$, or, in equivalent form, $h \sim a^2/L$. One can conclude from these estimations that the results of our considerations are valid (from the side of large thickness) if $\delta < a/h_* \sim 10^3$, or $h <10^{-1}$ cm, for $L \sim a$. From the side of small thickness the applicability of the results is restricted to the possibility of considering the liquid as a continuous medium, i.e., $h >10^{-6}$ cm. Thus there is a macroscopically wide interval of layer thickness where the results obtained are valid.

The problem of the stationary shape of a liquid droplet can be solved without the assumption of smallness of the gradient of the surface deformation if the capillary forces are taken into account (see, e.g., Ref. 13). This assumption is of importance for the representation of the van der Waals pressure as a power law of the layer thickness in Eq. (1). The condition $|\zeta'(x)| \ll 1$ is of crucial importance for calculations of the electric pressure at the surface of charged liquids, too (see the next Section).

3. MACROSCOPIC CHARGED DROPLET FORMED ON A SOLID SUBSTRATE

3.1. Equipotentially charged surface of a liquid in an electric field

In this Section the evolution of the shape of a charged droplet with increasing mass of the droplet and external electric field strength is studied. Calculations are carried out for two cases, where the droplet is suspended from a metallic substrate or is lying on the substrate. In the first case the direction of the stretching electric force acting on the liquid surface is the same as the direction of the force of gravity, and in the second case the forces have opposite directions. These situations correspond to conditions of experiments[12] with liquid hydrogen droplets. In the experiments the upper or the lower plate of a horizontally arranged flat capacitor play the role of the substrates.

It is supposed that the charges are localized under the free surface of the liquid and they create a quasi-two-dimensional layer, which totally screens the electric field in the bulk of the liquid (i.e., the electric field and the density of charges in the bulk of the liquid are equal to zero). The electric potential at the liquid surface is maintained equal to some constant value by an external battery, and the total number of positive charges localized under the surface can be varied due to a continuously working source of charges, which is placed in the bulk of the liquid.

A macroscopic situation will be considered here, i.e., the height of the droplet is supposed to be much larger than the critical thickness h_*. As was pointed out above, a typical value of the critical thickness is of the order of 10^{-4} cm, and it is smaller than droplet heights suitable for optical observations. The influence of the van der Waals forces on the shape of the macroscopic droplet is negligibly small, and one can exclude it from consideration. Meanwhile, the van der Waals forces are comparable with the electric and gravitational forces at the edges of the droplet, where the liquid depth becomes of the same order as the thickness of the thin liquid layer wetting the substrate, i.e., of the order of the critical thickness. As is shown in the previous Section, the influence of the wetting layer at the substrate surface on the shape of the droplet could be taken into account by using the effective boundary conditions (39) that read $\zeta'=0$ at the edges of the droplet. The thin liquid layer wetting the substrate outside the droplet should be considered to have zero thickness ($\zeta =0$) in the macroscopic treatment used in this Section.

It was shown above that almost all the volume of a neutral liquid covering a substrate is concentrated in a single droplet at the substrate surface. It is natural to assume that this property also holds for a charged liquid, and a single droplet should appear at the equipotentially charged surface of the liquid.

Here we consider a real ''two-dimensional'' situation in which the shape of the liquid surface depends on two coordinates in the (x,y) plane. We also assume that the droplet

formed at the surface has an axially symmetric shape, i.e., the liquid surface is described by an equation $z=\zeta(|\mathbf{r}|)$.

Calculations of the equilibrium shape of the droplet are carried out in two steps. First, the effective energy of the charged droplet formed at the capacitor plate is calculated as a function of the shape of the droplet and of the voltage U applied to the capacitor. After that, the dependence of the height A and the effective radius R of the droplet is found using the variation approach, from the condition that the effective energy acquires a minimal value at the equilibrium state.

Let us consider a droplet suspended on the upper plate of the flat horizontal capacitor (i.e., the droplet is under inverted gravitation conditions). The equilibrium shape of the liquid droplet with an equipotentially charged surface corresponds to a minimum of the effective energy (see Ref. 22)

$$\mathcal{E}=\mathcal{E}_{\text{mech}}-\frac{1}{8\pi}\int d^2\mathbf{r}\int_{\zeta}^{d}dz\mathbf{E}^2. \tag{40}$$

Here $\mathcal{E}_{\text{mech}}$ is the mechanical energy of the liquid (a sum of the surface energy and the energy of the liquid in the gravitational field), the last term in the right-hand side represents the energy of the electric field in the capacitor, $\mathbf{E}$ is the electric field strength in the gas phase, and d is the distance between the capacitor plates. The frame of reference is chosen the same as was used in the previous Section: the (x,y) plane coincides with the surface of the upper capacitor plate, from which the droplet is suspended, and the z axis is directed along the gravitational force.

The form of the expression for the electric field energy in a capacitor depends on the ratio between the horizontal size of the droplet (its effective radius R) and the distance d between the capacitor plates. In the calculations presented below we assume that the condition $d/R\ll1$ holds.

Also, in order to simplify the calculations it is assumed that the height of the droplet A is small in comparison to the distance d, $A\ll d$.

From this it follows that the angle of the slope of the surface with respect to the horizon is given in order of magnitude by a product of two small quantities, $|\nabla\zeta|\sim\zeta/R\sim(\zeta/d)\times(d/R)$, and it is a small quantity of high order. Restrictions for applicability of the results obtained, which follow from these assumptions, will be discussed later.

In order to determine the contribution of the electric field energy to the total effective energy (40) one should calculate the electric potential φ inside the capacitor. The electric potential obeys Laplace's equation (Δ is the Laplacian operator) and the boundary conditions at the upper and lower plates

$$\Delta\varphi=0, \quad \varphi|_{z=\zeta(\mathbf{r})}=0, \quad \varphi|_{z=d}=U. \tag{41}$$

The value of the electric potential at the charged surface of a droplet suspended from the upper plate is assumed to be equal to the value of the potential at the plate. This value is chosen equal to zero. The value of the potential at the lower plate is denoted as U.

It is convenient to introduce a new potential ψ defined by the equation $\psi=\varphi+E_0z$, where $E_0=-U/d$. As follows from Eq. (41), the boundary conditions for the ψ potential are the following:

$$\psi|_{z=\zeta(\mathbf{r})}=E_0\zeta, \quad \psi|_{z=d}=0. \tag{42}$$

In the case under study, $\zeta\ll d\ll R$, the potential ψ could be calculated using perturbation theory, with the liquid layer thickness ζ considered as a small function,

$$\psi=\psi^{(1)}+\psi^{(2)}+\dots, \tag{43}$$

where $\psi^{(1)}\sim\zeta$, $\psi^{(2)}\sim\zeta^2$, etc. In order to determine the boundary conditions for the functions $\psi^{(n)}$ one should substitute the expansion (43) into Eq. (42) and equate the terms of the same order. For the first-order terms the conditions read

$$\psi^{(1)}|_{z=d}=0, \quad \psi^{(1)}|_{z=0}=E_0\zeta. \tag{44}$$

We assume that the droplet has an axially symmetric shape, i.e., $\zeta=\zeta(r)$, where $r=|\mathbf{r}|$. The solution of the problem of the potential distribution with boundary conditions (44) is known from potential theory. In the region $\zeta\le z\le d$, where the electric field is not equal to zero, the solution can be found using a Bessel transformation. It reads

$$\psi^{(1)}(r,z)=E_0\int_0^{\infty}dtJ_0(rt)F(t)t\frac{\sinh t(d-z)}{\sinh td}, \tag{45}$$

where $F(t)=\int_0^{\infty}drrJ_0(rt)\zeta(r),$

and $J_0(t)$ is the Bessel function of order zero.

The Bessel transform $F(t)$ of the function $\zeta(r)$ is essentially nonzero if its argument $t\lesssim 1/R$. Thus the arguments of the hyperbolic functions in the right-hand side of Eq. (45) are of order $d/R\ll1$, and these functions can be expanded in series in their arguments. Below we need the expression for the derivative of the $\psi^{(1)}$ function. Calculations give the following relation:

$$\partial\psi^{(1)}/\partial z|_{z=0}=-E_0\zeta/d. \tag{46}$$

Here we use the inverse Bessel transformation in the calculations.

We will calculate the dependence of the electric field energy on the shape of the droplet up to third-order accuracy in the ratio ζ/d. The energy of the electric field in the capacitor is expressed via the ψ potential as

$$\mathcal{E}_{\text{el}}=\frac{1}{8\pi}\int d^2\mathbf{r}\int_{\zeta}^{d}dz(\nabla\psi)^2, \tag{47}$$

where we have neglected an inessential constant in the right-hand side of (47). In the same third-order approximation this expression can be reduced to an integral over the surface of the upper plate as follows:

$$\mathcal{E}_{\text{el}}=-\frac{E_0}{8\pi}\int d^2\mathbf{r}\left(\zeta\left[\frac{\partial\psi^{(1)}}{\partial z}\right]_{z=0}+\zeta^2\left[\frac{\partial^2\psi^{(1)}}{\partial z^2}\right]_{z=0}\right). \tag{48}$$

It follows from the relation obtained that the energy of the electric field written up to the third-order terms is expressed via the first-order term of the ψ potential and via the ζ function. One can eliminate the function $\psi^{(1)}$ from expression (48) using Eq. (46) and a similar equation for the second derivative of the potential obtained from the integral representation (45). This gives the following dependence of the electric field energy in the capacitor on the droplet shape:

$$\mathcal{E}_{el}=\frac{U^2}{8\pi d}\int d^2\mathbf{r}\left(\frac{\zeta^2}{d^2}+\frac{\zeta^3}{d^3}\right).$$

One can see from this expression that the energy of the electric field depends locally on the thickness of the liquid layer $\zeta(r)$. This results from the assumption that the effective radius of the droplet is large in comparison to the distance between the capacitor plates.

In calculating the contribution from the surface energy to the mechanical energy of the liquid to the same accuracy, one should take into account only the lowest-order terms in the angle of slope of the surface in the expression for the capillary energy.

The total effective energy of the system (40) calculated in the approximation adopted is given by the following expression:

$$\mathcal{E}=\frac{\alpha}{2}\int d^2\mathbf{r}(\nabla\zeta)^2-\frac{1}{2}\rho g\int d^2\mathbf{r}\zeta^2-\frac{U^2}{8\pi d}$$
$$\times\int d^2\mathbf{r}\left(\frac{\zeta^2}{d^2}+\frac{\zeta^3}{d^3}\right). \tag{50}$$

Note that the electric energy in (40) has the opposite sign to the mechanical energy.

3.2. Equilibrium shape of a charged droplet

Let us determine the dependence of the shape of a charged droplet on the voltage U applied to the capacitor. A nonlinear equation describing the shape of the droplet can be derived using a variational principle from expression (50) for the effective energy of the system in the same way as was done for Eq. (1). But the solution of the equation obtained in the 2D situation meets difficulties because of the absence of a first integral of the equation. In this work we determine the height and the radius of the droplet using a variational approach in which the shape of the droplet is approximated by some trial function.

We seek the coordinate dependence of the trial function ζ in a general axially symmetric form

$$\zeta(\mathbf{r})=Af\left(\frac{r}{R}\right), \tag{51}$$

where A is the droplet height and R is the effective radius of the droplet. Parameters A and R are positive variables playing the role of variational parameters in the problem. The function $f(x)$ is a bell-shaped function of the variable $x=r/R$. It is normalized by the conditions $f(0)=1$ and $f(x)\to0$ at $x\gg1$ (recall that the effective wetting angle at the edges of the droplet is equal to zero).

The dependence of the total energy of the liquid on the variational parameters A and R can be calculated by substituting the function (51) into expression (50). This gives the following expression:

$$\mathcal{E}=\frac{\alpha}{2}c_0A^2-\left(\frac{1}{2}\rho g+\frac{U^2}{8\pi d^3}\right)c_2A^2R^2-\frac{U^2}{8\pi d^4}c_3A^3R^2, \tag{52}$$

where the constants c_n are defined as

$$c_0=2\pi\int_0^\infty dxxf'^2(x),$$

$$c_n=2\pi\int_0^\infty dxxf^n(x)\quad(\text{at }n>0). \tag{53}$$

The region of integration in (53) is enlarged to infinity thanks to convergence of the integrals.

The values of the variational parameters in the equilibrium state can be determined from the condition that the effective energy of the liquid acquires a minimal value under the additional normalization condition (12). The normalization condition can be expressed via the variational parameters as

$$c_1AR^2=V. \tag{54}$$

The condition (54) can be taken into account using the Lagrange multipliers method, as was done earlier in calculations of the stationary shape of the neutral liquid surface. Thus the values of the parameters in the equilibrium state can be determined from the equations

$$\frac{\partial\widetilde{\mathcal{E}}}{\partial A}=0,\quad\frac{\partial\widetilde{\mathcal{E}}}{\partial R}=0, \tag{55}$$

where $\widetilde{\mathcal{E}}=\mathcal{E}-pAR^2$ and p is a Lagrange multiplier.

The solution of Eqs. (55) gives the following dependence of the droplet height A on the voltage U:

$$A=k_1V\left(\frac{U^2}{4\pi d^3}+\rho g\right)\left(\alpha-\frac{k_2U^2V}{4\pi d^4}\right)^{-1}. \tag{56}$$

The constants in (56) are equal to $k_1=c_2/2c_0c_1$, $k_2=c_3/c_0c_1$.

Note that the function $f(x)$ enters into expressions (54), (56) only as an integrand in the constants k_1, k_2, and c_1. Thus the choice of the explicit form of the function $f(x)$ has only a weak effect on the calculated values of the droplet sizes.

In order to estimate the values of the constants in (56) we choose the function $f(x)$ in the form

$$f(x)=q(J_0(x)-J_0(\beta_1)),\quad 0<x<\beta_1,$$
$$f(x)=0,\quad x>\beta_1. \tag{57}$$

Here $\beta_1\approx3.83$ is the least root the first-order Bessel function, $J_1(\beta_1)=0$, and $q=(1-J_0(\beta_1))^{-1}\approx0.71$ is a normalization constant. The explicit form (57) of the function $f(x)$ is chosen from the following considerations. The function (57) is a solution of the equation which describes the liquid surface shape in a linear approximation over the droplet's height. The exact shape of the droplet should be close to that function at a small nonlinearity level in the system, i.e., when the inequalities $|\nabla\zeta|\ll1$, $A/d\ll1$ hold.

The values of the constants estimated from definition (53) using the function (57) are $k_1=0.0754$, $k_2=0.106$, and $c_1=18.5$.

The dependence of the effective radius of the droplet on the voltage U can be calculated from Eq. (54) as $R=(V/c_1A)^{1/2}$, where A is given by Eq. (56). The droplet diameter D (i.e., the diameter of the circular base of the droplet) can be estimated as $D\approx7.66R$.

Let us analyze the result obtained. The droplet height A estimated from (56) grows infinitely when the voltage is increased to the value

$$U_{c2} = \left(\frac{4\pi\alpha d^4}{k_2 V}\right)^{1/2}. \tag{58}$$

At $U > U_{c2}$ Eqs. (55) have no solution. At these voltages the effective energy of the droplet as a function of amplitude A decreases with increasing A and, hence, has no minimum. That means that a suspended droplet is absolutely unstable at high voltages. Thus the voltage U_{c2} given by Eq. (58) can be considered as an estimate for the second critical voltage, at which the liquid droplet loses mechanical stability in the external electric field. At voltages higher than U_{c2}, discharge from the surface accompanied by transfer of liquid from the suspended droplet to the lower plate of the capacitor should take place. Expression (58) should be considered only as an order-of-magnitude estimate because in the case where the amplitude A is comparable with the distance d the theory developed is of a qualitative character.

Dependence (56) can be used to describe the evolution of the shape of the droplet formed from a liquid layer covering the lower plate of the capacitor, with increasing voltage. In this case the stretching electric force, which acts on the equipotentially charged surface of the droplet, is directed oppositely to the gravitational force. To obtain the voltage dependence of the amplitude of a droplet lying on a substrate one should change the sign of the constant g in Eq. (56). This gives the formula

$$A = 0 \quad \text{at} \quad U < U_{c1} = \sqrt{4\pi\rho g d^3},$$

$$A = k_1 V \left(\frac{U^2}{4\pi d^3} - \rho g\right)\left(\alpha - \frac{k_2 U^2 V}{4\pi d^4}\right)^{-1} \quad \text{at} \quad U > U_{c1}. \tag{59}$$

Note that the voltage U_{c1} coincides with the critical voltage at which the reconstruction of a thin equipotentially charged layer of liquid takes place, see Ref. 3. From the dependence (59) one could see that a droplet is formed at the surface of the liquid layer if the "renormalized" gravitational acceleration $g_{\text{eff}} = g - U^2/U_{c1}^2$ changes its sign from positive to negative with increasing voltage U. Thus at $U > U_{c1}$ the surface of the liquid layer condensed on the lower plate of the capacitor could be considered, as a first approximation, to be under "inverted gravitation conditions," where the effective gravitational acceleration is directed oppositely to the real gravitational force. This situation is quite similar to the case of the reconstruction of the thin van der Waals liquid layer considered in the previous Sections. But here the renormalization of the gravitational acceleration that acts on the liquid arises from the electric forces.

As one can see from Eq. (58), the second critical voltage U_{c2}, at which the droplet surface becomes unstable, does not depend on the gravitational acceleration. Thus in the "small angle" approximation used the voltages at which the discharge from the surface should take place have the same values in the cases of lying and suspended droplets.

We use the $A(U)$ dependence given by Eq. (56) for treatment the results of experiments[12] with charged hydrogen droplets suspended on a metal substrate. In these experi-
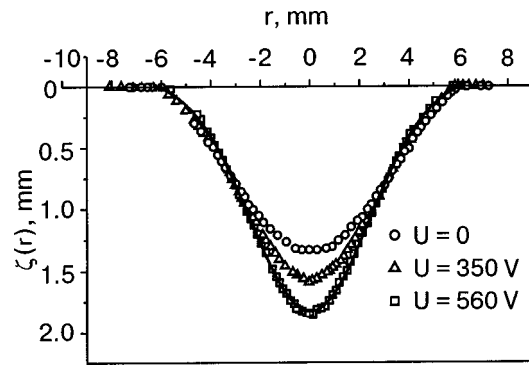

FIG. 6. Droplet profiles obtained by scanning snapshots of a suspended charged hydrogen droplet at different voltages U applied to the capacitor.

ments the droplet was created by condensation of hydrogen from a gas phase on a cooled upper plate of a horizontally arranged capacitor. This technique allows one to control the layer thickness over a wide range by using precise control of the substrate temperature and of the volume of gas introduced into the experimental cell.

In these experiments the evolution of shape of the suspended charged droplets with increasing voltage applied to the capacitor plates and with increasing volume of the droplet was studied.

Figure 6 shows the changes of the profile of the droplet with increasing voltage U, obtained by analysis of snapshots of the droplet. The volume V of the droplet was equal to 60 mm³ in this experiment. The distance between the capacitor plates was $d = 3$ mm. The experimental data in Figs. 7 and 8 are reproduced from Figs. 8 and 9 of Ref. 12. Figure 7 shows the dependence of the droplet height A on the voltage U obtained from plots in Fig. 6. The points represent the results of measurements, and the solid curve the dependence (56). Note that the voltage at which the discharge of the surface was observed is equal to $U_{c2} \approx 800$ V. Figure 8 demonstrates the evolution of the dependence of the height of the droplet on the droplet volume with increasing voltage U. The solid circles show the dependence of the amplitude A on the volume V measured at zero voltage $U = 0$. The squares show the same dependence measured at $U = 630$ V. The dashed lines correspond to the theoretical dependences (56) calculated at the given voltages.

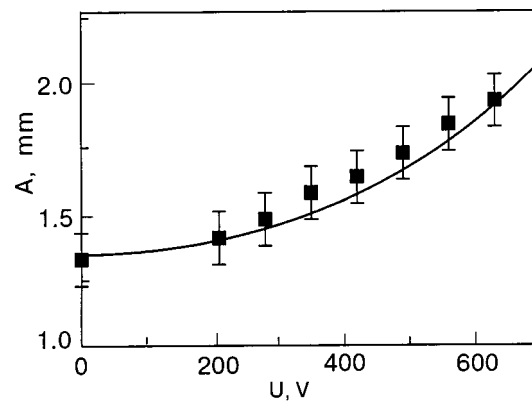

FIG. 7. Dependence of the height of the suspended droplet on the voltage applied to the capacitor. The volume of the droplet is equal to $V = 60$ mm³. Points—experiment, line—theoretical dependence (56).
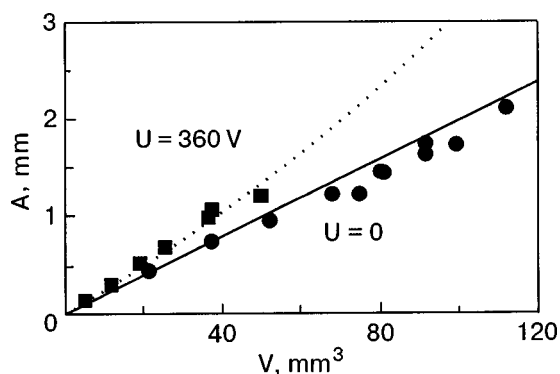
FIG. 8. Dependence of the droplet height on the volume of a neutral droplet, $U=0$ (circles), and of a charged droplet, $U=360$ V (squares). Points—experiment, lines—the dependence (56).

In the experiments the instability of a droplet at high voltages, accompanied by a discharge from the droplet surface, was also observed. The values of the second critical voltage U_{c2} measured in the experiments were approximately three times smaller than the values estimated from Eq. (58). This discrepancy can be attributed to the fact that the theory developed is of a qualitative character at voltages close to U_{c2}. The observed character of the development of the instability is different from that assumed in the calculations. Observation showed that the discharge was accompanied by the creation of a ''geyser'' from the surface, similar to that observed in experiments with the charged surfaces of bulk liquid hydrogen and helium.[12,23] The diameter of the geyser stream was much less than the capillary length a of the liquid, so the electric field has high gradients near the stream surface, and the discharge process can not be considered in the framework of the small-gradient approximation used in this paper. The charged surface becomes unsteady, and the appearance of electric current in the system should be taken into account, too. The mechanism of the geyser stream formation could be similar to that studied in Ref. 24 for singularity formation at the surface of liquid metal at high electric field.

4. CONCLUSIONS

It follows from our considerations that the flat surface of a thin neutral liquid film suspended on a solid substrate becomes unstable under inverted gravitation conditions if the thickness of the layer exceeds a critical value h_*. Development of the instability leads to the formation of a stationary wave of deformation of the liquid surface, i.e., to reconstruction of the surface. In contrast with the periodic reconstruction of the charged surface of a thick layer, the stable shape of the wave corresponds to the formation of a single hump at the center of the cell. The amplitude of the deformation wave increases with increasing mean thickness h of the layer. If the mean thickness of the liquid layer is significantly larger than the critical thickness, $h>10h_*$, the shape of the droplet can be described with good accuracy by Frenkel's macroscopic model, in which the effective boundary conditions of full wetting should be used.

The van der Waals forces are responsible for stabilization of the thin liquid background—a film wetting the sub-strate outside the droplet. The presence of such a film is important for transitions between states with several humps at the substrate and the state with a single hump.

The application of an electric field to the equipotential charged surface of liquid layer leads, in a first approximation, to renormalization of the gravitational acceleration (to an increase of the effective gravitational acceleration if the droplet is suspended from the metallic plate, and to a decrease of the effective gravitational acceleration if the droplet is lying on the plate).

The results of the theoretical considerations are in good agreement with experimental observations.

*E-mail: german@issp.ac.ru

[1] D. Book and E. Ott, Phys. Fluids **17**, 676 (1974).
[2] V. B. Shikin and E. V. Lebedeva, J. Low Temp. Phys. **119**, 469 (2000).
[3] D. M. Chernikova, Fiz. Nizk. Temp. **2**, 1374 (1976) [Sov. J. Low Temp. Phys. **2**, 669 (1976)].
[4] A. A. Levchenko, E. Teske, G. V. Kolmakov, P. Leiderer, L. P. Mezhov-Deglin, and V. B. Shikin, JETP Lett. **65**, 572 (1997).
[5] G. V. Kolmakov and E. V. Lebedeva, JETP **88**, 24 (1999).
[6] L. P. Gor'kov and D. M. Chernikova, JETP Lett. **18**, 68 (1973).
[7] L. P. Gor'kov and D. M. Chernikova, Dokl. Akad. Nauk USSR **228**, 829 (1976) [Sov. Phys. Dokl. **21**, 328 (1976)].
[8] V. B. Shikin and P. Leiderer, Fiz. Nizk. Temp. **23**, 624 (1997) [Low Temp. Phys. **23**, 468 (1997)].
[9] V. I. Melnikov and S. M. Meshkov, Zh. Éksp. Theor. Fiz. **82**, 321 (1982) [Sov. Phys. JETP **55**, 191 (1982)].
[10] P. Leiderer and M. Wanner, Phys. Lett. A **73**, 189 (1979).
[11] V. B. Shikin and Yu. P. Monarkha, *Two-Dimensional Charged Systems in Helium* [in Russian], Nauka, Moscow (1989).
[12] A. A. Levchenko, G. V. Kolmakov, L. P. Mezhov-Deglin, M. G. Mikhailov, and A. B. Trusov, Fiz. Nizk. Temp. **25**, 333 (1999) [Low Temp. Phys. **25**, 242 (1999)].
[13] Ya. I. Frenkel, Zh. Eksp. Teor. Phys. **18**, 659 (1948); Ya. B. Aron and Ya. I. Frenkel, Zh. Éksp. Teor. Fiz. **19**, 807 (1949).
[14] L. D. Landau and E. M. Lifshitz, *Fluid Mechanics*, Pergmon Press, Oxford (1987), Nauka, Moscow (1986).
[15] E. Sabisky and E. Anderson, Phys. Rev. A **7**, 720 (1973).
[16] S. Putterman, *Superfluid Hydrodynamics*, North Holland, New York (1974).
[17] H. Etz, W. Gomber, and P. Leiderer, Phys. Rev. Lett. **53**, 2567 (1984).
[18] Yu. P. Monarkha, Fiz. Nizk. Temp. **18**, 210 (1992) [Low Temp. Phys. **18**, 145 (1992)].
[19] Yu. Monarkha, U. Albrecht, K. Kono, and P. Leiderer, Phys. Rev. B **47**, 13812 (1993).
[20] M. A. Lavrent'ev and B. V. Shabat, *Methods of the Theory of Functions of Complex Variable* [in Russian], Nauka, Moscow (1987).
[21] V. B. Shikin, JETP Lett. **72**, 260 (2000).
[22] L. D. Landau and E. M. Lifshitz, *Electrodynamics of Continuous Media*, Pergamon Press (1975).
[23] A. P. Volodin, M. S. Khaĭkin, and V. S. Édel'man, JETP Lett. **26**, 543 (1977).
[24] N. M. Zubarev, JETP Lett. **73**, 544 (2001).

Influence of the magnetic dipole interaction on the properties of magnetic vortices in particles of small size

A. S. Kovalev* and J. E. Prilepsky

B. Verkin Institute for Low Temperature Physics and Engineering, National Academy of Sciences of Ukraine, pr. Lenina 47, Kharkov 61103, Ukraine

Two type of plaquette systems are proposed for modeling a vortex in an easy-plane two-dimensional Heisenberg ferromagnet with the dipole–dipole interaction of the magnetic moments of the lattice taken into account. The first plaquette describes a system with the boundary spins fixed in the easy plane perpendicular to the ''surface'' of the magnet, while in the second plaquette the boundary spins are fixed parallel to the ''surface.'' The properties of static vortex ordering of the magnetization and the transformation of the spectra of eigenmodes of the plaquettes upon a change in the parameters of the easy-plane exchange anisotropy and dipole–dipole interaction are investigated. It is shown that the region of stability of the various vortex solutions on the plane of the anisotropy and dipole–dipole interaction parameters is substantially different for these two plaquettes. The differences between the results obtained for the dynamics and structure of the vortex solutions with the dipole interaction taken into account and those obtained in a treatment including only the exchange interaction are analyzed. © *2004 American Institute of Physics.* [DOI: 10.1063/1.1645157]

1. INTRODUCTION

The dipole interaction plays an important role in stabilizing the long-range order of low-dimensional magnets, that of two-dimensional magnetic systems, in particular, and in the formation of the structure of the ordered state of magnetic media.[1,2] The interplay between the local anisotropy and the short-range exchange and long-range dipole interactions (the latter being by nature the most anisotropic) leads to a greater diversity of features of the magnetic ordering of such structures. In particular, the ordering of the magnetization determined by the dipole–dipole interaction (DDI) in a system differs from the ordering obtained when only the exchange interaction is taken into account. Without taking the long-range DDI into account it is impossible to explain the formation of domain structure in a magnetic sample,[3] although the form of the domain wall itself is determined solely by the competition between the exchange and local anisotropy.[4,5] For this reason the nonlinear topological excitations in different magnetically ordered media have for many years been treated theoretically in the framework of the classical Heisenberg model with only the exchange interaction and different sorts of anisotropy taken into account. This practice has also come about because of the computational difficulties in taking the slowly decaying DDI into account, although there have been papers investigating the influence of a nonlocal interaction on the nonlinear dynamics of magnets.[6] (In two-dimensional systems the nonlocal interactions can also be taken into account approximately by introducing an effective local anisotropic term.[7]) The exchange approximation often allows one to give a good qualitative and sometimes even quantitative explanation for a large number of experimental results concerning the nonlinear properties of magnets.[8]

Despite the undeniable success with the use of aniso-tropic exchange models for the theoretical description of the properties of magnetically ordered media, in studying real systems one often encounters a situation requiring rigorous consideration of the DDI. Only when the DDI is taken into account can one determine and investigate correctly the complex inhomogeneous ordering of the magnetization in the ground state of real magnetic structures, where, because of the presence of stray fields, the geometry of the sample begins to play an important role:[9] even under the condition of a uniform distribution of the magnetization a sample of finite size (if nonellipsoidal) will have nonuniform demagnetizing fields that can be taken into account only qualitatively by the introduction of anisotropic demagnetizing factors (see Ref. 10 and the references cited therein). Nonlocal interactions play an important role in the study of the properties of magnetic films.[11] In some rare-earth compounds called ''dipole magnets'' [12] the exchange interaction is anomalously small, and it is absolutely necessary to take the nonlocal interaction into account. It is the DDI that is responsible for the stability of the complex inhomogeneous states of diverse magnetic particles having sizes that vary from tens of nanometers to several hundred nanometers (the so-called ''magnetic nanodots'' and similar objects).[13,14] Nanodots are candidates for the creation of various devices which underlie ''magnetic logic'' schemes,[15,16] highly sensitive magnetic sensors,[17] spintronic devices, etc.[18] There is great interest in the study of the propagation of solitonic magnetic pulses in nanodot systems.[15,19]

Thanks to the presence of stray fields, nanodots made in the form of a cylinder with a low height can have a stable state with a vortex at the center of each dot.[13,14] A large number of papers have been devoted to the study of vortices in two-dimensional ferromagnets in the framework of the exchange model with easy-plane anisotropy[21–32] (a large bib-

liographic listing is given in the review by Mertens and Bishop[25]). In particular, there is significant interest in the unusual dynamic properties of magnetic vortices,[22,25,31,32] the transformation of the spectrum of eigenmodes of a two-dimensional magnet of finite size,[24–26,29–31] and the activation of magnon modes of a magnet with a vortex by an external influence.[24,27,28] A natural next step in the theoretical study of magnetic vortices is to take the DDI into account, since that is important in the experimental study of vortices in nanodots. Vortexlike structures have been observed in a numerical study of a two-dimensional monolayer of finite size in the case when the DDI is dominant over the anisotropy energy (see Ref. 33 and references therein). The existence of solutions of the vortex type for two-dimensional systems when the DDI is taken into account was pointed out in Refs. 20 and 34 (see also Ref. 1). An important theoretical problem is to elucidate the extent to which the results of the exchange approximation are modified when the long-range forces are taken into account and to what degree the data obtained without taking the DDI into account can be applied to the description of the properties of real systems.

In this paper we analyze the properties of the static vortex solution and the linear eigenmode spectra in the plaquette models illustrated in Figs. 1 and 2 (i.e., for two coordination spheres of a square spin lattice) but, in contrast to previous studies of this kind,[26,27,30,35] the DDI of the site spins is taken into account. Such models are sometimes called "core models," a name which reflects the fact that over a wide range of values of the anisotropy, the vortex core (the region in which the magnetization gradients are large) has a small size, and for a correct description of the properties of the system it is sufficient to consider the properties of the spins only near the center of the vortex. It has been shown previously[26,27] that in the exchange approximation the spectrum of magnon eigenmodes and the structure of the vortex solution arising in similar plaquette systems have a good qualitative similarity to the analogous properties of two-dimensional systems of large size. The question of the spectrum of linear eigenmodes of a magnetic nanodot containing a vortex is now the subject of active discussion (see Ref. 36 and the articles discussed in the text) and intensive experimental research.[37] Data on the vortex structure, dynamics, and spectra of nanodots containing a vortex are extremely important for understanding the physical nature of the process of dynamical magnetization reversal, which might potentially be used for a resonant change of state of a magnetic dot (i.e., in magnetic logic elements). However, as was pointed out above, direct calculation of the properties of nonlinear excitations in real systems is often rather complicated (even in the exchange approximation), and therefore the construction of simplified models capable of giving an analytical explanation of the results of experimental and numerical studies is an important problem from the standpoint of basic research on the properties of magnets.

In principle, the study of systems like that considered in this paper is also of independent interest in connection with the study of so-called "magnetic molecules." [38] Fixing the spins of the outer coordination sphere in the direction perpendicular (plaquette I) and parallel (plaquette II) to the "surface" of the plaquette (see Fig. 1) can be explained by
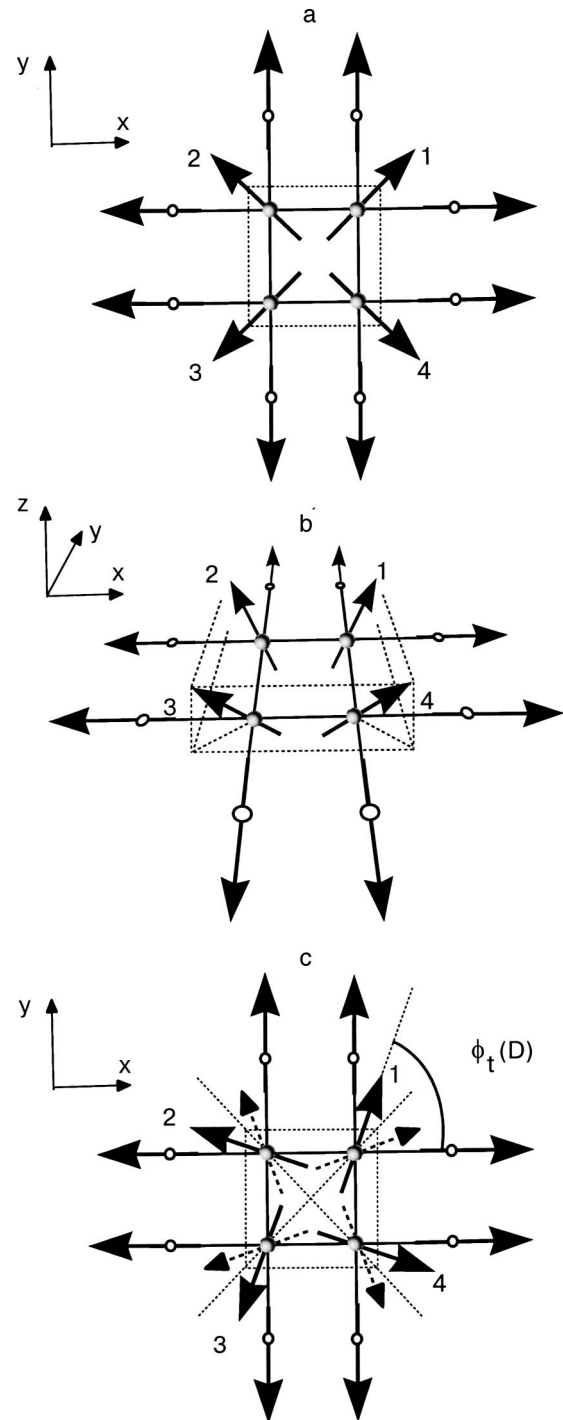

FIG. 1. Plaquette I with boundary spins fixed perpendicular to its "surface" (the unfilled circlets correspond to fixed spins): distribution of the spins in the plane of the vortex (a); three-dimensional view of the distribution of spins in an out-of-plane (OP) vortex (the in-plane distribution of the spins in the OP vortex is analogous to the case of an in-plane (IP) vortex; see text) (b); distribution of spins in a "twisted" in-plane (TIP) vortex (c). The dashed arrows correspond to the TIP vortex of opposite "chirality."

the presence of strong surface anisotropy, analogous to that arising on the surface of thin films.[2,39] If the plaquette is considered as a system that models the properties of a magnetic molecule, then the presence of such anisotropy may be due to the strong influence of the "matrix" (nonmagnetic environment) on the magnetic atoms of the outer coordination sphere.
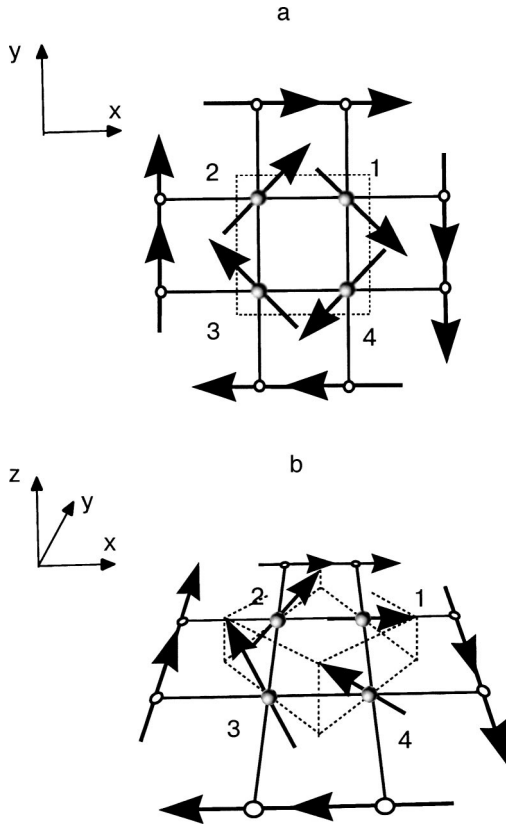
72   Low Temp. Phys. **30** (1), January 2004

A. S. Kovalev and J. E. Prilepsky

FIG. 2. Plaquette II with boundary spins fixed parallel to the "surface" (the unfilled circlets correspond to the fixed spins): distribution of spins in an IP vortex (a); three-dimensional view of the of the distribution of spins in an OP vortex (the IP distribution of the spins in the OP vortex is analogous to that in the IP vortex; see text (b).

1. MODEL AND STRUCTURE OF THE VORTEX SOLUTION

1.1. Equations of spin dynamics and the features of the vortex solution in the exchange approximation

In the framework of the classical discrete Heisenberg model the Hamiltonian of a two-dimensional ferromagnet with easy-plane exchange anisotropy and a dipolar interaction of the magnetic moments of the lattice has the form

$$\mathcal{H} = \mathcal{H}_J = \mathcal{H}_D = -J \sum_{i,\delta} (S_i^x S_\delta^x + S_i^y S_\delta^y + \lambda S_i^z S_\delta^z)$$
$$+ D \sum_{i,j} \left(\frac{\mathbf{S}_i \cdot \mathbf{S}_j}{r_{ij}^3} - 3 \frac{(\mathbf{S}_i \cdot \mathbf{r}_{ij})(\mathbf{S}_j \cdot \mathbf{r}_{ij})}{r_{ij}^5} \right), \quad (1)$$

where $\mathbf{S}_i$ is the classical site spin (henceforth the modulus of the spin vector is assumed to be the same for all sites and equal to unity), the indices i and j go over all sites of the two-dimensional spin lattice, and δ enumerates the nearest neighbors of the ith site. The exchange interaction constant J is positive in the case of a ferromagnet, and the exchange anisotropy parameter λ in the case of easy-plane symmetry varies in the range $0 \leq \lambda \leq 1$; $\mathbf{r}_{ij} = \mathbf{r}_i - \mathbf{r}_j$ is a vector connecting the ith and jth spin sites (measured in units of the intersite distance), and D is the dipole–dipole interaction constant. In dimensional units $D = (\mu_B g)^2 / 2a_0^3$, where μ_B is the Bohr magneton, g is the gyromagnetic ratio (Lande factor), and a_0 is the intersite distance, i.e., the physical case is for $D > 0$. The dynamics of the classical magnetization vector is

described by the Landau–Lifshitz equation (LLE).[3–5] For describing the spatial orientation of the vector $\mathbf{S}$ it is convenient to use as variables the z projection of the spin on the "hard" axis, $m_i = S_i^z$, and the azimuthal angle of the spin, $\varphi_i = \arctan(S_i^y / S_i^x)$; in these variables the LLE takes a Hamiltonian form, and φ_i and m_i play the role of canonically conjugate effective coordinates and momenta for the Hamiltonian $\mathcal{H}(m_i, \varphi_i)$. In these variables the LLE looks like

$$\frac{d\varphi_i}{dt} = \sum_\delta \left(\frac{m_\perp \delta m_i}{m_{\perp i}} \cos\varphi_{i\delta} - \lambda m_\delta \right) + D \sum_j \frac{1}{r_{ij}^3}$$
$$\times \left(m_j + \frac{1}{2} \frac{m_{\perp j} m_i}{m_{\perp i}} [\cos\varphi_{ij} + 3\cos(\varphi_i + \varphi_j - 2\alpha_{ij})] \right),$$
$$(2)$$

$$\frac{dm_i}{dt} = -\sum_\delta m_{\perp i} m_{\perp \delta} \sin\varphi_{i\delta} - D \sum_j \frac{m_{\perp i} m_{\perp j}}{2 r_{ij}^3}$$
$$\times [\sin\varphi_{ij} + 3\sin(\varphi_i + \varphi_j - 2\alpha_{ij})], \quad (3)$$

where

$$m_{\perp i} = \sqrt{1 - m_i^2}, \quad \varphi_{ik} = \varphi_i - \varphi_k,$$
$$\cos\alpha_{ij} = (r_i \cos\chi_i - r_j \cos\chi_j)/r_{ij},$$

and χ_i is the azimuthal coordinate of the ith spin site. In Eqs. (2) and (3) the time is measured in units of J^{-1} and the renormalization $D/J \to D$ is made, i.e., the variation of the renormalized D formally corresponds to the variation of J and a_0.

In a two-dimensional ferromagnet with easy-plane anisotropy (exchange or single-ion) a magnetic vortex is a topological defect. In the long-wavelength limit the solution of the LLE for a static magnetic vortex in an infinite system with allowance for only the exchange part of the Hamiltonian (1) was obtained in Refs. 21 and 22 (see also Ref. 32). In polar coordinates (r, χ) connected to the center of the vortex it has the form $\varphi = \chi + C$, $m = m(r)$, where C is an arbitrary constant, and an analytical expression for $m(r)$ does not exist. For large r the z projection of the magnetization of the vortex falls off exponentially, and at the center of the vortex it reaches a value $m = \pm 1$ (the different signs correspond to different polarization of the vortex); such a vortex is called an "out-of-plane" (OP) vortex. When the discreteness of the system is taken into account, another type of vortex is also possible, depending on the anisotropy: for strong anisotropy $\lambda < \lambda_c$ ($\lambda_c \approx 0.7$ for a square lattice; for other types of lattices the value differs somewhat[23,32]) the "in-plane" (IP) vortex configuration with $m \equiv 0$ is stable. At a lower value of the anisotropy the static vortex goes over to the OP configuration.[23,25,30,32] In a continuum description the IP vortex does not exist, since the energy of its core diverges logarithmically at the center of the vortex, while the energy of the OP vortex remains finite. In a discrete model the energy of the core of the IP vortex is finite, and it is stable for $\lambda < \lambda_c$. Taking the DDI into account destroys the invariance of the Hamiltonian of the system (1) with respect to a uniform rotation of the spins in the easy plane. In cylindrical magnetic nanodots the requirement that there be no stray

fields (minimization of the magnetic dipole interaction) leads to fixing of the value of the constant for a stable vortex lattice as $C = \pm \pi/2$ (see, e.g., Ref. 36), where the different signs correspond to the different chiralities of the vortex.

1.2. Modeling the vortex properties with the aid of a plaquette analysis

In plaquettes I and II (Fig. 1) the four spins of the inner (first) coordination sphere of the plaquette can change in their spatial orientation, while the spins of the second coordination sphere are fixed in the "easy" plane perpendicular (Fig. 1) and parallel (Fig. 2) to the "surface" of the plaquette (its lateral faces). Even in the exchange approximation the vortex state for such plaquettes, owing to the fixing of the spins of the outer sphere in a vortical configuration, is the ground state. For finding its explicit form it is necessary to find a static solution of the system of equations (2), (3) for four unfixed spins with indices $i = 1,2,3,4$. In the exchange approximation ($D = 0$) the IP configuration corresponds to the solution $\varphi_i = \pi/4 + \pi(i-1)/2$ for plaquette I and $\varphi_i = -\pi/4 + \pi(i-1)/2$ for plaquette II, $m_i = 0$ (Figs. 1a and 2a); the IP vortex is stable in the interval of anisotropy parameters $0 \leqslant \lambda \leqslant \lambda_c = \cos(\pi/4) = \sqrt{2}/2 \approx 0.71$. The difference in the critical value of the anisotropy λ_c from that obtained in Refs. 26 and 28 is due to a somewhat different fixing of the outer spins. This fact is not fundamental, since it entails only a slight quantitative change in the results without affecting the qualitative agreement. All of the analytical expressions from Refs. 26 and 28 for plaquettes with a fixed boundary remain valid if one sets $\lambda_c = \sqrt{2}/2$ in them. The static distribution of derivatives of the mobile spins for the OP configuration in the exchange approximation (Figs. 1b and 2b) is given by the following expressions: as in the IP case $\varphi_i = \pi/4 + \pi i/2$ for plaquette I and $\varphi_i = -\pi/4 + \pi i/2$ for plaquette II, and for the z projection one has $m_i \equiv m = \sqrt{1 - (\lambda_c/\lambda)^2}$ in both plaquettes.

The spectrum of plaquettes analogous to those considered in the present paper was investigated in Refs. 24, 26, and 28 in the exchange approximation. It contains four values of the frequency (the total number of modes is equal to the number of degrees of freedom of the Hamiltonian system, i.e., the number of free spins), which are classified by the discrete "azimuthal wave number" k, which takes the values $k = 0,1,2$. The spectrum of the plaquettes in the region of stability of the IP configuration ($\lambda < \lambda_c$) contains three values of the frequency Ω, i.e., three branches of the function $\Omega_k = \Omega_k(\lambda)$ (the mode with $k = 1$, i.e., the first azimuthal mode, is twofold degenerate). In the region of stability of the OP configuration the degeneracy of the first azimuthal modes ($k = 1$) is lifted, and the frequency dependence for them is split into a doublet, with the spin wave of the lower branch of the doublet traveling clockwise and the upper branch counterclockwise. The frequency dependence of Ω and the dependence of the amplitude ratio of the transverse and longitudinal oscillations of the spins for all the modes are given by formulas (8)–(21) of Ref. 28. (They can also be obtained by setting $D = 0$ in the corresponding formulas of the present paper.) We note that in an infinite system the value of the anisotropy parameter $\lambda = 1$ is critical: the magnetic anisotropy become easy-axis, and the magnetic vortex vanishes. In

the proposed plaquette model the vortex state is fixed by the boundary conditions. Therefore in this model the vortex exists for $\lambda > 1$ as well. But in analogy with the infinite system, all of the dependence on λ will be given below only for the region $\lambda < 1$.

The goal of the present study is to investigate the structure and stability of different vortex configurations of plaquettes and the spectra of linear excitations with the DDI taken into account.

2. PLAQUETTE I WITH A FIXED BOUNDARY WITH ALLOWANCE FOR THE DIPOLE–DIPOLE INTERACTION

2.1. Static vortex configuration and the dynamical equations for the eigenmodes

We take into account the dipole part of the Hamiltonian $\mathcal{H}_D$ and consider the influence of the DDI on the static IP and OP configurations of plaquette I. Taking into account the symmetry of the vortex solutions, we make the substitution $m_i = m$, $\varphi_i = \varphi + \pi(i-1)/2$ in Eqs. (2) and (3), and we set the time derivatives in them equal to zero. As a result, for the variables m and φ we obtain a system of two ordinary nonlinear equations:

$$\frac{m(1+aD)}{m}(\sin\varphi + \cos\varphi) - 2\lambda m + D\frac{m}{8}(\sqrt{2} + 16 - 3(\sqrt{2}$$
$$+ 8)\sin 2\varphi) = 0, \tag{4}$$

$$m_\perp(\cos\varphi - \sin\varphi)\left(1 + aD - \frac{3D}{8}m_\perp(\sqrt{2}+8)(\cos\varphi$$
$$+ \sin\varphi)\right) = 0, \tag{5}$$

where $a = 7/4 - 1/2\sqrt{2} - 13/25\sqrt{5} \approx 1.164$ is a numerical constant.

The first solution of this system corresponds, as before, to the IP configuration (Fig. 1a): $\varphi = \pi/4$, $\varphi_i = \pi/4 + \pi(i-1)/2$, $m = 0$. The solution for the OP configuration (Fig. 1b) looks as follows: the expression for φ is analogous to that obtained for the IP configuration, while the static OP magnetization m is given by the expression

$$m(\lambda; D)$$
$$= 2\frac{\sqrt{(\lambda - \tilde{\lambda}_c(D))[\lambda + 1/\sqrt{2} + D(1 + 1/2\sqrt{2} + a\sqrt{2})/2)]}}{2\lambda + D(1 + 1/2\sqrt{2})}. \tag{6}$$

Of course there exists an analogous OP configuration with negative polarization, i.e., with $m_i = -m(\lambda; D)$. The critical value of the anisotropy parameter separating the existence regions of the IP and OP configurations now becomes a function of the DDI parameter:

$$\tilde{\lambda}_c(D) = \frac{1}{\sqrt{2}} + \left(\frac{a}{\sqrt{2}} - \frac{1}{2} - \frac{1}{4\sqrt{2}}\right)D, \tag{7}$$

and the corresponding boundary on the plane of the parameters (D, λ) is shown by line 1 in Fig. 5a. However, as will be shown below, the given vortices with $\varphi = \pi/4$ exist only for a sufficiently weak DDI. With increasing dipole interac-

tion the vortex is transformed into a configuration with $\varphi \neq \pi/4$, which will be called a "twisted" in-plane vortex (indicated by a subscript "t" in the formulas; see Fig. 1c). Let us consider a twisted in-plane (TIP) vortex. The solution of equations (4) and (5) describing the static distribution of the magnetization in a TIP vortex is as follows: $m=0$, $\varphi = \phi_t(D)$, $\varphi_i = \phi_t + \pi(i-1)/2$,

$$\phi_t(D) = \frac{\pi}{4} \pm \arccos\left(1 - \frac{8(D-D_c)}{3\sqrt{2}DD_c(\sqrt{2}+8)}\right), \tag{8}$$

where $D_c = (3\sqrt{2} + 3/4 - a)^{-1} \approx 0.261$. Solutions of the TIP type can exist only for $D > D_c$ (see line 2 in Fig. 5a). The double sign $\pm$ in Eq. (8) is explained by the degeneracy of the TIP vortex with respect to its effective "chirality:" At the point of an IP–TIP or OP–TIP transition, two stable TIP solutions appear, i.e., a bifurcation of the solutions with respect to the angle φ occurs. The splitting off of the stable solutions from the unstable solutions at the IP–TIP transition (i.e., at the transition through the value $D=D_c$ at fixed λ from the region of stability of the IP vortex to the region of stability of the TIP vortex) occurs by a square-root law: for $D - D_c \ll D_c$ we have

$$\phi_t(D) \approx \frac{\pi}{4} \pm \frac{4}{D_c} \sqrt{\frac{(D-D_c)}{3\sqrt{2}(\sqrt{2}+8)}}. \tag{9}$$

The bifurcation diagram of the OP–TIP transition is more unusual (see Sec. 2.4).

We note that Eqs. (4) and (5) also admit continuously degenerate solutions for twisted out-of-plane (TOP) vortices. Thus the solutions on the plane of parameters (D,λ) correspond to a line $\lambda = \tilde{\lambda}_c^*(D)$, where $\tilde{\lambda}_c^*(D)$ is determined by the formula

$$\tilde{\lambda}_c^*(D) = D(5 + 1/\sqrt{2})/2. \tag{10}$$

On this straight line Eqs. (4) and (5) are satisfied identically if m and φ are related as

$$m_\perp = \frac{8}{3D(\sqrt{2}+8)} \frac{1+aD}{\cos\varphi + \sin\varphi}, \tag{11}$$

i.e., at a fixed D, to each $\pm m$ in the admissible interval $0 \leq m \leq 1$ there corresponds a definite value of φ (or of $\pi/2 - \varphi$). For $\varphi = \pi/4$ the TOP vortex goes over continuously to the OP vortex [for λ belonging to the straight line $\lambda = \tilde{\lambda}_c^*(D)$], and for $m=0$ the TOP vortex goes over to a TIP vortex. As will be seen below from an analysis of the stability of the different vortex configurations of the plaquette, such a continuously degenerate solution can be realized on the straight line $\lambda = \tilde{\lambda}_c^*(D)$ only for $D > D_c$.

Although we have obtained the dependence of the characteristics of the static vortex solutions on the model parameters, this does not mean that the IP and OP solutions found are stable over all of the corresponding intervals of λ values ($\lambda < \tilde{\lambda}_c(D)$ for the IP vortex and $\tilde{\lambda}_c(D) < \lambda < 1$ for the OP vortex). Stable solutions should correspond not just to an extremum but to a minimum of the Hamiltonian $\mathcal{H}(m_i, \varphi_i)$. It follows from an analysis of expression (8) that $\phi_t = \pi/4$ for $D = D_c$, and it can be assumed that the IP vortex becomes unstable for $D > D_c$. To find the true regions of stability of

the OP, IP, and TIP vortices (in terms of λ and D) it is necessary to analyze the values of the frequencies of the eigenmodes of the plaquette in the IP, OP, and TIP configurations and their dependence on λ and D (for analysis of the stability of the IP and OP solutions for a plaquette in the exchange approximation see Refs. 26 and 28).

The system of dynamical equations linearized about a static vortex state is written in general form as follows: introducing the small corrections μ and η to the static solutions, $m_i(t) = \mu_i(t) + m_i$, $\varphi_i(t) = \nu_i(t) + \varphi_i$, we obtain from (2) and (3) in the approximation linear in μ and ν:

$$\dot{\nu}_i = \sum_\delta \left\{ \left[\mu_i \frac{m_{\perp\delta}}{m_{\perp i}^3} - \mu_\delta \frac{m_i m_\delta}{m_{\perp i} m_{\perp\delta}} \right] \cos\varphi_{i\delta} - (\nu_i - \nu_\delta) \right. $$
$$\times \frac{m_i m_{\perp\delta}}{m_{\perp i}} \sin\varphi_{i\delta} - \mu_\delta \lambda \right\} + D \sum_j \frac{1}{2r_{ij}^3} \left\{ \left[\mu_i \frac{m_{\perp j}}{m_{\perp i}^3} \right. \right.$$
$$\left. - \mu_j \frac{m_i m_j}{m_{\perp i} m_{\perp j}} \right] [\cos\varphi_{ij} + 3\cos(\varphi_i + \varphi_j - 2\alpha_{ij})]$$
$$- \frac{m_i m_{\perp j}}{m_{\perp i}} [(\nu_i - \nu_j)\sin\varphi_{ij} + 3(\nu_i + \nu_j)\sin(\varphi_i + \varphi_j$$
$$\left. - 2\alpha_{ij})] + 2\mu_j \right\}, \tag{12}$$

$$\dot{\mu}_i = \sum_\delta \left\{ \left[\mu_i \frac{m_i m_{\perp\delta}}{m_{\perp i}} + \mu_\delta \frac{m_\delta m_{\perp i}}{m_{\perp\delta}} \right] \sin\varphi_{i\delta} \right.$$
$$- (\nu_i - \nu_\delta)\cos\varphi_{i\delta} \right\} + D \sum_j \frac{1}{2r_{ij}^3} \left\{ \left[\mu_i \frac{m_i m_{\perp j}}{m_{\perp i}} \right. \right.$$
$$\left. + \mu_j \frac{m_j m_{\perp i}}{m_{\perp j}} \right] [\sin\varphi_{ij} + 3\sin(\varphi_i + \varphi_j - 2\alpha_{ij})]$$
$$- m_{\perp i} m_{\perp j} [(\nu_i - \nu_j)\cos\varphi_{ij} + 3(\nu_i + \nu_j)$$
$$\left. \times \cos(\varphi_i + \varphi_j - 2\alpha_{ij})] \right\}. \tag{13}$$

In explicit form for plaquette I in the IP or OP configuration we have the following system:

$$\dot{\nu}_1 = \frac{\sqrt{2}}{m_\perp^3}(1+aD)\mu_1 + (D-\lambda)(\mu_2 + \mu_4) + D\frac{\mu_3}{2\sqrt{2}}$$
$$+ m\left(1 + \frac{D}{2}\right)(\nu_4 - \nu_2) + \frac{D}{m_\perp^2}\left[\frac{3}{2}m^2(\mu_2 + \mu_4)\right.$$
$$\left. + \frac{m^2}{\sqrt{2}}\mu_3 - \left(3 + \frac{1}{\sqrt{2}}\right)\mu_1\right], \tag{14}$$

$$\dot{\mu}_1 = \left(-\sqrt{2(1+aD)}\right)m_\perp + Dm_\perp^2\left[3 + \frac{1}{\sqrt{2}}\right]\nu_1 + m$$
$$\times \left(1 + \frac{D}{2}\right)(\mu_4 - \mu_2) + Dm_\perp^2\left[\frac{3}{2}(\nu_2 + \nu_4) + \frac{\nu_3}{2\sqrt{2}}\right]. \tag{15}$$

Equations suitable in the region of the stable TIP vortex are obtained from (12) and (13) in an analogous way (with allowance for the symmetry of the TIP vortex):

$$\dot{\nu}_1 = \mu_1(1+aD)(\sin\phi_t + \cos\phi_t) + (D-\lambda)(\mu_2 + \mu_4)$$

$$+ D\frac{\mu_3}{2\sqrt{2}} - \frac{D\mu_1}{8}(\sqrt{2} + 3(8+\sqrt{2})\sin 2\phi_t), \quad (16)$$

$$\dot{\mu}_1 = -\nu_1(1+aD)(\sin\phi_t + \cos\phi_t) + \frac{D\sqrt{2}}{8}(\nu_1 - \nu_3)$$

$$+ \frac{3D}{8}\sin 2\phi_t([8+\sqrt{2}]\nu_1 + 4[\nu_2 + \nu_4] + \sqrt{2}\nu_3). \quad (17)$$

Three more pairs of equations in addition to (14), (15) and (16), (17) are obtained by cyclic permutation of the indices.

2.2. Eigenmodes and the stability region of the in-plane vortex

The classification of the eigenmodes of a plaquette with allowance for the DDI is the same as that given previously in the exchange approximation.[26,28] The most important is the symmetric mode (with $k=0$ and the lowest frequency), for which the solution has the form $\nu_i = \nu^0\sin\Omega t$, $\mu_i = \mu^0\cos\Omega t$, and the dependence of the frequency on the parameters λ and D reduces to the following:

$$\Omega_0^{IP}(\lambda;D) = \sqrt{2\sqrt{2}D_c^{-1}(\tilde{\lambda}_c(D)-\lambda)(D_c-D)}. \quad (18)$$

The vanishing of the frequency Ω_0^{IP} determines the boundaries of the stability region of the IP vortex: in our model they are specified by the inequalities $0<\lambda<\tilde{\lambda}_c(D)$, $0<D<D_c$ (the region bounded by lines *1* and *2* in Fig. 5a). The ratio of the amplitudes of the oscillations of the spins perpendicular to the easy plane and in the easy plane, μ^0/ν^0, for the symmetric mode in the IP region depends on λ and D as follows:

$$\mu^0/\nu^0 = \sqrt{\frac{\sqrt{2}(D_c-D)}{D_c(\tilde{\lambda}_c(D)-\lambda)}}. \quad (19)$$

This ratio tends to infinity for $\lambda \to \tilde{\lambda}_c(D)$, which indicates a transition to a new stable state (OP) after the IP–OP transition. For $D \to D_c$, on the contrary, because of the symmetry of the TIP vortex the ratio (19) goes to zero (a tendency toward a change of the in-plane ordering).

For a twofold degenerate (in the IP region of values of D and λ) first azimuthal mode, assuming that $\nu_i = \nu^{1,2}\sin(\chi_i - \Omega t)$, $\mu_i = \mu^{1,2}\cos(\chi_i - \Omega t)$, we have

$$\Omega_{1,2}^{IP}(\lambda;D) = \sqrt{\left(\sqrt{2} + D\left[\sqrt{2}a - 3 - \frac{3}{2\sqrt{2}}\right]\right)}$$

$$\times \sqrt{\left(\sqrt{2} + D\left[\sqrt{2}a - 3 - \frac{1}{2\sqrt{2}}\right]\right)}. \quad (20)$$

Finally, for the second azimuthal mode [$\nu_i = \nu^3\sin(2\chi_i - \Omega t)$, $\mu_i = \mu^3\cos(2\chi_i - \Omega t)$] the expression determining the dependence of its frequency on the parameters λ and D is

$$\Omega_3^{IP}(\lambda;D) = \sqrt{\left(\sqrt{2} + 2\lambda + D\left[a\sqrt{2} - 5 - \frac{1}{2\sqrt{2}}\right]\right)}$$

$$\times \sqrt{\left(\sqrt{2} + D\left[a\sqrt{2} - \frac{3}{2\sqrt{2}}\right]\right)}. \quad (21)$$

Relations (20) and (21) are valid only in the region ($0<\lambda<\tilde{\lambda}_c(D)$, $0<D<D_c$), where the IP vortex is stable.

2.3. Eigenmodes and the stability region of the out-of-plane vortex

As was shown previously, the OP vortex can be stable only in the interval $\lambda > \tilde{\lambda}_c(D)$. However, as will be found below, the stability region of the OP vortex acquires additional restrictions with growth of the DDI parameter. Let us consider the spectrum of frequencies of the system (12), (13) for the OP region.

The dependence of the frequency of a symmetric mode on the parameters λ and D is conveniently written in the form

$$\Omega_0^{OP}(\lambda;D)$$

$$= 2\sqrt{\frac{(\lambda - \tilde{\lambda}_c(D))(\lambda - \tilde{\lambda}_c^*(D))\left(2\lambda + \sqrt{2} + D\left[a\sqrt{2} + 1 + \frac{1}{2\sqrt{2}}\right]\right)}{2\lambda + D\left(1 + \frac{1}{2\sqrt{2}}\right)}}, \quad (22)$$

where $\tilde{\lambda}_c^*(D)$ is determined by expression (10), and the amplitude ratio of the oscillations of different polarization for this mode has the form

$$\mu^0/\nu^0 = m_\perp(\lambda;D)\sqrt{\frac{\lambda - \tilde{\lambda}_c^*(D)}{\lambda - \tilde{\lambda}_c(D)}}$$

$$\times \sqrt{\frac{2\lambda + D(1+1/\sqrt{2})}{2\lambda + \sqrt{2} + D(a\sqrt{2} + 1 + 1/2\sqrt{2})}}. \quad (23)$$

We see from expression (22) that a stable OP configuration exists only when two conditions hold simultaneously: $\lambda > \tilde{\lambda}_c(D)$ and $\lambda > \tilde{\lambda}_c^*(D)$. (When the opposite inequalities hold simultaneously the OP solution does not exist.) The dependence $\tilde{\lambda}_c^*(D)$ according to Eq. (10) is shown in Fig. 5a by the straight line *3*, which separates the existence regions of the OP and TIP vortices. All three critical dependences, $\tilde{\lambda}_c(D)$, $\tilde{\lambda}_c^*(D)$, and $D=D_c$ converge at a single point $D_* = D_c$, $\lambda_* = \tilde{\lambda}_c^*(D_c) = \tilde{\lambda}_c(D_c) = 8\sqrt{2}/([12\sqrt{2}+3-4a][5\sqrt{2}+1])$). Thus for an OP vortex the dependence of the critical value of the anisotropy parameter on the dipole interaction parameter is a nonlinear function:

$$\lambda_c(D) = \begin{cases} \tilde{\lambda}_c(D) & \text{for } 0<D<D_c, \\ \tilde{\lambda}_c^*(D) & \text{for } D_c<D. \end{cases} \quad (24)$$

Accordingly, the expression for the out-of-plane magnetization has the form

76   Low Temp. Phys. **30** (1), January 2004

A. S. Kovalev and J. E. Prilepsky

$$\tilde{m}(\lambda;D) = \begin{cases} m(\lambda;D), & \text{for } (0<D_c, \lambda>\tilde{\lambda}_c) \\ \quad \text{and for } (D_c<D, \lambda>\tilde{\lambda}_c^*), \\ 0, & \text{for } (D_c<D, \lambda<\tilde{\lambda}_c^*) \\ \quad \text{and for } (D<D_c, \lambda<\tilde{\lambda}_c), \end{cases} \tag{25}$$

where $m(\lambda,D)$ is determined by formula (6). It is of interest to note the following feature of expression (25) and the difference between it and (6). In the parameter region $0<D <D_c$ the dependence of the static out-of-plane magnetization of the OP vortex on λ has the standard bifurcation form: this dependence splits off from the OP solution $m(\lambda;D)=0$ by a square-root law at the point where the IP vortex ceases to be stable, i.e., for $\lambda \cong \lambda_c(D)$. In the region $D>D_c$ at the boundary of the existence region of the stable OP vortex, i.e., on the line $\tilde{\lambda}_c^*(D)$ (line *3* in Fig. 5a), the out-of-plane magnetization jumps by a finite amount $\delta m(D)$. This jump goes to zero at the point (D_*,λ_*) and grows by a square-root law for $D-D_c \ll D_c$:

$$\delta m \approx \frac{2\sqrt{2}\sqrt{1+4\sqrt{2}}}{\sqrt{3}[3+4\sqrt{2}]} \frac{\sqrt{D-D_c}}{D_c}.$$

The dependence of the out-of-plane magnetization on λ for $D<D_c$ and $D>D_c$ is given in Fig. 3. It is seen from expression (23) that for $D>D_c$ the ratio μ^0/ν^0 tends toward zero at $\lambda \to \tilde{\lambda}_c^*(D)$, i.e., the oscillations of the spins occur in the azimuthal direction, and the vortex has a tendency to "twist" (i.e., a tendency toward a transition to the TIP configuration with $\varphi \neq \pi/4$). For $D<D_c$ and $\lambda \to \tilde{\lambda}_c(D)$ the ratio μ^0/ν^0 tends toward infinity, and the vortex has a tendency to abandon the OP configuration and rotate to the IP configuration.

Let us consider the higher-lying modes using the data on the stability region of the OP configuration. For an OP vortex this question is important because even in the exchange approximation the modulus of the frequency of the first azimuthal mode can be smaller than the frequency of the symmetric mode.[29,31] Because of the lowering of the symmetry of the system in the region of the stable OP vortex, the de-
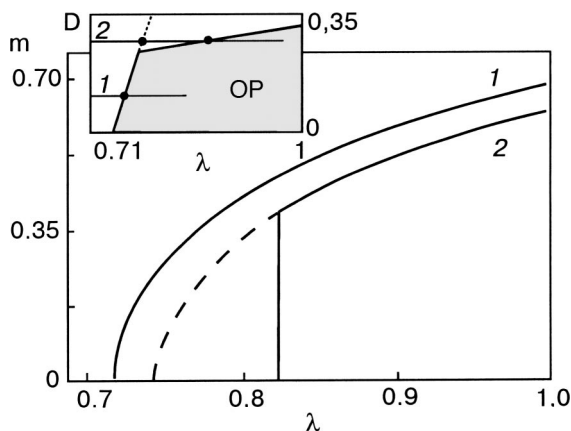

FIG. 3. Change in the dependence of the out-of-plane magnetization of a static OP vortex (25) for plaquette I on the parameter λ with increasing value of D. The curves shown correspond to the values $D=0.1$ (solid curve *1*) and $D=0.29>D_c$ (curve *2*, the dashed part of which corresponds to the instability region of the OP vortex). The inset shows the stability region of the OP vortex (shaded).

generacy of the first azimuthal modes is lifted. The dependence of the frequencies of these modes on the parameters λ and D is as follows:

$$\Omega_{1,2}^{OP}(\lambda;D) = 2m(\lambda;D)\left(1+\frac{D}{2}\right) \mp \sqrt{U_1(\lambda;D)W_1(\lambda;D)}, \tag{26}$$

where

$$U_1(\lambda;D) = \frac{\sqrt{2}}{m_\perp^3(\lambda;D)} + D\left(\frac{a\sqrt{2}}{m_\perp^3(\lambda;D)} - 3 - \frac{3}{2\sqrt{2}}\right)$$
$$- \frac{m^2(\lambda;D)}{\sqrt{2}}\bigg),$$

$$W_1(\lambda;D) = \sqrt{2}m_\perp(\lambda;D) + Dm_\perp(\lambda;D)\left(a\sqrt{2}-m_\perp(\lambda;D)\right.$$
$$\times \left(3+\frac{1}{2\sqrt{2}}\right)\bigg). \tag{27}$$

The radicand in Eq. (26) remains positive in the entire existence region $(\lambda>\tilde{\lambda}_c, \lambda>\tilde{\lambda}_c^*)$ of the OP configuration, and additional instability with respect to growth of the azimuthal modes does not arise. However, we note the qualitative difference of the behavior of the lower branch of the frequency dependence of the first azimuthal mode with allowance for the DDI (Fig. 5a) from the form of this dependence obtained in the exchange approximation:[24,29,31] on the plane of parameters λ and D there exists a region in which the frequency of this mode changes sign. (The sign of the frequency of the azimuthal modes indicates the direction of rotation of the traveling spin wave, i.e., in this region of parameters the spin wave of this mode begins to rotate counterclockwise, like a wave of the upper branch of the doublet of the first azimuthal modes.) The region where the frequency changes sign is denoted by shading in Fig. 5. Such a feature is found in analogous systems (both plaquette systems[26] and systems of large size[29,31]) in the exchange approximation, but with free spins at the boundary. It is interesting to note a consequence of this fact for systems of large size. As was shown in Ref. 31, the direction of rotation of a wave of the lower first azimuthal mode (called the translational Goldstone mode) can be interpreted as a small-amplitude rotation of the center of the OP vortex under the condition that the radial eigenfunction of this mode is sufficiently well localized in the vortex core. The direction of rotation of this mode (and, hence, of the small-amplitude rotation of the vortex) is determined completely by the type of boundary conditions: a negative value of the frequency should correspond to a fixed boundary, a positive value, to a free boundary. Since in our case the frequency of this mode in a system with fixed spins at the boundary can become positive, while the type of boundary conditions selects a definite (in our case opposite) direction of rotation of the vortex, one can conclude that in this region of parameters λ and D the direction of its rotation cannot be associated with the direction of rotation of the vortex. This, in turn, can happen if the radial eigenfunction of this mode is not localized in the vortex core. Thus, if the effect found here—a change in the direction of rotation of the lowest first

azimuthal mode—actually does take place in systems of large size with spins fixed perpendicular to the "surface," then it can be supposed that in that region of parameters the eigenfunction of this mode is poorly localized in the vortex core, and this mode itself cannot be considered responsible for the small-amplitude rotation of the center of the OP vortex. Interestingly, for the indicated mode there exists a narrow interval of values of the parameter D, close to D_c, where the frequency can change sign twice with increasing λ. This sort of dependence is not observed in the exchange approximation for a system with a free boundary.

For the second azimuthal mode we have

$$\Omega_3^{OP}(\lambda;D) = \sqrt{F_1(\lambda;D)G_1(\lambda;D)}, \tag{28}$$

where

$$F_1(\lambda;D) = \frac{\sqrt{2}}{m_\perp^3(\lambda;D)} + 2\lambda + D\left(\frac{a\sqrt{2}}{m_\perp^3(\lambda;D)} - 2 - \frac{1}{2\sqrt{2}} \right.$$
$$\left. - 3\frac{1+m^2(\lambda;D)}{m_\perp^2(\lambda;D)} \right),$$

$$G_1(\lambda;D) = \sqrt{2}m_\perp(\lambda;D) + Dm_\perp(\lambda;D)$$
$$\times \left(a\sqrt{2} - m_\perp(\lambda;D)\frac{3}{2\sqrt{2}} \right). \tag{29}$$

The ratio of the amplitudes of all the azimuthal modes is nonsingular in the stability region of the OP vortex, and all of the results on the frequency dependence for the azimuthal modes are valid only in the stability region of the OP vortex: $\lambda_c(D) < \lambda$. With increasing D the values of the eigenfrequencies in the IP and OP regions of the parameters λ and D decrease. This indicates that in this region of parameters an increase in the DDI weakens the coupling strength, and the influence of the DDI is opposite to that of the exchange.

2.4. Eigenmodes and the stability region of the twisted in-plane vortex

Let us consider the spectrum of eigenmodes of a plaquette in the stability region of the TIP vortex. From the foregoing analysis we can conclude that the domain of stability of the TIP vortex in terms of λ and D is given by the inequalities $\lambda < \tilde{\lambda}_c^*(D)$, $D > D_c$. The dependence of the frequency of the symmetric mode on the parameters λ and D is determined by the expression

$$\Omega_0^t = \sqrt{\frac{16D}{3D_c}}$$
$$\times \sqrt{\frac{(D-D_c)(\tilde{\lambda}_c^*(D)-\lambda)[D(3\sqrt{2}+3/4+a)+1]}{\sqrt{2}+8}}. \tag{30}$$

The frequency of this "soft" mode goes to zero with a square-root singularity at the points $\lambda = \tilde{\lambda}_c^*(D)$ (the TIP–OP transition) and at $D = D_c$ (the TIP–IP transition). The ratio of the amplitude of the oscillations of the spins perpendicular to the easy plane to the amplitude of the oscillations in the plane is given by the formula

$$\mu^0/\nu^0 = \sqrt{\frac{4}{3DD_c}}\sqrt{\frac{(D-D_c)[D(3\sqrt{2}+3/4+a)+1]}{(\lambda-\tilde{\lambda}_c^*(D))(\sqrt{2}+8)}}. \tag{31}$$

Expression (31) can be used to assess the symmetry of new solutions that will be stable at values of D and λ outside the stability intervals of the TIP vortex: for $\lambda \rightarrow \tilde{\lambda}_c^*(D)$, i.e., at the TIP–OP transition, this ratio goes to infinity, attesting to a tendency of the spins to come out of the plane, while for $D \rightarrow D_c$, i.e., at the TIP–IP transition, this ratio goes to zero, attesting to the tendency toward a change of the in-plane ordering.

The dependence of the frequency of the first azimuthal mode on the parameter D (it is independent of the value of the anisotropy λ) is as follows:

$$\Omega_{1,2}^t = \frac{\sqrt{(8\sqrt{2}[1+aD]^2+3D^2[3-2^{-3/2}])(3+2^{-3/2})}}{\sqrt{2}+8}. \tag{32}$$

For the highest second azimuthal mode we have

$$\Omega_3^t = \sqrt{\left(2\lambda+D\left(1+\frac{1}{\sqrt{2}}\right)\right)\left(\frac{8-\sqrt{2}}{8+\sqrt{2}}\frac{8(1+aD)^2}{3D(8+\sqrt{2})}+\frac{3D}{2\sqrt{2}}\right)}. \tag{33}$$

In the stability region of the TIP vortex the values of the eigenfrequencies grow with increasing D, i.e., the effective strength of the spin–spin couplings increases with increasing D. This indicates that the DDI is dominant in this region. At the TIP–IP transition the frequency dependence of the azimuthal modes has a kink, while at the TIP–OP transition the frequency dependence, except for that of the "soft" zeroth mode, has a jump. The reason for this lies in the fact that at the OP–TIP transition we have a rather unusual threshold bifurcation diagram, which is shown in Fig. 4. Upon a change in the parameter D at a fixed value $\lambda > \lambda_*$ (Fig. 4a) the main bifurcation occurs at a point on the line $D = \tilde{D}_c^*$, where the two stable OP vortices with different polarization and zero chirality are abruptly transformed into two stable TIP vortices with different chirality and zero polarization. Here there are unrealized bifurcations at points on the lines D_c and D_c^*, where there arise two unstable TIP vortices with different chirality (at $D = D_c$) and two unstable OP vortices with zero chirality (at $D = D_c^*$). At a fixed value $D > D_c$ (Fig. 4b) the main bifurcation (on the line $\lambda = \tilde{\lambda}_c^*$), at which the polarization and chirality of the vortex change abruptly, is preceded by an unrealized bifurcation in which two unstable OP solutions with zero chirality arise.

From all of the dependences presented in this Section one can obtain expressions for the frequencies of a purely dipolar system by taking D to the limit. In particular, when only the dipole interaction is taken into account, the TIP vortex has the configuration: $m = 0$, $\phi = \pi/4 - \arccos(4a/[3+4\sqrt{2}]) \approx -0.069\pi$, or $m = 0$, $\phi = \pi/4 + \arccos(4a/[3+4\sqrt{2}]) \approx 0.569\pi$.
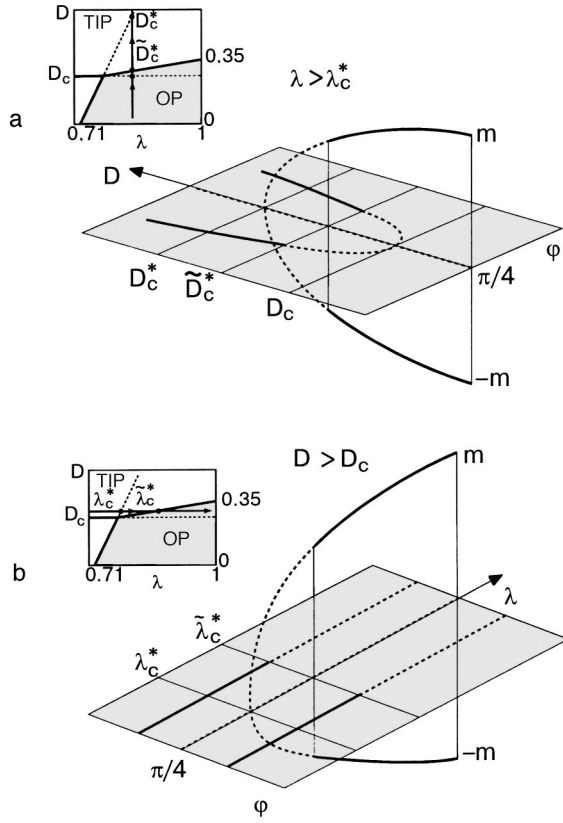
FIG. 4. Bifurcation diagrams of the TIP–OP transition (the stable solutions are indicated by solid lines, the unstable by dashed lines). The OP–TIP transition upon a change in the parameter D at a fixed λ. $\tilde{D}_c^*$ corresponds to the value of D on the straight line $\lambda = \tilde{\lambda}_c^*(D)$ (a). The TIP–OP transition upon a change in λ at constant D (b). The insets show schematically the lines corresponding to each diagram on the plane of parameters λ and D.

3. PLAQUETTE II WITH A FIXED BOUNDARY WITH THE DIPOLE–DIPOLE INTERACTION TAKEN INTO ACCOUNT

3.1. Static vortex configuration and the dynamical equations for the eigenmodes

For plaquette II (Fig. 2) with boundary spins fixed parallel to the lateral boundaries of the plaquette, the static vortex configurations $[m_i = m,\ \varphi_1 = \varphi,\ \varphi_i = \varphi + \pi(i-1)/2]$ are determined by the following pair of equations replacing the system of equations (4), (5):

$$\frac{m(1-bD)}{m}(\cos\varphi - \sin\varphi) - 2\lambda m + D\frac{m}{8}(\sqrt{2}+16-3(\sqrt{2}$$
$$+8)\sin 2\varphi) = 0, \qquad (34)$$

$$m_\perp(\cos\varphi + \sin\varphi)\left(1 - bD - \frac{3D}{8}m_\perp(\sqrt{2}+8)(\cos\varphi$$
$$-\sin\varphi)\right) = 0, \qquad (35)$$

where

$$b = \frac{7}{8} - \frac{1}{\sqrt{2}} - \frac{8}{25\sqrt{5}} \approx 0.0248$$

is a numerical constant.

As in the case of plaquette I, Eqs. (34) and (35) admit solutions for a static IP vortex with a structure analogous to the IP vortex in plaquette I in the exchange approximation (Fig. 2a), i.e., with $m=0$ and $\varphi = -\pi/4$. There is also a possible OP solution analogous to the solution in the exchange approximation (Fig. 2b) with $\varphi = -\pi/4$ and

$$m = 2\frac{\sqrt{(\lambda - \lambda_c(D))\left(\lambda - D\left[\frac{1}{\sqrt{2}}+5+b\sqrt{2}\right]/2 + \frac{1}{\sqrt{2}}\right)}}{2\lambda - D(1/\sqrt{2}+5)}. \tag{36}$$

It is seen from Eq. (36) that the OP vortex exists when the inequalities $\lambda > \lambda_c(D)$ and $\lambda > \tilde{\lambda}_c(D)$ hold simultaneously, where

$$\lambda_c(D) = D(1/\sqrt{2}+5-b\sqrt{2})/2 + 1/\sqrt{2}, \tag{37}$$

$$\tilde{\lambda}_c(D) = D(1/\sqrt{2}+5+b\sqrt{2})/2 - 1/\sqrt{2}. \tag{38}$$

The critical values of the parameters D_* and λ_* at which the dependence $\lambda_c(D)$ changes to $\tilde{\lambda}_c(D)$ at the boundary of the existence region of the OP vortex are $D_* = 1/b$ and $\lambda_* = (10+\sqrt{2})/4b$, respectively. Figure 5b shows only the region of anisotropy parameter $0 < \lambda < 1$ with the line $\lambda_c(D)$, since $\lambda_* \approx 115 \gg 1$. It will be shown below that the OP vortex is stable only in the parameter region $\lambda > \lambda_c(D)$, $\lambda > \tilde{\lambda}_c(D)$. At the very boundary of the existence region of the OP vortex the dependence of the out-of-plane magnetization (36) has the bifurcation form standard for the IP–OP transition.

Plaquette II also admits solutions in the form of TIP and TOP vortices. The solution for the TIP vortex is as follows: $m=0$ and $\varphi = \phi_t(D)$, where the function ϕ_t is given by the formula
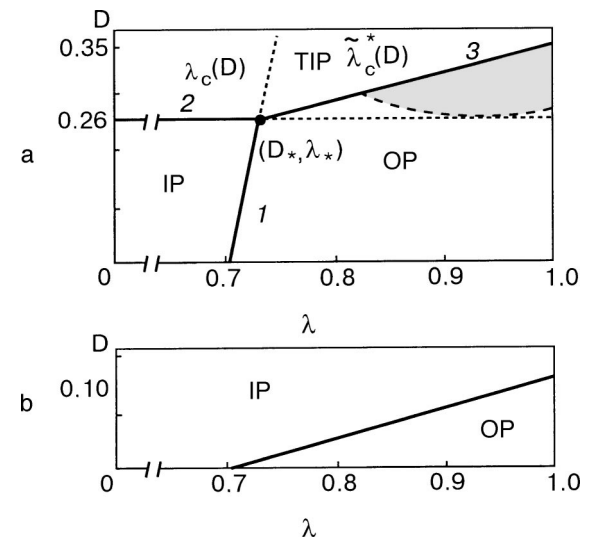

FIG. 5. Regions of stable vortex solutions on the plane of parameters λ and D for the different plaquettes. The stability regions of the IP, OP, and TIP vortices in plaquette I, separated by the curve $\lambda_c(D)$ [Eq. (24)]. The dotted lines separate the region of parameters where the sign of the frequency of the lower first azimuthal mode changes sign; this curve is determined by the equation $\Omega_1^{OP}(\lambda;D)=0$, where Ω_1^{OP} is given by expression (26) (a); the stability regions of the IP and OP vortices in plaquette II, separated by the straight line $\lambda_c(D)$ [Eq. (37)] (b).

$$\phi_t(D) = \pm \arccos\left(\frac{8}{3\sqrt{2}D}\frac{1-bD}{\sqrt{2}+8}\right) - \frac{\pi}{4}. \qquad (39)$$

In addition, for system (34), (35) there formally exist two solutions of the twisted out-of-plane (TOP) type, in which the distribution of the magnetization is given by the formulas $\varphi = \phi_t^{OP}(\lambda;D)$, $m = m_t(\lambda;D)$, and

$$\phi_t^{OP}(\lambda;D) = \pm \arccos\left(\frac{8}{3\sqrt{2}D}\frac{1-bD}{m_\perp^t(\lambda;D)(\sqrt{2}+8)}\right) - \frac{\pi}{4},$$

$$m_t(\lambda;D) = \sqrt{\frac{2(\lambda - \lambda_c^t(D))}{2\lambda + D(1+2^{-3/2})}},$$

$$\lambda_c^t(D) = \frac{8(1-bD)^2}{3D(\sqrt{2}+8)} - D(1+2^{-3/2})/2, \qquad (40)$$

where $m_\perp^t = \sqrt{1-m_t^2}$. However, it can be shown that the TIP and TOP vortices are unstable at all values of the parameters D and λ in the intervals investigated. Thus only the OP and IP vortices are stable in plaquette II, as will be demonstrated below.

To elucidate the stability of the different vortex configurations it is necessary to study the spectrum of linear excitations on top of them. The dynamical equations for the eigenmodes in the IP and OP configurations look like

$$\dot{\nu}_1 = \frac{\sqrt{2}}{m^3}(1-bD)\mu_1 + (D-\lambda)(\mu_2+\mu_4) + D\frac{\mu_3}{2\sqrt{2}}$$

$$+ m\left(1+\frac{D}{2}\right)(\nu_4-\nu_2) - \frac{D}{m^2}\left[\frac{3}{2}m^2(\mu_2+\mu_4)\right.$$

$$\left. + \frac{m^2}{2\sqrt{2}}\mu_3 - \left(3+\frac{1}{2\sqrt{2}}\right)\mu_1\right], \qquad (41)$$

$$\dot{\mu}_1 = \left(-\sqrt{2}(1-bD)m - Dm^2\left[3+\frac{1}{2\sqrt{2}}\right]\right)\nu_1 + m$$

$$\times\left(1+\frac{D}{2}\right)(\mu_4-\mu_2) - Dm^2\left[\frac{3}{2}(\nu_2+\nu_4) + \frac{\nu_3}{\sqrt{2}}\right], \qquad (42)$$

and three more pairs of equations obtained by a cyclic permutation of the indices.

3.2. Eigenmodes and the stability region of the in-plane vortex

The dependence of the frequency of the zeroth symmetric mode for the stability region of the IP vortex of plaquette II is given by the expression

$$\Omega_0^{IP} = \sqrt{2(\lambda_c(D)-\lambda)(\sqrt{2}+D[6+3/2\sqrt{2}-b\sqrt{2}])}. \quad (43)$$

At the point of the IP–OP transition on the line $\lambda = \lambda_c(D)$ for $\lambda < \lambda_*$ this dependence goes to zero with a square-root singularity (ordinary bifurcation). For $\lambda > \lambda_*$ the transition is of a more complicated character, but because $\lambda_* \gg 1$, this process will not be considered further. The ratio of the am-

plitudes of the oscillations of the spins in the zeroth mode in the perpendicular directions has the usual form for an IP–OP transition:

$$\mu^0/\nu^0 = \sqrt{\frac{(\sqrt{2}+D[3/2\sqrt{2}-b\sqrt{2}])}{2(\lambda_c(D)-\lambda)}}, \qquad (44)$$

which indicates a tendency to abandon the out-of-plane ordering at $\lambda \to \lambda_c(D)$ ($\mu^0/\nu^0 \to \infty$ on this line). For the twofold degenerate first azimuthal mode we have

$$\Omega_{1,2}^{IP} = \sqrt{(\sqrt{2}+D[3-b\sqrt{2}])}\sqrt{(\sqrt{2}+D[3-b\sqrt{2}-1/2\sqrt{2}])}. \qquad (45)$$

For the second azimuthal mode we obtain the following dependence:

$$\Omega_3^{IP} = \sqrt{(\sqrt{2}+2\lambda+D[1+1/\sqrt{2}-b\sqrt{2}])}$$

$$\times \sqrt{(\sqrt{2}+D[3/2\sqrt{2}-b\sqrt{2}])}. \qquad (46)$$

The ratios of the amplitudes of the azimuthal modes do not have singularities, and their frequencies remain real for all λ and D. The values of the frequencies increase with increasing D, i.e., growth of D leads to stabilization of the IP vortex. We note that the IP vortex in plaquette II is stable even for a purely dipolar system, i.e., for all the expressions obtained in this Section one can obtain expressions for a dipolar system by taking D to the limit in them. The reason for stability of this configuration, unlike the case for plaquette I, is that in such a configuration of the plaquette there are no surface "magnetostatic charges," i.e., the magnetic dipole contribution obtained in the continuum limit is minimized; the magnetostatic charge density itself is determined by the magnetization component perpendicular to the surface of the sample.

3.3. Eigenmodes and the stability region of the out-of-plane vortex

For an OP vortex of the region $(\lambda_c(D) < \lambda, \tilde{\lambda}_c(D) < \lambda)$ for the zeroth symmetric mode we obtain the following dependence:

$$\Omega_0^{OP} = 2\sqrt{\frac{(\lambda-\lambda_c(D))(\lambda-\tilde{\lambda}_c(D))(2\lambda+D)}{2\lambda - D(5+1/\sqrt{2})}}, \qquad (47)$$

where $\tilde{\lambda}_c(D)$ is determined by expression (38). This dependence goes to zero with a square-root singularity at the point of the OP–IP transition $\lambda = \lambda_c(D)$ (for $\lambda < \lambda_*$). The ratio of the amplitudes of the oscillations of different polarization for this mode has the standard form for an OP–IP transition:

$$\mu^0/\nu^0 = \frac{m_\perp(\lambda;D)}{2}\sqrt{\frac{(2\lambda+D)(2\lambda-D[5+1/\sqrt{2}])}{(\lambda-\lambda_c(D))(\lambda-\tilde{\lambda}_c(D))}}, \qquad (48)$$

and goes to infinity on the line of transition $\lambda = \lambda_c(D)$.

The frequencies of the first azimuthal modes are determined by expression (26) with the substitution $U_1, W_1 \to U_2, W_2$, where

$$U_2(\lambda;D) = \frac{\sqrt{2}}{m_\perp^3(\lambda;D)} + D\left[\frac{1}{m_\perp^2(\lambda;D)}\left(\frac{m^2(\lambda;D)}{2\sqrt{2}}\right.\right.$$

$$\left.\left. + 3 + \frac{1}{2\sqrt{2}}\right) - \frac{b\sqrt{2}}{m_\perp^3(\lambda;D)} - \frac{1}{2\sqrt{2}}\right],$$

$$W_2(\lambda;D) = \sqrt{2}m_\perp(\lambda;D) + Dm_\perp(\lambda;D)$$

$$\times\left(m_\perp(\lambda;D)\left[3 - \frac{1}{2\sqrt{2}}\right] - b\sqrt{2}\right). \qquad (49)$$

The dependence of the frequency of the second azimuthal mode on D and λ is given by formula (28) with the substitution $F_1, G_1 \rightarrow F_2 G_2$, where

$$F_2(\lambda;D) = \frac{\sqrt{2}}{m_\perp^3(\lambda;D)} + 2\lambda + D\left(\frac{3}{2\sqrt{2}} + \frac{3m(\lambda;D)}{m_\perp^3(\lambda;D)}\right.$$

$$\left. - \frac{b\sqrt{2}}{m_\perp^3(\lambda;D)} - 2\right),$$

$$G_2(\lambda;D) = \sqrt{2}m_\perp(\lambda;D) + Dm_\perp(\lambda;D)$$

$$\times\left(\frac{3m_\perp(\lambda;D)}{2\sqrt{2}} - b\sqrt{2}\right). \qquad (50)$$

The frequencies of the azimuthal modes remain real for all λ and D, and taking these modes into account does not narrow the stability region of the OP vortex. The ratios of the amplitudes of the oscillations of the spins in perpendicular directions does not have any singularities in the stability region of the OP vortex. We note that for plaquette II the frequency of the lower branch of the doublet of azimuthal modes remains negative in the entire stability region of the OP vortex, as in the exchange approximation (i.e., the wave corresponding to this mode rotates clockwise, as does the vortex itself). This may mean that taking the DDI into account when the outer spins are fixed parallel to the boundary of the plaquette does not lead to delocalization of the wave function corresponding to this mode, as was predicted for systems with a perpendicular fixing of the spins.

CONCLUSION

In this article we have considered, for the example of two spin plaquettes, the properties of the static vortex ordering of the magnetization and the transformation of the spectra of linear eigenmodes in an easy-plane two-dimensional Heisenberg ferromagnet with the exchange and dipole interactions taken into account simultaneously. Since previously in an analysis of analogous plaquette systems of small size in the exchange approximation it was found that the properties of the static vortex solutions and the features of the spectrum of such systems in a vortex configuration are qualitatively similar to the analogous properties of systems of large size,[26,28] there are grounds for assuming the presence of a qualitative similarity of the results obtained for a plaquette with those for systems of large size. The main results of this study reduce to the following.

1. When the surface spins are fixed perpendicular to the boundary (plaquette I), which takes place in the presence of

a large surface anisotropy of the sample or for a strong influence of the "matrix" surrounding the magnetic molecule, there can exist a new stable type of vortices (TIP) which are absent in the exchange approximation. The reason for this is that taking the DDI into account lifts the degeneracy of the ground state and makes it favorable for the magnetization to order parallel to the lateral boundary of the sample. For boundary conditions corresponding to plaquette II, taking the DDI into account leads to the situation that the the the "azimuthal" distribution of the magnetization in the vortices becomes the only one possible.

2. Stability diagrams, shown in Fig. 5, have been obtained for the plaquettes. We showed that when the DDI become dominant, the TIP vortex in plaquette I and the IP vortex in plaquette II become the only stable types of vortices. This is due to the circumstance that taking the DDI into account leads to additional effective easy-plane anisotropy. We showed that the IP–OP transition in the plaquettes has the standard bifurcation form of the solution, with a square-root growth of the static OP magnetization, while the IP–TIP transition in plaquette I has a square-root growth of the twist angle. Moreover, we have demonstrated that the OP–TIP transition in plaquette I is accompanied by a jump in the OP magnetization.

3. We have considered and analyzed the feature of the spectrum of plaquette eigenmodes that can arise when the DDI is taken into account. Increasing the value of the parameter D leads to a decrease in the values of the frequencies of all the eigenmodes for plaquette I in the OP and IP configurations and for plaquette II in the OP configuration. In the stability region of the TIP vortex for plaquette I and the IP vortex for plaquette II the values of the frequencies increase with increasing D. It is necessary to note the difference in the behavior of the ratio of the amplitudes of the IP and OP oscillations for the symmetric mode at $\lambda \rightarrow \lambda_c(D)$ for the OP vortex in plane I: in the region $D < D_c$ this ratio $\mu^0/\nu^0 \rightarrow \infty$, while for $D > D_c$ we have $\mu^0/\nu^0 \rightarrow 0$, which can be important for constructing simplified slightly nonlinear models. An interesting feature of the spectrum of eigenfrequencies of the linear spin modes of plaquette I is the change in direction of rotation of the wave of the lowest first azimuthal mode at certain values of the parameters D and λ. If this effect takes place in systems of large size, it can lead to delocalization of this mode outside the core of the OP vortex. The behavior of the frequency dependence of this mode for plaquette II, on the contrary, is analogous to that which takes place in the exchange approximation. Thus it can be assumed that the results obtained in the exchange approximation can also be suitable when the DDI is taken into account for a qualitative analysis of large systems with "outer" spins parallel to the boundary of the sample.

*E-mail: kovalev@ilt.kharkov.ua

[1] V. M. Rozenbaum, V. M. Ognenko, and A. A. Chuĭko, Usp. Fiz. Nauk **161**(10), 79 (1991) [Sov. Phys. Usp. **34**, 883 (1991)].

[2] K. De'Bell, A. B. MacIsaac, and J. P. Whitehead, Rev. Mod. Phys. **72**, 225 (2000).

[3] L. D. Landau and E. M. Lifshitz, "Toward a theory of magnetic permeability of ferromagnetic objects," in *Collected Works of L. D. Landau* [in Russian], Nauka, Moscow (1969), Vol. 1, p. 128; U. F. Braun, *Micromagnetism* [in Russian], Nauka, Moscow (1979).

[4] A. M. Kosevich, B. A. Ivanov, and A. S. Kovalev, *Nonlinear Magnetization Waves. Dynamic and Topological Solitons* [in Russian], Naukova Dumka, Kiev (1983).

[5] A. M. Kosevich, B. A. Ivanov, and A. S. Kovalev, Phys. Rep. **194**, 117 (1990).

[6] A. S. Kovalev, A. M. Kosevich, and I. V. Manzhos, Zh. Éksp. Teor. Fiz. **94**(11), 222 (1988) [Sov. Phys. JETP **67**, 2301 (1988)]; V. V. Kisiliev and A. P. Tankeev, J. Phys.: Condens. Matter **7**, 2087 (1995); **8**, 10219 (1996).

[7] A. I. Akhiezer, V. G. Bar'yakhtar, and S. V. Peletminskii, *Spin Waves*, North-Holland, Amsterdam (1968), Nauka, Moscow (1967).

[8] A. J. Mikeska and M. Steiner, Adv. Phys. **40**, 191 (1991).

[9] R. P. Cowburn, D. K. Koltsov, A. O. Adeyeye, and M. E. Welland, Europhys. Lett. **48**, 221 (1999).

[10] A. Aharoni, J. Appl. Phys. **83**, 3432 (1997).

[11] M. Sparks, Phys. Rev. B **1**, 3831 (1970); B. A. Kalinikos, Izv. Vyssh. Uchebn. Zaved. Fiz. **8**, 42 (1981); B. A. Kalinikos and A. N. Slavin, J. Phys. C **19**, 7013 (1986); S. O. Demokritov, B. Hillerbrands, and A. N. Slavin, Phys. Rep. **348**, 441 (2001).

[12] A. G. Anders, S. V. Volotskii, S. V. Startsev, A. Feger, and A. Orendacheva, Fiz. Nizk. Temp. **21**, 52 (1995) [Low Temp. Phys. **21**, 38 (1995)].

[13] R. P. Cowburn, D. K. Koltsov, A. O. Adeyeye, M. E. Welland, and D. M. Tricker, Phys. Rev. Lett. **83**, 1042 (1999); R. P. Cowburn, J. Phys. D **33**, R1 (2000).

[14] T. Shinjo, T. Okuno, R. Hassdorf, R. Shigeto, and T. Ono, Science **289**, 930 (2000).

[15] R. P. Cowburn and M. E. Welland, Science **287**, 1466 (2000); R. P. Cowburn, J. Magn. Magn. Mater. **242−245**, 505 (2002).

[16] S. Tehrani, E. Chen, M. Durlam, M. DeHerrera, J. M. Slaughter, J. Shi, and G. Kerszykowski, J. Appl. Phys. **85**, 5822 (1999).

[17] R. P. Cowburn, D. K. Koltsov, A. O. Adeyeye, and M. E. Welland, J. Appl. Phys. **87**, 7082 (2000).

[18] http://www.dapra.mil/dso/thrust

[19] I. R. Karetnikova, I. M. Nefedov, M. V. Sapozhnikov, A. A. Fraerman, and I. A. Shershavskiĭ, Fiz. Tverd. Tela (St. Petersburg) **43**, 2030 (2001) [Phys. Solid State **43**, 2115 (2001)].

[20] P. I. Belobrov, V. A. Voevodin, and V. A. Ignatchenko, Zh. Éksp. Teor. Fiz. **88**, 889 (1985) [Sov. Phys. JETP **61**, 522 (1985)]; A. A. Fraerman and M. V. Sapozhnikov, J. Magn. Magn. Mater. **192**, 191 (1999).

[21] A. M. Kosevich, V. P. Voronov, and I. V. Manzhos, Zh. Éksp. Teor. Fiz. **84**, 148 (1983) [Sov. Phys. JETP **57**, 86 (1983)].

[22] A. V. Nikiforov and É. B. Sonin, Zh. Éksp. Teor. Fiz. **83**, 642 (1983) [Sov. Phys. JETP **56**, 373 (1983)].

[23] G. M. Wysin, Phys. Lett. A **240**, 95 (1998).

[24] J. E. Prilepsky, "Properties of vortices in two-dimensional easy-plane ferromagnets" [in Russian], *Author's Abstract of Candidate's Dissertation, Kharkov (2003)*.

[25] F. G. Mertens and A. R. Bishop, *Nonlinear Sciences at the Dawn of the 21st Century*, Lecture Notes in Physics, P. L. Christiansen, M. P. Soerensen, and A. C. Scott (eds.), Springer, Berlin (2000), p. 137.

[26] A. S. Kovalev and J. E. Prilepsky, Vestnik KhNU. Ser. Fiz. **417**, 32 (1998); *ibid.* **440**, 25 (1999).

[27] A. S. Kovalev and J. E. Prilepsky, Fiz. Nizk. Temp. **28**, 1292 (2002) [Low Temp. Phys. **28**, 921 (2002)]; Yu. Gaididei, T. Kamppeter, F. G. Mertens, and A. R. Bishop, Phys. Rev. B **59**, 7010 (1999); *ibid.* **61**, 9449 (2000).

[28] A. S. Kovalev and J. E. Prilepsky, Fiz. Nizk. Temp. **29**, 71 (2003) [Low Temp. Phys. **29**, 55 (2003)].

[29] G. M. Wysin and A. R. Völkel, Phys. Rev. B **52**, 7412 (1995).

[30] G. M. Wysin, Phys. Rev. B **49**, 8780 (1994).

[31] B. A. Ivanov, H. J. Schnitzer, F. G. Mertens, and G. M. Wysin, Phys. Rev. B **58**, 8464 (1998).

[32] M. E. Gouvea, G. M. Wysin, A. R. Bishop, and F. G. Mertens, Phys. Rev. B **39**, 11840 (1989).

[33] E. Y. Vedmedenko, H. P. Oepen, A. Ghazali, J.-C. S. Levy, and J. Kirschner, Phys. Rev. Lett. **84**, 5884 (2000).

[34] J.-C. S. Levy, Phys. Rev. B **63**, 104409 (2001).

[35] C. E. Zaspel, C. M. MacKennan, and S. R. Snaric, Phys. Rev. B **53**, 11317 (1996).

[36] B. A. Ivanov and C. E. Zaspel, Appl. Phys. Lett. **81**, 1261 (2002).

[37] V. Novosad, M. Grimsditch, K. Yu. Guslienko, P. Vavassori, Y. Otani, and S. D. Bader, Phys. Rev. B **66**, 052407 (2002).

[38] L. Thomas, F. Lionti, R. Ballou, D. Gatteschi, R. Sessoli, and B. Barbara, Nature (London) **383**, 145 (1996); J. Kortus, M. R. Pedersen, C. S. Hellberg, and S. N. Khanna, J. Eur. Phys. D **16**, 177 (2001); N. Fujima, J. Eur. Phys. D **16**, 185 (2001).

[39] A. Moshel and K. D. Usadel, Phys. Rev. B **49**, 12868 (1994).

Translated by Steve Torstveit

LOW-TEMPERATURE PHYSICS OF PLASTICITY AND STRENGTH

Strain hardening of metals and alloys in the superconducting state

V. V. Pustovalov,* I. N. Kusmenko, N. V. Isaev, V. S. Fomenko, and S. É. Shumilin

B. Verkin Institute for Low Temperature Physics and Engineering, National Academy of Sciences of Ukraine, pr. Lenina 47, Kharkov 61103, Ukraine

The strain hardening of single crystals of pure Al and a Pb–In alloy in the normal (N) and superconducting (S) states is investigated. It is found that the strain hardening coefficients satisfy the inequality $\theta_S > \theta_N$ irrespective of whether the SN transition is brought about by an external magnetic field or temperature. © *2004 American Institute of Physics.* [DOI: 10.1063/1.1645158]

1. INTRODUCTION

The transition of a metal from the normal to the superconducting state at temperatures below T_c (the critical temperature for superconductivity) is accompanied by appreciable changes of its plasticity: a decrease in the flow stress and increases in the stress relaxation depth and the creep rate.[1] To explain these effects, which are sometimes referred to as the ''softening'' of a metal at the NS transition, several theoretical models have been proposed, based on an increase in the mobility of dislocations due to a decrease in the electron drag in the superconducting phase. These models have explained the experimental temperature dependence of the softening effects, which is similar to the temperature dependence of the superconducting energy gap and of the coefficient of friction for dislocations in a crystal, and also the strong dependence of the magnitude of the effects on the concentration and strength of the barriers impeding the motion of the dislocations. However, the influence of the NS transition on the defect structure and rate of strain hardening of a crystal has turned out to be more complicated, and the observed effects do not reduce to a ''softening'' in the superconducting state. For example, it was found in Ref. 2 that equal creep deformations of pure lead at a temperature below T_c in the N state (in the magnetic field of a superconducting solenoid) and in the S state lead to a different increment of the resistivity: deformation in the S state causes a larger increase in the resistivity. The authors conjectured that deformation in the superconducting state is accompanied by a faster formation of crystal lattice defects. Since the main contribution to the increase in the resistivity comes from point defects arising at intersections of dislocations, the growth of the number of intersection events in the superconducting state was explained by an increase in the velocity and density of mobile dislocations due to a change in the conditions of their dynamic drag. Analogous results were obtained in Refs. 3 and 4 in a study of the change in the defect structure of single-crystal and polycrystalline lead during its active deformation. The deformation of samples at a temperature $T < T_c$ in the N and S states was accompanied by a monotonic growth of the resistivity, but the rate of growth was higher in the S state. The observed growth of the

resistivity was due to the contribution of point defects (vacancies and interstitial atoms), and the formation of the dislocation structure did not depend on the electronic state of the sample. The additional generation of point defects during deformation in the S state was explained by a decrease in their energy of formation and a change in the dislocation dynamics. A direct comparison of the strain hardening coefficients during stress relaxation[5] and active deformation[6,7] in the N and S states has confirmed the hypothesis of a different rate of accumulation of deformation defects: the hardening coefficient depended on the state of the sample. In a number of cases the electronic state of the deforming sample was cyclically alternated by repeatedly turning the magnetic field of a superconducting solenoid on and off. Under such conditions the strain hardening rate of Pb–Bi alloys grew in proportion to the number of cycles.[8] As a result of cyclic alternation of the state, the strain hardening rate of a Pb–In alloy even exceeded that in the S state.[9] The growth of the hardening coefficient, proportional to the growth of the resistivity to the 0.5 power, was explained by an additional increment of the dislocation density as a result of the motion of the interface between the normal and superconducting phases during the repeated switching on and off of the magnetic field.

Thus besides the known effects of ''softening'' of metallic crystals at the superconducting transition under conditions of an unchanged defect structure (during the characteristic time of the superconducting transition in the magnetic field field of a solenoid) there are additional strain ''hardening'' effects observed in a crystal both in the superconducting state and as a result of cyclic alternation of the states. Such a hardening of the superconductor apparently reflects the complex dynamics of dislocation processes during the restructuring of the electron energy spectrum of the metal at the time of the phase transition and the subsequent deformation. In this regard it is of interest to study the strain hardening of a superconductor under conditions such that the superconducting transition is brought about not only by an external magnetic field but also by the a change in the deformation temperature. That is the problem addressed in this paper.

2. EXPERIMENTAL TECHNIQUE

We studied Al single crystals of 99.999% purity and also single crystals of the alloy Pb–5 at. % In (the purity of the initial materials was 99.999% for Pb and 99.997% for In). The aluminum single crystals were grown by the Bridgman method in two ways: I—in the form of a long, flat single crystal of complex shape and arbitrary orientation, which was then cut into 5 identical samples suitable for tensile straining; II—in a knock-down graphite mold, making it possible to obtain 10 flat samples for straining from a single seed crystal. The lead–indium single crystals were grown by method II. The samples for deformation had a length of 15 mm and a cross section of 3×1 mm. The orientation of the single crystals is indicated in the figures.

The aluminum samples of type I were deformed at a constant rate of 1.1×10^{-5} s^{-1} at a temperature $T = 0.52$ K ($T < 0.5 T_c$, where $T_c = 1.175$ K is the critical temperature of the superconducting transition in aluminum[10]), and the tensile straining diagrams were recorded in load–time coordinates. The technique of straining at ultralow temperatures is described in detail in Ref. 11. In the first series of experiments, after the diagrams were converted to coordinates of shear stress τ versus shear strain ε, the hardening coefficients $\theta = \partial \tau / \partial \varepsilon$ were compared for samples deformed only in the superconducting or only in the normal state (in a longitudinal field of strength $H > H_c$, where $H_c = 104$ Oe is the critical magnetic field in aluminum[10]). In a second series of experiments we recorded the change in the hardening rate of the same sample as a result of the superconducting transition in the magnetic field of a solenoid. The aluminum single crystals of type II were deformed at a constant rate of 1.1×10^{-4} s^{-1}, and the strain hardening coefficients at two temperatures, $T_1 = 1.0$ K and $T_2 = 1.3$ K, chosen such that $T_1 < T_c < T_2$, were compared.

The Pb–5 at. % In single crystals, oriented for easy slip, were deformed at a rate of 1.1×10^{-5} s^{-1}, with the sample simultaneously heated in the vicinity of the critical temperature of the superconducting transition $T_c = 7.05 – 7.1$ K.[10] The drift of the signal corresponding to zero load on the sample was monitored before and after the experiment. The strain hardening coefficients θ of the same sample above and below T_c were determined from the strain diagram.

3. EXPERIMENTAL RESULTS AND DISCUSSION

The hardening curves in coordinates of shear stress versus shear strain obtained for two aluminum single crystals of the same orientation at a constant temperature $T < 0.5 T_c$ in a medium of liquid He^3 are shown in Fig. 1. The dashed curve corresponds to deformation of a superconducting sample, the solid curve to that of a normal sample, which was placed in the magnetic field of a superconducting solenoid with $H > H_c$. It is seen that the critical shear stress for the superconducting sample is lower than that of the normal sample, $\tau_{0S} < \tau_{0N}$. The difference of the stresses, $\Delta \tau_{0NS} = \tau_{0N} - \tau_{0S}$, amounts to 0.27–0.30 MPa for different pairs of samples. At the same time, the strain hardening rate of the superconducting sample is markedly higher than that of the normal sample: $\theta_S > \theta_N$ (in the region of strains $\varepsilon \lesssim 0.15$ their ratio is $\theta_S / \theta_N \approx 1.43$). As a result, to maintain a given rate of

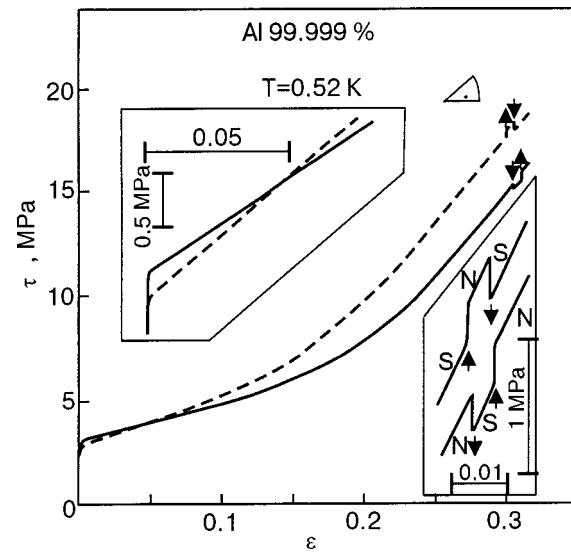FIG. 1. Curves of the hardening of Al single crystals in the normal (solid curve) and superconducting (dashed curve) states at $T = 0.52$ K, $\dot{\varepsilon} = 1.1 \times 10^{-5}$ s^{-1}. The inset on the left shows the initial parts of the curves. The inset on the right shows the jumps in the flow stress at the *NS* and *SN* transitions in the region of high strains.

strain for $\varepsilon > 0.05$ it is necessary to apply a larger stress to the superconducting sample than to the normal sample. In this sense one can speak of a hardening of the superconducting sample, which for $\varepsilon \approx 0.3$ reaches a value of more than 2.7 MPa. At large deformations $\theta_S / \theta_N \approx 1.01$. It is important to note that an *SN* or *NS* transition (in a magnetic field) at any point of the $\tau(\varepsilon)$ curves is accompanied by an increase $\Delta \tau_{SN}$ or decrease $\Delta \tau_{NS}$, respectively, of the level of flow stress (see the inset in Fig. 1), but the jump in stress is an order of magnitude smaller than the difference of the stresses in the region of large strains.

The observed hardening effect $\theta_S > \theta_N$ can be explained by differences in the defect structure of the initial single crystals and by features of its evolution in the course of deformation, arising either in the external magnetic field or as a result of a change in the electronic state of the crystal at the phase transition. Our data pertain to single crystals of a single growth series, with the same orientation and with nearly the same defect structures, as is indirectly indicated by the sign and absolute value of $\Delta \tau_{0NS}$, which agree with published data on the jump in stress in the same aluminum sample.[12] However, an influence of the initial structure on the value of the coefficient θ is not ruled out, and it is therefore important to compare the hardening observed on different samples with the hardening of one single-crystal sample deformed in the *S* and *N* states. Characteristic parts of the tensile straining curve $\tau(\varepsilon)$ of an aluminum single crystal at a temperature of 0.52 K with *SN* transitions in an external magnetic field are presented in Fig. 2. At low strains (Fig. 2a) the *SN* transition is accompanied by an increase of the flow stress by an amount $\Delta \tau_{SN} = 0.27$ MPa, while the hardening coefficient falls ($\theta_S > \theta_N$) by approximately 10%. The observed increase in the stress $\Delta \tau_{SN}$ is equal to the difference of the critical shear stresses $\Delta \tau_{0NS} = \tau_{0N} - \tau_{0S}$ of the normal and superconducting samples in the previous experiment. The decrease of the hardening coefficient at the transition of the crystal to the *N* state (see Fig. 2) also agrees
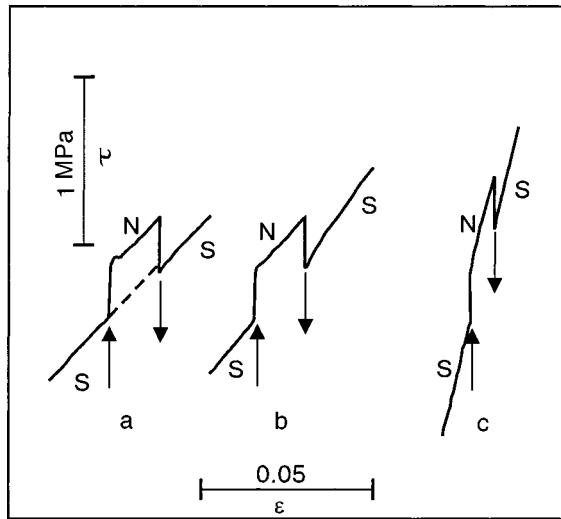
FIG. 2. Parts of the hardening curve of an Al single crystal with a change of the electronic state of the sample in the first (a), transient (b), and second (c) stages of deformation at $T = 0.52$ K.

FIG. 3. Hardening curves of Al single crystals in the normal (solid curve) and superconducting (dashed curve) states at temperatures above and below T_c. The inset shows the initial part of the curves. $\dot{\varepsilon} = 1.1 \times 10^{-5}$ s^{-1}.

with the data for different samples, although the ratio $\theta_S / \theta_N \approx 1.1$ is noticeably smaller than in the previous experiment. The reverse transition to the S state is accompanied by a decrease in the flow stress $\Delta\tau_{NS}$ and an increase in the coefficient θ. In the transient region (Fig. 2b) the parameters of the hardening curve at the SN transition change change in a similar way, but at high strains (Fig. 2c) the influence of the SN transition decreases. Thus one observes qualitative agreement between the data obtained on a single sample and on different samples: at a temperature below T_c the superconducting transition causes an increase in the rate of strain hardening of the crystal.

Since all of the previous experiments have been done in an external magnetic field produced by a superconducting solenoid, one of the causes of the observed effect might be a dynamic disturbance of the defect structure of the crystal as a result of the turning on and off of the magnetic field or a nonuniform distribution of the magnetic field in the plane of a sample of finite length. The influence of the field in these cases is obviously stronger the higher the field strength, and it is therefore important to note the qualitative agreement of the effects observed in aluminum and in lead and its alloys.[9] In spite of the fact that the critical magnetic field strength H_c of aluminum is almost an order of magnitude less than the second critical field H_{c2} of the Pb–5 at. % In alloy,[10] the character of the observed hardening effects at the superconducting transition in magnetic field remains unchanged.

Of fundamental importance for assessing the role of magnetic field are experiments in zero field, when the superconducting transition is brought about by a change in temperature. Making use of the fact that in the low-temperature region the yield stress and the strain hardening coefficient of aluminum are weakly dependent on temperature,[12] these parameters were measured at different temperatures above and below T_c, i.e., under conditions of a superconducting transition in the absence of magnetic field. The results for single crystals (growth series II) deformed in the vicinity of $T_c = 1.175$ K, are illustrated in Fig. 3. One of the hardening curves, at $T_1 = 1.0$ K, corresponds to straining in the super-
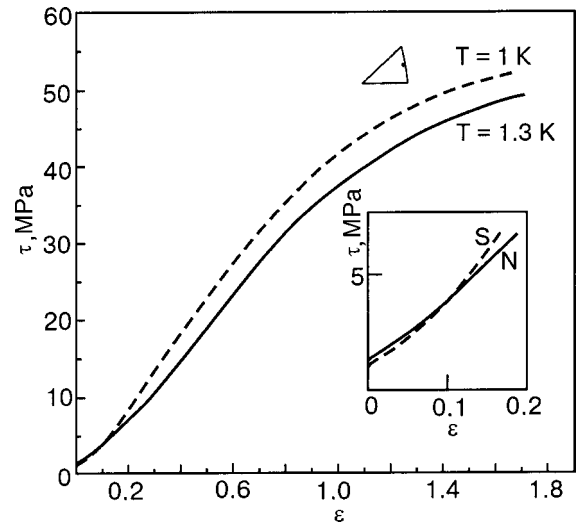
conducting state (the dashed curve), while the other, at $T_2 = 1.3$ K, corresponds to the normal state (solid curve). Under these conditions the difference of the critical stresses $\Delta\tau_{0NS} = \tau_{0N} - \tau_{0S} = 0.1$ MPa decreases sharply in comparison with the director for $T = 0.52$ K (see Figs. 1 and 2), in agreement with the known experimental and theoretical dependence of $\Delta\tau_{0NS}(T)$ discussed in Ref. 1. At $\varepsilon > 0.1$ the hardening rates, as before, obey the inequality $\theta_S(T_1) > \theta_N(T_2)$: for a given rate of strain the superconducting sample requires a greater stress be applied in comparison to the normal sample. The ratio $\theta_S(T_1) / \theta_N(T_2) = 1.68$, and the maximum difference of the flow stresses is 1.2 MPa. With allowance for the different growth conditions and orientation of the single crystals of series I and II, these estimates agree with the data calculated from the hardening curves in Figs. 1 and 2. Thus a qualitative analogy is observed between the results of experiments in an external magnetic field and an experiment in which the temperature of the sample is varied near T_c: the strain hardening coefficient of aluminum is larger in the superconducting state than in the normal state.

For further assessment of the influence of experimental conditions on the result of an experiment, it is of interest to combine the advantages of the two techniques: to compare the strain hardening rate for the same sample at temperatures above and below the critical, i.e., under conditions of a superconducting transition in the absence of magnetic field. For such a comparison to be reliable, the hardening of the crystal due to the evolution of its defect structure in the course of the deformation with simultaneous heating should be minimal; this is most characteristic of the easy-slip stage. Since it is difficult to arrange such slip in aluminum because of the very high energy of a stacking fault, we chose the alloy Pb–5 at. % In with a suitable crystallographic orientation as the object of study. A typical result for the three samples studied by straining with heating (the heating rate was $\dot{T} < 10^{-3}$ K/s) is illustrated in Fig. 4. It is seen that: in the region $T < T_c$ a change in the heating rate does not affect the value of $\delta\dot{\tau}$, which at a fixed strain rate is proportional to the coefficient θ_S; at the transition through T_c the heating rate is
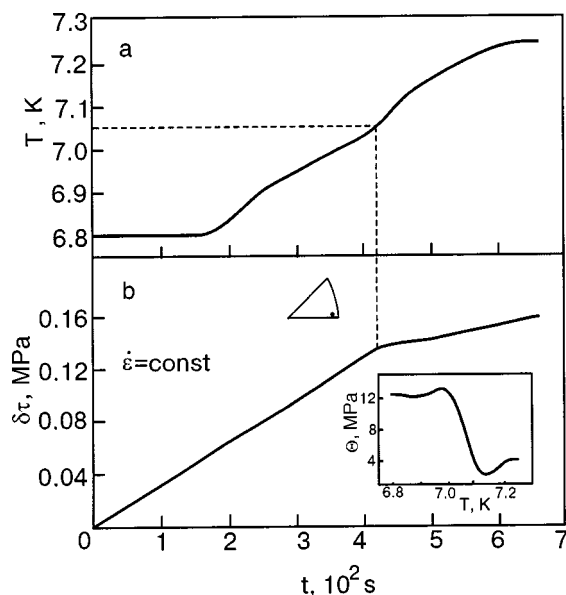
FIG. 4. Strain hardening of a Pb–5 at. % In single crystal in the easy-slip stage: variation of the temperature of the crystal with time (a); the increase of the flow stress as a function of the straining time at a strain rate $\dot{\varepsilon} = 1.1 \times 10^{-5}$ s^{-1} (b). The inset shows the temperature dependence of the strain hardening coefficient θ in the vicinity of T_c.

count the electron drag forces at low temperatures and do not consider their influence on the increase of the density of mobile dislocations and the mechanisms of formation of dislocation pileups as a basic structural element of the deformed material. Meanwhile, a clear experimental example of the influence of the electronic state on plastic deformation of a crystal is the jumplike deformation at a constant rate of loading: as a result of the destruction of superconductivity by an external magnetic field the depth and frequency of the jumps of the load increase sharply. The phenomenological models of this effect presuppose that dislocation pileups capable of breaking through the barriers on account of the high stresses at the head of a pileup are formed in the course of the deformation. It may be that, because of the low values of the heat capacity and thermal conductivity at helium temperatures, a local heating occurs when an obstacle is broken through, promoting the avalanche motion of the dislocations.[12,14] It has not been possible to prove the influence of the electron drag and heat capacity in the S and N states on the intensity of such motion. However, it can be assumed that the development of jumplike deformation as a result of the SN transition is due to features of the strain hardening of type-I and type-II superconductors, which were observed in our study: the decrease of the hardening coefficient ($\theta_S < \theta_N$) and the jump in stress $\Delta\tau_{SN} > 0$ at the SN transition in an external magnetic field can promote unstable flow of the crystal, which under certain conditions explains the increase in intensity of jumplike deformation in the normal state; the change of θ at the superconducting transition in zero magnetic field observed in a hard superconductor near T_c may be due to a change in the heat capacity and kinetic constants of the crystal and to the development of heating processes in the dislocation slip bands.

The results obtained show that besides a decrease of the flow stress (softening) of the single crystals studied at the NS transition, their plastic deformation in the superconducting state is characterized by a higher strain hardening coefficient than in the normal state. This means that a phenomenological model for strain hardening of a superconducting crystal should incorporate fluctuation–dynamic mechanisms of dislocation motion in connection with both the low-temperature region itself and with the fundamental characteristics of the superconducting transition.

*E-mail: pustovalov@ilt.kharkov.ua

constant but a noticeable drop in the value of $\delta\dot{\tau}$ is observed; there is no jump in the flow stress at $T = T_c$: $\Delta\tau_{SN} = 0$. For different samples the ratio of the hardening coefficients varied in the range $2 < \theta_S/\theta_N < 3$. The time of the experiment was not more than 1/10 the time of deformation at a fixed rate in the easy-slip stage. Prior to the start of the experiment all of the samples were preliminarily deformed by 5–7% above the yield point.

The experimental results presented in Figs. 1–4 show that the observed hardening effect in the superconducting state $\theta_S > \theta_N$ is not due to the natural variations in the defect structures of the initial (undeformed) crystals or to the influence of the external magnetic field on the defect structure in the course of the deformation of the samples. The change in the strain hardening coefficient of superconducting crystals should be assigned to features of the plasticity of metals and alloys in the low-temperature region.

Among the known low-temperature features of plasticity are the anomalous temperature dependence of the yield point of a number of metals and alloys,[13] the jumplike character of their plastic flow,[14] and the change in the flow stress, stress relaxation depth, and creep rate at an SN transition.[1] At present it is assumed that the majority of the phenomena listed are due to a combination of the fluctuation and dynamic mechanisms for the overcoming of potential barriers in the crystal lattice by the mobile dislocations. As the temperature is lowered, the inertial properties of the dislocations play a more important role because of the change in the electron drag, which depends not only on the temperature but also on such fundamental characteristics of a superconductor as the value of the energy gap and the density of the superconducting component.

The known models of strain hardening (see reviews[15,16]), which postulate equality of the flow stress to the frictional stress acting on a mobile dislocation, do not take into ac-

[1] V. I. Startsev, V. Ya. Il'ichev, and V. V. Pustovalov, *Plasticity and Strength of Metals and Alloys at Low Temperatures* [in Russian], Metallurgiya, Moscow (1975) s. 328.

[2] I. A. Gindin, V. P. Lebedev, and Ya. D. Starodubov, Fiz. Tverd. Tela (Leningrad) **14**, 2025 (1972) [Sov. Phys. Solid State **14**, 1748 (1972)].

[3] V. P. Lebedev and V. S. Krylovskiĭ, Fiz. Tverd. Tela (Leningrad) **18**, 3648 (1976) [Sov. Phys. Solid State **18**, 2124 (1976)].

[4] V. P. Lebedev and V. S. Krylovskiĭ, Metallofizika (Kiev) **8**, 114 (1986).

[5] V. I. Dotsenko, A. I. Landau, and V. V. Pustovalov, Phys. Status Solidi B **66**, 279 (1974).

[6] I. N. Kuz'menko, Author's Abstract of Candidate's Dissertation [in Russian], Kharkov, FTINT AN USSR (1984).

[7] V. P. Lebedev and V. S. Krylovskiĭ, Fiz. Tverd. Tela (Leningrad) **33**, 2994 (1991) [Phys. Solid State **33**, 1690 (1991)].

[8] D. A. Didenko and V. V. Pustovalov, Fiz. Nizk. Temp. **1**, 1428 (1975) [Sov. J. Low Temp. Phys. **1**, 648 (1975)].

[9] V. P. Lebedev, V. S. Krylovskii, and V. M. Pinto Simoes, Fiz. Nizk. Temp. **23**, 1128 (1997) [Low Temp. Phys. **23**, 848 (1997)].

[10] B. W. Roberts, *Properties of Selected Superconductive Materials*, NBS Technical Note No. 724 (1972).

[11] I. N. Kuz'menko, V. V. Pustovalov, and S. É. Shumilin, Prib. Tekh. Éksp., No. 1, 196 (1988).

[12] L. N. Kuzmenko and V. V. Pustovalov, Cryogenics **25**, 346 (1985).

[13] V. I. Dotsenko, A. I. Landau, and V. V. Pustovalov, *Present-Day Problems of the Low-Temperature Plasticity of Materials* [in Russian], Naukova Dumka, Kiev (1987).

[14] V. V. Pustovalov, Fiz. Nizk. Temp. **26**, 515 (2000) [Low Temp. Phys. **26**, 375 (2000)].

[15] A. L. Roĭtburd, in *Physics of Strain Hardening of Single Crystals* [in Russian], Naukova Dumka, Kiev (1972).

[16] O. V. Klyavin, in *Physical Processes of Plastic Deformation at Low Temperatures* [in Russian], Naukova Dumka, Kiev (1974).

Translated by Steve Torstveit

Nonlinear acoustic effects arising from dislocations in niobium single crystals

P. P. Pal-Val,* V. D. Natsik, L. N. Pal-Val, and Yu. A. Semerenko

B. Verkin Institute for Low Temperature Physics and Engineering, National Academy of Sciences of Ukraine, pr. Lenina 47, Kharkov 61103, Ukraine

The temperature dependence of the logarithmic decrement δ and dynamic Young's modulus E in niobium single crystals of high purity is investigated in a wide interval of low temperatures $3\,\text{K} \leq T \leq 300\,\text{K}$. Measurements are made by means of a two-component composite vibrator method under excitation of longitudinal vibrations with a frequency of 88 kHz and a relative amplitude of the acoustic strain varying in the range $5 \times 10^{-9} < \varepsilon_0 < 7 \times 10^{-5}$. In the temperature interval 50–200 K a nonlinear effect is registered: an amplitude-dependent contribution to the decrement and Young's modulus is observed when the amplitude of the ultrasound reaches a threshold value $\varepsilon_{0c} \gtrsim 10^{-5}$. The dependence of the threshold value ε_{0c} on temperature and on preliminary plastic deformation of the sample is established. The amplitude dependences $\delta(\varepsilon_0)$ and $E(\varepsilon_0)$ at $\varepsilon_0 > \varepsilon_{0c}$ and their transformation with temperature are investigated in detail. Analysis shows that the nonlinear effects are due to the breakaway of ultrasonically excited dislocations from impurity atoms. The experimental results are in satisfactory agreement with the conclusions of the Granato–Lücke theory of athermal dislocation hysteresis and its generalization to the case of thermally activated hysteresis proposed by Indenbom and Chernov. © *2004 American Institute of Physics.* [DOI: 10.1063/1.1645159]

1. INTRODUCTION

Study of the acoustic properties of crystals in the low-temperature region reveals a number of linear and nonlinear effects which owe their origin to dislocations, as is evidenced by their dependence on the dislocation density and other parameters of the dislocation structure. An analysis of these effects on the basis of the present-day theoretical ideas about the low-temperature mobility of dislocations yields information about the fine details of the dynamic behavior of dislocations, e.g., about the interaction of dislocations with impurities and with the Peierls potential relief, about the influence of the electronic viscosity and quantum fluctuations on the motion of dislocations, etc.

Among the linear acoustic effects it is customary to include the relaxation resonances—peaks of the sound absorption and the corresponding "steps" on the dynamic Young's modulus defect—which are observed in studies of the temperature and frequency dependences of the acoustic properties of crystals. The nonlinear effects, as a rule, appear in the form of a dependence of the sound absorption and dynamic Young's modulus on the amplitude of the acoustic strain. Here the criterion of observation and the character of the nonlinear effects also depend substantially on temperature and on the sound frequency.

The data of acoustic measurements are an indirect, macroscopically averaged reflection of dislocation processes in crystals. To make it possible to obtain the quantitative characteristics of the corresponding elementary events occurring on the microscopic scale it is necessary to interpret the results of acoustic measurements with the use of microscopic models that reflect the specifics of the dynamic behavior of dislocations under the action of an acoustic wave and their interaction with the phonon and electron subsystems of the

crystals, with the potential relief, and with various defects of the crystal structure.[1–8] Although it is possible to achieve qualitative agreement of the experimental results with the predictions of the theory on the whole, the interpretation of nonlinear (amplitude-dependent) dislocation effects[2,9] encounters a number of difficulties, the cause of which lies in the complexity and diversity of the dynamic behavior of dislocations under different experimental conditions. A number of questions still remain open for discussion. Among them is the question of the shape of the hysteresis in the dependence of the dislocation strain on the applied stress under sign-varying loading of a crystal, which is intimately related to the question of the character of the depinning of dislocations from local pinning centers: the breakaway of a double dislocation segment from an isolated obstacle, the "catastrophic" breakaway of dislocations from a set of obstacles, the "dry" friction effect in the motion of a dislocation line through an impurity, etc. The question of the functional form of the amplitude dependence of the sound absorption and Young's modulus has not yet been conclusively answered. Finally, the question of the influence of thermal and quantum fluctuations on the motion of dislocations through barriers of different natures and on the acoustic effects involving dislocations is of significant interest. The experimental data currently available are insufficient to give unambiguous answers to the questions posed above.

Very little experimental data has been obtained up till now on the low-temperature nonlinear acoustic properties of bcc metals, in which the mobility of dislocations can be governed by the braking action of both Peierls barriers and impurities. The main goal of the present study was the experimental investigation and analysis of the nonlinear acoustic effects in niobium, which is a typical representative of metals

with the bcc structure. The features in the acoustic absorption and dynamic Young's modulus due to the dynamic properties of dislocations are investigated in the kilohertz frequency range over a wide interval of low temperatures. Although the linear acoustic properties of niobium at temperatures of 2–300 K have been systematically investigated in several studies,[8,10–13] there is practically no information in the literature about the nonlinear properties.

2. EXPERIMENTAL TECHNIQUE

As the object of study we used a niobium single crystal of high purity, with a reduced residual resistance $RRR \equiv R_{300}/R_0 = 10000$. The values of the RRR were determined by measuring the temperature dependence of the electrical resistance of the sample in the interval 2–300 K. For this the sample was placed in an external magnetic field, which was used to bring the sample to a normal state at temperatures below the superconducting transition temperature $T_c \approx 9.3$ K,[14] and then the experimental data were extrapolated to 0 K and zero field. A spectral analysis showed that the main substitutional impurities were Mo, Ta, and Zr atoms. The number of interstitial impurities N, O, and H was reduced by a long high-temperature annealing, first in flowing oxygen at a pressure of $\sim 10^{-3}$ Pa and then in an ultrahigh vacuum $\sim 10^{-8}$ Pa.[15]

The samples were in the form of cylindrical rods 4.2 mm in diameter and ~ 24 mm long. The crystallographic orientation of the longitudinal axis of the sample had the $\langle 100 \rangle$ direction and was determined with the aid of the Laue diffraction pattern to an accuracy of $\pm 1°$. The initial density of dislocations in the sample was $\sim 5 \times 10^5$ cm^{-2}. To elucidate the influence of dislocations on the acoustic properties of niobium, we studied samples both in the initial state and with a larger dislocation density. Immediately before the acoustic measurements were made, fresh dislocations were introduced in the sample by means of plastic deformation by a four-point bend at room temperature to a value of the residual plastic deformation of $\varepsilon_{pl} = 0.65\%$.

The acoustic measurements were made using a two-component composite vibrator.[16,17] Longitudinal standing waves with a frequency $f \approx 88$ kHz were excited in the samples. The ultrasonic strain amplitude ε_0 and the temperature T were varied in the intervals $5 \times 10^{-9} < \varepsilon_0 < 7 \times 10^{-5}$ and 2 K$< T < 340$ K, respectively. In the experiments the temperature dependence and amplitude dependence of the logarithmic decrement $\delta(T, \varepsilon_0)$ and resonance frequency of the composite vibrator were measured, and the results were used to calculate the dynamic Young's modulus $E(T, \varepsilon_0)$.[17] To monitor possible irreversible changes in the structure of the sample due to the high-amplitude ultrasound, the amplitude dependences $\delta(\varepsilon_0)$ and $E(\varepsilon_0)$ were measured both on increasing and decreasing amplitude of the ultrasonic strain.

3. RESULTS OF THE MEASUREMENTS

3.1. Amplitude-independent background of the internal friction and Young's modulus

The measured temperature–amplitude dependences of the logarithmic decrement $\delta(\varepsilon_0, T)$ and the dynamic Young's modulus $E(\varepsilon_0, T)$ can be represented in the form of a sum of
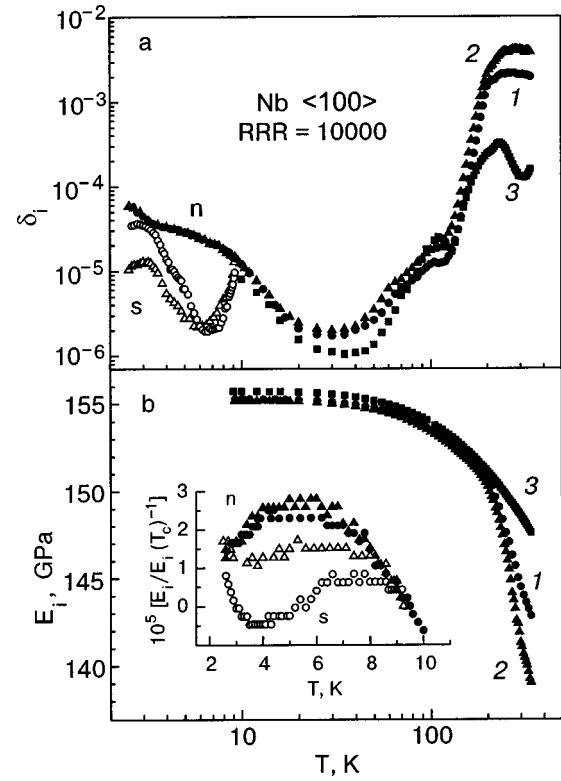

FIG. 1. Temperature dependence of the logarithmic decrement (a) and dynamic Young's modulus (b) in niobium, measured in the amplitude-independent region: ●, ○—undeformed sample (curve *1*); ▲, △—sample plastically deformed to $\varepsilon_{pl} = 0.65\%$ (curve *2*); ■, □—annealed sample (curve *3*). The filled symbols are for the *n* state, the unfilled symbols for the *s* state.

two components: linear (background) terms δ_i and E_i, depending only on the temperature, and amplitude-dependent terms δ_H and E_H:

$$\delta(\varepsilon_0, T) = \delta_i(T) + \delta_H(\varepsilon_0, T), \tag{1a}$$

$$E(\varepsilon_0, T) = E_i(T) + E_H(\varepsilon_0, T). \tag{1b}$$

A specific feature of the nonlinear acoustic properties of niobium as compared to other bcc metals studied previously is the existence of amplitude dependence of δ and E against a complex background of nonmonotonic temperature dependences $\delta_i(T)$ and $E_i(T)$ (see Fig. 1). The data shown in the figure were obtained on an undeformed sample (curve *1*), a sample deformed by 0.65% (curve *2*), and a sample that was annealed after deformation (curve *3*). The curves of $\delta_i(T)$ and $E_i(T)$ have several characteristic features pertaining to different temperature intervals.

First of all, one notices the significant change in the decrement (by 3–4 orders of magnitude) within the temperature range studied. This is explained mainly by the presence of a broad relaxation maximum (the so-called α peak[13]) on $\delta_i(T)$, the position of which on the temperature scale is sensitive to the structural state of the sample and lies in the interval 240–280 K. In addition, on rapid cooling of the samples in the existence region of the superconducting state $T < T_c \approx 9.3$ K, the $\delta_i(T)$ curves in both the normal (*n*) and superconducting (*s*) states exhibit the so-called Kramer–Bauer peak located at a temperature of 2–3 K.[8,10] Both peaks correspond to steps on the temperature dependence of the
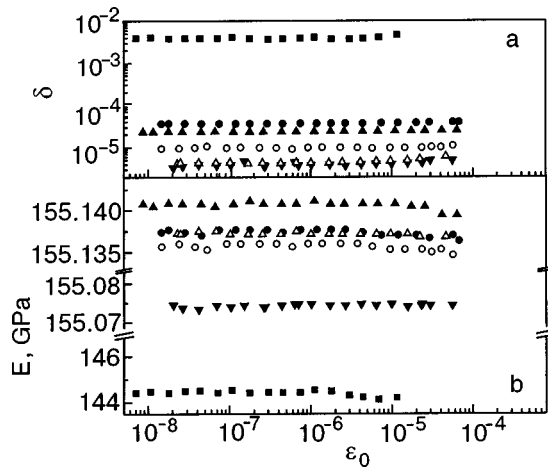
FIG. 2. Influence of the ultrasound amplitude on the decrement (a) and dynamic Young's modulus (b) in the temperature region $T \lesssim 25$ K and at $T = 300$ K: ▼—25 K, $\varepsilon_{pl}=0$; ▲—6 K, n state, $\varepsilon_{pl}=0.65\%$; △—6 K, s state, $\varepsilon_{pl}=0.65\%$; ●—3 K, n state, $\varepsilon_{pl}=0.65\%$; ○—3 K, s state, $\varepsilon_{pl}=0.65\%$; ■—300 K, $\varepsilon_{pl}=0$.

FIG. 3. Amplitude dependences of the decrement (a) and dynamic Young's modulus (b) in the temperature interval 55–185 K in the undeformed sample.

modulus $E_i(T)$. The superconducting transition in both the undeformed and deformed niobium has a substantial effect on the temperature dependence of the acoustic characteristics below T_c: it leads to decreases in the decrement and dynamic Young's modulus.

A preliminary plastic deformation and annealing of the sample have practically no effect on the background losses below T_c in the n state. At higher temperatures the value of δ_i increases slightly after deformation and decreases markedly as a result of annealing. Accordingly, the value of the Young's modulus decreases after plastic deformation and increases after high-temperature annealing in a high vacuum. The maximum sensitivity of the background component to plastic deformation is observed in the s state and also in all cases in the temperature region in which the relaxation resonances (the absorption peak and the steps on the modulus defect) are located.

3.2. Amplitude dependences of the decrement and dynamical Young's modulus

The plots in Fig. 2 show that in the temperature region $3\,\text{K}<T<25\,\text{K}$ at the ultrasound amplitudes used in the experiment, $\varepsilon_0<7\times10^{-5}$, there is practically no amplitude dependence of the decrement and Young's modulus irrespective of whether the measurements were made on an undeformed or deformed sample, in the n or in the s state, in the region of the Kramer–Bauer peak or outside it. The same sort of behavior of $\delta(T,\varepsilon_0)$ and $E(T,\varepsilon_0)$ was also registered in the temperature region $210\,\text{K}<T<300\,\text{K}$ near the α peak.

Noticeable dependence of the acoustic properties of niobium on the sound amplitude was revealed in the intermediate temperature region $50\,\text{K}<T<200\,\text{K}$. Figure 3 shows the amplitude-dependent components of the decrement, $\delta_H(T,\varepsilon_0)=\delta(T,\varepsilon_0)-\delta_i(T)$, and of the relative change in Young's modulus, $E_H(T,\varepsilon_0)/E_i(T)=[E(T,\varepsilon_0)-E_i(T)]/E_i(T)$, measured in this temperature interval. It is seen that the critical amplitude ε_{0c} for the start of the nonlinear effects has approximately the same value for the $\delta_H(T,\varepsilon_0)$ and $E_H(T,\varepsilon_0)/E_i(T)$ curves. This parameter has

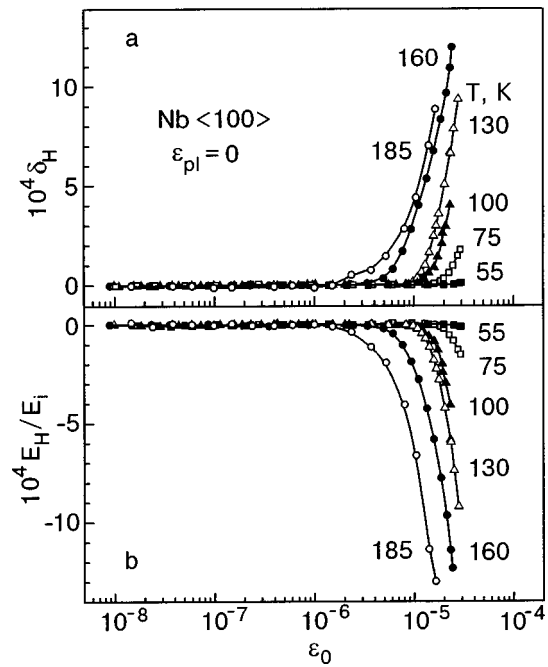appreciable temperature dependence: ε_{0c} increases with decreasing temperature. Moreover, upon changes in T the amplitude-dependent parts of the $\delta_H(T,\varepsilon_0)$ and $E_H(T,\varepsilon_0)/E_i(T)$ curves in the chosen semilogarithmic coordinates shift as a whole while remaining practically parallel to one another. In the sample plastically deformed by $\varepsilon_{pl}=0.65\%$ the behavior of the amplitude dependences remains qualitatively the same (see Fig. 4). However, the critical am-
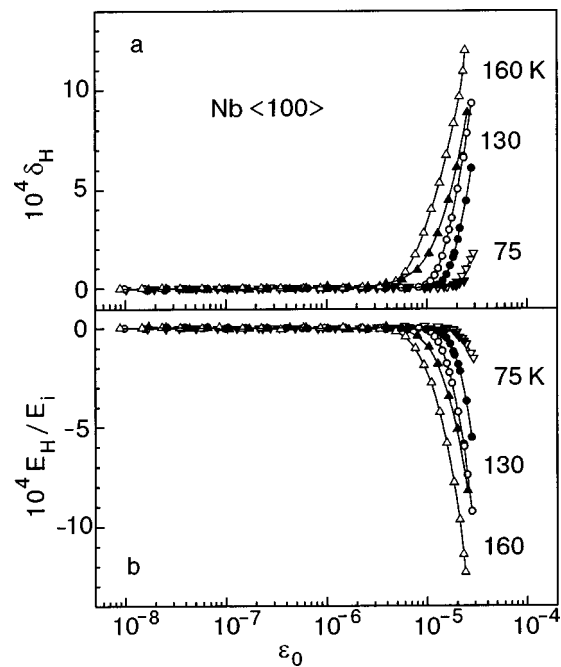

FIG. 4. Influence of plastic deformation on the amplitude dependence of the decrement (a) and dynamic Young's modulus (b): unfilled symbols—$\varepsilon_{pl}=0$; filled symbols—$\varepsilon_{pl}=0.65\%$; ▽, ▼—75 K; ○, ●—130 K; △, ▲—160 K.

plitude ε_{0c} for the start of nonlinear effects increases noticeably at all values of the temperature.

It should be noted that the $\delta_H(T,\varepsilon_0)$ and $E_H(T,\varepsilon_0)/E_i(T)$ curves shown in Figs. 2–4 are completely reversible, i.e., the values of the decrement and modulus defect measured on increasing and then decreasing ultrasound amplitude agree with each other to within the experimental error.

4. DISCUSSION

4.1. Linear effects

In this paper we mainly discuss amplitude-dependent (nonlinear) acoustic effects. Ultrasonic anomalies in the linear region of ultrasound absorption and the change of the elastic moduli in single-crystal and polycrystalline niobium of different purity and orientation have been discussed in detail in Refs. 8 and 10–13. Here it is appropriate merely to recall that the low-temperature Kramer–Bauer peak is a consequence of the resonance interaction of elastic vibrations with chains of geometric kinks on dislocations in the process of their thermally activated diffusion in the Peierls relief of the second kind.[8,10] This process is characterized by extremely low activation energies $U_0 \sim 3 \times 10^{-3}$ eV. The elementary mechanism responsible for the high-temperature α peak, as was shown in Ref. 13, is the nucleation of a pair of kinks on dislocation segments lying in the valleys of the Peierls relief of the first kind. This process corresponds to values of the activation energy $U_0 \cong 0.15$ eV.

It should be noted that both of the relaxation resonances are due to the initial dislocation structure of niobium—a system of screw or mixed dislocations arising during preparation of the samples in the slip planes {011} and {112} and located in the valleys of the Peierls relief. Electron microscope studies show that the plastic deformation of niobium crystals at room temperature gives rise to dislocations with a predominantly edge component,[18] and their dislocation lines are oriented at an angle to the valleys of the Peierls relief, and their mobility is mainly controlled by the impurity atoms. These dislocations have a definite influence on the parameters of the relaxation processes under discussion but do not lead to any fundamental changes in the conditions of their observation.[8,12]

4.2. Functional form of the dependences $\delta_H(\varepsilon_0,T)$ and $E_H(\varepsilon_0,T)$

The presence of amplitude dependence in these characteristics attests to the nonlinear character of the elastic and inelastic responses of the crystal to an externally applied periodic load. To establish the nature of the nonlinearity it is necessary to carry out an analysis of the functional form of the amplitude dependences and their behavior upon changes in temperature, and also to establish the value of r, the ratio of the amplitude-dependent component of the decrement to the relative value of the amplitude-dependent component of the Young's modulus: $r = \delta_H(\varepsilon_0)E_i/E_H(\varepsilon_0)$. Since in the investigated region of frequencies, vibration amplitudes, and temperatures the most likely mechanism of nonlinearity is the dislocation mechanism, the following analysis is based

mainly on the known theoretical ideas about dislocation hysteresis due to the breakaway of dislocations from impurity pinning points.

There exist several theoretical studies of the dislocation-related amplitude-dependent internal friction. Historically the first and most popular is the Granato–Lücke theory of dislocation hysteresis losses.[1] Using a string model of the dislocation, those authors made the assumption that an individual event contributing to the dislocation deformation (and hence, bringing about an additional sound absorption and modulus defect which increase with amplitude) is activationless "catastrophic" breakaway of dislocation segments from comparatively weak local pinning centers (e.g., impurity atoms). For an exponential distribution of lengths L of the dislocation segments an exponential dependence was obtained for the amplitude-dependent part of the decrement δ_H on the amplitude of the applied shear stress in the slip plane $\sigma_0 = G\varepsilon_0 = \Omega E\varepsilon_0$ (G is the shear modulus, Ω is an orientational factor that depends on the mutual position of the load axis, the normal to the slip plane, and the direction of the Burgers vector **b**):

$$\delta_H = \frac{8Gb^2\Lambda L_N^3}{\pi^4 CL_c}\left(\frac{\sigma_m}{\sigma_0} - 1 + \ldots\right)\exp\left(-\frac{\sigma_m}{\sigma_0}\right); \qquad (2a)$$

$$\sigma_m = \pi F_m/4bL_c. \qquad (2b)$$

Here b is the modulus of the Burgers vector, Λ is the dislocation density, L_N is the distance between insurmountable dislocation pinning centers (for example, nodes of a dislocation network), L_c is the mean length of a dislocation segment, which characterizes the average distance between "weak" obstacles (impurities and other point defects); $C \cong Gb^2/2$ is the linear tension of a dislocation,; σ_m is the critical stress for activationless breakaway of a dislocation; F_m is the maximum force binding a dislocation to a pinning center.

Strictly speaking, the conclusions of the theory of Ref. 1 are valid only for $T = 0$ K. In its subsequent modifications[2,19,20] it was shown that in the region of relatively low temperatures the character of the pinning of dislocations and, hence, the functional form of the amplitude dependences do not change when the temperature is raised, i.e., the dependence $\delta_H(\sigma_0)$ remains exponential as before. Taking thermal fluctuations into account reduces to a renormalization of the critical stress σ_m for breakaway, i.e., to its replacement by some effective stress with a value that should decrease with increasing temperature. At sufficiently low acoustic stresses ($\sigma_0 \ll \sigma_m$) one can restrict consideration in expression (2a) to one term of the expansion in the preexponential. In this case the agreement of the experimental data with the conclusions of the theory can be checked in the so-called Granato–Lücke coordinates, $\ln(\delta_H\varepsilon_0^{1/2})-(\varepsilon_0^{-1})$ (the power of 1/2 for ε_0 allows us to take into account the nonuniformity of the strain in the sample when the composite vibrator method is used). Figure 5 shows such reconstructed plots of $\delta_H(T,\varepsilon_0)$ for an undeformed niobium sample in the temperature interval where nonlinear effects are observed, 55 K$<T<$185 K (the initial data are presented in Fig. 3). It is seen that the experimental points conform well to the straight lines. The slope of the straight lines decreases with

increasing temperature, which leads to a decrease in the critical stress σ_m. In the case when L_c is constant this is equivalent to a decrease of the effective maximum binding force of the dislocation to the pinning centers F_m [see expressions (2a) and (2b)].

The problem of the breakaway of a double dislocation loop from a local pinning center at finite temperatures $T > 0$ K was considered in the Indenbom–Chernov theory of thermally activated dislocation hysteresis in Ref. 6. The following expression was found for the amplitude-dependent decrement δ_H:

$$\delta_H = L_{\min}^2 \int_{L_{\min}}^{L_N} L N(L) dL; \tag{3a}$$

$$L_{\min} = \bar{F}_m(T)/b\sigma_0. \tag{3b}$$

Here $\bar{F}_m = \bar{F}_m(T,f)$ is the temperature-dependent and sound-frequency-dependent critical value of the binding force of the dislocation to a defect, which brings about a thermally activated breakaway of the dislocation from the defect over an oscillation period. According to the theory,[6] at a constant value of the frequency f the change in temperature is equivalent to a change in the scale along the axis of load (strain). Consequently, the curves of the amplitude dependence of the decrement $\delta_H(T,\varepsilon_0)$ should go over to each other when the stress scale is changed or, equivalently, they should be parallel in a semilog plot in the coordinates $\delta_H - \log(\sigma_0)$. Such behavior is actually observed for the amplitude dependences obtained for niobium in the temperature interval 25–185 K (see Fig. 3). The functional form of $\delta_H(\sigma_0)$ in this case is determined by the type of distribution of the lengths of the dislocation segments. For an exponential distribution the amplitude dependence is also exponential:

$$\delta_H = \Lambda L_{\min}^2 \left(1 + \frac{L_{\min}}{L_c}\right) \exp\left(-\frac{L_{\min}}{L_c}\right), \tag{4}$$

and for the case of a power-law (with a power m) distribution function for the segment lengths we obtain the expression

$$\delta_H = \frac{\Lambda L_c^2}{m-2} \left(\frac{L_{\min}}{L_c}\right)^{-m+4}. \tag{5}$$

A power-law form of $\delta_H(\sigma_0)$ is also predicted by a number of other theories (see, e.g., Refs. 21–25) which use different models for describing the amplitude-dependent internal friction. Kharitonov[21] calculated the hysteresis losses in the breakaway of a dislocation pinned by impurities of different strengths. Asano,[22] building on the ideas of Davidenkov[23] and Pisarenko,[24] investigated the nonlinear losses associated with an above-barrier dislocation line viscously overcoming the stress field of the point defects surrounding it (the mechanism of "dry" friction). In this case it is assumed that reversible microplastic deformation is present, and the hysteresis loop on the $\sigma(\varepsilon_d)$ curve (ε_d is the dislocation strain), unlike the case for the breakaway mechanisms of Refs. 1, 2, and 6, does not pass through zero. Asano obtained the same power law for the amplitude-dependent decrement and modulus defect:
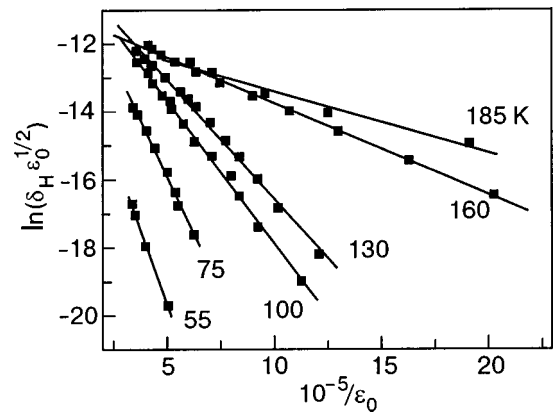

FIG. 5. Amplitude dependences of the decrement in an undeformed niobium sample in the temperature interval 55–185 K, plotted in Granato–Lücke coordinates.[1]

$$\delta_H \sim \varepsilon_0^n; \quad E_H/E_i \sim \varepsilon_0^n. \tag{6}$$

Such a model of the vibrations of a dislocation inside a Kottrell impurity atmosphere was also considered in the paper by Gelli.[25] The power-law character of the $\delta_H(\sigma_0)$ curves can easily be revealed in a log–log plot in the coordinates $\ln(\delta_H) - \ln(\sigma_0)$. However, a check done for the amplitude dependences $\delta_H(\varepsilon_0)$ and $E_H(\varepsilon_0)/E_i$ obtained in the present study showed that they, unlike the data obtained previously on high-purity iron,[26] are not described by the power law of the type in (6).

Thus in the investigated interval of temperatures and amplitudes the nonlinear losses in niobium are described satisfactorily in both the framework of the Granato–Lücke theory[1,2] and by the Indenbom–Chernov theory[6] under the assumption that the distribution of the impurities along the dislocation lines in niobium corresponds to an exponential distribution of the lengths of the dislocation segments.

4.3. Activation analysis

According to Eq. (2a), the slope of the straight lines in Granato–Lücke coordinates is determined by the value of the critical stress for breakaway, $\sigma_m = \pi F_m/4bL_c$. The results presented in Fig. 5 show that the value of σ_m decreases monotonically with increasing temperature in the interval 55–185 K. If it is assumed that the mean length L_c of the dislocation segments remains unchanged upon the change in temperature, then the observed behavior may be evidence of a lowering of the effective value of the binding force F_m of the dislocation to the pinning centers with increasing temperature: $F_m \rightarrow \bar{F}_m(T)$. With the assumptions made, the temperature dependence of the effective binding force of a dislocation to the obstacles, obtained with the use of the experimental data, is shown in Fig. 6 in the coordinates $T - \bar{F}_m(T)/\bar{F}_m(100 \text{ K})$.

The above interpretation of the influence of temperature on the nonlinear acoustic effects corresponds to the conclusions of the Indenbom–Chernov theory of thermally activated hysteresis.[6] In the "binding energy" approximation the amplitude-dependent decrement δ_H depends only on one parameter, $L_{\min} = \bar{F}_m/b\sigma_0$ [see Figs. (3a) and (4)]. The function $\bar{F}_m = \bar{F}_m(T,f)$ is a solution of the equation
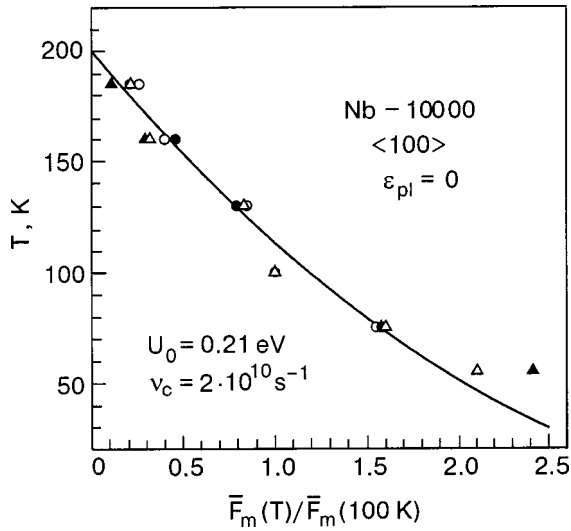
FIG. 6. Activation graph constructed by two methods: from the change in slope of the straight line in the Granato–Lücke coordinates (see Fig. 5) ($\triangle$) and from the change in the amplitude of the vibrations for sections of a series of $\delta_H(\varepsilon_0, T)$ curves at $\delta_H = $ const in Fig. 3 ($\blacktriangle$—$\delta_H = 1 \times 10^{-5}$; $\bigcirc$— $\delta_H = 5 \times 10^{-5}$; $\bullet$—$\delta_H = 1 \times 10^{-4}$). The solid curve shows the theoretical dependence (8).
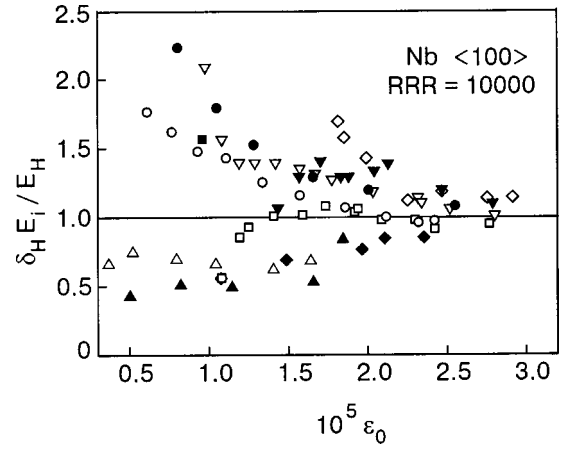

FIG. 7. Dependence of the parameter $r = \delta_H E_i / E_H$ on the amplitude of the acoustic strain at different temperatures in the initial sample (unfilled symbols) and after plastic deformation by $\varepsilon_{pl} = 0.65\%$ (filled symbols): $\diamondsuit$, $\blacklozenge$—75 K, $\square$, $\blacksquare$—100 K; $\triangledown$, $\blacktriangledown$—130 K; $\bigcirc$, $\bullet$—160 K; $\triangle$, $\blacktriangle$—185 K.

$$U(F) \cong k_B T \ln\left(\xi \frac{\nu_c}{f} \right), \tag{7a}$$

$$F = bL\sigma_0, \quad \nu_c \cong \frac{1}{2L_c}\left(\frac{C}{A} \right)^{1/2}, \tag{7b}$$

where $U(F)$ is the effective activation energy for the process of thermal-fluctuation breakaway of a dislocation segment of length L from a pinning center,[6,20] k_B is Boltzmann's constant, ξ is a constant of the order of unity, ν_c is an eigenfrequency of the vibrations of a dislocation segment of length L_c; $A = \rho b^2$ is the mass per unit length of the dislocation line; ρ is the density of the material. The $\delta_H = $ const tie lines of a series of amplitude dependences measured at different temperatures can be interpreted as the tie lines $L_{min} = $ const, and from the $\sigma_0(T)$ curve [and, hence, from $\bar{F}_m(T)$] one can assess the stress dependence of the activation energy, $U(bL_{min}\sigma_0)$. The results of such a procedure done for several values $\delta_H = $ const have been plotted in arbitrary units on the same graph as the data obtained in the framework of the Granato–Lücke theory (Fig. 6). The good agreement of the results obtained by the two substantially different methods is notable.

The use of expressions (2b) and (7b) allows one to obtain self-consistent estimates $L_c \approx 1 \times 10^{-5}$ cm and $\nu_c \approx 2 \times 10^{10}$ s^{-1}, while extrapolation of the data of Fig. 6 to $\bar{F}_m = 0$ gives the value of the binding energy U_0 of a dislocation to an obstacle [in units of $k_B \ln(\xi\nu_c/f)$]. To reduce the arbitrariness in making the extrapolation and determining U_0 one can use some sort of theoretical dependence of the activation energy on the stress. The use of the quadratic dependence proposed in Ref. 19,

$$U(F) = U_0(1 - F/F_m)^2, \tag{8}$$

which is in good agreement with the experimental results (the solid curve in Fig. 6) allows one to estimate the binding energy of the dislocations to the pinning centers as $U_0 = (0.21 \pm 0.01)$ eV.

4.4. Ratio δ_H / E_H

In the majority of studies of nonlinear acoustic effects it is the amplitude dependence of the absorption of ultrasound (the logarithmic decrement) that is analyzed, while the question of the functional form of the amplitude dependence of the modulus defect, as a rule, is not discussed. It was noted in the paper by Granato and Lücke[1] that for a catastrophic breakaway of dislocations at low sound amplitudes, $E_H(\varepsilon_0)/E_i$ behaves like $\delta_H(\varepsilon_0)$, so that to a first approximation the ratio of the amplitude-dependent decrement and Young's modulus should not depend on the amplitude and should have a value of the order of unity: $r = \delta_H E_i / E_H \sim 1$. A more detailed analysis in Ref. 9 showed that amplitude dependence of r can be absent only in the case when $\delta_H(\varepsilon_0)$ and $E_H(\varepsilon_0)/E_i$ are power-law functions with the same exponent n [see expression (6)]. Here the value of r is larger the greater the value of n, and the expected range of variation of r turns out to be substantially different for different models of the dislocation hysteresis. For the case of catastrophic breakaway one has $0.36 < r < 1.15$ for exponents in the range $1 < n < 10$. Under more general assumptions about the functional form of $\delta_H(\varepsilon_0)$ and $E_H(\varepsilon_0)/E_i$ the value of r in the framework of the catastrophic breakaway model cannot exceed $r_{max} = 2$. In the case when a hysteresis mechanism of the "dry" friction type is realized (when the dislocation segments overcome a large number of obstacles during a period of the vibrations), the values of r should be much larger ($1.33 < r < 5.41$ for $1 < n < 10$), and there should be no amplitude dependence of r.

Figure 7 shows the amplitude dependence of r obtained for various temperatures for undeformed and deformed samples of niobium. One notices the large scatter of the experimental points corresponding to the initial regions of the amplitude dependences (for small ε_0 the values of r lie in the interval $0.4 \lesssim r \lesssim 2.2$). The scatter may be due to the circum-

stance that the extraction of the small values of δ_H and E_H/E_i from the background of the rather sizable measured values of the decrement and Young's modulus in the initial parts of the amplitude dependences is associated with significant errors. These errors decrease with increasing δ_H and E_H/E_i as ε_0 increases. The scatter of the experimental points decreases noticeably, and a clear tendency for r to approach unity may be discerned. Such behavior of r has been obtained previously in studies of the amplitude dependence of the internal friction in iron[26] and zinc.[27] Unlike the data obtained in zinc,[27] in the present study we did not reveal any systematic change in the parameters of the dependence $r(\varepsilon_0)$ with changing temperature. At some temperatures the values of r at small amplitudes were less than unity, while for others they were greater than unity. We also did not discern any systematic change of r as a result of the the preliminary plastic deformation.

The indicated features of the behavior of r can be judged as one more piece of evidence that the high purity of the niobium sample makes it possible to achieve, in the investigated regions of temperature and ultrasound frequency, such experimental conditions which, according to the theories,[1,2,6] are necessary for reversible breakaway of dislocation segments from local pinning centers.

4.5. Influence of plastic deformation

Comparing the data of the undeformed sample and the sample preliminarily deformed at room temperature, we can see that the plastic deformation leads to a shift of the amplitude dependences $\delta_H(\varepsilon_0)$ and $E_H(\varepsilon_0)/E_i$ in the direction of higher amplitudes (see Fig. 4). This influence of plastic deformation was observed in the present study for the first time and is directly contrary to the influence that has usually been registered in other crystals, in particular, in single crystals of other bcc metals—iron,[26,28,31] molybdenum,[29,30] and tungsten.[31] It is known that as a result of plastic deformation the parameters of the dislocation structure of crystals changes substantially: the dislocation density Λ increases and there are changes in the mean length L_c of the dislocation segments and in the length distribution $N(L)$ of the segments. At small degrees of plastic deformation in rather pure crystals an increase in L_c can occur, both on account of the formation of fresh, comparatively long dislocation segments and on account of the tearing away of dislocations existing prior to the deformation from the Kottrell impurity atmospheres. Since an increase of the mean length of the dislocation segments leads to a decrease in the critical stress for the breakaway of the dislocations [see expressions (2) and (4)], the conditions for breakaway of dislocations from pinning centers become easier, and that should cause the amplitude dependences to shift to lower amplitudes of the ultrasound. The shift in the opposite direction of the amplitude dependences $\delta_H(\varepsilon_0)$ and $E_H(\varepsilon_0)/E_i$ which we observed in the present study may be a consequence of a decrease in L_c in the deformed sample. Moreover, if a catastrophic breakaway of dislocation segments occurs, then the shift of the amplitude dependences may also be due to a substantial decrease in the distance L_N between insurmountable obstacles [see expression (2)]. The cause of this change in the parameters of the dislocation structure may be multiple slips in the

sample. For the chosen geometry of loading of the sample, all four easy-slip systems have the same Schmid factors, which even in the early stage promote the development of slip simultaneously in several mutually intersecting planes. Here the probability of intersection of dislocations of different slip systems and the formation of additional insurmountable pinning centers (nodes of the dislocation network) increases substantially, and that can lead to a decrease of both L_N and L_c. For a conclusive answer to this question further studies of the dislocation structure of deformed niobium samples should be done by the methods of direct structural analysis, e.g., with the use of a high-voltage electron microscope.

4.6. The high- and low-temperature regions

At first glance the absence of amplitude dependence in the temperature region $210\ \text{K} < T < 300\ \text{K}$, near the α point, and in the low-temperature region $3\ \text{K} < T < 55\ \text{K}$, looks just as unusual. Indeed, in iron[26,28] the presence of the α peak had no effect whatsoever on the amplitude dependences: the amplitude dependences were obtained both below and above the temperature of the α peak, and their behavior corresponded to the ideas of thermally activated dislocation hysteresis[6] in the entire range of temperatures investigated. The authors of Refs. 26 and 28 came to the conclusion that the α peak and the amplitude dependences in iron are a reflection of different thermally activated dislocation processes: the formation of kink pairs on non-screw dislocations, and the breakaway, from local pinning centers, of dislocations crossing the primary Peierls relief at a small angle. Further, a study of deformed niobium samples at a frequency of 0.5 Hz in Ref. 32 revealed noticeable amplitude-dependent effects near and above the temperature of the α peak, which was observed near 135 K at that vibrational frequency. This even suggested to the authors that the microscopic mechanism of the α peak is the thermally activated depinning of dislocations from pinning centers in accordance with the Koiwa–Hasiguti model.[4] However, the absence of amplitude dependence of the acoustic characteristics in the temperature region 210–300 K in the present study finds a natural explanation if one turns to the result in Fig. 6, which gives the temperature dependence of the relative change in the effective binding force of dislocations to obstacles. Upon extrapolation of the graph to the value $\bar{F}_m = 0$ the intercept on the vertical axis at $T \approx 200\ \text{K}$ is the value of the temperature above which the activationless breakaway of dislocations should begin. Thus the absence of amplitude dependence in the temperature interval 210–300 K may be due to the circumstance that the dislocation breakaway mechanism responsible for the amplitude dependence at $55\ \text{K} \leqslant T \leqslant 185\ \text{K}$ is completely exhausted in the region $T > 200\ \text{K}$. The coincidence with the temperature position of the α peak is accidental and is due to the choice of frequency used to excite vibrations in the sample.

The absence of amplitude dependence of the acoustic characteristics in the low-temperature region can be explained by the circumstance that the values of ε_0 achieved in the experiment are too low to cause breakaway of the dislocation segments at temperatures $T < 25\ \text{K}$. However, extrapolation of the graph in Fig. 6 to $T = 0\ \text{K}$ in accordance with expression (8) shows that the amplitude dependence of

$\delta_H(\varepsilon_0)$ should be observed all the way down to the lowest temperatures, and it should have values not lower than $\delta_H \approx 1 \times 10^{-4}$. The observed discrepancy between the experimental data and the predictions of the theory may be due to the fact that the use of formula (8) for interpretation of the data of a low-temperature experiment is incorrect, and one must use a function which is smoother in the region of high values of F, which correspond to low temperatures. The threshold behavior of the dependence $U(F)$ was noted previously in a study of the amplitude dependences in molybdenum of high purity.[33] Such a form of the dependences $U(F)$ may mean a sharp decrease in the activation volume $V = -dU/d\sigma$ upon reaching low temperatures. The corresponding estimates show that at liquid helium temperatures the activation volume should decrease to a value $V \sim 1-2 \text{ b}^3$, whereas expression (8) gives a value $V \sim 60-80 \text{ b}^3$ in this same temperature interval.

CONCLUSIONS

1. The amplitude dependences of the decrement and Young's modulus defect in niobium single crystals of high purity are due to a thermally activated breakaway of dislocations from local (impurity) pinning centers. The evidence for this comes from the functional form of the amplitude dependences, their behavior upon a change in temperature, and also the ratio between the values of the amplitude-dependent components of the decrement and Young's modulus.

2. In the temperature region 55–185 K the behavior of the amplitude dependences is consistently described by the Granato–Lücke theory of athermal dislocation hysteresis and its generalization by Indenbom and Chernov to the case of thermally activated dislocation hysteresis.

3. The interpretation of the experimental results in the framework of these theories allows one to conclude that the distribution of the dislocation segments over lengths in the high-purity niobium crystals studied is exponential, and one can estimate the binding energy of the dislocations to the pinning centers as $U_0 \approx 0.21$ eV.

The fact that amplitude dependence was not observed in the temperature region $T < 25$ K in the experiments and the unusual change of the parameters of the amplitude dependences after plastic deformation do not yet have a definitive interpretation; these questions will require further study.

*E-mail: palval@ilt.kharkov.ua

[1] A. V. Granato and K. Lücke, J. Appl. Phys. **27**, 583 (1956).
[2] A. V. Granato and K. Lücke, J. Appl. Phys. **52**, 7136 (1981).
[3] G. Alefeld, J. Appl. Phys. **36**, 2642 (1965).
[4] M. Koiwa and R. R. Hasiguti, Acta Metall. **13**, 1219 (1965).
[5] A. Zeger and P. Shiller, in *Physical Acoustics*, edited by W. P. Mason, Vol. 3, Part A, Academic Press, New York (1965), Mir, Moscow (1969).
[6] V. L. Indenbom and V. M. Chernov, Phys. Status Solidi A **14**, 347 (1972).
[7] V. D. Natsik and P. P. Pal-Val, Mater. Sci. Eng., A **164**, 312 (1993).
[8] P. P. Pal-Val, V. D. Natsik, and L. N. Pal-Val, Fiz. Nizk. Temp. **21**, 647 (1995) [Low Temp. Phys. **21**, 505 (1995)].
[9] A. B. Lebedev, Philos. Mag. A **74**, 137 (1996).
[10] V. D. Natsik and P. P. Pal-Val, Fiz. Nizk. Temp. **23**, 1229 (1997) [Low Temp. Phys. **23**, 922 (1997)].
[11] P. P. Pal-Val, Fiz. Nizk. Temp. **23**, 1250 (1997) [Low Temp. Phys. **23**, 938 (1997)].
[12] P. P. Pal-Val, V. D. Natsik, L. N. Pal-Val, and Yu. A. Semerenko, Fiz. Nizk. Temp. **25**, 748 (1999) [Low Temp. Phys. **25**, 558 (1999)].
[13] P. P. Pal-Val, V. D. Natsik, L. N. Pal-Val, and Yu. A. Semerenko, Fiz. Nizk. Temp. **27**, 547 (2001) [Low Temp. Phys. **27**, 404 (2001)].
[14] B. Fellmuth, D. Elefant, and J.-I. Mönch, Phys. Status Solidi A **100**, 597 (1987).
[15] B. Fellmuth, H. Maas, and D. Elefant, Metrologia **21**, 169 (1985).
[16] P. P. Pal'-Val' and H.-J. Kaufmann, Fiz. Nizk. Temp. **9**, 325 (1983) [Sov. J. Low Temp. Phys. **9**, 163 (1983)].
[17] V. D. Natsik, P. P. Pal-Val, and S. N. Smirnov, Akusti cheskiĭ zhurnal **44**, 640 (1998).
[18] L. P. Kubin, Comments Condens. Matter Phys. **14**, 69 (1988).
[19] L. J. Teutonico, A. V. Granato, and K. Lücke, J. Appl. Phys. **35**, 220 (1964).
[20] K. Lücke A. V. Granato, and L. J. Teutonico, J. Appl. Phys. **39**, 5181 (1968).
[21] A. V. Kharitonov, Akust. Zh. **11**, 226 (1965).
[22] S. Asano, J. Phys. Soc. Jpn. **29**, 952 (1970).
[23] N. N. Davidenkov, Zh. Tekh. Fiz. **8**, 483 (1938).
[24] G. S. Pisarenko, in *Energy Dissipation in Mechanical Oscillations* [in Russian], Izd-vo AN USSR, Kiev (1962), p. 146.
[25] D. Gelli, J. Appl. Phys. **33**, 1547 (1962).
[26] P. P. Pal-Val, Fiz. Nizk. Temp. **25**, 83 (1999) [Low Temp. Phys. **25**, 63 (1999)].
[27] V. Ya. Platkov and I. K. Nosolev, Izv. Ross. Akad. Nauk Fiz. **57**, 26 (1993).
[28] P. P. Pal-Val, V. D. Natsik, and S. Kadeckova, Philos. Mag. A **56**, 407 (1987).
[29] P. P. Pal-Val and H.-J. Kaufmann, Cryst. Res. Technol. **19**, 1049 (1984).
[30] P. P. Pal'-Val', H.-J. Kaufmann, and V. I. Startsev, Fiz. Tverd. Tela (Leningrad) **27**, 852 (1985) [Sov. Phys. Solid State **27**, 522 (1985)].
[31] G. S. Baker and S. H. Carpenter, J. Appl. Phys. **38**, 3557 (1967).
[32] R. Klam, H. Schultz, and H. E. Schaefer, Acta Metall. **28**, 259 (1980).
[33] H.-J. Kaufmann and P. P. Pal-Val, Phys. Status Solidi A **62**, 569 (1980).

Translated by Steve Torstveit

ERRATA

Erratum: Anisotropy of the critical current and the guided motion of vortices in a stochastic model of bianisotropic pinning. II. Observed effects (**Low Temp. Phys. 28, 312 (2002)**)

V. A. Shklovskij and A. A. Soroka
Fiz. Nizk. Temp. **30**, 126 (January 2004)
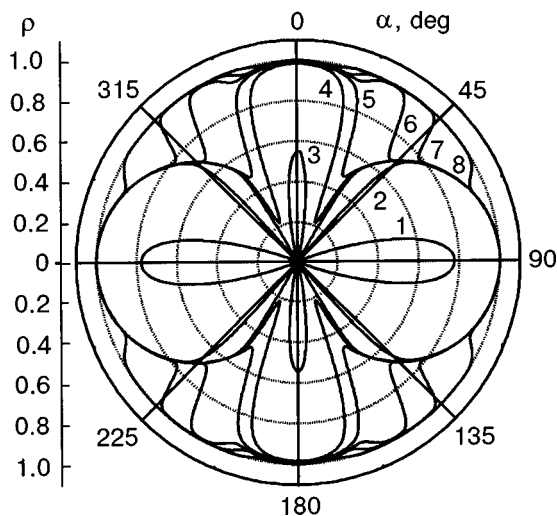
Figure 10 should have the following form:

FIG. 10. Series of graphs of the function $\rho(\alpha)$ for a sequence of values of the parameter j: 0.66 (*1*), 1 (*2*), 1.34 (*3*), 1.43 (*4*), 1.48 (*5*), 1.7 (*6*), 2 (*7*), 3 (*8*) for $p=1.4$, $\tau=0.01$, $\varepsilon=0.001$, $k=1$; $\alpha^*=27°$.